The Majorana Neutrinoless Double-Beta Decay Experiment

Pre-conceptual Design Proposal

November 22, 2006

The *Majorana* Collaboration

Alexander Barabash, Sergey Konovalov, Igor Vanushin, Vladimir Yumatov
Institute for Theoretical and Experimental Physics, Moscow, Russia

Viktor Brudanin, Slava Egorov, K. Gusey, S. Katulina, Oleg Kochetov, M. Shirchenko, Yu. Shitov, V. Timkin, T. Vvlov, E. Yakushev, Yu. Yurkowski
Joint Institute for Nuclear Research, Dubna, Russia

Yuen-Dat Chan, Mario Cromaz, Brian Fujikawa, Reyco Henning, Donna Hurley, Kevin T. Lesko, Paul Luke, Akbar Mokhtarani, Alan Poon, Gersende Prior, Nikolai Tolich Craig Tull
Lawrence Berkeley National Laboratory, Berkeley, California

Dave Campbell, Kai Vetter
Lawrence Livermore National Laboratory, Livermore, California

Steven Elliott, Gerry Garvey, Victor M. Gehman, Vincente Guiseppe, Andrew Hime, Bill Louis, Geoffrey Mills, Keith Rielage, Larry Rodriguez, Richard Schirato, Laura Stonehill, Richard Van de Water, Hywel White, Jan Wouters
Los Alamos National Laboratory, Los Alamos, New Mexico

Cyrus Baktash, Jim Beene, Fred Bertrand, David Radford, Chang-Hong Yu
Oak Ridge National Laboratory, Oak Ridge, Tennessee

Hiroyasu Ejiri, Ryuta Hazama, Masaharu Nomachi, Shima Tatsuji
Osaka University, Osaka, Japan

Craig Aalseth, Ronald Brodzinski, James Ely, Tom Farmer, Jim Fast, Eric Hoppe, Brian Hyronimus, David Jordan, Jeremy Kephart, Richard T. Kouzes, Harry Miley, John Orrell, Jim Reeves, Robert Runkle, Bob Schenter, John Smart, Bob Thompson, Ray Warner, Glen Warren
Pacific Northwest National Laboratory, Richland, Washington

Fraser Duncan, Aksel Hallin, Art McDonald
Queen's University, Kingston, Ontario

Henning O. Back, James Esterline, Mary Kidd, Werner Tornow, Albert Young
Triangle Universities Nuclear Laboratory, Durham, North Carolina and Physics Departments at Duke University and North Carolina State University

Phil Barbeau, Juan Collar, Keith Crum, Smritri Mishra, Brian Odom, Nathan Riley
University of Chicago, Chicago, Illinois

Frank Avignone, Richard Creswick, Horatio A. Farach, Todd Hossbach, George King
University of South Carolina, Columbia, South Carolina

Tina Keller, Dongming Mei
University of South Dakota, Vermillion, South Dakota

William Bugg, Tom Handler, Yuri Efremenko, Brandon White
University of Tennessee, Knoxville, Tennessee

John Amsbaugh, Tom Burritt, Jason A. Detwiler, Peter J. Doe, Alejandro Garcia, Mark Howe, Robert A. Johnson, Michael G. Marino, Sean McGee, R. G. Hamish Robertson, Alexis G. Schubert, Brent VanDevender, John F. Wilkerson
University of Washington, Seattle, Washington

Contents

1 Executive Summary

Neutrinoless double-beta decay provides the physics community with the opportunity to build on our successes in understanding the neutrino and crafting a new standard model. With the results from Super-Kamiokande, SNO, KamLAND, and other neutrino experiments we have demonstrated that neutrinos are massive, change flavor, and play an important role in the universe. These results have yielded the first physics beyond the standard model in nearly four decades. Even with these impressive results, neutrinos continue to provide some of the most exciting opportunities in understanding our universe. Theoretical prejudices for Majorana neutrinos have existed for decades and neutrinoless double-beta decay is the only practical technique that can determine whether neutrinos are Majorana or Dirac particles. For the first time we can mount experiments that probe the neutrino-mass region below the upper limits set by direct kinematical searches (tritium) and suggested by observational cosmology, while planning scaled approaches that can address the lower bounds of mass defined by the atmospheric and solar plus reactor neutrino oscillation experiments. Measuring the absolute mass of neutrinos and determining their Majorana nature are two of the most important goals of the physics community today. We propose here a plan and process for achieving these goals.

The objective of the first experimental phase of Majorana is to build a 120-kg array of high-purity Ge, enriched to 86% in ^{76}Ge, to search for neutrinoless double-beta ($0\nu\beta\beta$) decay[1]. The physics goals for this first phase are to:

- Probe the quasi-degenerate neutrino mass region above 100 meV.
- Demonstrate that backgrounds at or below 1 count/ton/year in the $0\nu\beta\beta$-decay peak 4-keV region of interest (1 count/ROI/t-y) can be achieved that would justify scaling up to a 1 ton or larger mass detector.
- Definitively test the Klapdor-Kleingrothaus claim [Kla04] of an observation of $0\nu\beta\beta$ decay in ^{76}Ge in the mass region around 400 meV.

These goals are consistent with recommendations from the *DNP/DPF/DAP/DPB Joint Study on the Future of Neutrino Physics* [Fre04] and the conclusions on $0\nu\beta\beta$ decay reported by the Neutrino Scientific Assessment Group (NuSAG) [NUSAG05]. They are also supported by the recent recommendations of HEPAP's Particle Physics Project Prioritization Panel (P5) October 2006 Particle Physics Roadmap [P5RM06]. All of these reports have emphasized the need to study $0\nu\beta\beta$ decay in different isotopes and with different experimental techniques.

Our proposed method uses the well-established technique of searching for $0\nu\beta\beta$ decay in high-purity Ge-diode radiation detectors that play both roles of source and detector. The technique is augmented with recent improvements in signal processing and detector design, and advances in controlling intrinsic and external backgrounds. Progress in signal processing from segmented Ge-diode detectors potentially offers significant benefits in rejecting backgrounds, reducing sensitivity of the experiment to backgrounds, and providing additional handles on both signals and backgrounds through multi-dimensional event reconstruction. Development of sophisticated Cu-electroforming methods allow the fabrication of ultra-low-background materials required for the construction of next-generation experiments. It is important to note that Ge-based detectors are the only next-generation $0\nu\beta\beta$ experiments that are currently proposing to perform near background-free measurements in the $0\nu\beta\beta$-decay peak region of interest. This will be a critical factor in convincing the community of the validity of any future result that claims to observe this rare decay mode.

The initial Majorana experiment will consist of 114 ^{76}Ge crystals in the form of high-resolution intrinsic germanium detectors, deployed in two 57-crystal modules, located deep underground within a low-background shielding environment. This represents more than an order-of-magnitude increase

[1] 103 kg of ^{76}Ge.

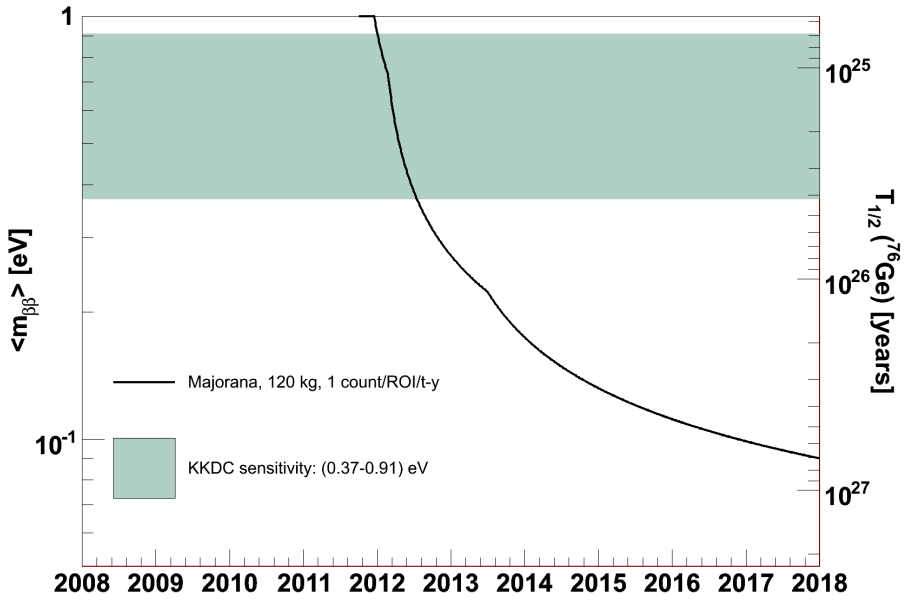

Figure 1.1: Anticipated sensitivity of the proposed 120-kg Majorana experiment as a function of calendar year. The assumed project schedule is discussed briefly in Section 3.2.4 and in more detail in the separate *Majorana Draft Management Plan* document. Note KKDC refers to the positive $0\nu\beta\beta$ decay result reported by Klapdor-Kleingrothaus *et al.*[Kla04].

in the mass of enriched isotope over previous generation Ge-based experiments. The justification for a detector mass size of 120 kg is directly linked to all three of the science goals:

- To achieve sensitivity to masses within the quasi-degenerate neutrino mass region within a reasonable time frame (5 years), which will equal or surpass other international efforts that are currently underway.
- To field a sufficiently sized array to allow demonstration of backgrounds for a 1 ton detector, both in terms of realistically sized modules and to provide statistically significant background measurements.
- To perform a precision test within a reasonable time frame of the Klapdor-Kleingrothaus claim. The Majorana experiment will have much lower background and substantially higher statistical significance than other efforts.

Observation of a sharp peak at the $\beta\beta$ endpoint would quantify the $0\nu\beta\beta$-decay rate, demonstrate that neutrinos are Majorana particles, indicate that lepton number is not conserved, and provide a measure of the effective Majorana mass of the electron neutrino. As shown in Figure 1.1, Majorana will either conclusively establish the Klapdor-Kleingrothaus claim of double-beta decay, discover a Majorana mass below Klapdor-Kleingrothaus's sensitivity, or will significantly improve the lower limits on the decay lifetime from the current level of about 2×10^{25} years to about 7×10^{26} years, corresponding to an upper limit of 90 meV on the effective Majorana electron-neutrino mass.

This document is organized into three chapters:

- Chapter 2, **Majorana Science Motivation**, provides an introduction to the physics motivation for neutrinoless double-beta decay, summarizes the guidance from the physics community, explains how one extracts neutrino mass information from the observables, provides information on previous $0\nu\beta\beta$ results, and discusses considerations for next-generation double-beta decay experiments.

- Chapter 3, **The Majorana Experiment**, presents the advantages of a ^{76}Ge based $0\nu\beta\beta$ experiment, justifies selecting a mass of 120 kg, defines our current reference plan and provides a complete technical description of the currently envisioned experiment. This chapter also presents alternative technical options under examination.

- Chapter 4, **Majorana Backgrounds and Sensitivity**, defines the sensitivity to $0\nu\beta\beta$, explains methods to mitigate backgrounds, discusses methods to assay the activity of materials, summarizes the current Majorana background budget, and presents our current estimate of sensitivity to neutrino mass.

There are also two accompanying, but separate, documents to this pre-conceptual design proposal.

- The *Majorana Project Research and Development Plan* presents the proposed project R&D plan. It also provides summary information on some of our previous pre-conceptual R&D accomplishments and presents a summary of outstanding R&D issues within the context of risk mitigation.

- The *Majorana Draft Management Plan* explains the project's organization and presents an outline of how we propose to manage the construction process. This document also provides information on the Work Breakdown Structure based on the current reference plan, along with an estimated budget and project schedule.

The proposed Majorana Scientific Collaboration would consists of about 100 scientists and 16 collaborating institutions from four countries, with extensive experience in double-beta decay and ultra-low-background experiments. The scientific and technical experience of this team is ideally matched to the experimental requirements and the team is strongly motivated by the opportunity to address very fundamental scientific questions. The excitement that this challenge offers is reflected in the very high quality of graduate students, postdocs, and young faculty that we have been able to attract to the collaboration.

Neutrinoless double-beta decay experiments have the potential to dramatically alter our understanding of neutrinos, fundamental interactions, and the role neutrinos play in the universe. Majorana offers an opportunity to lead this quest with an experiment deployed in North America.

2 Majorana Science Motivation

This is an exciting time in our quest to understand neutrinos — fundamental particles that play key roles in the early universe, in cosmology and astrophysics, and in nuclear and particle physics. Recent results from atmospheric, solar, and reactor-based neutrino oscillation experiments (Super-Kamiokande, SNO, and KamLAND)[Ash04, Ahm04, Ara04] have provided compelling evidence that neutrinos have mass and give the first indication after nearly forty years of study that the Standard Model (SM) of nuclear and particle physics is incomplete.

2.1 Physics Motivation for Neutrinoless Double-Beta Decay Experiments

With the realization that neutrinos are massive, there is an increased interest in investigating their intrinsic properties. Understanding the neutrino mass generation mechanism, the absolute neutrino mass scale and the neutrino mass spectrum are some of the main focuses of future neutrino experiments.

Lepton number L is conserved in the Standard Model because neutrinos are assumed to be massless and there is no chirally right-handed neutrino field. The guiding principles for extending the Standard Model are the conservation of electroweak isospin and renormalizability, which do not preclude each neutrino mass eigenstate ν_i to be identical to its anti-particle $\bar{\nu}_i$, or a "Majorana" particle. However, L is no longer conserved if $\nu = \bar{\nu}$. Theoretical models, such as the seesaw mechanism that can explain the smallness of neutrino mass, favor this scenario. Therefore, the discovery of Majorana neutrinos would have profound theoretical implications in the formation of a new Standard Model while yielding insights into the origin of mass itself. If neutrinos are Majorana particles, they may fit into the leptogenesis scenario for creating the baryon asymmetry, and hence ordinary matter, of the universe. As of yet, there is no firm experimental evidence to confirm or refute this theoretical prejudice. Experimental evidence of neutrinoless double-beta $0\nu\beta\beta$ decay would definitevely establish the Majorana nature of neutrinos (see Section 2.2).

A complete understanding of the neutrino mass matrix depends on four types of data: neutrino oscillations, direct kinematical measurements, cosmological observations, and neutrinoless double-beta decay. The results of atmospheric, solar, and reactor neutrino oscillation experiments have provided evidence for neutrino mass, and have determined the relative splitting of the mass eigenstates. These experiments show that at least one neutrino has a mass greater than $\sim$50 meV. The absolute scale can only be obtained from direct mass measurements (such as ^{3}H end point measurements [Osi01]), cosmological observations [Spe03], or by $0\nu\beta\beta$ decay in the case of Majorana neutrinos. Not only is neutrinoless double-beta decay the only practical method to uncover the Majorana nature of neutrinos, it is also the only practical method to reach an absolute mass scale sensitivity of $<$50 meV (see Section 2.2).

In addition, neutrinoless double-beta decay experiments complement long-baseline neutrino oscillation experiments in establishing the hierarchy of the neutrino mass eigenstates (see Section 2.2.2). In a $0\nu\beta\beta$ experiment, the mass hierarchy can be determined by probing the Majorana neutrino mass (see Figure 2.2). To reach the Majorana mass sensitivity of $<$50 meV requires a target mass of the order of 500 to 1000 kg. The Majorana collaboration has adopted an experimental program in pursuit of this goal.

2.1.1 Community Guidance

The nuclear and high energy physics communities have recently stressed the need for neutrinoless double-beta decay experiments. The scientific motivation for their undertaking has been amply described and strongly endorsed by several recent national reviews including: the 2000-2001 Nuclear Science Advisory Committee's (NSAC) Long Range Plan; the National Research Council's (NRC) 2002 Quarks to Cosmos study, the NRC's Neutrino Facilities Assessment Committee 2003 report; the 2005 American Physical Society's (APS) Multidivisional Joint Study on the Future of Neutrino

Physics; a detailed assessment from the Neutrino Scientific Assessment Group (NuSAG), a joint sub-committee formed by the NSAC and the High Energy Physics Advisory Panel (HEPAP) to advise DOE and NSF on specific questions related to the U.S. neutrino physics program, issued in September 2005; and the Particle Physics Project Prioritization Panel (P5) HEPAP Subpanel's Particle Physics Roadmap report of October 2006.

The *APS DNP/DPF/DAP/DPB Joint Study on the Future of Neutrino Physics* [Fre04] report gives as its first of three recommendations:

> *We recommend, as a high priority, a phased program of sensitive searches for neutrinoless nuclear double-beta decay.*

This study also provided the field with advice on how to carry out such investigations. They recommended a high priority to perform a precision measurement with sensitivity to the neutrino mass in the "quasi-degenerate" region (greater than about 100 meV). The study suggested that experiments will require approximately 200 kg of target mass to accomplish this goal, with the precise quantity dependent on isotope-specific parameters such as phase-space volume and nuclear matrix elements, and experiment-specific parameters such as background, detector energy resolution, and the length of data collection period. The study further recommended that this initial configuration should be scalable to a 1-ton-scale experiment that would have a discovery potential near the mass scale defined by atmospheric neutrino oscillation experiments (about 45 meV). Finally, the study recognized the need to undertake multiple $0\nu\beta\beta$ experiments with different isotopes and experimental techniques. This will provide the required independent confirmation of any reported discovery. In addition, multiple $0\nu\beta\beta$ experiments will allow a probe of the isotope-dependent uncertainties, such as those associated with nuclear matrix element calculations, and help deduce neutrino properties of fundamental importance.

The report [NUSAG05] from the Neutrino Scientific Assessment Group (NuSAG) made similar recommendations, to

> *... explore the region of degenerate neutrino masses ($\langle m_\nu \rangle > 100$ meV). The knowledge gained and the technology developed in the first phase should then be used in a second phase to extend the exploration into the inverted hierarchy region of neutrino masses ($\langle m_\nu \rangle > 10 - 20$ meV).*

The NuSAG report also recommended that three U.S. based next-generation $0\nu\beta\beta$ experiments, CUORE [Arn04], EXO [Aki05], and Majorana (listed alphabetically), have the highest funding priority. In addressing Majorana the report stated:

> *The excellent background rejection achieved from superior energy resolution in past ^{76}Ge experiments must be extended using new techniques. The panel notes with interest the communication between the Majorana and GERDA ^{76}Ge experiments which are pursuing different background suppression strategies. The panel supports an experiment of smaller scope than Majorana-180 that will allow verification of the projected performance and achieve scientifically interesting physics sensitivity, including confirmation or refutation of the claimed ^{76}Ge signal. A larger ^{76}Ge experiment is a good candidate for a larger international collaboration due to the high cost of the enriched isotope.*

Finally, HEPAP's Particle Physics Project Prioritization Panel (P5) October 2006 Particle Physics Roadmap [P5RM06] states as one of its recommendations regarding neutrino physics:

> *The three techniques to measure neutrino-less beta decay, CUORE, EXO, and Majorana should be investigated vigorously, leading to a selection of one technique for an experiment at the 1-10 ton scale.*

Based on the community guidance coupled with an assessment of the international context of proposed next generation double-beta decay experiments, the Majorana collaboration has adopted an experimental program with an initial mass of 120 kg of 86% enriched ^{76}Ge. This will allow results from Majorana to be competitive with other proposed next-generation experiments despite an anticipated delayed start of construction compared to some of these other efforts. Additional details and justification for this initial mass are provided in Section 3.2.

With the goal of ultimately realizing a 1-ton scale detector, the Majorana collaboration has also established a formal cooperative agreement with the GERDA collaboration, an European ^{76}Ge $0\nu\beta\beta$ effort. The collaborations have agreed to share resources and knowledge where appropriate in their parallel development of the two different detector designs with the eventual objective of combining strengths in a joint future experiment that will employ the best technology for reaching a Majorana mass sensitivity below 50 meV. This is discussed in more detail in Section 3.2.4.

2.2 Double-Beta Decay Processes

Ordinary beta decay of many heavy even-even nuclei is energetically forbidden. However, a process in which a nucleus changes its atomic number (Z) by two while simultaneously emitting two beta particles is energetically possible for some even-even nuclei. Such two-neutrino double-beta decay ($2\nu\beta\beta$)

$$^{Z}A \Rightarrow^{Z+2} A + 2e^{-} + 2\overline{\nu}_e, \tag{2.1}$$

is an allowed second-order weak process that occurs in nature, although its rate is extremely low. Half-lives for this decay mode have been measured at $\sim 10^{19}$ years or longer in several nuclei.

The more interesting process is zero-neutrino double-beta decay ($0\nu\beta\beta$),

$$^{Z}A \Rightarrow^{Z+2} A + 2e^{-}, \tag{2.2}$$

where no neutrino is emitted. Unlike $2\nu\beta\beta$, $0\nu\beta\beta$ violates lepton number conservation and hence requires physics beyond the Standard Model. One can visualize $0\nu\beta\beta$ as an exchange of a virtual neutrino between two neutrons within the nucleus. In the framework of the $\mathrm{SU}_L(2)\times$ U(1) Standard Model of weak interactions, the first neutron emits a right-handed anti-neutrino. However, the second neutron requires the absorption of a left-handed neutrino. In order for this to happen, the neutrino must have mass so that it is not in a pure helicity state, and the neutrino and anti-neutrino have to be indistinguishable. That is, the neutrino would have to be a massive Majorana particle.

2.2.1 Decay Rate

Many processes have been proposed to drive neutrinoless double-beta decay; for example, intrinsic right-handed currents and the exchange of supersymmetric particles. Regardless of the process, the existence of $0\nu\beta\beta$ implies the existence of a non-zero Majorana neutrino mass term [Sch82]. Hereafter the discussion is restricted to the $0\nu\beta\beta$ process due to the Majorana mass term.

The decay rate for $0\nu\beta\beta$ is expressed as follows:

$$\left[T^{0\nu}_{1/2}\right]^{-1} = G^{0\nu}(E_0, Z)\left|\langle m_\nu\rangle\right|^2 \left|M^{0\nu}_F - (g_A/g_V)^2 M^{0\nu}_{GT}\right|^2 \tag{2.3}$$

where $G^{0\nu}$ is the two-body phase-space factor including the coupling constant, $M^{0\nu}_F$ and $M^{0\nu}_{GT}$ are the Fermi and Gamow-Teller nuclear matrix elements, and g_A and g_V are the axial-vector and vector relative weak coupling constants. The quantity $\langle m_\nu\rangle$ is the effective Majorana electron neutrino mass given by:

$$\langle m_\nu\rangle \equiv \left|U_{e1}\right|^2 m_1 + \left|U_{e2}\right|^2 m_2 e^{i\phi_2} + \left|U_{e3}\right|^2 m_3 e^{i\phi_3}, \tag{2.4}$$

where the U_{ei} are the elements of the leptonic mixing matrix, $e^{i\phi_2}$ and $e^{i\phi_3}$ are the relative CP phases (± 1 for CP conservation) and $m_{1,2,3}$ are the neutrino mass eigenvalues. In theories with

CP violation, ϕ_2 and ϕ_3 become arbitrary angles that depend on linear combinations of one Dirac (testable in neutrino oscillations) and two Majorana CP-violating angles.

The conventional form of the leptonic mixing matrix U is[2]:

$$\begin{bmatrix} |\nu_e\rangle \\ |\nu_\mu\rangle \\ |\nu_\tau\rangle \end{bmatrix} = \begin{bmatrix} c_{12}c_{13} & s_{12}c_{13} & s_{13}e^{-i\delta} \\ -s_{12}c_{23} - c_{12}s_{23}s_{13}e^{i\delta} & c_{12}c_{23} - s_{12}s_{23}s_{13}e^{i\delta} & s_{23}c_{13} \\ s_{12}s_{23} - c_{12}c_{23}s_{13}e^{i\delta} & -c_{12}s_{23} - s_{12}c_{23}s_{13}e^{i\delta} & c_{23}c_{13} \end{bmatrix} \times \begin{bmatrix} e^{i\alpha_1} & 0 & 0 \\ 0 & e^{i\alpha_2} & 0 \\ 0 & 0 & 1 \end{bmatrix} \times \begin{bmatrix} |\nu_1\rangle \\ |\nu_2\rangle \\ |\nu_3\rangle \end{bmatrix} \quad (2.5)$$

where $c_{ij} = \cos\theta_{ij}$, $s_{ij} = \sin\theta_{ij}$ and θ_{ij} are the three mixing angles. The diagonal matrix that contains Majorana CP phases does not appear in neutrino oscillations.

Atmospheric neutrino oscillation data [Tos01, Hai03] indicate maximal mixing in the 2-3 sector (i.e. θ_{23} is near 45°). Solar and reactor neutrino oscillation data [Aha05, Ara04, Bah03, Egu03, Fuk02, Ahm01, for example] give $\theta_{12} \sim 34°$. The CHOOZ and Palo Verde experiments [Apo99, Boe01] constrain θ_{13} to be $<\sim 10°$. In addition, these experiments have indicated values of $\delta m^2_S \approx 8 \times 10^{-5}\text{eV}^2$ for the mass-squared splitting in solar/reactor neutrino oscillations and $\delta m^2_{AT} \approx 2 \times 10^{-3}\text{eV}^2$ for atmospheric neutrino oscillations. The matter effect in the sun enables the sign of δm^2_{AT} to be determined with m_2 greater than m_1. The parameters α_1, α_2 and δ in Equation 2.5 (and hence ϕ_2 and ϕ_3) are currently unknown.

2.2.2 Majorana Neutrino Mass

The measured values of δm^2_S (solar) and δm^2_{AT} (atmospheric) given earlier restrict the pattern of masses to two possible hierarchies, "normal" and "inverted", shown in Figure 2.1.

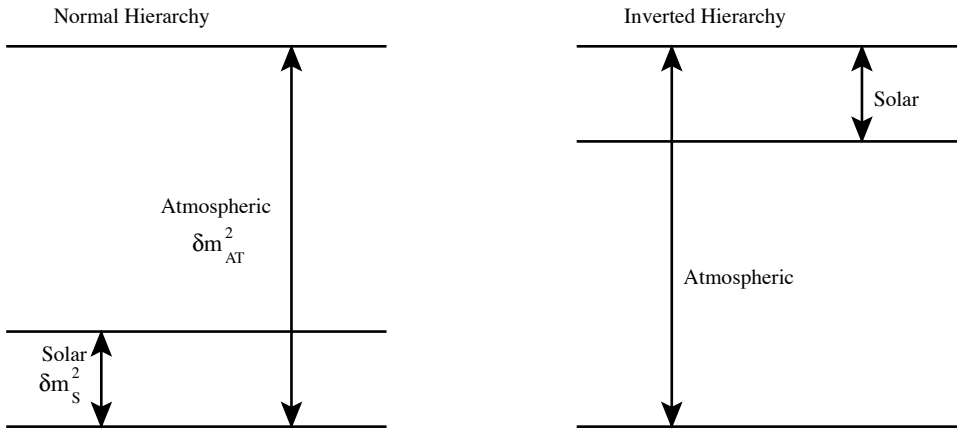

Figure 2.1: Normal and inverted mass hierarchies. In both cases, our notation defines the lightest mass as m_1 and the heaviest as m_3.

Defining the lightest mass as m_1 and the heaviest mass as $m_3 = \sqrt{\delta m^2_{AT} + m^2_1}$, we can write $m_2 = \sqrt{\delta m^2_S + m^2_1}$ in the case of normal hierarchy and $m_2 = \sqrt{\delta m^2_{AT} - \delta m^2_S + m^2_1}$ in the case of inverted hierarchy. From these we can write $|\langle m_\nu \rangle|$, for normal and inverted hierarchy respectively, in terms of the mixing angles, δm^2_S, δm^2_{AT}, and the CP phases as [Bar02, Pas02]:

[2]This is the convention suggested by the Particle Data Book [Hag02]

Table 2.1: Approximate numerical predictions of $|\langle m_\nu \rangle|$ in milli-electron Volts for both hierarchies, and CP phase relations for specified values of the lightest mass eigenstate m_1.

Normal Hierarchy				Inverted Hierarchy			
$e^{i\phi_2} = -1$		$e^{i\phi_2} = +1$		$e^{i\phi_2} = -e^{i\phi_3}$		$e^{i\phi_2} = +e^{i\phi_3}$	
m_1 meV	$\lvert\langle m_\nu \rangle\rvert$	m_1 meV	$\lvert\langle m_\nu \rangle\rvert$	m_1 meV	$\lvert\langle m_\nu \rangle\rvert$	m_1 meV	$\lvert\langle m_\nu \rangle\rvert$
20	10	20	20	0	22	0	45
60	30	60	60	30	27	30	54
100	50	100	100	100	55	100	110
200	100	200	200	200	103	200	205
400	200	400	400	400	201	400	403

$$|\langle m_\nu \rangle| = \left| c_{13}^2 c_{12}^2 m_1 + c_{13}^2 s_{12}^2 e^{i\phi_2} \sqrt{\delta m_s^2 + m_1^2} + s_{13}^2 e^{i\phi_3} \sqrt{\delta m_{AT}^2 + m_1^2} \right| \tag{2.6}$$

$$|\langle m_\nu \rangle| = \left| s_{13}^2 e^{i\phi_3} m_1 + c_{13}^2 c_{12}^2 \sqrt{\delta m_{AT}^2 + \delta m_s^2 + m_1^2} + c_{13}^2 s_{12}^2 e^{i\phi_2} \sqrt{\delta m_{AT}^2 + m_1^2} \right| \tag{2.7}$$

With the approximation $\theta_{13} = 0$ and the further approximation of $\delta m_S^2 << \delta m_{AT}^2$, Equations 2.6 and 2.7 reduce to:

$$|\langle m_\nu \rangle| = m_1 \left| c_{12}^2 + s_{12}^2 e^{i\phi_2} \sqrt{1 + \frac{\delta m_s^2}{m_1^2}} \right| \tag{2.8}$$

$$|\langle m_\nu \rangle| = \sqrt{m_1^2 + \delta m_{AT}^2} \left| c_{12}^2 e^{i\phi_2} + s_{12}^2 e^{i\phi_3} \right| \tag{2.9}$$

These approximate expressions are accurate to a few percent. It should be noted that the observed value of $\theta_{12} \sim 34^\circ$, together with the values for δm_s and δm_{AT}, are crucial for making the effective mass observable by realistic $0\nu\beta\beta$ detectors even in the small m_1 region, since for most of the available parameter space $|\langle m_\nu \rangle|$ cannot be null due to phase cancellation. Numerical values for $|\langle m_\nu \rangle|$ are obtained from Equations 2.8 and 2.9 by using the value of $\theta_{12} = 30^\circ$ and the central values for the δm^2 as summarized above, and are given in Table 2.1. In Figure 2.2, the range of possible values of $|\langle m_\nu \rangle|$ are shown. Qualitatively, one should consider $\sqrt{\delta m_{AT}^2} \approx 45$ meV as the physics driver for the next generation of experiments.

Barger *et al.* [Bar02] derive constraints on m_1 for a given value of $|\langle m_\nu \rangle|$. Using the approximations given above and the assumption that $m_1^2 \gg \delta m_S^2$, the relationships of the normal and inverted hierarchies are:

$$|\langle m_\nu \rangle| \leq m_1 \leq \frac{|\langle m_\nu \rangle|}{c_{12}^2 - s_{12}^2} \tag{2.10}$$

$$\sqrt{|\langle m_\nu \rangle|^2 - \delta m_{AT}^2} \leq m_1 \leq \frac{\sqrt{|\langle m_\nu \rangle|^2 - \delta m_{AT}^2 (c_{12}^2 - s_{12}^2)}}{c_{12}^2 - s_{12}^2} \tag{2.11}$$

Under the assumption of $m_1^2 \gg \delta m_S^2$, Barger *et al* also derive similar constraints for the sum of the neutrino masses, $\Sigma \equiv m_1 + m_2 + m_3$, which are important in the consideration of neutrino hot dark matter:

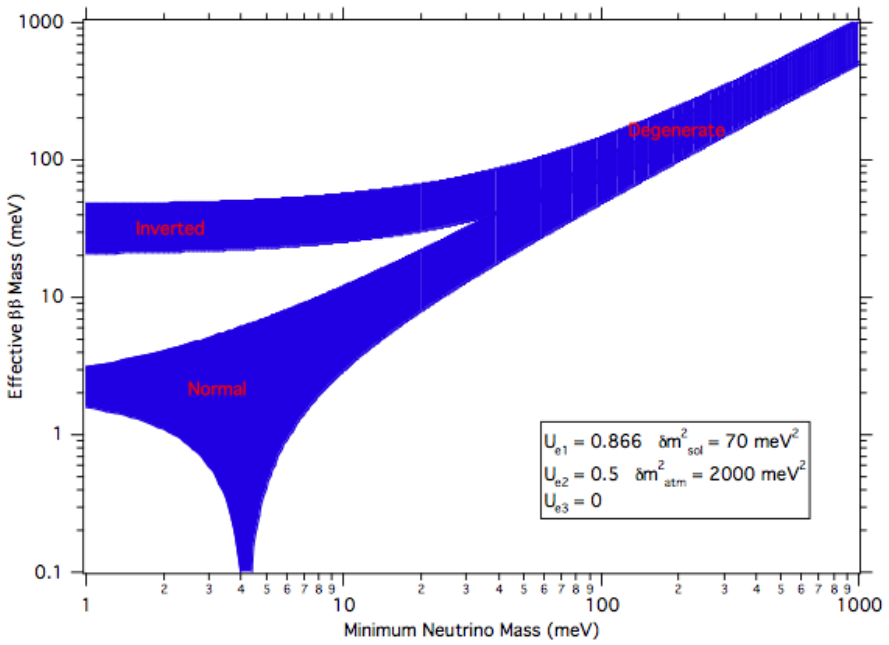

Figure 2.2: The allowed regions for the effective double-beta decay mass as a function of smallest mass. The assumed mixing parameters are indicated in the figure. The regions appropriate to the normal, inverted and degenerate hierarchies are indicated.

$$2\left|\langle m_\nu\rangle\right| + \sqrt{\left|\langle m_\nu\rangle\right|^2 \pm \delta m^2_{AT}} \leq \Sigma \leq \frac{2\left|\langle m_\nu\rangle\right| + \sqrt{\left|\langle m_\nu\rangle\right|^2 \pm \delta m^2_{AT}\cos(2\theta_{12})}}{\left|\cos(2\theta_{12})\right|} \tag{2.12}$$

where the plus signs are for normal hierarchy and the minus signs for inverted hierarchy. Equation 2.12 can be simplified significantly for values of $|\langle m_\nu\rangle|$ achievable in next generation experiments [Avi02]. When $\delta m^2_{AT} << \Sigma^2$, $\delta m^2_{AT} \leq 0.005$ eV^2 (99.73% *CL*) and $\cos(2\theta_{12}) = 0.5$, we have:

$$\left|\langle m_\nu\rangle\right| \leq \frac{\Sigma}{3} \leq 2\left|\langle m_\nu\rangle\right| \tag{2.13}$$

Thus a $0\nu\beta\beta$ experiment with a mass sensitivity of $|\langle m_\nu\rangle| \sim 30$ meV can define the sum Σ in the region of 0.1 – 0.2 eV. It is evident that next generation neutrinoless double-beta decay experiments are absolutely necessary for a more complete understanding of neutrinos.

2.3 Nuclear Matrix Elements

The observation of $0\nu\beta\beta$ would have profound qualitative physics conclusions. However, the interpretation of those results quantitatively requires a knowledge of the nuclear matrix elements. Nuclear matrix element calculations involve either the quasiparticle random phase approximation (QRPA) technique or nuclear shell model (NSM). Although the two methods have a similar starting point (a Slater determinant of independent particles), they are complementary in their treatment of correlations. QRPA uses a large number of "active" nucleons in a large space but with a specific type of correlation suited for collective motion. NSM uses a small number of nucleons within a limited space but with arbitrary correlations.

The nuclear structure factor F_N relates the Fermi and Gamow-Teller nuclear matrix elements in Equation 2.3:

$$F_N \equiv G^{0\nu} \left| M_F^{0\nu} - (g_A/g_V)^2 M_{GT}^{0\nu} \right|^2 . \tag{2.14}$$

The common practice of using the spread of all previously calculated values for F_N as the theoretical uncertainty in the matrix element calculations ignores recent progress in the field. Such an averaging approach results in a factor of 10 uncertainty in F_N and therefore a factor of ~ 3 in $|\langle m_\nu \rangle|$. Recent improvements have shown consistency between various QRPA calculations, and are complementary to the parallel efforts in the shell model calculations described below.

The best recent published NSM calculations for ^{76}Ge by Caurier *et al.* [Cau99][3] can be compared to those from QRPA. Their difference could be as large as a factor of 2.5 in the predicted ^{76}Ge $0\nu\beta\beta$ decay rates. This factor would indicate a theoretical uncertainty of 1.6 in the deduced Majorana mass. However, recent progress indicates that NSM and QRPA are in better agreement [Pov06]. As is clear from the discussion below, progress is being made in understanding the discrepancy in the matrix element calculations. In our study of ^{76}Ge $0\nu\beta\beta$ sensitivity to neutrino mass, we assume a conservative factor of 2 uncertainty.

2.3.1 The Quasiparticle Random Phase Approximation

In 1986, Vogel and Zirnbauer introduced the Quasi-Particle Random Phase Approximation (QRPA) [Vog86]. Until recently, there have been many developments and variations, frequently with widely disparate results.

Previously, an accurate calculation of the $2\nu\beta\beta$ matrix elements was considered a necessary but not sufficient condition to cross-check the machinery used to determine $0\nu\beta\beta$ matrix elements, because the intermediate nuclear states are very different in the two cases. Recently however, Rodin *et al.* showed, in the context of QRPA and Renormalized QRPA (RQRPA), that this is not the case [Rod03]:

> "*When the strength of the particle-particle interaction is adjusted so that the $2\nu\beta\beta$ decay rate is correctly reproduced, the resulting $M^{0\nu}$ values become essentially independent on the size of the basis, and on the form of different realistic nucleon-nucleon potentials. Thus, one of the main reasons for variability of the calculated $M^{0\nu}$ within these methods is eliminated.*"

Accordingly, one would conclude that accurate measurements of $2\nu\beta\beta$ half-lives **will** have a very meaningful impact on the predictions of $0\nu\beta\beta$ matrix elements in the same nuclei.

Rodin *et al.* investigated the dependence of $M^{0\nu}$ on the choice of the single-particle (sp) space by comparing three different, yet realistic, nucleon-nucleon interactions including: the Bonn-CD [Mac89], the Argonne [Wir95], and the Nijmegen [Sto94] potentials. The result is that $M^{0\nu}$ varies very little over 9 different combinations of sp-space and interactions. The effect of neglecting single-particle states far from the Fermi-level was investigated for ^{76}Ge, ^{100}Mo, ^{130}Te, and ^{136}Xe. In the case of ^{76}Ge, the following three sp-spaces were used: i) the 9 levels of the oscillator shells N=3 and 4; ii) the addition of the N=2 shell, and finally; iii) the 21 levels from all states in the shells with N=1, 2, 3, 4, and 5. For each change in sp-space, the residual interaction must be adjusted by adding a pairing interaction and a particle-hole interaction renormalized by an overall strength parameter, g_{ph}. The value $g_{ph} \sim 1$ was found to reproduce the giant Gamow-Teller resonance in all cases. Finally, QRPA equations include the effects of a particle-particle interaction, renormalized by an overall strength parameter g_{pp} that in each case was adjusted to reproduce the known $2\nu\beta\beta$ rate correctly. This final adjustment was found to be key in producing very similar results from all the chosen basis or interaction. Through these systematic analyses [Rod03, Rod06] of different QRPA calculations, their differences in the derived nuclear matrix elements are now understood; thus the

[3] Caurier *et al.* gives $M_F^{0\nu}$=0.19 and $M_{GT}^{0\nu}$=1.58.

long-standing spread in QRPA calculations has been greatly narrowed. In the most complete QRPA calculation to-date [Rod06], the ^{76}Ge nuclear matrix element $M'^{0\nu}(=F_N/G^{0\nu})$ ranges from 2.3 to 2.7. If one assumes $|\langle m_\nu \rangle|$=50 meV and $M'^{0\nu}$=2.4, the ^{76}Ge $0\nu\beta\beta$ half-life is 2.3×10^{27} years.

2.3.2 The Shell Model[4]

Germanium-76 is a good isotope for $0\nu\beta\beta$ studies because the matrix element calculations are more tractable for this relatively low-A isotope. It is anticipated that future shell model calculations for this isotope will be very reliable. The shell model interactions generally are based on G-matrices from realistic nucleon-nucleon interactions, with small phenomenological terms that are fit and well constrained by data other than double-beta decay. As single particle energies are also fit, nothing remains to be adjusted for $\beta\beta$.

A full-shell calculation, in which the sum over huge intermediate spaces of 1^+ states is done exactly by Lanczos moments techniques, has been done for the neighboring $2\nu\beta\beta$ nucleus ^{82}Se by Caurier *et al* [Cau96]. The appropriate model space is $1f_{5/2}$-$2p_{3/2}$-$2p_{1/2}$-$1g_{9/2}$. The corresponding ^{76}Ge calculation was done as a series, increasing the number (t) of particles allowed in the $g_{9/2}$ shell. Results were obtained for t = 0, 2, 4. Clearly it would be best to allow any $g_{9/2}$ occupation, but that produces a very large model space. But t = 4 is crucial because there are three strongly mixed 0^+ bands near the ^{76}Ge ground state, and these correspond to 0, 2, and 4 neutrons being promoted to the $g_{9/2}$ shell. We know these bands strongly mix because of studies of Ge isotopes as a function of neutron number, and show dramatic level-crossing effects in which spectroscopic factors of the ground and excited state "reverse" with the addition of two neutrons. The standard QRPA calculation lacks the essential t = 4 band. The resulting $2\nu\beta\beta$ rates are reasonable, and converge toward the experimental value with increasing t. As expected from the argument above, the change from t = 2 to t = 4 is significant for the $2\nu\beta\beta$ rate.

Excitingly, these calculations can be improved. Progress in standard shell model work has advanced since 1996. New methods [Ohs02] might even be able to handle the full-shell ^{76}Ge calculation now. These calculations are only as good as the input effective interaction, which generally are determined empirically. In 2002 Honma *et al.* [Hon02] did the analog of Brown-Wildenthal for the $f_{7/2}$-$f_{5/2}$-$p_{3/2}$-$p_{1/2}$ shell, fitting over 600 matrix elements empirically. This is not exactly what is needed for double-beta decay, but it shows that we are getting very close to a Brown-Wildenthal style interaction for ^{76}Ge.

The use of a shell-model space implies nontrivial wave function normalizations and effective operator contributions due to the neglected high-momentum shells. There is real progress in tackling this problem (see for example Ref. [Bed99]) using the theory of effective operators. It also may be possible to "sneak up" on this issue by doing test cases in much lighter nuclei, then applying the deduced effective operators to heavier cases like ^{76}Ge. Effective operator theory is almost hopeless except in the case of full-shell shell-model calculations. Thus the progress in shell model calculations lays the groundwork for the application of effective operator theory.

^{76}Ge is a critical double-beta decay isotope. Generally, calculations for large-A nuclei require severe shell model truncations and employ effective interactions that have not been carefully constrained to data, in the manner of Brown-Wildenthal. Both full-shell calculations and Brown-Wildenthal -style interactions are unlikely for heavier nuclei in the foreseeable future. But improved calculations are likely to be carried out for ^{76}Ge. In particular several larger collaborative efforts are underway in the U.S. [Hax06]and in Europe [Ver05] that intend to use large arrays of high-performance computers to perform improved shell-model calculations. If $0\nu\beta\beta$ is observed, the matrix element calculation will be a critical input into the interpretation of the result. It is very likely that confidence in the calculations for this isotope will improve.

[4]We wish to acknowledge a large contribution to this section by Prof. Wick Haxton, Univ. of Washington.

Table 2.2: Best reported limits on $0\nu\beta\beta$ half lives. The mass limits and ranges are those deduced by the authors and their choices of matrix elements within the cited experimental papers. All limits are quoted at the 90% confidence level, except for the Klapdor-Kleingrothaus [Kla04] result, where the bounds are for the 99.7% confidence level. Backgrounds are given in cnts/keV/kg-year, and are included if given in the original publication. (Note that in most of this document we refer to Majorana backgrounds in cnts/ROI/t-y, where we multiply by the width of the ROI, which for ^{76}Ge detectors is typically 4 keV.)

Isotope	**Half-Life (y)**	$\|\langle m_\nu \rangle\|$ **(eV)**	**Exposure** (kg-yr)	**Background** (cts/keV/kg-yr)	**Reference**
^{48}Ca	$>1.4\times10^{22}$	< 7.2-44.7	4.23		[Oga04]
^{76}Ge	$>1.9\times10^{25}$	<0.32-1	35.5	0.19	[Kla01d]
^{76}Ge	$>1.6\times10^{25}$	<0.33-1.35	8.9	0.06	[Aal02a]
^{76}Ge	$=1.2\times10^{25}$	=0.24-0.58	71.7	0.11	[Kla04]
^{82}Se	$>1.9\times10^{23}$	< 1.3-3.2	0.68		[Sar05]
^{96}Zr	$> 1\times10^{21}$	<16.3-40	0.0084		[Arn98]
^{100}Mo	$>3.5\times10^{23}$	< 0.7-1.2	5.02	3.5×10^{-3}	[Sar05]
^{116}Cd	$>1.7\times10^{23}$	< 2.2-4.6	0.15	0.03	[Dan00]
^{128}Te	$>7.7\times10^{24}$	< 1.1-1.5	Geoch.	Geoch.	[Ber93]
^{130}Te	$>1.8\times10^{24}$	< 0.2-1.1	10.85	0.18	[Cap05]
^{136}Xe	$>4.4\times10^{23}$	< 2.2-5.2	4.84		[Lue98]
^{150}Nd	$>3.6\times10^{21}$	< 4.9-17.1	0.015		[Bar05]

2.4 Previous Neutrinoless Double-Beta Decay Results

Over the past thirty years, a number of double-beta decay nuclei have been studied using a wide variety of experimental techniques. (For details, see recent reviews by Avignone *et al.* [Avi05], Barabash [Bar04], Ejiri [Eji05], Elliott and Engle [Ell04], and Elliott and Vogel [Ell02].) Table 2.2 summarizes the best $0\nu\beta\beta$ half-life limits and deduced effective Majorana neutrino mass limits for different nuclei. One conclusion that can be drawn from the table is that the most sensitive experiments are the ones where the source and detector are one and the same.

The most sensitive experiments to date are the Ge-based Heidelberg-Moscow and International Germanium Experiment (IGEX) experiments, both of which have been completed. The $0\nu\beta\beta$ half-life limit of $\tau_{1/2} > 1.9 \times 10^{25}$ y set by the Heidelberg-Moscow collaboration [Kla01a] was acquired using 5 Ge crystals, enriched to 86% in ^{76}Ge, with a total mass of 10.96 kg. The IGEX collaboration [Aal02a] obtained a limit of $\tau_{1/2} > 1.6 \times 10^{25}$ y using 6 similarly enriched Ge crystals with a total mass of 8.9 kg. The longest half-life bound corresponds to an effective Majorana neutrino mass $|\langle m_\nu \rangle|$ of $< 0.32 - 1$ eV, depending on the theoretical nuclear matrix elements chosen. Using the recommended ^{76}Ge matrix element from the most recent Renormalized QRPA (RQRPA) calculations (Rodin *et al.* [Rod06]), $|\langle m_\nu \rangle|$ is < 0.55 eV.

A recent claim for an observation of $0\nu\beta\beta$ in Ge has been put forth in Klapdor-Kleingrothaus *et al.* [Kla01a, Kla02b, Kla04]. Their assertion is controversial [Aal02a, Kla02a, Har02, Fer02, Zde02] and is highly dependent on the assumed background model. In Klapdor-Kleingrothaus's most recent results for 71.7 kg-years of 76Ge exposure [Kla04], a $0\nu\beta\beta$ signal was claimed with a 4.2σ significance with a corresponding half-life of 1.2×10^{25} y (see the left panel of Figure 2.3).

This result, with a background rate in the region-of-interest of 0.11 cnts/keV/kg-year, implies at the 3σ level that the effective Majorana neutrino mass would lie between 0.24-0.58 eV. Clearly there is a need to definitively verify or refute this result. If the Klapdor-Kleingrothaus half-life central value is correct, the 120 kg Majorana measurement would in 5 years (520 kg-years) expect to observe

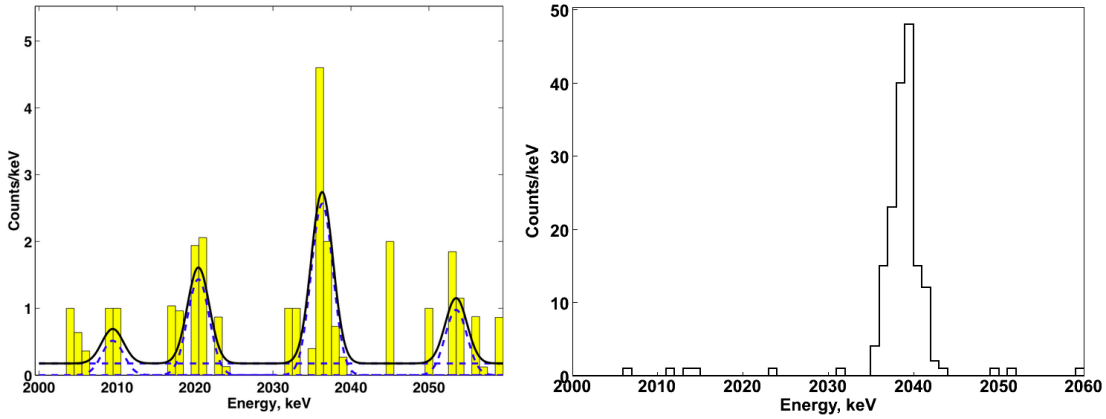

Figure 2.3: Left panel: The pulse shape selected energy spectrum for a subset (51.4 kg-years) of the Klapdor-Kleingrothaus [Kla04] data. The $0\nu\beta\beta$ peak is located at 2039 keV. The other peaks are identified as ^{214}Bi lines. Note that analysis cuts have been applied that should favor single site events. Right panel: Simulation results for the expected 120 kg Majorana observation after 5 years, assuming the Klapdor-Kleingrothaus half-life and assuming Majorana backgrounds and analysis cuts described in Chapter 4. The Majorana background goal is to attain backgrounds of about 1 count/ROI/t-y after analysis cuts have been applied.

145 counts in the region-of-interest with a background of less than one count (see the right panel of Figure 2.3).

If the Klapdor-Kleingrothaus result is verified, it is critical to measure the decay rate with an uncertainty small compared to the nuclear matrix element uncertainty. To refute the result, an experiment must have sensitivity to exclude the result with convincing statistics and reduced backgrounds. The proposed phased approach of the Majorana project can fulfill these goals.

2.5 Next-Generation Neutrinoless Double-Beta Decay Measurements

Next-generation $0\nu\beta\beta$ experiments must have sufficient mass to acquire reasonable statistics while striving to reduce backgrounds to as near zero as possible. These radioactive backgrounds can be intrinsic to the active detector or contaminants of the surrounding materials. Much of the engineering effort for a next-generation experiment is aimed at obtaining or fabricating materials with ultra-low radioactivity.

Design considerations for any next-generation detector include:

- *Energy resolution.* Superior energy resolution would allow the separation of the $0\nu\beta\beta$ peak from the $2\nu\beta\beta$ tail, and would improve the signal-to-background ratio by reducing the width of summing window placed about the signal peak.

- *Isotopic enrichment.* An ideal detector is one that maximizes the usage of $0\nu\beta\beta$ source material while minimizing the overall mass of the active detector material. Such configuration argues for an isotopically enriched, elemental source-detector.

- *Choice of $\beta\beta$ isotope.* Choosing a $\beta\beta$ decay process with a large phase volume (large Q value and large Z) would enhance the $0\nu\beta\beta$ signal rate and place it above many potential radioactive backgrounds. In addition, choosing an isotope with a large nuclear matrix element and relatively slow $2\nu\beta\beta$ rate would enhance the $0\nu\beta\beta$-to-$2\nu\beta\beta$ ratio in the region of interest.

- *Daughter identification.* Identifying the daughter in coincidence with the $\beta\beta$ decay would eliminate most potential backgrounds except $2\nu\beta\beta$.

- *Event reconstruction and active background rejection.* Event reconstruction, providing kinematic data such as opening angle and individual electron energy, can aid in the elimination of backgrounds. This data might also help elucidate the decay process if a statistical sample of $0\nu\beta\beta$ events are observed. In addition, event reconstruction with good spatial resolution and timing information can help reject correlated background events and provide additional tests for potential signals.

- *Nuclear matrix element uncertainties.* The interpretation of limits or signals would be easier for isotopes that are better understood theoretically.

- *Demonstrated detection and detector manufacturing technology.* Using established detection technology reduces risks (for example, in background contamination), and shortens the time required for detector manufacturing and deployment. Strategies to further reduce the intrinsic detector radioactivity are only possible if the detector manufacturing techniques are well understood.

No experiment, past or proposed, can be optimized for all of these characteristics. Based on the above considerations, the Majorana Collaboration believes that ^{76}Ge offers the best combination of capabilities and sensitivity. Ge detectors have the best energy resolution of all proposed arrays of detectors. The enriched-Ge detectors proposed for Majorana use elemental Ge thus maximizing the target mass to total mass ratio. The 2-MeV Q-value for ^{76}Ge is small enough to produce a very favorable ratio of the neutrinoless decay mode relative to the standard-model 2ν mode, and yet is large enough to be above many problematic radioactive backgrounds. Segmentation of the detectors, event reconstruction and modern pulse-shape analysis provide powerful event classification capability. The granularity and timing of the detectors permits excellent event-to-event correlation for background reduction and study. Ge detectors have been operated in large arrays for extended periods with very high duty cycle making them an especially well-demonstrated technology even in large arrays with significant masses.

3 The Majorana Experiment

3.1 Overview

The physics goals of the Majorana collaboration's first phase search for neutrinoless double-beta decay ($0\nu\beta\beta$) are to:

- Probe the quasi-degenerate neutrino mass region above 100 meV.
- Demonstrate that backgrounds can be achieved at or below 1 count/ton/year in the $0\nu\beta\beta$-decay peak 4-keV region of interest (1 count/ROI/t-y), which would justify scaling up to a 1 ton or larger mass detector.
- Definitively test the Klapdor-Kleingrothaus *et al.* claim [Kla04] of an observation of $0\nu\beta\beta$ in ^{76}Ge in the mass region around 400 meV.

To realize these goals, we intend to expand on the internal-source technique originally introduced by Fiorini [Fio67] of using high-purity Ge (HPGe) crystals. We believe that ^{76}Ge offers the best combination of capabilities and sensitivities for a next-generation $0\nu\beta\beta$-decay experiment, in particular because:

- The detectors consist of elemental Ge which maximizes the source-to-total-mass ratio.
- ^{76}Ge has a favorable nuclear matrix element, $\left|M^{0\nu}\right| \sim 2.4$.
- ^{76}Ge has a reasonably slow $2\nu\beta\beta$ decay rate, $T_{1/2} = (1.4 \pm 0.2) \times 10^{21}$ y [Aal96, Kla01b].
- Germanium detectors have superior energy resolution, 0.16% at 2.039 MeV.
- The processes of producing intrinsic high-purity Ge diodes eliminates or minimizes U and Th chain impurities.
- An array of Ge detectors provide powerful signal-to-background discrimination techniques: granularity, pulse-shape analysis, segmentation, and timing.
- The ability to enrich ^{76}Ge from the natural abundance of 7.44% to 86% has been demonstrated.
- Well-understood technologies are available now – commercial segmented Ge diodes and existing, well-characterized large Ge arrays.

The advantages of ^{76}Ge are clear when one considers that the most sensitive $0\nu\beta\beta$-decay half-life limits have been obtained using Ge (IGEX & Heidelberg-Moscow) detectors ($T_{1/2} > 1.9 \times 10^{25}$y (90%CL)).

Our collaboration proposes to construct an array of 86%-enriched ^{76}Ge crystals contained in an ultra-low-background structure. This maximizes the concentration of crystals while minimizing the structural materials. Our current reference design is based on modules each containing 57 close-packed, 1.1 kg, enriched, segmented, germanium crystals enclosed in an ultra-pure copper cryostat. These modules are contained within a graded shield that consists of a low-background inner shield surrounded by structural and additional gamma- and neutron-shielding materials, which are themselves surrounded by an active veto system. A cross section of the detector apparatus is shown in Figure 3.1. Our design draws on the collaboration's extensive experience in past $2\nu\beta\beta$ and $0\nu\beta\beta$ experiments, low energy solar and reactor ν experiments, and large-array γ-ray tracking detectors, as well as recent advances in the production of ultra-low-background construction materials, germanium detector technology and electronic signal processing. The modular design is scalable, with the proposed first phase consisting of two modules having a total mass of 120 kg of 86% enriched ^{76}Ge. This initial phase is aimed at addressing neutrino masses in the ∼100 meV region, at achieving ultra-low backgrounds at the level required in future larger-mass experiments, and in demonstrating the feasibility of scaling to larger experiments using a modular approach.

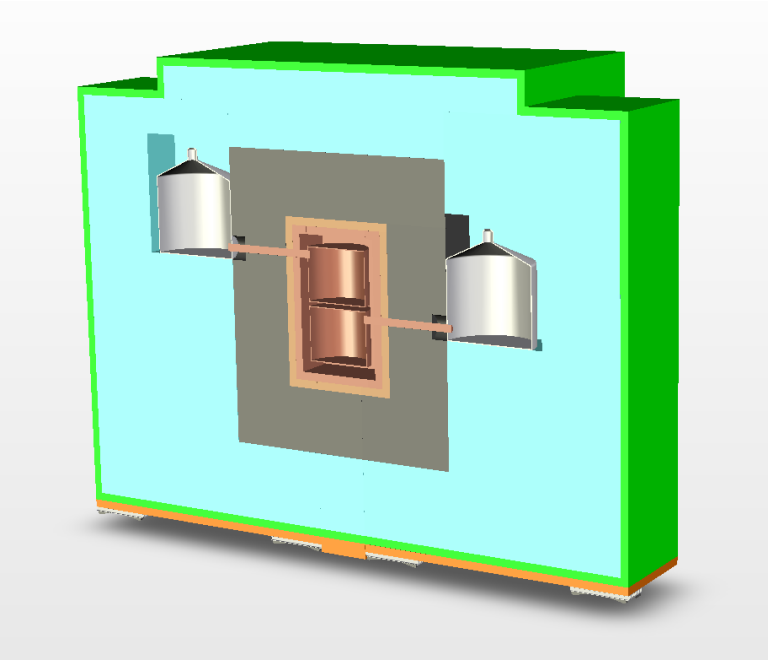

Figure 3.1: Cross-sectional view of the module arrangement within the shielding.

3.2 Detector Mass

The selection of our initial detector mass to be 120 kg of 86% enriched ^{76}Ge is driven by our physics goals and guided by the community's recent recommendations on the optimum path forward in next-generation searches for neutrinoless double-beta decay. The justification for a detector mass size of 120 kg is directly linked to all three of the science goals:

- To achieve sensitivity to masses within the quasi-degenerate neutrino mass region within a reasonable time frame (5 years), which will equal or surpass other international efforts that are currently underway.
- To field an array large enough to allow demonstration of backgrounds for a 1 ton detector, with modules of a realistic size, and providing statistically significant background measurements.
- To perform a precision test within a reasonable time frame of the Klapdor-Kleingrothaus *et al.* claim. The Majorana experiment will have much lower background and substantially higher statistical significance than other efforts.

The choice of 120 kg is also made within the context of being competitive with other international efforts.

3.2.1 Sensitivity

In terms of physics reach, in the absence of background the sensitivity of $0\nu\beta\beta$ decay experiments to neutrino mass scales as the $\sqrt{\text{Detector Mass}}$. The presence of background reduces this sensitivity, and in the limiting case where no signal is observed and the experiment is dominated by background (≥ 5 counts in the $0\nu\beta\beta$ peak region of interest) the sensitivity to neutrino mass scales as the fourth root of the detector mass. Thus the optimum detector size is sensitively connected both to the

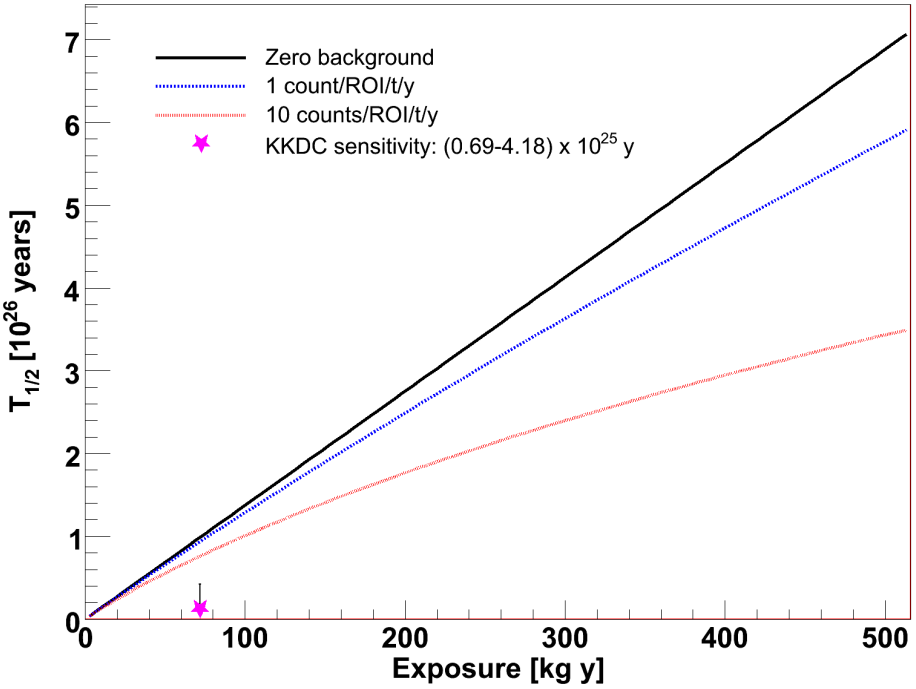

Figure 3.2: Majorana sensitivity for the half-life of ^{76}Ge $0\nu\beta\beta$ as a function of exposure at 90% C.L. Three different background models are shown, zero background, our goal of 1 count/ROI/t-y, and 10 cnts/ROI/t-y.

expected backgrounds and the signal. The asymptotic dependence of sensitivity on exposure time can be seen in Figure 3.2, which compares sensitivity as a function of exposure for three different background assumptions. From this plot one can see that our background goal of 1 count/ROI/t-y is driven largely by our need to demonstrate feasibility for a 1 ton scale detector. For the 120 kg mass detector, a factor of 10 more background would result in a factor of two reduction in the half-life sensitivity, which translates to a 30% reduction of sensitivity to neutrino mass.

A related and principal concern is obtaining statistically significant sensitivity to backgrounds. Clearly, for the 4 keV region-of-interest centered about the $0\nu\beta\beta$ peak, one will have no statistical significance even after an exposure of 1 t-y. Instead one relies on substantially larger nearby energy windows and examining potential background sources from peaks at known energies. Even using this strategy, one must have sufficient mass (10% of a 1 ton scale) in order to confidently estimate backgrounds in the $0\nu\beta\beta$ peak ROI. For example, if we meet our background goal of 1 count/ROI/t-y and we count for 0.5 t-y, we will observe approximately 12 counts within a 100 keV window centered on 2 MeV. Hence, with 120 kg of Ge, we will have the sensitivity to demonstrate that our background is low enough to justify a 1-ton experiment.

3.2.2 Scale and Modularity

There are a number of advantages in taking a phased, modular approach. In particular one can optimize many of the construction and assembly procedures while also bringing portions of the array on-line in the most timely manner (this is discussed in more detail in Section 3.7). It is also

important to demonstrate at this stage that the size of modules and the process of constructing these modules is comparable to what will be needed in the 1 ton experiment. This is again largely driven by the extreme background and material purity requirements. One must also consider the sometimes-conflicting mechanical and electrical read-out requirements that impact the optimum module size. Based on current considerations, our reference plan for the 120 kg Ge array assumes that we would field two modules, each containing 57 crystals. We are still performing simulation studies and a quantitative analysis of alternative configurations in order to determine the optimum configuration.

3.2.3 Global Neutrinoless Double-Beta Decay Efforts

Internationally, there are three collaborations that are currently funded or partially funded and are constructing or planning to construct next-generation $0\nu\beta\beta$ experiments with active masses on the scale of 40 - 200 kg.

- The GERDA experiment, an approved project to be sited at the Gran Sasso underground facility, also uses ^{76}Ge as its $\beta\beta$ source and intends to deploy about 40 kg of detctors[Abt04]. Their enriched ^{76}Ge crystals will be suspended in a large cryogenic bath of liquid argon (LAr). The LAr is expected to have low radioactivity and also acts as a shield against external background radiation. The collaboration will start with 18 kg of existing detectors and eventually add additional segmented detectors for a total of ∼40 kg. GERDA expects to eventually attain sufficient statistics to test the Klapdor-Kleingrothaus *et al.* claim, but will realistically not provide a precision measurement, nor have the sensitivity to approach the 100 meV mass scale. The GERDA and Majorana Collaborations have reached an agreement to share resources and knowledge where appropriate in their parallel development of the two different detector designs. The ultimate goal is to combine the strength of the two Collaborations in a future experiment that will employ the best technology for reaching a Majorana neutrino mass sensitivity of below 50 meV.

- The EXO collaboration is constructing EXO200, a 200 kg enriched ^{136}Xe detector with an active mass of 160 kg. They have estimated they will be able to test the Klapdor-Kleingrothaus *et al.* claim at the 2σ significance level [Gra05]. They expect to start installing the detector and collecting data at the Waste Isolation Pilot Plant in NM in 2007.

- The CUORE collaboration is proposing to build a cryogenic bolometer that measures the energy released in the decays of ^{130}Te in crystals of TeO_2 [Arn04]. The crystals need not be enriched, as ^{132}Te has a natural isotopic abundance of 34.1%. CUORE is envisioned to consist of a total of 19 towers of crystals, for a total mass of 750 kg of TeO_2, which corresponds to a mass of 206 kg of ^{132}Te. They expect to start collecting data in 2011.

Given the importance of backgrounds to detector sensitivities, it is worth noting that three of the next-generation experiments (GERDA, EXO, and Majorana) have set similar goals for background counts/keV/t-y, around 0.5-1 cnt/keV/t-y, while CUORE has set an initial goal about 10 times larger at 10 cnt/keV/t-y. When one folds in the expected detector resolution, only the Ge based detectors, GERDA and Majorana, are aiming at nearly background-free measurements in the region of interest.

3.2.4 Majorana in the Global Context

In the context of these efforts it is reasonable to ask the question "Can Majorana field a competitive experiment?" In March 2006 we convened an external panel to assess the technical and project readiness of our proposed 120 kg experiment. The panel concluded that we were technically ready to proceed and that only a limited scope of R&D activities remain to be completed. However, the

panel recommended that we aggressively pursue the construction of the first 60 kg module in order to be competitive, both in sensitivity and timeliness, with other international efforts that are currently underway.

The collaboration has comprehensively examined the issue of mounting a "fast" 60 kg experiment, and considered a number of potential measures that might allow us to field a first module as quickly as possible. As part of this process, we have also factored in the general funding guidance that we have received from the DOE Office of Nuclear Physics, i.e. that based on current budget projections any $0\nu\beta\beta$ experiment supported by the DOE Office of Nuclear Physics will have modest funds available during the first few years that the project is supported.

The key findings of our examination are as follows:

- Any Majorana project schedule will be constrained by the DOE capital funding process. Under DOE Order 413 the typical times for projects to move through the CD gates from CD-1 to CD-3 is about 24 months. Assuming we can meet these typical times, indicates that construction funding would start in FY2010. An optimized, but realistic project schedule is shown in Table 3.1. The exact schedule will of course depend on the eventual funding profile. In this optimized schedule, in order to field the first 60 kg module as soon as possible, we have assumed that the collaboration would be able to place long lead time orders for enriched isotope in FY2009.

- We considered mass options of 60, 120, and 180 kg and calculated the expected sensitivity based on our projected schedule. Figure 3.3 displays the expected sensitivity for Majorana as a function of calendar year for the three different mass options. We also generated comparison plots that overlay the projected Majorana sensitivity with expectations for the other three next-generation experiments. For these comparisons we have used the nuclear matrix elements from Rodin [Rod06]. For each comparison, we used the particular experiment's stated background goals and projected schedule. For simplicity we have assumed 100% livetime and that each experiment would continue to run through 2018. Examining Figures 3.4, 3.5, 3.6, and 3.7 one sees that a 120 kg array mass would put Majorana in a competitive position relative to other next-generation experiments. From Figure 3.4, it is clear that Majorana will be at an initial disadvantage because of its delayed start, but with a 120 kg of material, Majorana will be in a position to surpass GERDA by 2015. It is also important to realize that there are good reasons for doing both GERDA and Majorana: different technical approaches, different techniques for background mitigation, and the eventual common goal that the two collaborations will merge and move forward with the best technology for mounting a 1 ton experiment.

- We considered relaxing our stringent background requirements. This would allow us to both reduce costs and accelerate the schedule. However, after performing a quantitative analysis, we concluded that to be competitive, we must hold to our original background goal. This is clearly illustrated in the Figures 3.4, 3.5, 3.6, and 3.7, where we compare Majorana with backgrounds of 1 count/ROI/t-y with sensitivity curves for the other experiments. For completeness, we have also included Figure 3.8 that compares Majorana backgrounds of 1 count/ROI/t-y with backgrounds of 10 counts/ROI/t-y.

- We need to be as ready as possible once we have received enriched material and start fabricating detectors. This argues for increased emphasis on understanding and characterizing our backgrounds in advance of having enriched detectors. As described in the *MajoranaProject R&D Plan* we are focusing on fielding a prototype module as early as possible, using available natural Ge crystals that will allow us to demonstrate the key technical requirements.

- Smaller self-contained modules might be able to be produced more quickly, and at a lower initial cost. They have the advantage that once a module is on-line, it can be left on-line, maximizing livetime. But there are also potential down-sides, such as greater overall cost, increased shield

complexity, and potential reduction in analysis cut efficiencies. We are continuing to examine optimum module size.

Table 3.1: Optimized Project Schedule

Year	Expected Activity
FY07 Q2	Some initial R&D funding
	no Project Engineering and Design (PED)
FY08	A limited amount of PED and R&D
FY09	PED and R&D
FY09 Q2	Long-lead time order
FY10 Q2	Start of Construction funding

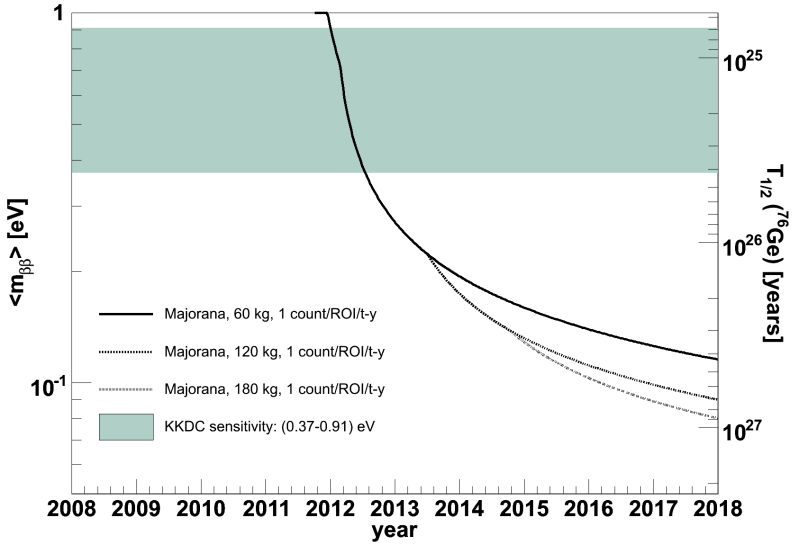

Figure 3.3: Comparison of Majorana sensitivity to $0\nu\beta\beta$ decay for three different mass options as a function of calendar year. The start time for Majorana is based on the optimized project schedule, given in Table 3.1. The 120 and 180 kg experiments build on the data taken with the previously fielded modules.

In summary, with 120 kg of enriched germanium, Majorana can successfully address the recommendations from both the *DNP/DPF/DAP/DPB Joint Study on the Future of Neutrino Physics* [Fre04] and the Neutrino Scientific Assessment Group (NuSAG) [NUSAG05] Additionally, having 120 kg of material places us in a good position to discuss a potential future combined GERDA and Majorana 1-ton-scale experiment.

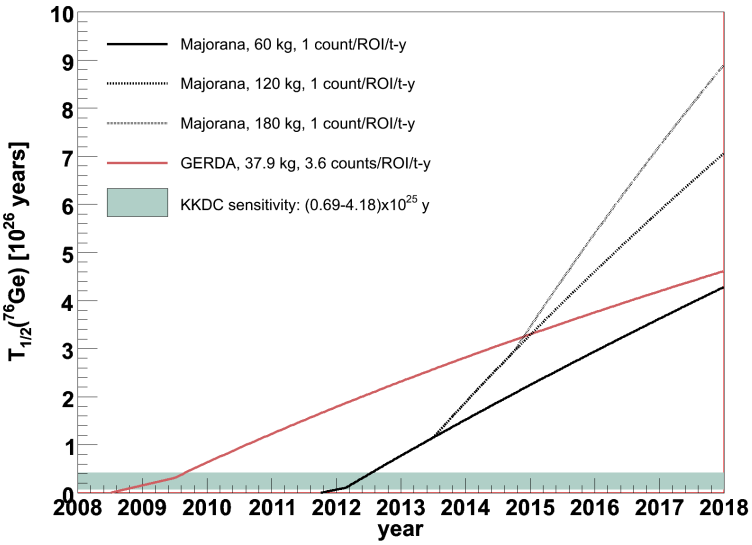

Figure 3.4: A comparison of Majorana and GERDA half-life sensitivities to $0\nu\beta\beta$ decay as a function of calendar year on a linear scale. Assumed masses and backgrounds are as stated in the figure. The start time for GERDA is based on recent GERDA projections. The start time for Majorana is based on the optimized project schedule, given in Table 3.1.

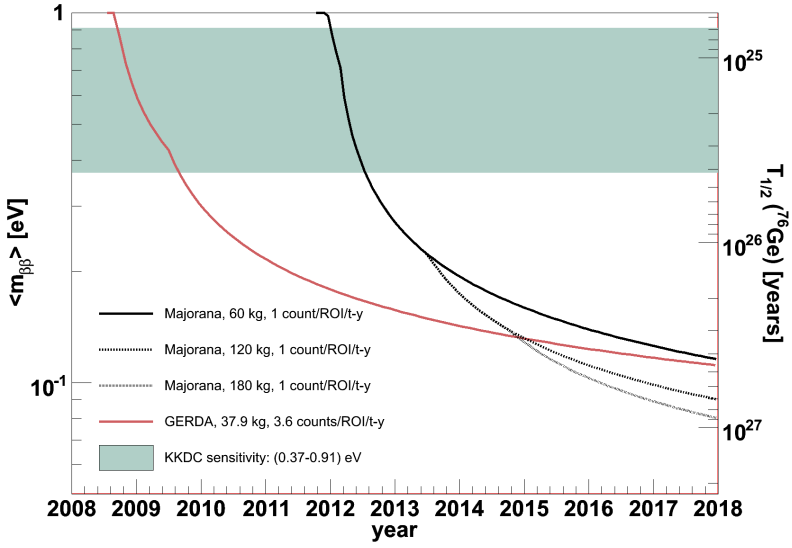

Figure 3.5: Comparison of Majorana sensitivity and GERDA sensitivity to $0\nu\beta\beta$ decay as a function of calendar year. Assumed masses and backgrounds are as stated in the figure. The start time for GERDA is based on recent GERDA projections. The start time for Majorana is based on the optimized project schedule, given in Table 3.1.

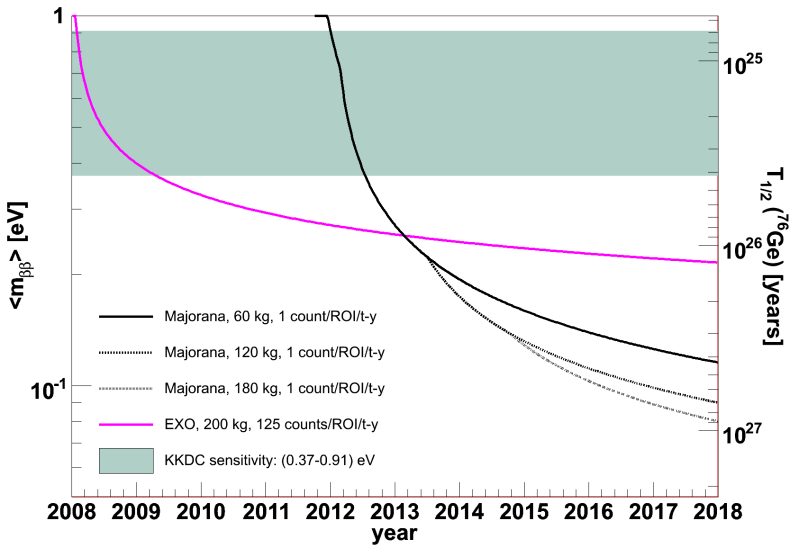

Figure 3.6: Comparison of Majorana sensitivity and EXO sensitivity to $0\nu\beta\beta$ decay as a function of calendar year. Assumed masses and backgrounds are as stated in the figure. The start time for EXO is based on recent EXO projections. The start time for Majorana is based on the optimized project schedule, given in Table 3.1.

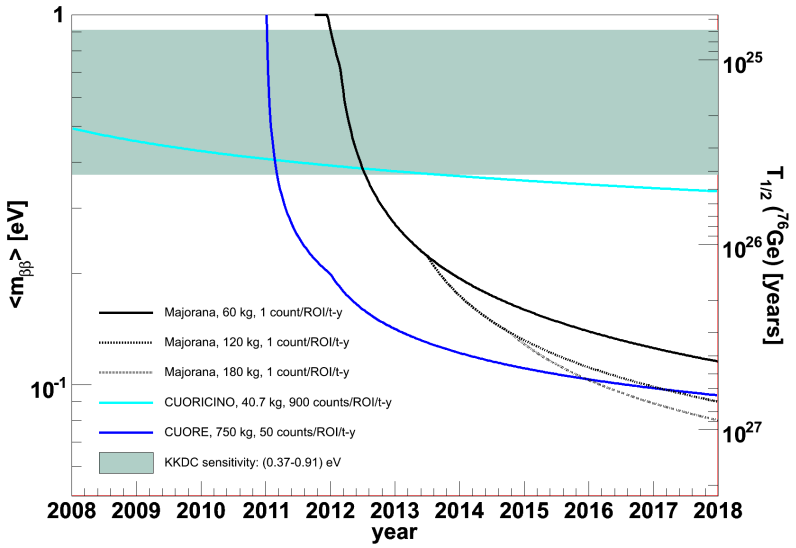

Figure 3.7: Comparison of Majorana sensitivity and Cuoricino/CUORE sensitivity to $0\nu\beta\beta$ decay as a function of calendar year. Assumed masses and backgrounds are as stated in the figure. The start time for CUORE is based on recent CUORE projections. The start time for Majorana is based on the optimized project schedule, given in Table 3.1.

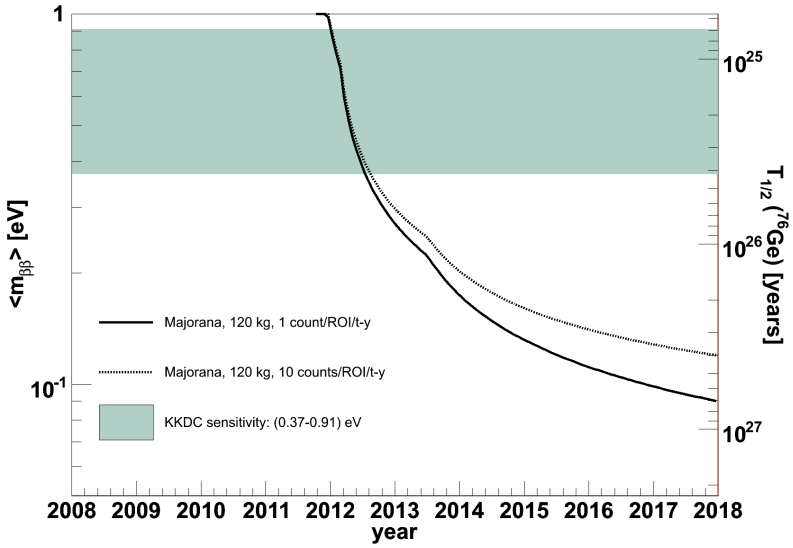

Figure 3.8: Comparison of Majorana sensitivity to $0\nu\beta\beta$ decay for 120 kg as a function of calendar year assuming backgrounds of 1 count/ROI/t-y or 10 counts/ROI/t-y. The start time for Majorana is based on the optimized project schedule, given in Table 3.1.

3.3 The Majorana Technical Design Reference Plan

In the following subsections we present technical details of our current reference design for the Majorana experiment. In many sections we also include information on various alternatives that have been considered, or that in a few cases are still being evaluated. This reference plan does not necessarily represent the final Majorana design, but it demonstrates that at the pre-conceptual design stage we have an overall plan that is technically achievable. The systems or components described in the following sections correspond to Majorana subsystems that have been defined within the work breakdown structure (WBS).[5] A summary of the current reference plan is included as a table in Appendix F.

3.4 Production of Enriched ^{76}Ge

3.4.1 Overview

The Majorana experiment requires that the detector material be significantly enriched in the germanium isotope ^{76}Ge in order to meet the physics goals of the experiment and to maximize the potential to observe neutrinoless double-beta decay. The natural abundance of ^{76}Ge is only 7.83%, but typical enrichments of 86% are currently achievable with gaseous centrifuge for kilogram quantities of enriched germanium. Higher enrichments may be possible. Previous ^{76}Ge double-beta decay experiments (including IGEX and Heidelberg-Moscow) and the on-going project SEGA have demonstrated that semiconductor diodes can be fabricated from this 86%-enriched material with characteristics comparable to natural Ge.

The gas centrifuge enrichment process, depicted schematically in Figure 3.9, starts with the centrifuging of natural germanium in a gaseous form (GeF_4). The gas is then converted into germanium oxide, and then into Ge metal via a chemical reduction process that also serves to purify the Ge of electrochemical impurities. Further purification is achieved by zone refinement. The polycrystalline zone refined bars are then sent to a crystal-pulling facility for the beginning of the detector production phase described in Section 3.5. Production rates at known facilities are sufficient for the needs of Majorana, and would likely be able to support enrichment services for several experiments simultaneously. Throughout the process, exposure of germanium to cosmic rays must be minimized. These aspects of the Ge enrichment process are discussed in detail in the following sections.

3.4.2 Enrichment Techniques

There are many methods for separating and purifying different chemical elements and for enriching certain isotopes. These isotopic separation methods include chemical and physical processes (for example rectification or chemical exchange techniques), diffusion, centrifuging, electromagnetic separation, laser ionization separation, and plasma ion-cyclotron separation methods. Chemical and physical processes are only useful for separation of light elements but are not useful for enriching germanium. Laser and plasma techniques in principle could be developed to separate and enrich ^{76}Ge; however, there are no currently operational technologies for this isotope. Electromagnetic techniques (similar to mass spectroscopy) are useful for small quantities, but would be cost-ineffective and time consuming for the quantities necessary for Majorana. The method of gaseous centrifuge enrichment is the most cost-effective and technologically developed method of germanium enrichment currently in use that could produce the necessary quantity in the time required, and is therefore chosen as the baseline for Majorana.

In the gaseous centrifuge process, natural germanium is converted to germanium tetrafluoride (GeF_4) and introduced into the centrifuge. The process incorporates many cycles of centrifuging to

[5] For more information on the WBS please see Chapter 2 of the *Majorana Draft Management Plan* document and also the full WBS found in Supplementary Documents.

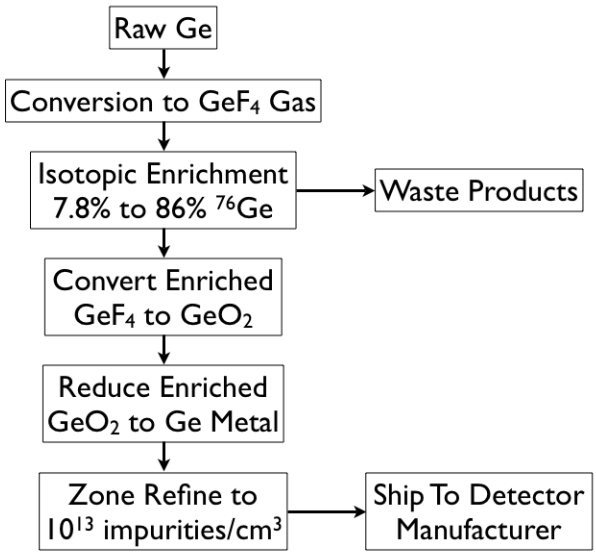

Figure 3.9: An example enrichment process diagram.

achieve the desired enrichment of nominally 86% in ^{76}Ge. The enriched GeF_4 gas is then converted into solid germanium oxide (GeO_2).

There are many centrifuge separation and enrichment facilities around the world, but the capability to enrich the required amount of germanium needed is only available at a handful of facilities, with facilities in Russia currently being the most cost-effective (see Appendix D). Smaller scale neutrinoless double-beta decay experiments using ^{76}Ge have obtained, and are currently obtaining, enriched germanium of sufficient purity from these Russian facilities. These facilities appear to have the production capacity to meet the anticipated time-scale for the Majorana experiment.

There are several promising new directions in isotope separation that might enable ^{76}Ge enrichment at a significantly lower cost. There have been some advances in plasma enrichment processes, most notably in the mirrored plasma enrichment process (MPEP), in which UCLA has developed a significantly improved method of collecting the enriched isotope. This improvement significantly increases the duty cycle of the batch enrichment process. The estimated cost for enriching ^{76}Ge with MPEP is significantly lower than current enrichment methods. There has also been research into thermoacoustic diffision to significantly increase separation and enable diffision methodologies to become competative with centrifuge enrichment for germanium. The results are promising and may provide an economic source for ^{76}Ge assuming a large scale production facility could be developed. Finally, an investigation into a cryogenic distillation column in which larger quantaties of germanium isotopes can be separated is proceeding under a DOE Small Business Innovation Research (SBIR) grant. The column is anticipated to use germanium hydride gas as the feed source for the distillation process. The SBIR will fund a pilot-sized column to demonstrate the feasibility of the process, and if successful, could lead to an industrial sized production facility. The cryogenic distillation column has the potential to significantly lower the costs of enriching germanium. These three alternative methods of ^{76}Ge production are being closely watched by the Majorana collaboration and, if proven successful on an industrial scale, may provide a cost-effective alternative to gaseous centrifuge enrichment.

3.4.3 Chemical Reduction

At the end of the gaseous enrichment process, the enriched GeF_4 is converted into GeO_2 for transport. The GeO_2 must be subsequently converted into Ge metal via a chemical reduction technique, which removes oxygen from the material along with many electrochemical impurities. However, the impurity level after chemical reduction is still too great to achieve crystals operable as radiation detectors. In order to further reduce the impurity levels, zone refinement is required. In order to facilitate the zone refinement process, the Ge metal is typically cast into long bars of approximately 10 kg in mass. From experience in IGEX, we anticipate a materials loss of $\sim$4% per batch during chemical reduction. Possibilities for recycling some of this material are discussed in Section 3.4.5.

3.4.4 Zone Refinement

Zone refinement is a process in which a heat source is moved slowly down the length of a bar of polycrystalline Ge, melting the material locally. During this process, the bar is sealed inside a vessel with a cover gas to prevent oxidation. Electrochemical impurities, which have favorable segregation coefficients, are swept along the induced melting zones down to the ends of the bar, leaving a pure central region that can be pulled into single crystal Ge and fashioned into radiation detectors. After zone refinement, the polycrystalline metal is tested to have resistivity $>40\ \Omega$ cm.

There are typically two phases of zone refinement, with the first phase performed at the same site as the chemical reduction process. This first phase of zone refinement reduces the total impurity concentration to approximately 10^{13} cm^{-3}. The second phase of the zone refinement is typically performed at the crystal pulling facility just prior to the crystal growth. This second phase reduces the impurity concentration to $\sim 10^{10}$ cm^{-3}.

3.4.5 Material Accounting

The depleted GeF_4 byproduct of the enrichment phase is not needed for this experiment. However, due to the cost of the enriched germanium, it is imperative that the discarded material during the chemical reduction and zone refinement processes be collected and recycled. The ends of the zone-refined bars that are discarded in one cycle may be inserted back into the pre-zone refinement or pre-chemical reduction phases of later cycles, and hence waste during this phase can be minimized. Waste does occur, however, during chemical reduction, primarily due to residue material left behind in the purification apparatus. Most of this material is pushed out by the next batch. Existing chemical reduction facilities can deliver steady-state single batch yields of 96%.

A simple model of the Germanium processing and materials accounting has been developed in Appendix G. After summing losses over the many cycles necessary to process all of the Ge, the 4% per-batch losses in the chemical reduction phase compound to $\sim$10% loss of the total processed material. Another $\sim$10% loss of enriched material occurs in detector fabrication processes (see Section 3.5.4). Such high losses make a significant impact on the total cost of project. Part of the Research and Development effort of Majorana will be to investigate and construct more efficient recovery processes (see *Majorana Project R&D Plan*). We hope to reduce the net loss by a factor of 2 or more.

3.4.6 Shipping and Storage Considerations

In addition to removing electrochemical impurities that determine the semiconductive properties of the Ge crystals, the chemical reduction, zone refinement, and crystal pulling processes leave the Ge radiologically very pure. In order to maintain this purity, the material must not only be handled carefully, but must also be shielded from cosmic radiation, which produces by spallation various radioactive isotopes in the Ge. Of particular concern for Majorana are ^{68}Ge and ^{60}Co, whose contributions to the background are discussed in detail in Section 4.2. The contamination levels of

these two isotopes are essentially reset to zero by the gaseous centrifuge process. Zone refinement will significantly reduce ^{60}Co, perhaps again to zero, however ^{68}Ge will continue to accumulate. The accumulation of this species drives the criteria for the total allowable exposure time for the separated isotope. Approximately 1 atom of ^{68}Ge is created per kg per day of exposure to a surface cosmic ray flux. To achieve our background goal, this activation rate implies a limit of ∼100 days of exposure to surface-rate cosmic rays for the isotope from separation until its installation in a deep underground site. A detailed Quality Assurance program monitoring the Ge time history will be required.

Much of the anticipated surface exposure occurs at the enrichment site, while Ge is being aggregated for shipment. The availability of shallow underground storage at the enrichment facility would provide a factor of 100 or more exposure reduction, allowing Ge to be stored for weeks or even months without activating appreciable amounts of ^{68}Ge.

If the enrichment occurs overseas, for example at a Russian facility, then the shipping time to domestic operations presents the next most serious potential surface exposure. Unfortunately, shipping the material quickly by air is not a very good solution, because the high-energy neutron flux is about 15 times more intense at the cruising altitude of aircraft than at ground level. Hence 12 hours of shipment by air at 12,000 meters would be the equivalent of 8 days exposure at sea level. While land/sea transit would be much slower and may involve some complicated border crossings, the exposure would be half or less that of air shipment, if sophisticated shielding and placement were utilized. We are exploring the construction of a ∼2 m cube concrete shipping container, with the Ge positioned near the bottom, giving roughly 5 meter water equivalent overburden. Using such shielded shipping containers is projected to result in a roughly ten-fold decrease in ^{68}Ge activation in transit, thus ∼30 days of exposure will be reduced to the equivalent of only ∼3 days. The shipping container could then be used for on-site storage at the chemical reduction and zone refinement facilities, potentially with an augmented overburden, while awaiting processing.

The remainder of the surface exposure during the enrichment phase occurs during the chemical reduction and zone refinement processes themselves. Surface exposure will also occur during crystal pulling and detector manufacturing, discussed in Section 3.5. We are exploring the possibility of moving these processes underground; however, the feasibility of this option with regards to the project budget and schedule have not been demonstrated at this time. The quantitative impact of shielded shipping and storage on backgrounds in Majorana is discussed in Section 4.2 and will be studied further in the R&D phase of Majorana (see *Majorana Project R&D Plan*).

3.4.7 Quality Assurance of Germanium Procurement

At each phase of the enrichment process, the quality of the product must be ensured. The production facilities will provide analysis and certification; however, Majorana collaborators will perform additional analysis for independent verification. After enrichment of a batch, samples on the order of a few grams will be collected. Part of the sample will be analyzed using ICPMS to ensure the proper enrichment has been obtained, particularly the suppression of the low-mass isotopes of Ge. The rest of the sample will be archived in case future analysis is required. After the chemical reduction phase, samples will again be collected and analyzed to ensure the enrichment and purity have been maintained. Enrichment values for each detector produced will be recorded and archived for the data analysis phase of the project.

3.5 Detector Design, Engineering and Fabrication

3.5.1 Overview

The use of well-established detector designs and technology present the Majorana collaboration with a variety of detector configurations and design options with which to optimize signal robustness, background rejection, and background mitigation. Recent developments in HPGe detector

technology are providing new options highly suited to double-beta decay searches. The principal factors influencing detector design include:

- **Limiting backgrounds and the introduction of contamination and radioactivity.** This requires careful quality control for all detector components and production processes. Low background material must be used throughout. One must introduce a minimum of non-active material near the detector and reduce as much as possible the connections and electronics close to the detector. The shielding and support materials must be carefully screened for radiopurity and production and assembly procedures must be controlled.

- **Increasing the ability to reject background signals by enabling analysis procedures and techniques.** These techniques include the identification of single-site and multi-site energy depositions within the detectors and single-site time-correlated analyses. Therefore, the detector should be designed to provide sufficient information for supporting analyses involving both spacial and temporal correlations between signals.

- **Increasing the ability to measure and characterize backgrounds and to interpolate and extrapolate background signals into physics analysis "regions of interest".** In addition to straightforward rejection of background signals, it will be important to characterize the full background and physics signals and to extrapolate irreducible backgrounds into the physics analysis regions.

- **Increasing ability to produce a robust and reproducible measurement and physics analysis, and provide adequate tests and confirmations of any physics discovery.** Any result, positive or negative, will need to be extremely robust. The Majorana signal analysis will necessarily require a self-consistent analysis of the full energy spectrum of the detectors and a quantitative explanation of all signal and background peaks.

The detector design criteria are a function of the discovery threshold for the experiment (the effective neutrino mass) and consequently the detector time exposure. The goal for the current proposal is to perform a sensitive double-beta decay measurement and to demonstrate robust technologies, background levels, and analysis capabilities necessary to scale the experiment to the $\sim$1 ton scale.

The primary tool for distinguishing potential neutrinoless double-beta decay event candidates from the many background sources relies on identifying single-site energy depositions and discriminating them from background events that deposit energy in distributed spatial points in the detector volume. $0\nu\beta\beta$ decay is identified by two final state electrons sharing the full decay energy (Q-value = 2039 keV). These electrons deposit their energy within $\sim$2 mm of the decay vertex. Many troubling background signals are created by the Compton scattering of high energy γ-rays with the energy deposited in a single site accidentally equivalent to 2039 keV. Detecting the residual γ-ray energy in other detectors or within the same detector provides a powerful method for identifying and rejecting these backgrounds.

Hence an analysis of spatially and temporally correlated energy depositions provides an additional tool for the rejection of radioactive background signals. Detector multiplicity and segmentation along with pulse-shape analysis enable such rejection capabilities. Segmentation can be in a single dimension, for example, a simple z-axis segmentation (resulting in a stack of cylinders), or in multiple dimensions. Unsegmented coaxial detectors can deliver radial discrimination of multiple energy depositions in a single detector with pulse-shape analysis (as was done with IGEX and Heidelberg-Moscow), as well as provide some ability to establish a radial fiducial volume "cut". Simple "z-segmentation" can provide additional position resolution and thus discrimination between multiple depositions at a common radius, but with different z coordinates. Adding adequate azimuthal segmentation effectively enables three-dimensional spatial reconstruction of events. In general, a higher degree of segmentation results in increased reconstruction resolution, and hence

finer discrimination between single-site and multiple-site depositions and improved ability to perform a full 3-dimensional fiducial analysis, equivalent to a (solid-state) Time-Projection-Chamber. It also enhances the ability to perform single-site time correlated analysis by reducing the effective pixel size for each event origin, and hence the event rate in each pixel. These advanced capabilities come at the price of a much larger quantitiy of small parts such as cable, and their selection must be optimized against their ability to overcome added backgrounds.

Whereas most earlier $0\nu\beta\beta$ studies have concentrated on explaining backgrounds in the $0\nu\beta\beta$ region of interest (ROI), a more robust analysis for the next generation of experiments will be necessary, providing a self-consistent extraction of the full energy spectrum. Consequently all the gamma-, beta-, and alpha-decay signals in the detector will need to be quantitatively understood and analyzed to produce a convincing statement of signals or absence of signals in the $0\nu\beta\beta$ ROI. Better event reconstruction capability and finer spatial event resolution should permit a more accurate analysis of the full energy spectrum by enabling multi-dimensional analysis of background and physics signals.

The technology of mass-producing highly segmented detectors with 36, 40, and more segments is being rapidly advanced, notably by GRETINA [Des05], AGATA [Sim05], and TIGRESS [Sve05a]. GRETINA in particular has provided very encouraging initial analyses that events can be reconstructed with a position uncertainty of $\sim$2 mm. Even without absolute event vertex reconstruction, events with multiple energy deposits can be identified and rejected. Preliminary results from these efforts indicate that a minimum separation of 4 mm will be achievable.

Although intuitively the best design would appear to be the one with the highest degree of segmentation feasible, this is not necessarily the case. Higher detector segmentation requires more contacts, more front-end electronics, and more associated "small parts", all of which increase the risk of introducing additional backgrounds and contamination. The higher segmentation significantly increases the complexity of the detector and the detector assembly. Finally detector production rates and costs influence the choice of segmentation and detector design.

3.5.2 Key Detector Characteristics and Parameters

The following subsections briefly list the key detector characteristics and parameters. The principal elements influencing their choice and optimization are presented. The preferred detector geometry is a closed-end semi-coaxial cylindrical detector, although alternative geometries are possible, including true coaxial and planar detectors. We will present a more qualitative evaluation of potential detector configurations and segmentations in Section 3.6 The detector manufacturing process is described in detail in Appendix E. The principal manufacturing steps are outlined below in Section 3.5.4.

Neutrinoless double-beta decay events will deposit energy in a single small region of a detector. Many backgrounds result in multiple energy depositions. A reasonably close-packed array of detectors enables the efficient rejection of several types of radioactive backgrounds by increasing the probability of detection for multiple Compton-scattered γ-rays in adjacent detectors or in adjacent detector segments. The crystal-to-crystal rejection of backgrounds as well as single-site time correlation identification of radioactive decay chains favor a larger number of smaller crystals. Issues of detector production, introduction of backgrounds close to the detectors with signal leads and electronics, surface-to-volume ratios (important for controlling surface contamination) and assembly of the array favor fewer and more massive crystals. Simple segmentation schemes, without full event reconstruction, can effectively partition a single crystal into multiple isolated segments with the same ability to reject backgrounds. Therefore, the detector design would naturally select geometries and detector masses that permit segmentation and high production yields.

The commercial production of Ge detectors is limited by the ability to produce (grow) single Ge crystals and to produce p-n junction diodes from these crystals. The single crystal boules naturally favor right circular cylindrical geometries. Therefore, cylindrical or coaxial detectors are the natural choice to efficiently use the precious Ge material. Ge detectors have also been produced

Table 3.2: Detector characteristics of recent Ge arrays used in nuclear γ-ray spectroscopy.

Detector or Array	**Crystal Geometry**	**Diameter (mm)**	**# of Segments**	**Year Ordered**	**Crystals per Unit**	**Units Produced**	**References**
Gammasphere	cylindrical coax	70	2	1995	1	65	
MSU (SeGA)	cylindrical coax	70	32	2001	1	18	[Mue01]
Canberra Clover	cylinder/square	50	2	2002	4	30	
EXOGAM (Clover array)	cylinder/square	60	4	2001	4	10	[Fra04] [Sim00]
TIGRESS Prototype (Clover array)	cylinder/square	60	8	2003	4	12	[Sve05a] [Scr05] [Sve05b]
Miniball	tapered regular hexagon	70	6	2002	3	6	[Ebe01]
GRETINA Prototype 2	tapered regular hexagon	70	36	1998	1	1	[Des05] [Lee03]
GRETINA Prototype 3	tapered regular hexagon	80	36	2004	3	1	[Des05] [Lee03]
GRETINA Production Unit	tapered irregular hexagon	80	36	2005	4	1	[Des05] [Lee03]
AGATA	tapered hexagon	80	36	2003	3	2	[Sim05]

in planar geometries with two-dimensional segmentation schemes as well, either in pixelated or so-called double sided strip configuration. However, this type of detector requires guard rings and therefore non-sensitive areas at the edge of the detector to minimize the degradation of the charge collection due to surface effects at the outside and passivated surface. More efficient use of Ge material is achieved with coaxial Ge detectors. To minimize the passivated area and maximize the sensitive volume in coaxial detectors they are typically built in so-called closed-end geometries with a bore hole only on one side. This bore hole with a central electrode is necessary to achieve sufficiently high electrical fields to achieve not only depletion throughout the crystal but to achieve high mobility of the charge carriers.

Table 3.2 presents detector characteristics for several recent Ge detector arrays used in nuclear γ-ray spectroscopy employing coaxial HPGe detectors with a wide range of segmentation schemes. They range from two-fold segmentation for Gammasphere to 36-fold segmented detectors for GRETINA and AGATA. In addition, a forty-fold segmented, coaxial HPGe detector was built and demonstrated for Compton imaging applications, combining two-dimensional segmentation with digital signal processing.

Several recent γ-ray arrays required substantial machining and reshaping of the crystals to obtain the required close-packing of adjacent crystals. This criterion is not anticipated for Majorana. Indeed, the experiment is able to accommodate a reasonable range of sizes without loss of physics capabilities. The coaxial detector geometries favor longer z-axis geometries for minimizing edge fields and fringing effects in the vicinity of the closed end.

Diameters ranging from 50 to 80 mm and lengths between 70 and 90 mm are listed in Table 3.2. The detector production yield declines with larger dimensions. A diameter of $\sim$65 mm appears to be an empirical threshold for obtaining high detector yields. Detector lengths of $\sim$70 mm are routinely produced. Our baseline 62 mm diameter by 70 mm long detector contains $\sim$1.1 kg of Germanium, of which 86% is ^{76}Ge (0.946 kg).

Complementary to the implementation of closed-end coaxial HPGe detectors with bore holes that

reach typically through about 80% of the detector crystal, it was recently shown that the length can be reduced to only a few millimeters resulting in a more Ge-drift-like detector configuration. This modified electrode design was recently demonstrated to provide low noise resulting in a low energy trigger threshold and excellent energy resolution as well as excellent pulse-shape capabilities to distinguish multiple interactions. The latter is due to the low electrical fields in the crystal and the increased range of drift distances as well as the small electrode configuration enabling the so-called small pixel effect reflecting the fact that the signal at the small central readout electrode is only measured just before the charge is actually collected.

3.5.3 Detector Performance Goals

In the following two sections we discuss a number of key detector performance specifications. In some cases these parameters will impact detector production rates. Detailed discussions of the impact of these parameters on backgrounds are contained in Sections 4.1 and 4.2.

Energy resolution Energy resolution can affect the physics reach of neutrinoless double-beta decay experiments by increasing the background signals in the $0\nu\beta\beta$ region of interest, for example due to spillage into the region of interest from events in nearby γ peaks or the $2\nu\beta\beta$ spectrum itself. This systematic effect is more severe for relatively low-resolution detectors, such as gaseous Time Projection Chambers, where the energy resolution is typically a few percent. For Ge detectors the energy resolution is typically <0.2% and the associated systematic error is negligible.

Detectors of the size and geometry proposed for Majorana typically achieve an energy resolution of 0.16% FWHM at 2 MeV. The energy response to monoenergetic gamma rays is well characterized and the effects of non-gaussian (long) tails are very small.

Pulse-shape analysis As demonstrated previously, pulse-shape analysis of signals from the central contact of coaxial HPGe detectors provide a very sensitive tool to distinguish single-site from multiple-site gamma-ray interactions. This sensitivity exists, however, only primarily along the radius of the detector. The minimum radial distance of two interactions that can be distinguished is typically in the order of 4 mm. To obtain complementary sensitivity along the depth or along the ϕ direction, the detector needs to be segmented and then transient image charges can be used to provide the ability to distinguish single from multiple interactions.

Impact of segmentation on detector signals There is some evidence that the process of segmenting the detectors may perturb the collection of electronic signals in the immediate vicinity of the segment boundaries. A calibration and detector characterization (with low energy γ-rays) may be required to quantify such effects. Such a calibration, discussed more in Section 3.12.5, would be required to understand the specific geometry of each crystal, in any event. This characterization is similar to efforts being carried out for γ-ray tracking detectors.

Detector segmentation has an additional positive effect on detector signals. Electric field variations across a single segment are smaller than variations across an entire crystal. As a result, finer segmentation tends to improve event radius reconstruction.

3.5.4 Detector Manufacturing/Production Requirements

Outline of steps required to produce Ge detectors

- **Zone Refinement** As discussed in Section 3.4.4, the enriched Ge metal undergoes a second stage of zone refinement to remove electrochemical impurities at the crystal pulling facility. This second stage of zone refinement reduces the impurity concentration to $\sim 10^{10}$ cm^{-3}.

- **Crystal Production** The zone refined polycrystalline bars are remelted and single crystals are "pulled" with a Czochralski crystal puller. The single crystal boules are then machined into detector blanks and the general crystal properties determined (e.g. resistivity). Depending on the impurity concentration, the discarded boule ends may be included in the next batch to be zone refined. If large amounts of impurities are present, the ends may instead be sent back to the chemical reduction facility to undergo reconversion into GeO_2 and chemical reduction to metal.

- **Detector Fabrication** The single crystals are then machined to shape the detector and introduce the coaxial hole and chemical etching and lapping to remove local damage. The surfaces are then doped or implanted to produce the p-n diode junction. Finally, surface electrodes are applied and leads and electrical components installed to the crystal. Segmentation requires the use of masks or other means to produce electrodes, providing electrically isolated-segments.

Contamination control Among the inherently less-radiopure aspects of the detector design are the electrical contact and the readout components such as cables and front-end electronics. This contamination becomes more important with higher segmentation. Part of the Majorana R&D plan involves research into evaluating and potentially making contacts and readout components with lower mass and improved radiopurity.

The potential for introducing contamination, particularly in the final detector fabrication steps, will require careful Quality Assurance and Quality Control (QA/QC). The specific QA/QC requirements will need to be developed as our integrated background model and detector simulations mature. Careful negotiations with the detector manufacturers and vendors to assure a rigid conformance to project procedures will be required. It is anticipated that a significant on-site presence by project scientists and engineers will be necessary to assure this conformance.

Detector production rate To meet project goals we anticipate a requirement of manufacturing two detector blanks per week. This rate conforms to the isotope delivery schedule of ∼100 kg/year and a final detector production rate of 75 kg/year in ∼70 detectors/year. Recent informal discussions with vendors that produce detector blanks suggest this rate can be sustained. There are unresolved details about minimum batch sizes and integrated cosmic ray exposures for the batches that will require additional discussions with potential vendors.

The production of a large number of highly segmented detectors may represent a challenge for known detector vendors. There are indications the vendors would be amenable to discussions of opening additional manufacturing lines, perhaps domestically, to satisfy Majorana's production requirements.

Enriched material recycling The intrinsic value of the enriched material is high enough that a material recycling program is indicated. Therefore, effectively all the material not used in a detector blank will be recycled and re-zone refined. This will include pieces of the crystalline boules not accepted for detector blanks, cuttings, and failed detectors. Detector manufacturing involves machining and etching of surfaces. Hence cutting, lapping, and etchant wastes are also produced. Some of this material can be recovered readily; other sources of waste are less easily cleaned and transformed into starting materials. Of particular concern is sludge: mixed etchants, Ge mixed with lapping compounds, and other similar wastes.

The Ge material processing model described in Appendix G estimates that compounded losses during the detector production stage amount to ∼10%, half of the total material losses. The other half occurs during the chemical reduction stage, see Section 3.4.5. We estimate an additional 7 kg of enriched mass will be rejected in the production of the last usable boule. This material would be a candidate for future experiments or for blending down to make lower enrichment crystals.

An analysis by Oak Ridge National Laboratory indicates that the dissolved Ge may be recoverable from the etch solutions. Negotiations with the crystal and detector manufactures will address the recycling of materials. The detailed QA/QC program and material recycling will be determined in the contract negotiations and qualified in the R&D Detector phase of the project.

Detector manufacturing in a shielded environment As discussed in Section 4.2, the accumulation rate of ^{68}Ge due to cosmic radiation sets a limit of ∼100 days on the surface exposure time of the Ge following enrichment. In the Ge enrichment phase we are exploring options to process, store, and ship the material in shielded environments to minimize the surface exposure (see Section 3.4.6). Similarly, we are pursuing the possibility of performing crystal pulling and detector manufacturing in an underground environment. Even a few hundred meters water equivalent shielding reduces the cosmic ray activation to a negligible rate. A report discussing this option is included in Appendix E. The feasibility of underground detector manufacturing is potentially an expensive and time-consuming proposal and will require detailed negotiations with commercial vendors. Moreover, we estimate that Majorana's background level goals can be achieved with above-ground detector manufacturing. At this time, underground detector manufacturing is not part of the Majorana baseline plan.

Initial detector quality control tests The acceptance tests for the detectors will require detailed negotiations with the vendors but will likely test the basic functionality of the detectors either singly or in sets of three in their final detector holders. Energy resolution, leakage current, depletion voltage, crystal orientation, and segment functionality would likely be obtained at the vendors. Complete characterization will be performed underground by the collaboration.

3.6 Evaluation of Detector Configuration and Segmentation Schemes

This section describes the quantitative evaluation and comparison of possible detector configurations for the Majorana experiment. Above, we discussed aspects which are important in the evaluation and choice of a specific configuration qualitatively, in the following we will discuss these aspects more quantitatively. All the aspects discussed above, ranging from common issues to implementation-specific issues, need to be taken into account in order to quantitatively evaluate possible implementation schemes in terms of sensitivity and physics impact, cost, and schedule.

This section reflects the culmination of an effort to evaluate detector configurations and segmentation schemes for the planned Majorana experiment. It presents a quantitative comparison between possible detector implementations to confirm, refine, or potentially redefine the baseline for Majorana, to identify and quantify critical risks to the expected performance, cost, and schedule and finally, to provide guidance for R&D efforts to address and minimize these risks.

In the following we will briefly discuss the process used to evaluate possible detector configuration and segmentation schemes. We will then briefly discuss the four different implementations chosen for a more detailed analysis, the metric we use for the evaluation and the results of this study, including guidance for the R&D phase.

The process to evaluate possible detector configuration and segmentation schemes for the Majorana experiment consists of several steps. First, we need to define and select configurations we want to evaluate. We need then to identify all issues potentially impacting the performance, cost, and schedule and to determine their impact on the metric that is to be defined. This step comprises input from Monte-Carlo simulations, the detector manufacturer, previous and ongoing R&D, and the mechanical and electrical design of the experiment as discussed previously. Based on the outcome and complementary considerations, we decide what configuration to adopt for the Majorana baseline. Figure 3.10 summarizes the process graphically.

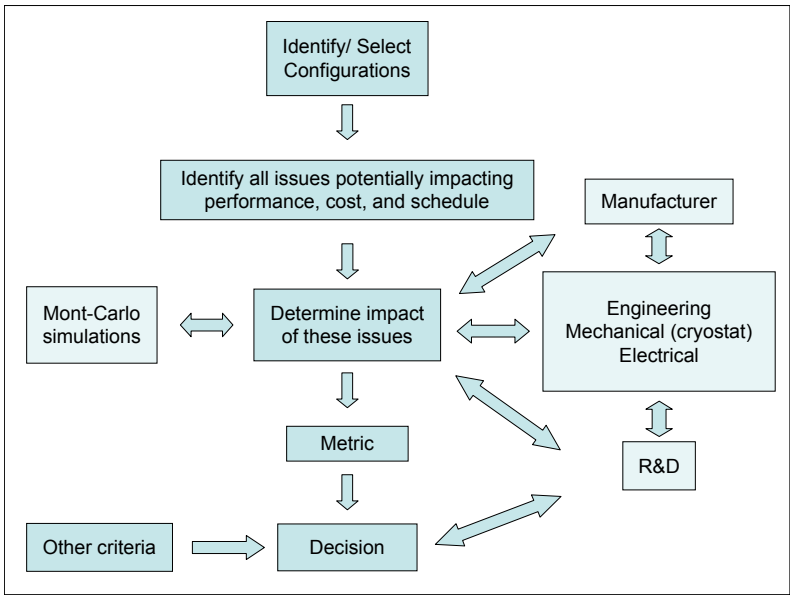

Figure 3.10: Detector implementation evaluation path.

3.6.1 Selection of Detector Implementations for Evaluation

High-purity Ge detectors have been built in cylindrical (coaxial) and planar geometries for more than 30 years. Both configurations have been implemented with one- and two-dimensional segmentation. Two-dimensional segmentation can be achieved by either pixilation of one electrode or forming orthogonal strips of both electrodes. Planar HPGe detectors in double-sided strip configuration are one example of the latter. While small segment geometries for planar detectors have been realized, this type of detector requires guard rings and therefore non-sensitive areas at the edge of the detector to minimize the degradation of the charge collection due to surface effects at the outside and passivated surface. More efficient use of Ge material is achieved with coaxial Ge detectors. To minimize the passivated area and maximize the sensitive volume in coaxial detectors they are typically built in so-called closed-end geometries with a bore hole only on one side. The bore hole with a central contact is necessary to achieve sufficiently high electrical fields to achieve not only depletion throughout the crystal but high mobility of charge carriers. Since p-type crystals can be grown more efficiently to larger dimensions this type is generally being used. In addition, with p-type detectors trapping effects are reduced, and generally slightly better energy resolution is obtained. P-type detectors are fabricated with the n+ Li-drifted contact on the outside electrode to obtain efficient and full depletion from the outside and the p+ B-implanted contact inside. While the inside B-contact is very thin (typically <1 μm) the Li drifted contact is typically more then 100 μm thick and can increase up to 1 mm due to the high mobility of Li in Ge. The thickness of the outside-Li contact provides an advantage for Majorana since this dead layer absorbs external alpha-particle background. However, the high mobility of Li and the associated drift instability prevents p-type detectors from being segmented efficiently with sufficient robustness and stability. The established way to segment coaxial detectors is by using n-type detectors and segmenting the outside B-implanted contact using masks and photolithography techniques. Hundreds of detectors have been produced in this way over the last ten years. They range from two-fold segmented detectors, e.g. for Gammasphere, to

40-fold segmented detectors for Compton imaging applications. While the pulse-shape obtained at the central contact in coaxial detectors can provide radial separation of multiple interactions in any implementation, pulse-shapes obtained in segmented detectors can provide improved sensitivity in the radial separation but, more importantly, in complementary directions as well. A high-degree of segmentation, such as a 6x6-fold segmentation, as is being developed for the new generation of gamma-ray tracking arrays or for Compton imaging, enables the full reconstruction of gamma-rays within the detectors.

In a change to the normal implementation of closed-end coaxial HPGe detectors with bore holes that reach typically through about 80% of the detector crystal, it was recently shown that the length of the bore hole can be reduced to only a few millimeters, resulting in a more Ge-drift-like detector configuration. This modified-electrode design was recently demonstrated to provide low noise resulting in a low energy trigger threshold and excellent energy resolution as well as excellent pulse-shape capabilities to distinguish multiple interactions. The latter is due to the low electrical fields in the crystal and the increased range of drift distances as well as the small electrode configuration enabling the so-called small pixel effect reflecting the fact that the signal at the small central readout electrode is only measured just before the charge is actually collected.

Based on this discussion, we have chosen four types of possible HPGe detector configurations to be evaluated more quantitatively: 1.) Non-segmented p-type detectors; 2.) Modestly segmented n-type detectors; 3.) Highly segmented n-type detectors, and; 4.) Ge-drift-like or so-called modified electrode detectors. These configurations cover the range of technologically feasible Ge detector implementations. The modified electrode approach is the only one which is not well established yet but can be potentially very useful for Majorana if more detectors can be successfully demonstrated. Figure 3.11 shows a range of one- and two-dimensional segmentation schemes. Figure 3.12 illustrates the modified electrode implementation in contrast the conventional, closed-end coaxial detector approach.

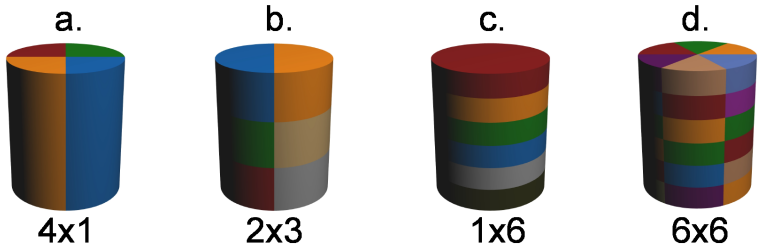

Figure 3.11: Possible segmentation schemes for Majorana, ranging from modest (a,b,c) to high (d) segmentation.

Our collaboration has recently demonstrated that it is possible to segment coaxial p-type detectors with an outside Li-drifted contact by cutting grooves into the crystal to electrically isolate the segments. However, critical aspects such as the degradation in charge collection due to these grooves and the associated impact on pulse-shape analysis and the long-term stability remain to be demonstrated. We therefore chose not to include this approach in the list of configurations right now. The same is true for amorphous contact technology, which has been developed over the last ten years to replace the Li contact in segmented HPGe detectors. This technology is being successfully used in planar detectors, again in double-sided strip configuration, however, no coaxial detector has been built to date.

In the following we will briefly discuss each of the four configurations including advantages and drawbacks.

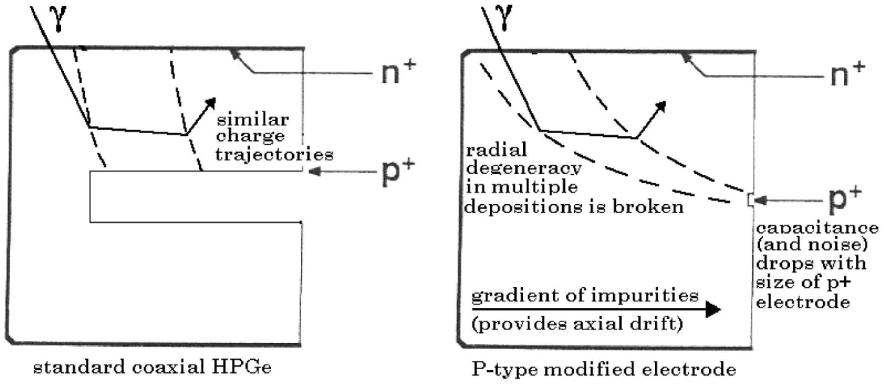

Figure 3.12: Closed-end coaxial Ge detector (left) versus the modified electrode Ge detector implementation (right).

Non-segmented p-type detectors P-type detectors are associated with the lowest risk in terms of cost and schedule. This type of detectors are not only widely used but have been used previously in $0\nu\beta\beta$ experiments. They can be built by several manufacturers and production rates can be adjusted easily. Detector fabrication, acceptance, characterization as well as deployment are less complex than for the other options. The thick outside Li contact provides shielding from surface activities. Only one readout channel is required from the central contact for each crystal minimizing the background due to contacts, cables, and other small parts. On the other hand, background suppression can only been done by radial pulse-shape analysis and using the detector granularity, e.g. by suppressing events associated with gamma-ray interactions in multiple detectors, similarly to the previous $0\nu\beta\beta$ experiments. Considering the still ongoing debate about the results of these experiments, however, more information to better understand observed features and to demonstrate consistency in the data, particularly when observing the $0\nu\beta\beta$ signal is asked for to potentially increase the physics reach for Majorana. To improve the granularity in this approach we consider not only 1.1 kg detectors but also smaller units such as 0.55 kg.

Modestly segmented n-type detectors Many modestly segmented n-type detectors with 2-12 segments have been fabricated over the last 10 years primarily for nuclear physics experiments. Detectors with a moderate degree of segmentation are a good compromise between the advantages of segmented detectors in identifying background events and the added cost and risk of more complicated highly segmented designs. Segmentation of the detector can provide sub-segment position resolution for the energy depositions in the crystal, through analysis of position-dependent "image charge" signals that are induced in neighboring segments, as is done for gamma-ray tracking detectors. While the position resolution would be improved with more highly-segmented detectors, the resulting additional gains in background suppression are small and may be outweighed by the added cost and complexity. In simulations, a modest segmentation of between four and eight segments per crystal provides most of the background rejection capabilities. However, even with only moderate segmentation, detailed characterization of each detector's response as a function of position will be necessary. Also, compared to non-segmented designs, additional contacts and cables will be required for the segment signals; this adds a risk of extra background sources close to the detectors. We evaluated three different modest segmentation schemes, a 4x1, 2x3, and 6x1 as shown in Figure 3.11 to obtain a better sampling of the trade-offs within approach.

Highly segmented n-type detectors The combination of high segmentation and pulse-shape processing of the segment signals provides the ability to fully reconstruct gamma-rays within the instrument, as shown in nuclear physics and Compton imaging applications. In this way it might provide the best way in characterizing every event observed in the instrument and therefore provide the most information to address questions in signal robustness, unforeseen backgrounds, and systematic uncertainties. However, it represents by far the most complex implementation in terms of detector manufacture, characterization, deployment, and operation. In addition, it requires design and potentially deployment modifications due the significantly increased number of readout channels. The proposed approach for highly segmented detectors would leverage from the significant investment and R&D from GRETINA to produce a scalable small array of crystals. This small array (9 crystals) would be mounted in a single cryostat, would approximate the Germanium mass in a single GRETINA detector and would, within a factor of 2, equal the number of signal leads from a single GRETINA detector. There is the potential to adopt some of the existing engineering of cooling ∼9 kg of Ge, and routing ∼200 to 300 cables from a single cryostat, with the caveat that low-background solutions are not necessarily compatible with these existing designs. The use of warm FETs for the segment signals and cold FETs for the central energy channel would also be borrowed. The use of smaller arrays would permit units to be assembled, debugged, characterized and kept on-line, while additional mass is introduced with subsequent units with a minimum of interference and down-time. This scheme would permit the manufacturer to accomplish much of the initial assembly work, under the watchful eye of the collaboration, and focus qualified industrial workers to accomplish much of the technically challenging work. The real driver for high segmentation designs is the full three-dimensional reconstruction of events and the corresponding rejection of background events. Such designs have the potential ability to reconstruct events and validate potential discoveries with multidimensional analyses and fiducialization of events.

Ge-drift-like or so-called modified electrode detectors A p-type modified-electrode HPGe detector as shown in Figure 3.12 has been developed with the goal of detecting the very soft (sub-keV) recoils expected from coherent neutrino-nucleus scattering in a reactor experiment. The changes in the electrode structure result in a drop in capacitance to ∼1 pF. Combined with modern-day FETs this leads to a low-enough energy threshold in a massive-enough device (0.5 kg) to make the measurement possible. A gradient of charged impurities along the crystal axis allows for an efficient charge collection, resulting in an optimal energy resolution, similar to that from a standard p-type coaxial device. The modified distribution of field lines in this new device breaks the radial degeneracy that limits the ability of coaxial detectors to distinguish single from multiple interactions, resulting in background rejection capabilities comparable to segmented devices, but without the introduction of irreducible backgrounds via additional cabling, small parts, etc. Besides this optimal background rejection with a single-channel device, the advantages of this type of detector for Majorana are numerous: potential increased speed of manufacture and reduction in costs, simpler construction and data analysis, decreased thermal load and photon path, an enhanced ruggedness characteristic of p-types, and a diminished sensitivity to surface (alpha) contaminations. In this last respect, several measures are under study that would reduce this type of background to negligible levels for this type of device: pairing detectors with their passivated ends face-to-face (the only surfaces sensitive to alphas in these devices), and (separately) possibly detecting Particle Induced X-ray Emission (PIXE) from alphas entering one of them. The present limitation of this approach is the fact that only one detector of this type exists. While its manufacture (CANBERRA) was uneventful, detector makers estimate a minimum of six devices needed before the reproducibility of its characteristics, speed and cost of production, largest crystal mass feasible, and generation of waste can be assessed. A request for funding towards this end has been made to NSF/DOE within the recent DUSEL call for proposals.

Table 3.3: Implementation-specific radioactive background suppression schemes. The * indicates that exquisite time resolution makes 1-D PSA in the modified electrode design much more powerful than for a standard p-type detector.

Implementation	**Suppression capabilities**				
	Detector-Detector (granularity)	1-D PSA (∼radial)	Segmentation	2-D PSA	3-D PSA
P-type	✓	✓			
Modest Segmentation	✓	✓	✓	✓	
High Segmentation	✓	✓	✓	✓	✓
Modified Electrode	✓	✓*			

3.6.2 Metric to Compare Selected Detector Configurations

We have adopted as metric the half-live sensitivity for the $0\nu\beta\beta$ decay in ^{76}Ge as a function of time. This metric allows us to compare the four above defined detector configurations quantitatively in terms of physics performance such as sensitivity, background rejection, signal acceptance, cost and schedule. In this way we can incorporate the different fabrication, characterization, and deployment schedules, the background associated with common and implementation-specific materials and the background suppression for each configuration and therefore the sensitivity as well as the cost as a function of time. This metric allows us to quantitatively compare the sensitivity during the construction as well as operation phase. We can define uncertainties for each parameter which translates into a range of sensitivities which can be expected for a given time. In addition, it allows us to identify potentially critical parameters and risks to performance, cost, and schedule which need to be addressed before construction begins. It therefore provides the necessary guidance for potentially remaining R&D efforts. We need to point out here that this metric is not taking into account information which would provide systematic characterization, e.g. of the signal if measured or unforeseen background. A more quantitative systematic analysis is more complex and will be performed in the near future.

Following the established baseline geometry for Majorana, we have employed the MaGe Monte-Carlo simulation package to determine the background within the detectors. Each component of the Majorana assembly, ranging from the shielding to the detector itself, is associated with a total activity deduced from a given specific activity and mass. We have developed mass models for all experiment specific components. MaGe provides background levels and spectra observed in the Ge detectors. It also provides energy-, background-, and implementation-specific suppression factors. These include the so-called granularity using detector multiplicities and "radial" PSA which is employed for all configurations, segment multiplicities for segmented detectors, and three-dimensional PSA for higher segmented detectors which allow transient signal analysis (2D-PSA) or even full track reconstruction (3D-PSA). Table 3.3 shows the implementation-specific background suppression schemes. All configurations provide detector-to-detector as well as one-dimensional pulse-shape analysis (1-D PSA) suppression capabilities. The modest segmentation provides additional granularity due to segmentation and potentially complementary pulse-shape analysis of the segment signals (2D-PSA). Finally, highly segmented detectors in combination with pulse-shape analysis provide three-dimensional position granularity (3D-PSA) within one detector.

To determine the sensitivity for each configuration in terms of the achievable half-life we have identified all potential issues which can impact performance, cost, and schedule. We have generated a list of common and implementation-specific issues for all phases of the Majorana experiment ranging from the R&D phase to the operations phase. We have evaluated detector fabrication options, costs, and schedules with relevant detector manufacturers and we have defined acceptance, characterization, and deployment tasks and schedules as input for the evaluation metric. We have incorporated all important components to determine radioactive backgrounds and the impact on measured backgrounds through Monte-Carlo simulations as discussed elsewhere. Achieved and published specific backgrounds as well as backgrounds which we believe can be achieved were used. Background suppression by distinguishing single-site from multiple site interactions was calculated by Monte-Carlo simulations as well. Except for the modified electrode configuration, the minimum distance to enable the separation of two interactions was assumed to be 4 mm with a minimum of 50 keV for either interaction. This minimum separation criteria was applied for the radial separation for all configuration and in all three dimensions for the high segmentation implementation. The pulse-shape analysis based separation is in addition to the detector-to-detector and the segment-segment granularity and suppression with energy thresholds of 5 keV for each channel. Due to the expected increased pulse-shape sensitivity of the modified electrode approach, we use here 2 mm as minimum distance along the electrical field lines to distinguish two interactions, again with a minimum of 50 keV for either interaction. A more detailed discussion can be found in the report "Evaluation of Detector Configuration and Segmentation Schemes for the Majorana Experiment", which is currently being finalized.

Figure 3.13 shows the estimated sensitivity for the evaluated detector configurations as a function of time. For each design, a single module of 60 kg is assumed. For comparison purposes, in this figure, all four configurations have identical production and delivery times. Because the four configurations have similar backgrounds, the four sensitivity curves have similar magnitudes, and the differences mainly result from the different detection efficiencies for $0\nu\beta\beta$ decay.

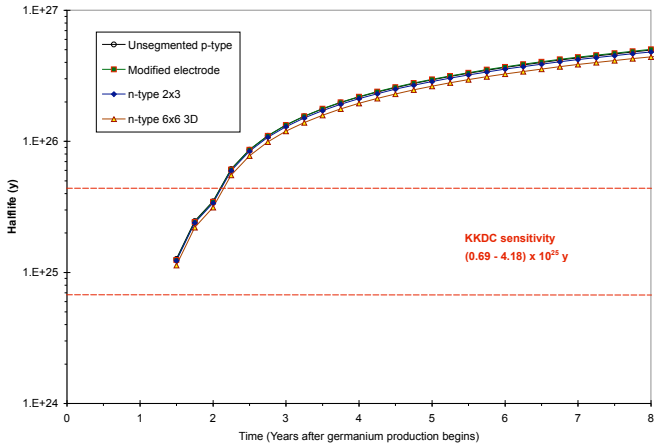

Figure 3.13: Sensitivity in terms of half-life as a function of time for a range of evaluated detector configurations. All four configurations are assumed to have identical production and delivery times.

Figure 3.14 again shows the estimated sensitivity for the evaluated detector configurations as a function of time for one 60 kg module. In this figure, in contrast to Figure 3.13, we have attempted to include an estimate of detector delivery dates. The start time reflects the date of our assumed first delivery of an enriched ^{76}Ge crystal which is ready for detector fabrication.

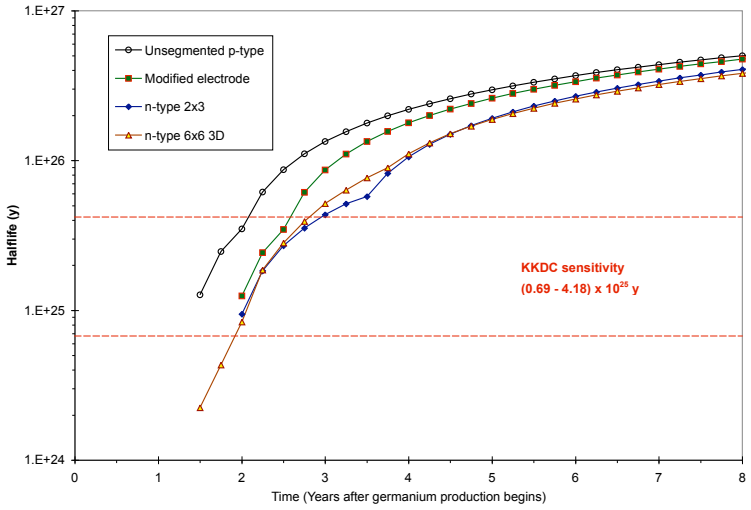

Figure 3.14: Sensitivity in terms of half-life as a function of time for a range of evaluated detector configurations. An estimate of detector delivery dates has been made for each configuration.

Except for the highly-segmented implementation, all configurations are deployed in two steps, first with about 20 kg and the second step with the remaining 40 kg. The highly segmented approach follows a more modular approach with six 9-detector and one 6-detector module deployments. P1 reflects the deployment of 1.1 kg detectors, p2 the deployment of twice as many 0.55 kg detectors. PME indicates the modified electrode approach with an optimistic start assuming they can be built at a rate as regular non-segmented p-type detectors and a delayed start following closer the fabrication and deployment schedule of the modest segmentation. N4 reflects a four-fold, n6 a six-fold segmentation of a n-type detector representing the modest segmentation approach. N36 finally represents the most complex, 36-fold segmented detector implementation. It can be seen that within two years after the first crystals are produced, the currently best limit can be achieved in any implementation. It is interesting to note that the fast deployment and the low background of p-type detectors provide in principal the highest sensitivity. In contrast, the slower deployment in addition to the increased background due to additional parts results in the highly segmented as the approach with the smallest sensitivity. The additional suppression capabilities are not able to compensate for the slower deployment and additional background. However, taking the uncertainties for each implementation into account, the ultimately achievable sensitivities are very similar.

In addition to the metric expressed in terms of the sensitivity a very important aspect, particularly with regard to the scalability of the proposed module Majorana approach, is the deduced background rate in the 4 keV wide region of interest around 2039 keV. Figure 3.15 shows the back-

ground rate and its composition for the range of evaluated detector configurations.

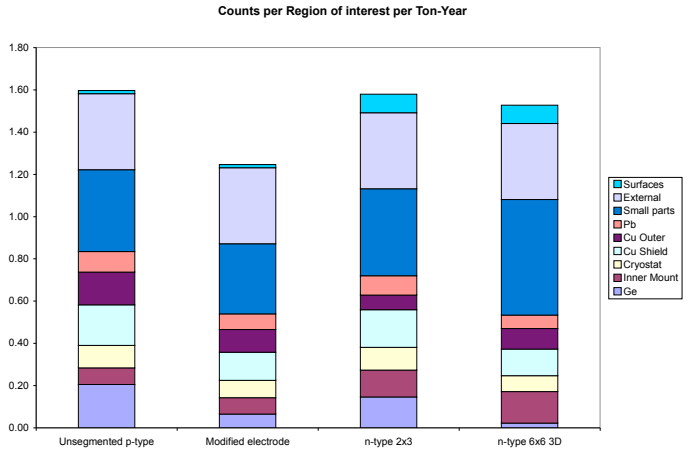

Figure 3.15: Background rates expressed in events/year/ton in the region of interest of 4 keV around 2039 keV for ^{76}Ge.

It can be seen that with small non-segmented p-type detectors the goal of 1 event per ton-year in the region of interest can be achieved. However, all implementations will be close to this goal if the assumed background levels can be achieved.

3.6.3 Systematic Considerations

So far, we have focused on the achievable sensitivity as a function of time in terms of mass, backgrounds, and background suppression. We have included specific backgrounds of individual components to the best of our current knowledge. The overall instrument model contains all components and the mass model reflects the currently best estimate to build and actually operate such a system. However, we have not included systematic aspects which allow us to strengthen and provide more support for the signal in case we observe the $0\nu\beta\beta$ signal. As seen by the disagreement on the results by Klapdor-Kleingrothaus we need to be able to provide more degrees of freedoms and systematic analysis tools to convince the scientific community of the signal than was done previously. Analyses, such as considering individual crystals, segments, or even three-dimensional locations in the detector can provide the necessary consistency checks to prove the existence of the signal. We have to be careful to weigh the systematic analysis and number of data cuts with the amount of available data, e.g. with the statistical significance of these cuts. The goal will be not only to provide consistency checks of the $0\nu\beta\beta$ signal but also other signals such as the much stronger $2\nu\beta\beta$ decay. A quantitative understanding of the $2\nu\beta\beta$ decay process, e.g. the spectrum and intensity provides an important basis to validate the response of the instrument.

A potentially more important and critical factor for the performance of the Majorana experiment is unforeseen and unpredictable backgrounds. While the Majorana experiment strives at minimizing backgrounds from all components and to enable a quantitative understanding of the predicted backgrounds, not all potential background sources can be controlled as previous low-background and

underground experiments have demonstrated. The ability to deal with these backgrounds is a very important criteria in selecting a specific detector configuration as well. These backgrounds need to be identified and the impact minimized or mitigated.

The evaluation of systematic aspects is more difficult to handle and ultimately requires a full understanding of the instrument response.

3.6.4 Conclusions and Guidance for R&D Effort

Based on the quantitative evaluation of Ge detector configurations which are feasible for the proposed Majorana experiment, and considering our current state of knowledge, the 6-fold segmented n-type detector remains as our reference design. This implementation represents the best trade-off between proven and established technology (minimizing the associated technical risk) and performance (physics performance risk particularly with regard to systematic uncertainties).

The modified electrode promises very high sensitivity with a minimum number of components and readout channels. If this technology can be demonstrated to be produced and operated reliably and produced at a rate which is comparable to the conventional non-segmented p-type detector, this approach can be envisioned to be adopted as reference design. The highly segmented detector approach provides the most capabilities in addressing systematic uncertainties. However, it represents by far the most complex instrument. Although produced for nuclear physics experiments in large numbers now, the benefits of the 3D reconstruction remain to be fully explored and demonstrated for the Majorana experiment.

As one important result of this evaluation, we find that the background, particularly of the small parts close to the detectors, such as cables and electronics are critical to the overall achievable sensitivity for all implementations. As high priority we have therefore identified the determination and reduction of background levels in these components as well as schemes to ensure the low background levels. In terms of detector configuration and associated risks we find that the modified electrode needs to be studied in more detail and needs to be demonstrated. Further, the high segmentation option needs to evaluated more quantitatively to demonstrate the feasibility for Majorana in terms of fabrication, background suppression and systematic capabilities. While a 6x6 fold segmentation scheme was chosen for this evaluation, a reduced number of segments such as 6x3 or 3x6 segmentation schemes could provide similar capabilities. The option to leave components for the readout out if too much background from small parts is observed as suggested by previous reviews remains to be explored as well. While essential for the high segmentation option, an approach deploying smaller modules, could provide a faster and more reliable deployment for all configurations. It would reduce the interference with the already operational part of the experiment and would allow us to easier deploy different configurations to optimize the performance during the assembly and construction. At the same time it would enable the development and demonstration of technologies with improved capabilities that can be implemented and deployed at a later stage. For example, one could envision to first deploy non- or only modestly segmented detectors while at a later stage introduce modified electrode or finer segmented detectors.

3.7 Germanium Module Production

3.7.1 Overview of the 57-Crystal Module Design

Central to the concept of a scalable Majorana detector is the 60 kg module, consisting of 57 germanium detectors arrayed in a single conventional vacuum cryostat assembled entirely from ultra-low background materials. This is an extension of the cryostat design for the 7-detector close-packed array for the PNNL-USC double-beta decay collaboration [Bro84, Bro85a, Bro85b] and the MEGA cryostat deployed at WIPP by PNNL and LANL [Kaz04] which is capable of operating upto 16 detectors. The detector module provides cooling, vacuum insulation, an ultra-clean environment,

mechanical support, and management of the many cables and front end electronics chips. The modular approach is essential for a phased turn-on of the Majorana detector system, providing early engineering runs that can be used to get the DAQ system operational, do preliminary background studies and develop analysis tools for background rejection while the remaining detector mass is being assembled. The data from these engineering runs can also provide early physics results comparable in statistical precision to previous experiments.

Materials All items residing within the detector shield must be fabricated from ultra-low-background (ULB) materials and screened for radiopurity prior to use. The principle material will be electroformed copper produced underground to eliminate cosmogenic radioactivity. Details of the production process appear below in Section 3.7.3. PolyChloroTriFluoroEthylene (PCTFE) (Kel-F®) is the leading candidate for non-conductive structural elements, although other engineering plastics are under investigation. Silicon is also considered an alternative for the largest components if plastics cannot be found with sufficiently high radiopurity. Kapton®, Teflon®, Polyethylenenapthalate (PEN) and Polyethylene Terphtalate (PET) are the leading candidates for electrical circuit insulators, either for use in flex cables or circuit boards. A limited palette of other screened materials will be required, including FETs, feedback resistors, bias voltage blocking capacitors and electrical circuit interconnects.

Mechanical design The cryostat design needs to balance several factors. A large, close-packed array with the full detector mass in one cryostat would be optimal for identification of Compton scattered events and identification of coincident signals between crystals due to the minimal inactive mass within the array. In addition, the outer crystals of the array would provide considerable shielding for the inner crystals from radioactivity entering from the outside, either from the shield or the cryostat vessel. Finally, this arrangement would minimize the radiative thermal load on the cryogenic cooling system.

On the other hand there are several advantages to a modular design with multiple cryostats. Electronics considerations favor shorter cable runs, both from the detector to the FET and from the FET to the preamp. This is the limiting factor in the height of the cryostat shown below in Figure 3.16. Detector delivery is expected to occur over a prolonged period and it would not be sensible to have detectors for which large expenditures have been made sitting idle awaiting delivery of the remaining detectors. Therefore, the module design should allow for installation of smaller detector masses, while allowing for subsequent expansion to the full detector mass without undue risk to, or down time for, the operating detectors. There is the risk of contamination of the inside of the shield volume that must be considered as well when accessing an installed cryostat.

A balanced approach has been adopted which mounts 57 crystals in each cryostat. Technical details on the development of the concept for the 57-crystal module are outlined in Appendix H. The reference plan cryostat design is shown in Figure 3.16. The cryostat will be a cylindrical vessel roughly 40 cm diameter by 40 cm height with a thick cold plate at the top of the cryostat from which the 19 detector strings hang, enclosed by a thermal shroud mounted to the cold plate. The cryostat, cold plate and thermal shroud will be fabricated using ULB electroformed copper. The thickness of these components is under study. In principle this copper is the lowest radioactivity material we will have available and therefore a relatively thick cryostat wall can be used, eliminating any concern about collapse of the vacuum vessel (e.g. due to shock waves in the facility from blasting in the mine). In addition, these components provide shielding between the front end electronics and the germanium detectors, also favoring thicker material. A combination of thermal, mechanical and background analyses will be used to determine the preferred thickness of these components, the upper limit being set by considerations of the copper plating process (time and material quality).

The detector strings, shown in Figure 3.17, consist of a thick copper "lid", three low mass copper support tubes and three low mass PCTFE detector support trays. Cables will run vertically from the detector contacts to the string lid, where the central contact will be capacitively coupled to a

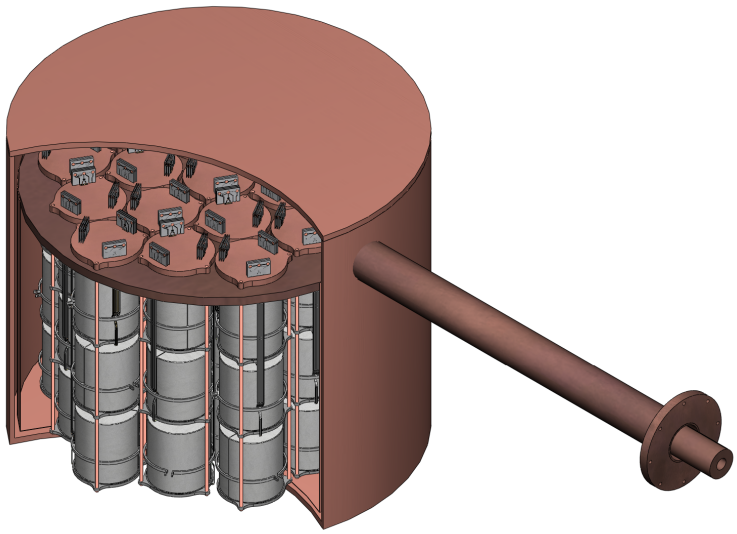

Figure 3.16: A Majorana detector module with a close-packed array of 19 detector strings, each with three detectors. The strings are supported from a copper cold plate cooled by a long cold finger extending through the lead detector shield. A thermal shroud mounted to the cold plate creates an ∼85 K enclosure surrounding the crystals providing shielding from the warm vacuum vessel walls. The predominant construction material is ultra-pure electroformed copper.

low-background front end electronics chips mounted above the string lid. The front-end leads and the outer contacts will then be routed out of the detector along the cold finger. The string lid provides some shielding between the front end electronics and the detectors, allowing the FETs to be located near the germanium to maximize available bandwidth. The detector string is simply lowered through a hole in the cryostat cold plate until the string lid seats on the cold plate.

With the exception of the lid and electronics mounted to it, the string components reside between the crystals within the array. Hence their mass should be minimized, not only to reduce local sources of background, but also to reduce absorption of γ-rays by non-active material within the detector array. The support tubes are 6 mm diameter with 0.2 mm wall thickness produced from electroformed copper. The detector support trays will be fabricated from virgin PCTFE, with their layout designed to minimize their mass while providing the required detector mechanical support and center contact connection. If PCTFE does not have the required radiopurity, silicon can be used for the detector trays. PCTFE hoops will be used to provide contact pressure for the external crystal contacts. Alternative materials (including ETFE, polyimide, UHMW-PE and Celazole-PBI) are being studied to evaluate radiopurity as well as cryogenic mechanical performance and vacuum properties.

Thermal design The guiding principle in the module design is to use radiation as the thermal path to cool the detectors, rather than conduction or convection. This implies that the detectors are fully enclosed in a low temperature surface within a vacuum insulation space, with minimal heat load introduced by stray conductance or self-heating. The crystals themselves have very little ($\ll$1 mW/crystal) self-heating since any appreciable leakage current renders them inoperable electronically. Both the supports and the cables will be thermally shorted to the cold plate at the top of the detector string and hence will not provide any thermal load on the crystals. Thus the crystals

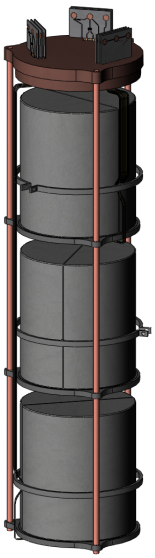

Figure 3.17: A conceptual design of the three crystal detector string. The three detectors sit on support trays coupled to three thin support tubes which in turn are supported from a copper lid. Plastic flex cables bring the signals from the crystals up through the lid to the front end electronics boards mounted above the lid.

should be in thermal equilibrium with the thermal shroud and cold plate that surround them. In addition, the LN_2, which acts as a thermal sink, is located outside the lead and copper detector shielding, with a ULB copper cold finger providing the thermal path from the detector array to the LN_2. This principle for thermal management is based on industry practice and has been successfully demonstrated on large customize electroformed copper cryostats with the MEGA experiment at WIPP.

The radiative heat load from the warm vacuum cryostat surface (area of 0.75 m^2, T=300 K, emissivity of <0.03) to the thermal shroud and cold plate is <10 W. The crystal operating temperature should be below 90 K, hence the thermal resistance between the thermal shroud and the LN_2 must be below 1 K/W. Contact resistance at the joints is a significant issue in this regime; therefore the conductivity of the cold finger itself should be as large as possible to reduce its contribution. At this temperature copper has a conductivity of about 530 W m^{-1} K^{-1}. As an example, a cold finger with an outer diameter of 8 cm, an inner diameter of 3 cm, and a length of 70 cm has a thermal resistance of 0.3 K/W. The MEGA cryostat, which has a similar geometry, was able to reach a cold plate temperature below 90 K in under 24 hours.

The front end electronics, specifically the FET, are the other major source of heat in the system. Typical FET operation for HPGe detectors generates about 40 mW per channel. With one FET in the cryostat per detector, the total load is ∼2 W. The FETs should not be operated at temperatures below ∼120 K. This is easily achieved by thermally isolating the front end boards from the cold plate and cold detector string lids. The cables from the front end boards to the vacuum feed-throughs outside the detector shield will be coupled to a secondary cold finger to remove the bulk of the FET power through a cooling path independent from the detector cooling.

Impact of segmentation on module design The specific choice of a segmentation scheme (i.e. number of segments per crystal) impacts a few aspects of the mechanical and thermal design

of the Majorana modules. In general, higher segmentation requires more electrical read-out cable. Other components held constant, increasing cable mass will change the mechanical design needed to support the increasing mass. It may be optimal to adjust the mechanical design to accommodate the increased mass, a hypothetical example being a secondary cross arm. In a similar way, increased cable penetrating into the cryostat may increase the thermal load on the module cooling. This must be accounted for in the final design. The time required to assemble a module will also likely increase as segmentation increases (see below). Finally as the cable mass increases, it becomes increasingly important to monitor and control the radio-purity of the cables. These are the primary design issues that change as a function of segmentation scheme choice.

Signal amplification and shaping electronics The signal handling strategy is to place the minimum electronics within the cryostat to avoid potential sources of background, while meeting the performance specifications with regard to noise and bandwidth. In addition, the electronics within the cryostat will be shielded from the detectors by the cold plate and detector string lids. Similarly, the cryostat walls shield detectors in adjacent cryostats from these electronics. Low mass cables screened to have low levels of naturally occuring radioactivity will be employ in the inner shield readout circuit. Our baseline assumes charge-sensitive preamps with resistive feedback.

The general goals for the electronics are:

- Constructed from radiopure materials
- Resolution of $\sim$1 keV at 60 keV (reflecting electronics noise)
- Bandwidth $\gtrsim$ 20 MHz
- Threshold $\lesssim$ 5 keV (requires controlled microphonics)
- Dynamic range $>$ 10 MeV
- Gain matched to digitizer dynamic range
- Output impedance matched to digitizer requirements
- Capable of driving signals 10 m to digitizers
- Minimize additional capacitance in readout

The implementation of these requirements is to locate only the front end FET, feedback resistor and HV coupling capacitor for the central contact within the cryostat, with the preamplifier, shaper and analog signal driver located outside the shield. The front-ends for the outer contacts will be located entirely outside of the shield. Experience from other segmented HPGe arrays such as GRETINA indicate that if pulses from the central contact are captured with high enough bandwidth, low-bandwith information from the outer contacts is already sufficient for 3D charge deposition reconstruction. Signals within the cryostat will be carried on Kapton® or other plastic based flex circuits, while the signals between the preamps and digitizers will be run on coaxial cables. Filter capacitors will be engineered into the front end board circuit so that no additional discrete components are required for this purpose. A prototype circuit board is shown in Figure 3.18. This circuit is fabricated on a commercial copper-clad Teflon® material, but may be incorporated into the end of the flex circuits to reduce materials and electrical interconnects.

Kapton®, PEN, or PET flex technology may offer the best possibility for ULB cables for use within the cryostat, in large part due to the control one has over the parent materials used to produce these cables. In addition the electrical properties of these cables can be tailored to meet the requirements of each circuit, and pads for mounting of FETs, resistors and other components can be engineered into the cable itself. Miniature coax cable with Teflon® insulation is an alternative

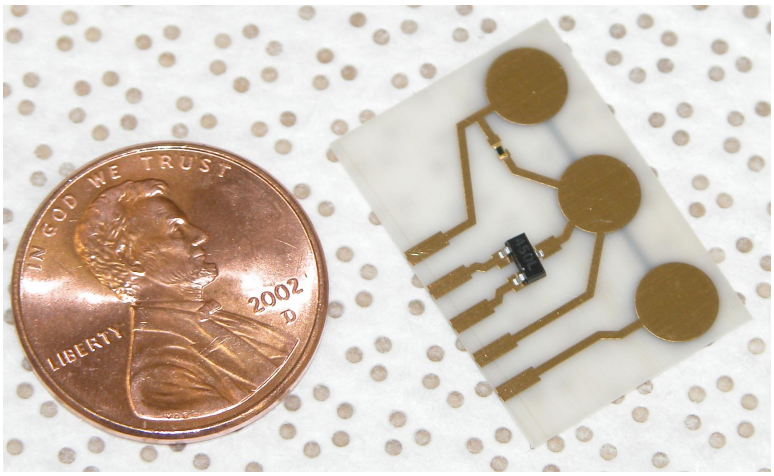

Figure 3.18: The latest prototype front end electronics board. The board is fabricated on CuFlon, a Teflon® circuit board material 15 mils thick. The circular metal pads are filter capacitors built into the board layout. The board holds the FET and feedback resistor, both bare die on silicon substrates with wirebond connections to the circuit board.

solution that is well understood electrically, and screening of commercially available products is ongoing. Radio-purity is likely to drive the decision between flex cables and miniature coax cables. It is worth noting, there are three rather different cables involved in the detector assembly. The first cable must make contact directly to the crystals and carries the low level analog signals <30 cm to the front end board at the top of the detector string. The second cable type is a variant on this, but for the HV contact. In principle this can be the same type of cable with a discrete blocking capacitor located on the front end board. However, this capacitor must by produced from ULB materials and it may be preferable to create a cable which also acts as this capacitance, i.e. a wide strip line with HV on one side of the plastic and the signal trace going to the FET on the other side. The third cable type carries the signals from the front end boards out through the cross-arm to the vacuum feed-throughs. This cable is about 1 m in length, may incorporate the front end circuitry (FET and resistor mounting pads, filter capacitance) and may carry signals from multiple crystals.

The vacuum feed-throughs need to pass on the order of 10^3 signals per cryostat without significant cross-talk or pickup. These will connect the signals from the flex cables inside the cryostat to the preamp circuits mounted just outside the vacuum space, adjacent to the dewar. The preamp circuits will be fully enclosed in a Faraday shield with the signals exiting the shield enclosure on coaxial cable. The main filtering capacitance for the HV lines will also be located in this enclosure.

3.7.2 Achieving, Maintaining, and Monitoring Cleanliness

The Majorana project depends critically on achieving and maintaining a very high level of cleanliness to avoid radioactive contamination of parts during handling. The entire laboratory facility, particularly the facilities and equipment for handling the cryostat components and germanium detectors, will be designed to eliminate as much as possible any direct exposure of these components to human contact to minimize the risk of surface contamination.

After final surface preparation each component will be placed in storage, either in sealed radon-proof (Tedlar®) bags, in a glove box flushed with radon reduced cover gas, or in a sealed container under vacuum. For assembly into modules, components will be introduced into glove boxes with radon free cover gas. Wherever possible, special handling fixtures fabricated from ultra-clean mate-

rials will be used to contact the parts.

We anticipate monitoring surface contamination using witness plates which will travel with the parts throughout the assembly process and/or located in each of the assembly stations. These witness plates would be assayed regularly to monitor the cleanliness of the assembly area and to ensure that contamination has not crept in to the processing.

3.7.3 Cu Electroforming Plan and Cryostat Construction

In this section we address only the production aspects of the copper electroplating process and cryostat assembly. Details of the electroforming process and copper purity are covered in Section 4.1.1.

The purity and quality of the plating bath will be continuously monitored in several ways. Bath chemistry, bath temperature, and plating voltage will be measured directly. Samples from the plating baths will be sent for assay periodically, along with coupons from the electroformed copper for each production sample. Presently, ICPMS offers the greatest sensitivity for these assays.

The cryostat and internal component electroforming will require seven different plating baths to handle the different part sizes and shapes while matching the production rates of the various components to the required schedule. In order to avoid schedule conflicts with production of copper for the inner shield, an independent set of baths will be used for that copper. The estimated production time for all parts for a cryostat, including joining parts with electro-deposition, is $\sim$20 weeks, including significant time contingency to reproduce any parts of insufficient quality: there is a built-in expectation that at least one part from each cryostat will be inadequate on the first attempt and will require replacement. The production schedule for the string components for 19 strings (enough parts for a full cryostat) is nearly identical.

The electroformed parts will require finish machining, followed by cleaning, chemical etch to remove surface contaminants (e.g. Rn), passivation, and drying. These processes will provide a finish which is also adequate even where low emissivity ($\epsilon < 0.03$) surfaces are required. At this point the parts will be sealed in evacuated Tedlar® bags or installed in vacuum storage cans to avoid contamination until it is time to assemble them. The entire assembly process, storage, and final loading of detector strings must take place in an environment free of Rn and other potential sources of surface contamination.

Each cryostat will be assembled, evacuated, baked and leak checked to verify that it is ready for use. An ultimate pressure below 10^{-6} torr is expected after bake-out. The cryostat will then be coupled to the dewar assembly, and the cold finger and cold plate will be installed. The cables which run along the cold finger from the vacuum feed-throughs to the string lids will be installed and a final leak check will be performed. Our current plan is to mate the cryostat and dewar assembly to the sliding monolith during this assembly step. At this point the cryogenic system can be filled. Due to the large cryopumping speed of the system we anticipate pressures below 10^{-8} torr, although 10^{-6} torr is satisfactory for detector operation. This is the final preparation prior to loading detector strings into the cryostats.

3.7.4 String Assembly and Testing

The detector string design is shown in Figure 3.17 above. The assembly of the string is done from the bottom up. The three support tubes and bottom crystal tray are preassembled. Next, the bottom crystal is set in place on its support tray and the cables are fixed to the detector contacts. The middle detector support tray is slid down the support tubes and locked in place. Then the middle detector is set in place on the tray, followed by installation of the cables to this detector's contacts. The third support tray, detector and cabling follow in a similar manner. The string lid is then installed and fixed to the copper support tubes. During installation the cables from the crystals must be fed through the slots in the string lid. At this point the front end electronics can be installed above the string lid. The expectation is that each string will take about one week to assemble.

After assembly, a quick continuity check can be made at room temperature to make sure all of the crystal contacts are connected to the cables. The string will subsequently be loaded into a test cryostat for electrical evaluation and final detector characterization with sources. It is anticipated that the full electrical testing and characterization will take two weeks to perform and that we will have some problematic strings which require further testing, evaluation and rework. In order to maintain a throughput of one string per week we plan to have two characterization stations and a third test cryostat dedicated to the reworked parts.

3.7.5 String Loading and Final Tests

Our current plan calls for integration of the cryostat and dewar into the sliding monolith when these components are first mated to each other. This allows the cryostat assembly to be supported in its final configuration prior to loading it with the germanium detector mass. The cables which run along the cold finger will also be installed prior to string loading.

The detector strings are loaded from the top of the cryostat vessel. A set of tooling will be developed which will allow us to lift the string from the test cryostat (or vacuum storage can), move it above the detector cryostat and lower it through an opening in the cold plate until the string lid seats on the cold plate. Several options are available for fixing the locations of the strings to the cold plate. Once in place, the final cable connections can be made and a room temperature electrical test can be done to verify that all cable connections are intact. In principle this entire process could be done in an environment isolated from the operator, with the possible exception of making the cable connections.

The detector array will need to be cooled for final detector operational tests. There is a trade-off to be made between the number of thermal cycles experienced by the detectors, the amount of handling done between cold tests and the amount of time during which significant detector mass is sitting idle awaiting the remaining mass required to complete a cryostat and bring it into operation. It is likely that the first cryostat will have a cold test performed after the first several strings are installed. This partially populated cryostat may even be installed to gain the earliest possible operational experience. Once we are satisfied that the procedures are adequate it may not be necessary to do any intermediate cold tests during installation of the strings in the cryostats. Ideally the fully populated cryostat will see no thermal cycles, i.e. it will remain cold from the initial electrical testing through the lifetime of the experiment.

The fully populated cryostat assembly will be an integral part of a sliding monolith, described in more detail in Section 3.8. This monolith will allow for smooth transportation from the assembly area into the detector hall and finally into the shield itself. It is imperative that no contamination is carried into the inner shield enclosure during this operation (see Section 3.13 for more discussion on commissioning procedures).

3.8 The Shield and Veto

The various backgrounds that shielding will reduce are summarized in Table 3.4. Shielding reduces signals from γ-rays originating in the experiment hall (from rock, construction materials, and possibly from shielding materials themselves), cosmic-ray μ's penetrating the shielding, and cosmic-ray μ-induced neutrons. The strategy is to provide extremely low-activity material for the *inner shield*. Surrounding this will be an *outer shield* of bulk γ-ray shielding material with lower radiopurity. This high-Z shielding enclosure will be contained inside a gas-tight Rn exclusion box made of stainless-steel sheet. Outside this bulk high-Z shielding will be a layer of hydrogenous material, some of which will be doped with a neutron absorber such as boron, intended to reduce the neutron flux. Together the outer shield and hydrogenous material form a Z-graded shield. Finally, active cosmic-ray anti-coincidence detectors will enclose the entire shield. The cross-sectional view of the Majorana apparatus depicted in Figure 3.1 shows the arrangement of the various shielding layers.

Table 3.4: A summary of the potential backgrounds that shielding will reduce.

Background Process	Shielding for Mitigation
Experimental hall environmental neutrons	Hydrogenous layer
Experimental hall environmental γ-rays	Outer shield
Radon	Gas containment volume
Radioactive contaminations in shielding material	Selection of inner shield materials
Cosmic rays: prompt and direct signal from μ's	Active anti-coincidence detector
Cosmic rays: prompt μ-induced secondary particles (e.g. spallation neutrons)	Active anti-coincidence detector, Z-graded outer shield, depth of laboratory
Cosmic rays: delayed μ-induced secondary particles (e.g. ^{68}Ge, ^{60}Co)	Depth of laboratory

3.8.1 The Passive Shield

In this subsection, we describe the passive shielding surrounding the detector modules. The design criteria are motivated in Section 4.1 and only the physical description of the shield is given here.

Inner shield Because of the sensitivity of germanium detectors to γ-rays, and the high efficiency of the Majorana apparatus, γ-rays from the inner region of the shielding are very dangerous. Therefore, materials with extremely low specific activity of radioactive isotopes must be used in this region. As described in Section 3.7.3, Cu can be purchased very pure and made ultra pure via electroforming and therefore meet the specifications required by the background model. The innermost layer of the shield will be 5 cm thick and built of electroformed Cu sheet. Electroforming the necessary amount of Cu for this layer is estimated to require 5 independent baths running for 195 working days. The next layer will also be 5 cm thick and will be composed of either electroformed sheet or stock commercial Cu if a sufficiently clean supply can be identified.

Outer shield Primordial radioactivities in the walls and construction materials of the experimental area constitute the largest source of background radiation, but the easiest source to mitigate. A sufficiently massive bulk shield, composed of radiologically clean material, surrounding the detector systems will effectively eliminate this source of external γ-ray background. The outer shield protects the detectors from gross environmental γ-rays from the rock, the construction materials, and other shielding materials. Typical rock at an underground location (e.g. SNOLAB) contains a few ppm U and Th. Calculations show that a lead shield $\sim$55 cm thick is sufficient to reduce the natural γ-ray radiation from the environment to a negligible level. That is, the count rate in the region of interest due to γ-rays from the rock walls will be well below that due to γ-rays from the electroformed copper. With the 10 cm of Cu forming the inner shield, this outer shield will be composed of 45 cm of lead providing a total 55 cm of high-Z shielding.

Rn exclusion box The high-Z inner and outer shields will be contained inside a metal box that will be gas tight. This box will permit the controlled purging of the gas within the inner cavity that contains the detector modules. This system will control Rn to the required level. The design of the shield and the Rn exclusion box will include entry ports for cables, cryogenic connections, and calibration source pathways.

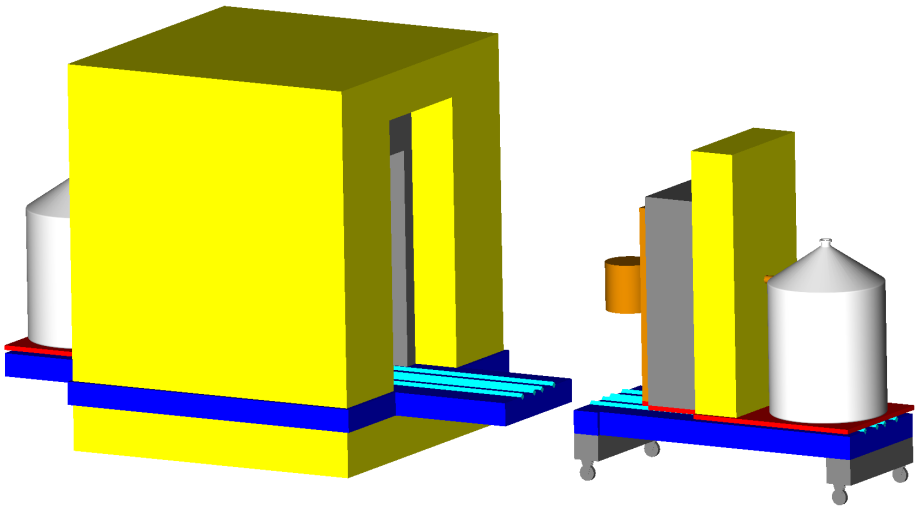

Figure 3.19: A schematic of a monolith on a truck ready for insertion into the shield structure.

Hydrogenous layer The flux of neutrons from spontaneous fission or (α,n) reactions in the rock confines of the underground laboratory can be reduced significantly by a thick plastic layer. For example, the simulations described in Section 4.3.1 indicate that 30 cm of polyethylene can sufficiently reduce these neutrons. The inner-most 5 cm of this 30 cm layer will contain polyethylene loaded with 30% boron for added neutron capture efficiency.

The monolith A monolith consists of a module of Ge detectors, the thicknesses and materials of the inner and outer shields, a panel of the Rn exclusion box, a cold finger that passes through these shielding layers, and the dewar, which provides the LN_2 cooling of the cold finger. All of these will ride upon a transport truck. The shape of the truck's incorporated shield will match a corresponding gap in the shield itself. The monolith will be positioned within this gap as the truck is driven along a track mounted upon a shield table that supports the high-Z shield above the plastics of the hydrogenous layer and the veto. The truck will be moved by either a motor driven axle or air bearings.

During assembly of the monolith, it resides on tracks upon an assembly table. When completed, the truck is transfered to a cart to transport the monolith to the shield table track. Figure 3.19 shows a schematic of a monolith on the transportation cart ready for insertion into the shield structure. Because the assembly table, transport cart, and shield table have a common height, there is no need for elevator hardware. The shield table will be of steel or Al construction and must be able to support the $\sim$60 t weight of the shield. Each monolith will weigh 5-10 t and therefore the assembly and transfer cart will also require stout construction. Once the monolith is inserted into the high-Z shield, the Rn box is sealed with a gasket and the hydrogenous layer and veto are put in place.

A given monolith may be at the assembly table for repair in addition to the initial assembly. Therefore, we will build two blank monoliths to fill the shield gaps during these periods. The gap in the shield and the shape of the monoliths will be "keyed" in order to ensure that any cracks through the shield require γ-rays take a circuitous path to enter the inner volume. Furthermore, the cold fingers may require a shadow shield to eliminate cracks that may arise due to their vacuum jacketing.

3.8.2 Veto System

Cosmic rays, of consequence at any reasonable depth, are composed almost exclusively of muons. These μ's produce ionization as they pass through materials, and therefore will produce primary pulses in any Ge detector they traverse. Furthermore, these μ's are capable of undergoing interactions with nuclei, resulting in spallation and fragmentation products, including numerous hadrons. While secondary protons are no more debilitating than the primary μ itself, secondary neutrons can be very high-energy and can travel through significant quantities of material before being thermalized and absorbed. These secondary neutrons undergo further nuclear interactions, resulting in additional new isotope production, some of which will have half-lives and decay energies sufficient to generate background events when these interactions take place in proximity to the detectors. An electronic anti-cosmic ray shield can be very effective in tagging those μ's, which pass through it and thus eliminate the primary energy deposition events in the Ge detectors and much of the secondary γ-ray and bremsstrahlung radiation generated in the vicinity of the detectors via interactions in the lead or other materials. Our proposal is to include an anti-cosmic ray shield constructed of active plastic scintillator and comprising one of the outermost layers of a graded bulk shield. As with the description of the passive shield above, the motivation for the design criteria of the cosmic-ray anti-coincidence system is described in Section 4.1. Here, we simply describe the concept design.

A 10 cm thick 4π plastic scintillator will suffice as a μ veto shield. Plastic sheets will cover all six sides of the shield with a minimum of gaps. Wavelength shifting fiber will span the plastic at regular intervals across its surface. These fibers will then connect to phototubes. This design will have a uniform response and high efficiency for observing the μ's and therefore, the μ rates expected in any of the available underground labs can be effectively cancelled. This active shield response can be recorded as an independent signal, permitting studies of backgrounds and system performance both in coincidence and anti-coincidence with the Ge detector system.

3.9 Data Acquisition

3.9.1 Digitization Electronics

Analog signals from the detectors are fed out through ports in the shield and sent along coaxial cables to an adjacent counting room for subsequent digitization and processing. Digital spectroscopy hardware platforms have become commercially available for this task and the data acquisition systems for the Majorana prototype module will use this commercial technology. For the full experiment, however, we may opt to build custom electronics in-house that are designed and optimized specifically to fit the needs of Majorana.

Both commercial and in-house electronics would essentially entail a series of ADCs read out by an on-board FPGA. Such a system has been custom-designed to readout the GRETINA detectors. A block diagram of the GRETINA digital signal processing (DSP) board is given in Figure 3.20 [Zim03]. This board provides 8-channel 12-bit digitization at 100 MHz with variable gain control. A Xylinx XC2V3000-5 Field-Programmable Gate Array (FPGA) performs digital leading edge and/or constant fraction discrimination and trapezoidal shaping on-the-fly. All processing parameters are programmable. The board also provides raw data sample storage of charge collection and various complex triggering capabilities (internal, external, veto functions, etc.). It has on-board FIFO memory and uses VME for readout.

The GRETINA DSP board is overkill for the Majorana experiment. In particular, Majorana does not need to perform advanced signal processing online in the FPGA. By selecting an FPGA and other components more appropriate to Majorana's needs, significant reduction in complexity and cost can be achieved. Other modifications could be implemented for Majorana, for example optimizing the number of channels per board with respect to the segmentation scheme, and using PCI rather than VME for the readout. The sampling window should be user-definable between $\sim$1 μs to several ms.

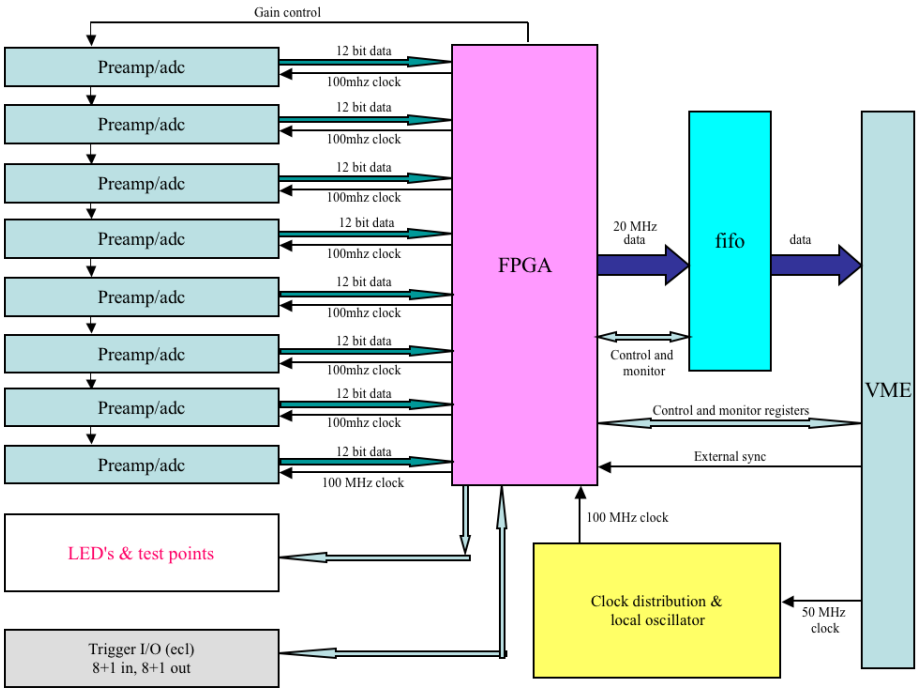

Figure 3.20: Block diagram of the GRETINA digital signal processing board [Zim03]. Electronics of similar design are proposed for use in Majorana.

Whenever a particular segment is hit, it is necessary to read out all segments on the same crystal. Signals from cross talk or bleed-over in neighboring segments may be too small to trigger their own readout, but contain information which can improve event reconstruction and identification. Full crystal readout is easy to program into the FPGA on the digitization board if all segments from a crystal are connected to the same board. However, depending on the form factor of the board and spare channel requirements it may be more optimal to trigger the readout with an external FPGA-based custom trigger board. Such a trigger board would incorporate veto signals and would provide additional flexibility for complex triggering schemes to perform calibrations and diagnostics. Triggering information will be readout using the same bus system as the electronics (VME or PCI).

To ensure accurate time-stamping of the signals, the trigger board would distribute its clock to the digitization boards. A common sync input for all modules allows a system synchronization pulse to simultaneously reset counters on all digitization boards. For absolute timing, the clock increments an additional counter in a Global Positioning System (GPS) module which the system synchronization pulse also resets. The GPS module will then provide an output indicating the absolute time corresponding to a system timer reset and hence an absolute time reference for each event.

In addition to digitization and triggering, the electronics hardware will also include a pulse distribution system to monitor gain stability, and a computer-controlled high voltage (HV) bias supply system for both the HPGe detector array and the phototubes of the anticoincidence shield. Each crystal and phototube will be powered on independent HV channels, allowing for optimization of the HV setting for each instrument, and enabling any channel to be taken offline without affecting the rest of the array. Separate, conventional instrumentation will derive veto signals from the anticoincidence shield.

3.9.2 DAQ Software

The DAQ software system will be constructed using the Object-oriented Real-time Control and Acquisition (ORCA) [How04] application to achieve the goal of providing a general purpose, highly modular, object-oriented, acquisition and control system that is easy to develop, use, and maintain. The object-oriented nature of ORCA enables a user to configure it at run-time to represent different hardware configurations and data read-out schemes by dragging items from a catalog of objects into a configuration window. Each object in the configuration is comprised of its own fully encapsulated data structures as well as support and diagnostic code. ORCA provides an application framework in which these software models can be connected together to represent systems of hardware, and can hence be thought of as being parts of an Object-oriented Software Bus, analogous to a standard hardware bus. This analogy is particularly useful when one of the objects represents a PCI crate, for example, into which one can plug PCI card objects. Other objects represent read-out tasks, control modules, or data analysis modules. Once placed in the configuration window, the object icons are connected to define the flow of data and commands. All connections and system configurations are done at run-time so that no recompilation of ORCA is needed to reconfigure the application for a different experimental setup. Thus ORCA will be used for the development test stands as well as the production system. ORCA is already highly developed, and is currently in use as the central DAQ software in the SNO NCD system and in the KATRIN experiment.

The ORCA run control subsystem allows for runs of unlimited length, as well as runs of a predetermined time length, which may be repeating. Of course, any run can be stopped or restarted manually at any time with the push of a button. Run numbers are automatically assigned for each run and there is a set of run identification bits that can be set to uniquely label special run-time conditions that need to be known during analysis. All system activities are logged and can be viewed in a status window.

A key feature of ORCA is the design of its data stream and how this stream is acquired for permanent storage. Each hardware object is responsible for reading out both its hardware and

writing its parameter settings into the header of the final data file. A supervisory list processor controls which hardware objects are used in the experiment and the order and hierarchy of the read-out scheme. In this fashion a user can completely reconfigure the data read-out without rewriting any code or re-compiling the application. Since all parameter settings are in the data file headers, ORCA can restore parameter settings to previous run conditions.

ORCA packages data from each hardware component into data records that can be handled generally by higher-level processors. The format of the data storage within the record is documented for each hardware object so that offline analysis applications can decode the data stream. Data files, status logs, and configuration files are accumulated locally and at the end of a run the files can be optionally sent to a remote file server. ORCA also has a built-in dispatcher object that can be used to stream the data to another machine for remote real-time building of the events and/or for remote monitoring of the data quality. The data path is visualized in Figure 3.21.

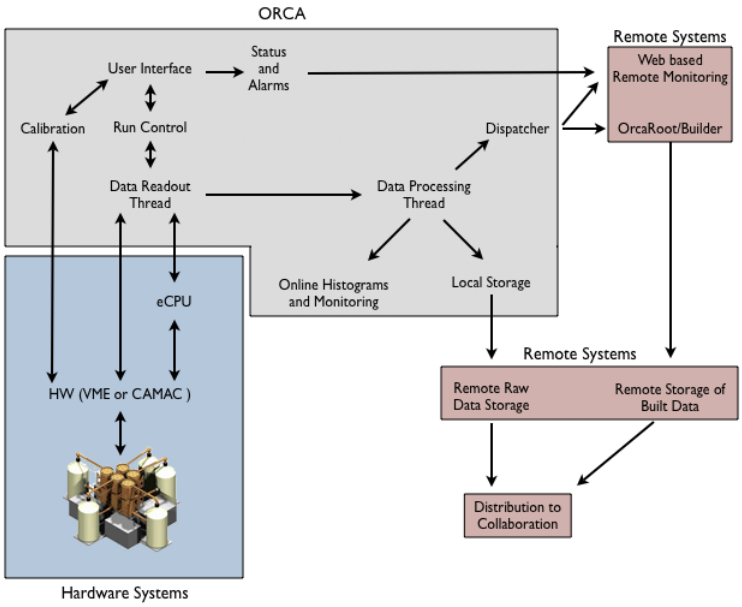

Figure 3.21: Block diagram of the data flow.

During a run, a general data collection and viewer object can be used to monitor the quality of the data. The data monitor uses information automatically written to the data stream header to feed the data into decoder objects, which enter the data into a data catalog from which histograms or waveforms can be selected and viewed. All objects that follow a designated protocol participate automatically in the use of this data catalog and viewer.

Automated calibration tasks can be incorporated into ORCA with a minimum of work. While they do require the creation of custom code, there are easy-to-follow examples to use as templates. Tasks can be started and stopped manually or can be run automatically on a schedule.

ORCA has a built in capability to receive commands from remote applications via a socket channel. Normally this facility is used to remotely start and stop runs, but it can also be used to send information to other applications. This communication channel will be used to integrate ORCA with the State of Health (SOH) system, described in Section 3.10. SOH alarms and messages

can be broadcast to ORCA for display and/or inclusion into the data file header or into the data stream. Likewise, ORCA can send information and commands to the SOH. Access to the ORCA socket channel can be restricted to a list of 'safe' machines.

3.10 State of Health and Slow Controls

In addition to the dedicated systems for the detector data acquisition and control of the electroforming processes, there will be a State of Health (SOH) and Slow Controls system to monitor environmental and process parameters associated with the Majorana operations and to allow remote operation of some of the Majorana infrastructure systems. The SOH system unencumbers the DAQ and process control systems by monitoring parameters that are not critically coupled to data taking or electroforming operations. The SOH system is responsible for:

- Personnel safety.
- Stewardship of high value components used in the project.
- Optimal operation of the experiment and ancillary processes.

It will consist of a suite of hardware and software tools to monitor and alarm on environmental parameters. Hardware and software interlocks will be used for "fail safe" shutdown of critical systems. The SOH system will be able to exchange data with the DAQ and electroforming process control systems. It will run autonomously in the event of communications failure with surface. It will archive data. While the emphasis of the SOH system will on monitoring, there will also be some "slow controls" incorporated into the system. The system will provide remote operation of the Majorana infrastructure to permit an orderly shutdown or start up if there are no personnel underground.

The hardware and software to implement the Majorana SOH system has not been selected yet. If it meets Majorana's needs, it may be advantageous to use the same SOH and slow controls system as the Host Facility (and thus take advantage of in house expertise at the site). However, while it is necessary for the Majorana and Facility SOH systems to be able to exchange data, the Majorana SOH will be configured to operate autonomously from the Facility slow controls. The SOH system will be accessible for monitoring and control at multiple locations in the Majorana experimental areas underground and from the Majorana surface control room. Off site and web based monitoring will also be possible. There will be audible alarms, email alerts and automatic paging for critical system monitoring.

3.10.1 Detector SOH

Some aspects of the health of the operational detector and the crystals that are being tested and characterized prior to assembly into operational modules will be monitored directly by the Majorana DAQ system (e.g. leakage current, crystal HV, data rate). Other parameters necessary for stewardship of the crystals and optimal operation of the experiment will be monitored by the SOH system. Detector related SOH functions will include:

- Monitoring of cryostat vacuum, detector temperature, LN_2 levels in cryostat dewars, quality of cover gas.
- Hardware fail safe for conditions that compromise the integrity of detectors. (e.g. vacuum quality, cryostat temperature)
- Monitoring of air temperature, pressure, humidity in detector and electronics areas.
- Vibration and seismic monitoring.

- DAQ electronics temperature monitoring.
- Smoke detectorion and fire extinguishers for electronics and high voltage racks.
- Detector power quality and UPS status monitoring.
- Exchange of data with the Majorana DAQ system. Some data collected from the SOH system will be incorporated into the Majorana data structure for physics analysis.

3.10.2 Electroforming SOH

The copper electroforming process will be designed for both autonomous operation and for remote control of critical aspects of the operation (turning on power supplies, adjusting electroforming parameters, etc). The SOH system will monitor ancillary information necessary to ensure the quality of the electroforming process and parameters that are safety related. The SOH system will include:

- Data exchange with the electroforming process control systems.
- Hardwired interlocks to electroforming systems power supplies and to the facility life safety systems for:
  - Fire (smoke and heat) detection.
  - Explosive gas detection.
- Spill detection from chemical baths (possibly hardware interlocked to bath electrolyte pumps).
- Air temperature, pressure, and humidity monitoring.
- Monitoring of bath cover gas quality (differential pressure relative to room, Rn or O_2 content).
- Air particulate counting.

3.10.3 Infrastructure SOH and Slow Controls

In addition to state of health monitoring specific to the detector operations and electroforming processes, there will be systems providing common services throughout the Majorana facilities. The infrastructure SOH and slow controls will include:

- Monitoring of LN_2 storage and distribution systems (liquid levels, status of liquid transfer).
- Monitoring of cover gas system (differential pressure relative to lab, flow rates, Rn and/or O_2 content).
- Remote operation of cover gas system.
- Wellness of all clean room modules (differential pressure between zones; HEPA filter dP; air particulate count; O_2, CO, NO levels; temperature, absolute pressure, humidity)
- Remote operation of clean room air handler systems
- Remote operation and monitoring of Radon Reduced Air (RRA) systems.

3.11 Simulations and Analysis Framework

3.11.1 MaGe

Monte Carlo (MC) radiation transport simulation models have been developed for Majorana using MaGe, an object-oriented MC simulation package based on the Geant4 [Ago03, All06] toolkit and optimized for simulations of low-background germanium detector arrays. MaGe is being jointly developed by the Majorana and GERDA [Abt04] collaborations, using professional programming techniques in consultation with collaborators from the National Energy Research Scientific Computing Center (NERSC) at LBNL. MaGe defines a set of physics processes, materials, constants, event generators, etc. that are common to these experiments, and provides a unified framework for geometrical definitions, database access, user interfaces, and simulation output schemes in an effort to reduce repetition of labor and increase code scrutiny.

The primary goals and requirements of the MaGe framework are:

- To use modern simulation tools to produce an easily adaptable and flexible platform with appropriate verification and anticipated longevity.
- To provide the collaboration with a physics simulation package to aid in the optimal design, operation and analysis of data from the Majorana experiment. The physics generators will concentrate on radioactive decays of background sources.
- The package must be well maintained, documented, and robust.
- It must accurately model detector response and resolution.
- The numerous physics processes (radioactive decay, signal generation, energy deposit, pulse formation and electronic response), normally modeled by separate software packages, shall be integrated into a single framework.
- Simulations of existing detectors must be performed and documented to verify the performance of the simulation software.

Concurrent Versions System (CVS) is used to coordinate simultaneous remote development of the code. The Doxygen package [Dox06] generates reference documentation, and Docbooks [Doc06] parses Standard Generalized Markup Language source text into the User's Guide. A modified Taligent [Tal06] naming convention has been adopted to maintain a consistent naming scheme for variables and classes. ROOT [Bru97] is used for output and analysis, although other formats (such as AIDA [AID06]) are also implemented. An interface to a PostgreSQL [Pos06] database has been implemented. The database is used to store calibration constant, materials definitions, geometry information, etc.

Numerous simulation projects are currently being pursued within the MaGe framework and many of their results have been used in other parts of this proposal. These projects include:

- A detailed study of background contamination in a realistic, fifty-seven 1-kg crystal detector array that has been used in the background budget.
- A detailed simulation of a Canberra Clover detector at Los Alamos to provide simulation data to compare to a known and understood Ge detector.
- A simulation of a Clover Detector at the TUNL freeelectron laser source to study the efficiency of generating a sample of pure single site events for segmentation and pulse-shape analysis studies.
- A simulation of a highly segmented Ge detector for pulse-shape and segmentation studies.

- Simulations of the SLAC 30 GeV e^- beam dump experiment [Tan03] and of general muon-nuclear interactions in rock and scintillator to verify spallation neutron generation and isotope production by cosmic rays.

All of the simulated GERDA geometries and tools are also part of this package.

3.11.2 Analysis Toolkit

A well designed, developed, and documented analysis software framework is conducive to successful and efficient collaborative analysis of experimental data. In particular, large collaborations, if left to their own devices, tend to develop multiple, disjointed analyses which must later be compared and combined. In order to minimize duplicated efforts and errors introduced in the translation between different frameworks, we propose to make an early effort to develop a unified analysis framework for Majorana

Many Majorana collaborators have experience developing and performing analyses in other large collaborations, such as SNO and KamLAND. These two experiments in particular use C++/ROOT-based analysis toolkits, QSNO [QSN06] and AKAT [AKA06], respectively, which we deem effective enough to serve as a template for a Majorana Analysis Toolkit (MAT). Like QSNO and AKAT, we propose to build MAT as a collection of C++ class libraries which use the ROOT classes as a backbone, and a data file format centered around the ROOT TTree and TFile objects. Users will use the MAT classes to create their own applications tailored to their particular analysis needs.

Goals and specifications The goals and specifications of the Majorana analysis framework include:

- The toolkit should be available from a central location/repository with easy access for collaborators only.
- Versions should be tagged and tracked using software such as CVS.
- Dependencies on external packages should be minimized.
- Efforts should be made to make the toolkit cross-platform compatible; in particular it should compile with minimal trouble under Linux, Mac OS X, and possibly also the Cygwin environment.
- The code should be well documented.
- External libraries written in different programming languages (e.g. FORTRAN-based waveform analysis routines) should be wrapped by C++ classes for integration with the toolkit.
- All classes should be organized into packages (e.g. Utilities, I/O, Pulse Shape Analysis, etc.) with, preferably, tree-like dependencies on other packages.
- Storage format of data into ROOT TTrees should be kept as simple as possible in order to maintain the ability to perform simple draw commands for fast analysis of the data, preferably without the need to pre-load MAT libraries into ROOT.
- Conversion of raw data into ROOT files should be invertible, so that the raw data can be recovered in its original format for debugging.
- The initial emphasis for the toolkit should be the development of high-level code (e.g. filters) for use with Monte Carlo data.

Modular processing We envision for the Majorana Analysis Toolkit a "modular processing design" which standardizes computations performed at the event-loop level. In this framework, the analysis is divided among several modules, each of which performs specific tasks at three different stages of data processing: at the beginning and end of the full analysis, at the beginning and end of each run processed, and at the event-by-event level. Such a framework can be implemented by creating a C++ base class with the following public functions defined:

```
StartAnalysis();
StartRun();
ProcessEvent(Event* event);
EndRun();
EndAnalysis();
```

Here, "Event" is a C++ class that encapsulates event-level data. With processing broken down in this way, it is easy to build applications consisting of both stand-alone modules working independently from each other as well as chains of modules working sequentially to perform complex tasks.

The modular processing design is a highly effective means of organizing an analysis, especially from the standpoint of coding, data processing, and algorithm optimization. As a coding architecture, modular processing provides many benefits, particularly in a collaborative environment. Here are a few:

- The concept of a module cleanly divides analysis tasks into distinct steps occurring at the various processing levels, improving code clarity. Clean, simple code is easy to debug and verify.
- Standard routines can be provided to manage the modular data processing, so that users never have to worry about how to open/close files, perform the event loop, etc., thereby simplifying the coding burden on the end user.
- Base-modules for performing low-level tasks, such as extracting a waveform from an event and sending it to another routine to be processed, can be constructed in order to further ease the coding burden on an end user.
- Multiple modules performing a similar task (e.g. pulse-shape analysis) using slightly different methods may be run side-by-side or swapped in and out of an analysis for fast and unambiguous comparison of results.
- For large data sets, the ability to perform multiple, independent analyses simultaneously by having users submit their modules to an official data production routine can reduce I/O resource usage significantly.

Higher level analysis Beyond event-level processing, there are a number of analysis tasks that can be implemented in MAT to further ease the coding burden on the user. For example, one can implement code inheriting ROOT's native MINUIT [Jam75] based unbinned fitting procedure for statistical event discrimination and spectral analysis. Other high-level tools could include visualization software (such as a waveform browser or a 3-D hit-map), classes to standardize analysis cuts, code implementing single-site time correlation searches, etc.

3.11.3 Database

The need to store and access various detector parameters and slow controls information naturally calls for a Majorana database. Such a database would be an SQL-based system that would support

local and remote creation, modification, and retrieval of relation data. The database would be mirrored on several hosts for safety and connectivity robustness. The database will interface with Majorana subsystems in the following ways:

- Slow controls data will be recorded to the database by the SOH system.
- Data taking parameter settings will be downloaded from the database, and read-out run conditions and data-taking diagnostics will be archived in the database via the DAQ system.
- Calibration parameters will be loaded to the database via the DAQ system and calibration analysis code. These parameters will made available for MC and analysis via software interfaces.
- Materials definitions, geometry information, and other physical constants relevant for MC and analysis will be accessible from the database via software interfaces.

3.11.4 Online Analysis and Detector Testing Software

The analysis team will prepare online analysis and detector testing software to assist in Majorana detector R&D, and the commissioning of detector subsystems. Software developed for the R&D phase will focus on analysis of MC output and detector design optimization studies. The online software will use the same analysis framework as the offline analysis code and will be integrated into the DAQ software. Onsite, the software will support analysis of detector tests in the assembly area, as well as full detector commissioning data. The same software will be used to monitor data taking during detector operations. The output of the online analysis will be arranged into easy-to-manipulate displays, using HTML interfaces where possible to enable remote detector monitoring.

3.11.5 Data Production and Distribution

Majorana will archive data onsite to buffer against communications failures between the site and Majorana institutions (similarly the data will be buffered underground in the event of communications failure between underground and surface). Majorana will also likely maintain a sufficient computing ability at the site for fast analysis during calibration data taking. Depending on data rates and disk resource availability, it may be possible to store all data onsite locally. We are also considering backing up data to tapes, which would be archived either on-site or at a remote tape library.

The remote data farms will be accessible by all collaborators. Depending on available resources and connectivity needs, it may be possible to locate several data farms in different geographical locations. Distribution of data to these sites may be achievable via the internet if data rates are low enough. Another option is to distribute data tapes via mail.

Access to the data files may be coordinated via the database. It may be desirable to restrict collaborator access for some subset of the data, for example if a blindness scheme is implemented in the data analysis.

3.12 Calibration

If the ^{76}Ge $0\nu\beta\beta$ half-life lies just below current limits or is consistent with the claim by [Kla04], after 5 years of run time the Majorana experiment will be able to measure the half-life with about $\sim$10% statistical uncertainty (see Section 4.6). This sets the scale for the size of acceptable systematic uncertainties and therefore how well the detector needs to be characterized through calibration. The experimentally determined half-life depends on the live time, amount of source, the efficiency of the detector. In this section we consider how each of these factors contribute to the overall uncertainty

Table 3.5: Depth dependence of the dead time due to the anti-coincidence system, assuming a veto time of 1 s.

depth	F	R=FA	f
2000 mwe	$10^5/\mathrm{m}^2$ y	0.013 Hz	1%
4000 mwe	3 x $10^3/\mathrm{m}^2$ y	4 x 10^{-4} Hz	4 x 10^{-4}
6000 mwe	2 x $10^2/\mathrm{m}^2$ y	2 x 10^{-5} Hz	2 x 10^{-5}

in the half-life determination. Furthermore, we describe how the calibration of the detector will address these uncertainties.

The primary characteristics of the detector array, and hence each individual detector, that we will want to calibrate are:

- The energy scale and its linearity
- The energy resolution and peak shape
- The time dependence of energy scale and resolution
- The absolute efficiency for double-beta decay
- Each analysis cutś efficacy (for signal and backgrounds)
- The efficiency of the active shield

3.12.1 Live Time

The veto dead time can be estimated as: $f = Rw = FAw$, where f is the fraction of time dead, R is the μ rate through the detector, w is the veto time window, F is the μ flux and A is the average cross-sectional area of the veto. Taking A as a 2 m square (i.e. 4 m^2) and w as 1 s, one can create a depth-dependent f. The result is shown in Table 3.5. The appropriate veto time for Majorana will be determined through analysis and set in software. Even with a 1% dead time, the uncertainty associated with veto dead time should be negligible, since the veto time is set in units of the accurate DAQ system clock.

Similarly, the dead time due to the segmentation anti-coincidence requirement will be small. A $0\nu\beta\beta$ decay will be rejected if it is preceded or succeeded by a background event within some coincidence time. The fast response of Ge detectors allows one to choose coincidence times on the order of a μs or less. IGEX demonstrated a background rate of $\sim 3 \times 10^{-4}$ Hz/kg for energies over 200 keV [Avi91]. Even conservatively assuming a factor of 10 to 100 increase for a threshold of $\sim$3 keV, this would correspond to an event rate on the order of 1 Hz for 120 kg of Ge. Considering that Majorana will be considerably cleaner than IGEX, the probability of a random coincidence between a $0\nu\beta\beta$ decay and a background event, and hence the dead time due to the segmentation cut, will be exceedingly small, and will have negligible uncertainty.

A deadtime correction will also need to be made for the single-site time correlation (SSTC) cut. This correction will depend not only on the cut duration, but also on the detector rates at different energies. However, we expect the impact of the SSTC cut on live time will be less than that of the veto time cut, and that it's uncertainty will be negligible.

3.12.2 Number of ^{76}Ge Atoms

The mass of the Ge can be determined to better than 1% by simply weighing the crystals. The enrichment will be known to better than 1-2% via ICPMS or mass spectrometry (see Section 3.4.7).

The fiducial volume, however, must be measured by determining the thickness of the dead layer with a source. This can be done for the outer contact during detector characterization before deploying the crystal by measuring the relative attenuation of several low-energy γ-ray lines from the same source. The location and intensity of the source are inconsequential, and as a result, the apparent fiducial volume of the crystal can be determined with a negligible uncertainty. Determining the thickness of the inner contact is more problematic, since to insert a source inside the coaxial hole is probably impossible. However, the approximate size of the dead layer is known and a conservative choice for its size can be used to deduce an upper limit on this uncertainty. For an uncertainty of 100 microns for the inner dead layer of an n-type detector that is 62 mm in diameter and has a core radius of $\sim$0.4 mm, the fiducial volume uncertainty is $\sim$0.1%.

During data analysis,it is possible that fiducial-volume cuts may be applied to the events. For example, the radial location of the event may be determined by pulse-shape analysis, and a radial cut used to discriminate against α particles detected at the outer surface. The corresponding effect on the fiducial volume can again be determined using low-energy γ-ray sources. However, the precision of the pulse-shape analysis will be energy dependent, so the relative uncertainty in this case is larger, probably of the order of 1%.

3.12.3 Efficiency

If the gain is imprecisely known, then the peak location is actually at a different position than assumed by the analysis. If the number of counts in the peak is too small for the location to be determined by a fit to the peak, then an error in efficiency will result. The IGEX and Heidelberg-Moscow obtained typical detector resolutions of $\sim$4 keV ($1\sigma \approx 1.5$ keV). For a region-of-interest of similar width, one would expect a selection efficiency of 83.8%. If the gain uncertainty is 0.2 keV (as previously achieved in IGEX) at 2039 keV, one would misestimate the efficiency by 0.5%, a small quantity. Note that the energy of the $0\nu\beta\beta$ transition is well known (2039.006 ± 0.050 keV [Dou01]) and introduces a negligible uncertainty in the efficiency.

If the resolution is uncertain, one makes a similar type of error, although it is two-sided. If the resolution is 4.0 ± 0.1 keV for example, one would have an acceptance uncertainty of about 1%. However, we expect to be able to determine the energy resolution to a higher accuracy than this from the periodic calibrations.

The pulse-shape analysis acceptance is also a contributor, and will need to be determined using single-site events from calibration sources. Hence, this uncertainty will be determined by source strength and calibration duration. For example, a 1% uncertainty could be obtained using a 3 Hz counting rate over about an hour, assuming that the PSA cut is similar for all segments. If 10000 counts are needed for each segment, longer calibrations will be required.

Efficiencies for accepting both signal and background events must also be be understood for the granularity cut, segmentation cut, SSTC cut, etc. We will be able to measure the cut effectiveness and therefore uncertainty in the contributing rate for some backgrounds (for example, external ^{208}Tl), but others (e.g. muon generated neutrons) will need to be estimated using simulations.

3.12.4 Calibration Specifications

Each monolith will have a low-background source pathway (possibly electroformed Cu tubing) with a plastic liner. This liner will be removable if inadvertent contamination occurs. The source will be parked in an external garage that will be valved off from the pathway. The pathway will be purged following each calibration to remove any Rn emanated from the source. The source itself will be encased (perhaps by electroforming Cu around it) in order to prevent leaving residue radioactivity within the pathway. A schematic of the calibration system is given in Figure 3.22.

In order to determine absolute efficiencies, we plan to deploy sources with modest to long half-lives, reproducible source locations, and good statistics. Our goal is to only have to calibrate about once every week for about an hour.

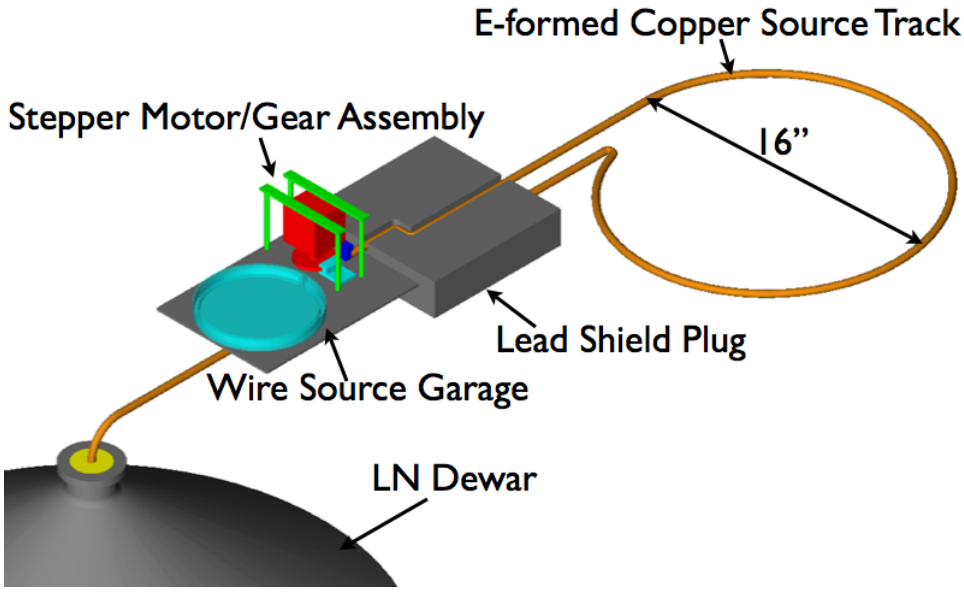

Figure 3.22: A schematic indicating the conceptual design of the calibration system. A motor drives sources through a low-background source pathway that passes through the shielding layers and encircles a 57-crystal module.

The gain for each detector channel needs to be determined precisely enough such that the summed resolution is not degraded significantly beyond the ∼4 keV intrinsic resolution of the individual detectors. Unusual peak shapes and poor resolution in individual detectors may widen our summed resolution; these issues will need to be addressed and controlled. The required dynamic range of the energy measurements could be fully calibrated with a Pb x-ray source plus an external Th source. There are a number of physical processes that need to be calibrated including double escape peak (DEP) events. An external Th source can provide the DEP signal, although a hot ^{56}Co source has γ-ray energies that provide a series of double and single escape peaks which span energies below and above the ROI. The source activities are only constrained by data acquisition bottlenecks.

Using a GPS clock and the planned electronics, we ought to be able to get relative timing between signals to 25 ns and absolute timing to ∼100 μs or less. This will be much better than required for any coincidence studies.

All anticipated systematic uncertainties are at the few percent level or lower. These errors are summarized in Table 3.6. The combined systematic error lies below the expected ∼10% statistical error for a KKDC-like signal rate. It is readily seen that sufficient calibration is not overly challenging.

3.12.5 The Detector Characterization System

Before each string of three detectors is added to its assigned module, it is important that each detector be thoroughly characterized, so that full use may be made of the powerful event reconstruction capabilities provided by pulse-shape analysis from multiple segments. The detectors will be scanned by well-collimated (linear or planar) γ-ray sources, using an automated motion control system to locate the source at precise required locations. The characterization will include surface scans with low-energy γ rays, together with longer Compton-scattering runs using higher-energy sources, to measure detailed signal waveforms from specific known locations within the crystal. The resulting

Table 3.6: A summary of the systematic errors in the Majorana experiment.

Effect	Uncertainty
Statistics ($T_{1/2} \sim 10^{25}$-10^{26} y)	∼10%
Live Time	
Veto anti-coincidence	<1%
Segment anti-coincidence	<1%
Number ^{76}Ge atoms	
Ge Mass	<1%
Enrichment	1%
Fiducial Volume	
Dead Layer Thickness Uncertainty	1%
Acceptance	
Gain	<1%
Resolution	3%
PSA	Few %
Segmentation Cut	Few %

measured waveforms can be used to test the calculated signals that form the "basis vectors" or signal libraries, for the pulse-shape analysis algorithm (see the relevant discussion in Sections 4.1.6 and 4.1.7.) It will also provide the data required to correct the the calculated signals for preamplifier bandwidth and cross talk. An automated computer-controlled source placement and data acquisition system with dedicated digital electronics will facilitate the collection of data at the required large number of source positions.

If the calculated signals are not sufficiently accurate for the PSA, then the basis may need to be made up of the measured waveforms instead of the calculated ones. Unfortunately, characterization techniques developed for GRETINA and AGATA use time-consuming coincidence scans, where γ rays are scattered by 90° from the collimated beam, through a second (planar) collimator perpendicular to the beam, into another detector. Requiring that the two detected energies match the Compton formula, and sum to the original γ-ray energy, ensures that the scattering location corresponds to the intersection of the beam with the plane of the second collimator. About a day of data collection is required at each position to obtain sufficient coincidence events. By using a number of collimators and coincidence detectors, waveforms from several locations can be collected simultaneously; nevertheless, a full characterization scan on a fine grid requires many months. Since the anticipated detector delivery schedule will limit the time available for each detector characterization to several weeks, coincidence scans of Majorana detectors can be used only to spot-check a limited number of selected positions. As discussed in the *Majorana Project R&D Plan*, we plan to investigate possible alternative methods that may require only singles data collection. This should reduce the time required for a full scan by roughly a factor of fifty.

There are several special requirements that the detector characterization system will need to satisfy. Firstly, the characterization will be performed underground in order to prevent cosmogenic backgrounds and maintain the radiopurity of the detectors. Since the crystals will be mounted in test cryostats for the scanning procedure, they will need to be handled with extreme care and under strict clean-room conditions. Secondly, the Majorana construction schedule and rate of crystal delivery will require several characterization setups running in parallel. Finally, the initial characterization must be accurate, reliable, and reproducible, so that crystals do not have to be removed from the Majorana array because they were insufficiently characterized.

A concept of the characterization scanning system is shown in Figure 3.23 [Bos06]. We will draw

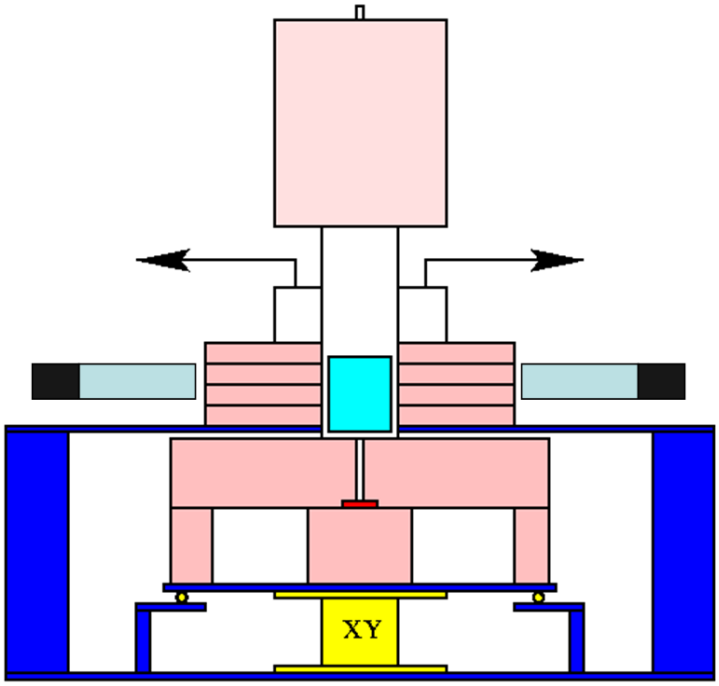

Figure 3.23: A schematic indicating the conceptual design of the detector characterization system, courtesy [Bos06]. A strong, tightly colimated source (shown in red) is mounted on a computer-controlled x-y translation platform. Gamma rays from the resulting vertical pencil beam can scatter inside the Ge crystal, through horizontal planar colimators, into coincident scintillator detectors. This "coincidence scanning" can therefore determine the waveform resulting from events at specific 3D coordinates in the Ge detector. The coincidence requirement, however, results in a very low event rate, so we plan to develop techniques for characterizing the detector without requiring the coincidence; see the text for details.

upon the GRETINA experience designing, building, and operating such systems.

In addition to the detector signal response, the detector characterization procedure will determine the following information for each crystal:

- Total and photopeak efficiencies as a function of γ-ray energy
- Leakage current and other electrical properties as a function of crystal temperature
- Energy calibration and resolution over a wide energy range (10 keV to $\sim$ 5 MeV)
- Deadlayer characteristics, where possible.

3.13 Testing, Integration and Commissioning

The final phase of construction is the commissioning phase. Here each component described above will be integrated into the whole, thoroughly tested, calibrated and characterized before entering the operations phase.

To facilitate this process, those involved in commissioning - along with the lab scientist and engineers who designed each element - will develop a Commissioning Plan that will enumerate all

procedures to be followed in this phase and the criteria each component and the integrated whole must attain before the pre-operations phase can be closed. In addition, the commissioning team is responsible for generating an Operational and Training Manual that will be used by subsequent detector operators and a site-specific experiment safety plan which details the procedures necessary to ensure operator and detector safety in its underground location. The commissioning team is also responsible for the development of Quality Assurance procedures and documentation that will track, confirm receipt, and enumerate a list of final-state tests that guarantee the functionality of all hardware components as they make their way to integration.

A significant part of the Commissioning Plan will describe the proper integration of each of the components into the whole. Essential to this is a functioning DAQ and SOH system for monitoring the component health and data quality as integration proceeds. For example, the modules must be shown to be properly functioning before installation into the cryostat. This assembly must pass all SOH criteria and have a functioning DAQ system before being integrated into the shield. In this way, each of the elements, and ultimately the whole experimental apparatus, will be shown to have met the criteria necessary to proceed into the operations phase of data-taking. Some of the expected tests on the individual elements follow.

Surrounding the entire experimental apparatus is an active veto shield designed to trigger on external particles that have the potential of creating false signals in the array. It will be necessary to determine that all sections of the shield are live and acting in proper coincidence not only with other elements of the shield but with the Ge modules contained within. This will be determined with timing and energy coincidence tests with neutron and high-energy β and γ sources, along with coincidence tests using through-going muons.

In addition to timing coincidence, there may be the possibility of some pulse-shape analysis of the events triggering the external veto system. The detected rates of these interactions will be compared with Monte Carlo expectations. These tests will be repeated before and after each of the individual Ge modules are inserted into the array. Also at this time, the cover gas system will be checked for adequate flow and quality.

Each of the Ge module arrays will be contained in and controlled through a separate cryostat system. During commissioning, the cryostat's baseline state of health will be monitored. This includes, among other things, temperature stability, system noise, high voltage stability and measurements of leakage currents.

Each Ge crystal in the module will be calibrated and characterized with a variety of sources, as described in Section 3.12. In addition, the background levels of each Ge crystal will be determined. Members of the collaboration have developed pulse-shape analysis techniques and single-site time coincidence tests that can be utilized to discern signal from background. All rates and detector resolutions will be cross-checked with Monte Carlo expectations and known $2\nu\beta\beta$ decay rates.

As individual modules are installed in the array, each of these tests will be repeated in a series of engineering runs that will also act as a shakedown of the DAQ and analysis tools. Ultimately, once each detector element has been characterized, including the crystals, veto system, and cryostats, Majorana will enter the operational phase.

3.14 Site Facilities

The site facilities for Majorana will provide a clean room environment located deep underground for the assembly and operation of the Majorana experiment. In addition to housing the detector, the underground site will provide assembly spaces for testing and characterization of the Ge crystals prior to assembly into detector modules. An important aspect of Majorana is the fabrication of key detector components from ultra pure copper electroformed in the underground laboratory to avoid cosmogenic activation. Data taking and detector testing will be overseen from an underground control room. Common services required by the Majorana operations (such as LN_2 and radon free cover gas) will be housed in a utility room and distributed to the detector and electroforming areas.

In addition to the underground facilities, Majorana will require space on surface to for monitoring the experiment and staging the installation of the experiment in the underground laboratory.

3.14.1 The Hosting Laboratory

In the design of the Site Facilities it is assumed that Majorana will be hosted at an operational laboratory complex. This complex will provide an underground environment that is a Class 10,000 or better clean room. It will have personnel facilities to make the facility habitable for 12 hour shifts underground and will have material handling facilities to transport equipment and material from the surface underground and clean them before being brought into the laboratory. Some storage space will be required in the Class 10,000 area of the hosting facility as well. Power, water, ventilation, communications, and mine safety infrastructure will be provided by the hosting laboratory. Emergency generator power will be provided by the hosting facility but not UPS. It is desirable for the site to provide Ultra Pure Water (UPW) for the electroforming facilities. Expertise for working at the underground site will be provided as well as personnel to assist Majorana activities (material handlers, cleaners, maintenance personnel). On surface the hosting laboratory will provide facilities for shipping and receiving off site and warehousing for storage of materials being shipped underground. There will be some laboratory space on surface to support the underground activities. There will be office space for the Majorana personnel stationed at site. It is assume that the host facility will normally support 24 hour, 7 days a week access. There will be a control room for monitoring the experiment when there are no personnel underground. There will be IT services and IT expertise to support the Majorana activities at site.

3.14.2 Underground Facilities

A conceptual design for the layout of the Majorana underground spaces is shown in Figure 3.24. The approximate areas of the spaces are tabulated in Table 3.7. While the amount of and functional association of the spaces required by Majorana are determined by the experiment, the exact layout will be constrained by the hosting laboratory. For instance it is not necessary for the electroforming facilities to be conjoined with the detector hall and assembly area. In total Majorana will require approximately 3,500 sq ft of space within the hosting facility's clean underground laboratory. Areas where the detector components may be exposed to air or where copper is electroformed or machined will be Class 100 clean rooms. The reference design presumes that these clean rooms will be prefabricated modules assembled underground. An alternate approach would be to fabricate the clean rooms using conventional construction techniques. The optimal methods for constructing the Majorana facilities will be determined in association with the hosting facility.

Detector area The modular design of the Majorana detector allows physics data taking with one or more modules in parallel with the characterization, assembly and testing of other modules. To facilitate these parallel activities there will be a Detector Hall housing the shielding blockhouse and veto system with an adjoining Detector Assembly Area in which the detector modules are assembled. Both Detector Hall and Assembly Area will be operated as Class 100 clean rooms. Part of the Detector Assembly Area will be used to characterize the Ge crystals prior to insertion into the detector cryostats. There will be several test cryostats and associated DAQ located in the Assembly Area. Entry to the Detector Hall will be through the Detector Assembly Room and entry to Detector Assembly will be through an air lock isolating the Class 100 spaces from the rest of the underground laboratory. The detector DAQ does not require extreme cleanliness and will be placed in a room adjoining the Detector Hall but maintained at the base site facility Class 10,000 rather than the Class 100 of the Detector Hall and Assembly room. Adjoining the Counting Room will be the underground control room where data taking will be controlled and monitoring of Majorana facilities will be done.

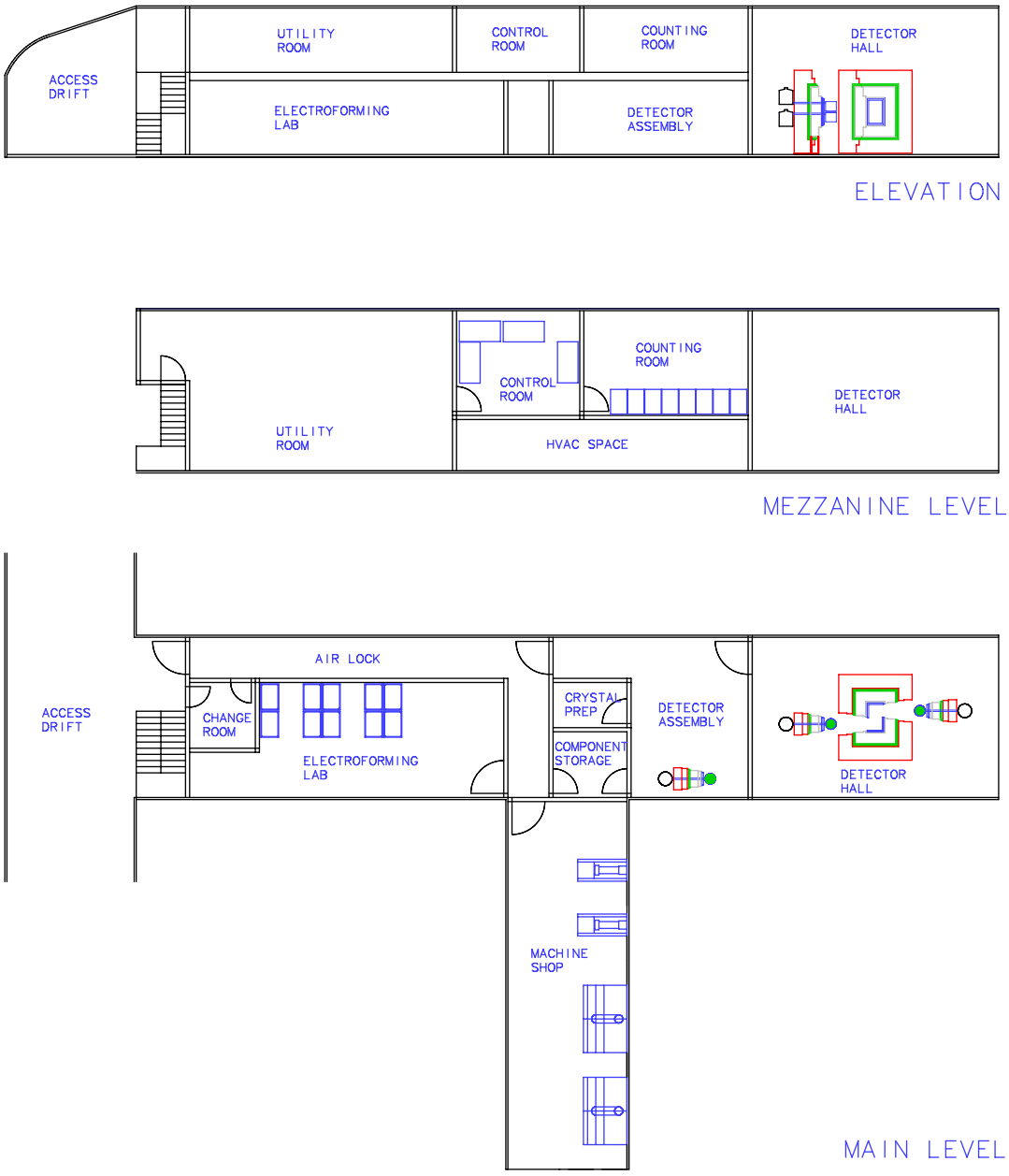

Figure 3.24: Conceptual View of the Majorana Underground Facility

Table 3.7: Underground Facility Spaces.

Space	Size (sq ft)	Class
Detector Hall	600	100
Detector Assembly	300	100
Crystal Prep	64	100
Air Lock	100	100
Change Room	64	10,000
Counting Room	260	10,000
Control Room	200	10,000
Utility Room	600	10,000
Electroforming Lab	400	100
Electroforming Machine Shop	650	100
Component Storage	72	100

Copper electroforming facilities The reference design for the Majorana detector and shielding block house requires the electroforming of approximately 2.5 tons of ultra pure copper in the underground facility. Majorana will construct an electroforming facility consisting of an Electroforming Lab, a Copper Machine Shop and a Component Storage Room to store the fabricated copper components prior to their being incorporated into the detector. These spaces will be Class 100. Services will include a radon free cover gas over the electroforming baths. The Majorana State Of Health and slow controls system described in Section 3.10 will allow remote monitoring of the electroforming when there are no personnel underground.

Utility room To support Detector and Electroforming areas, Majorana will require an utility space to house services specific for the experiment. The Utility Room will house liquid nitrogen systems, UPS and air handlers for the clean room modules. If the hosting laboratory does not provide ultra pure water, a water purification plant will be located in the Utility Room.

Underground services and consumables The basic services (power, cooling, air, water) will be provided by the host laboratory. Majorana will consume approximately 100 kW of electrical power which will then become heat which will have to be removed by the site cooling system. Some of the detector and electroforming systems will be maintained on UPS that Majorana will install. The detector systems are expected to consume approximately 500 L of liquid nitrogen per week for cooling the detector modules. A LN_2 storage tank will be situated in the Utility Room and a distribution system will allow the detector cryostats to be automatically filled. The reference design assumes that LN_2 will be transported from surface but the possibility of liquefying it underground is being considered. Boil off from the liquid nitrogen will be used to provide a cover gas to exclude radon gas from the copper electroforming baths and storage of the detector components after fabrication. Cover gas will also be used to exclude radon from the detector shielding blockhouse. A State Of Health and slow controls system will monitor the health of the underground facilities and to provide some control of the copper electroforming systems remotely from surface.

The possibility of working in a Radon Reduced Air (RRA) environment is being considered for the assembly and fabrication areas for the experiment. If it is decided that Radon Reduced Air is a viable option then a RRA plant will be installed in the Utility Room and provide RRA to the appropriate areas. Options for RRA under consideration are:

- Piped air from surface

- Carbon filtration
- Aged bottled air

The solution chosen will depend on the purity requirements determined by the Majorana background model and the detector assembly procedures developed for cryostat fabrication and assembly.

3.14.3 Surface Facilities

On surface, Majorana will require a staging area to receive the equipment and materials for the construction of the underground laboratory. Some laboratory space will be required on surface for inspection and testing of detector components prior to their being shipped underground. Office space will be required for the Majorana personnel stationed at site. A surface control room will be required for monitoring the experiment and the electroforming facilities when there are no personnel underground. Majorana has not yet decided on the configuration of computing services for data analysis. However, regardless of where data analysis is done, Majorana will require IT facilities for local archiving and fast analysis of calibration data. IT support will also be necessary for Majorana scientists stationed at the site.

3.14.4 Site Options

Two site options are available for Majorana which should be able to satisfy our site facility requirements, have sufficient overburden for shielding, and likely will match our anticipated schedule: SNOLAB in Sudbury, Ontario, Canada, and the Homestake Laboratory that is being developed by the state of South Dakota as a potential site for the U.S. Deep Underground Science and Engineering Laboratory (DUSEL).

SNOLAB would provide ∼6000 mwe overburden, making cosmogenic backgrounds generated in-situ essentially negligible (see Sections 4.1.3 and 4.2). The lab is currently under construction and will be ready for underground activity to begin in 2007. Currently the DUSEL site selection process is still underway, with leading candidate locations being the Homestake mine in Lead, South Dakota, and the Henderson mine in Empire, Colorado. The state of South Dakota has committed funds that would allow access and operation of the Homestake Laboratory well in advance of the NSF DUSEL schedule. The Homestake Laboratory would initially provide ∼4500 mwe, eliminating most cosmogenic backgrounds but perhaps necessitating more attention to the Majorana shield and veto designs compared to SNOLAB. The Homestake Laboratory site is also expected to be ready for underground activity in a favorable time period relative to Majorana's schedule, and would ultimately offer a deeper location, comparable to or exceeding SNOLAB depth.

At this time, Majorana has not committed to a specific site for its final location. Expressions of Interest and Letters of Intent have been sent to both SNOLAB and the Homestake Laboratory. SNOLAB has informed the collaboration that they "strongly endorsed" including Majorana in its initial experimental program. The Homestake Program Advisory Committee identified Majorana as an "outstanding opportunity". Furthermore, they recommended housing the experiment as early as is feasible and noted that early needs, such as the underground copper electroforming, should be accommodated as soon as funding and space is available.

In light of these two positive responses, we intend to carryout a careful site selection process. The decision will be based on objective criteria, focusing on Majorana's physics goals, schedule impact, cost effectiveness, and project risk. Our plan is to initiate this process once Majorana becomes an officially funded project.

4 Majorana Backgrounds and Sensitivity

The ideal $0\nu\beta\beta$ decay measurement would be background-free. Our goal for the first stage of Majorana comes close to this ideal, in that we aim to attain a background level in the region-of-interest[6] (ROI) of 1 count/ROI/t-y. We will show that such a level provides sensitivities that are close to those for the zero background case for 5 years of running with the Majorana 120 kg experiment. Achieving such low backgrounds is a formidable challenge and background considerations dominate all aspects of the experimental design. Based on available technology and our previous experiences in developing low background experiments we believe that our goal can be met using the proposed array of hyper-pure germanium crystals. Pushing the background down to the 1 count/ROI/t-ylevel also relies on recent technological developments with germanium detectors that should allow us to discriminate and reject a number of potential backgrounds that are distinguishable from the signal of interest.

4.1 Methods to Mitigate Backgrounds

Mitigation of backgrounds is crucial to the success of any rare decay search. For the case of germanium solid-state detectors, decades of research have yielded a host of techniques to reduce backgrounds. These techniques include the use of ultra-pure materials for the construction of detector components in the proximity of the crystals, shielding the detector from external natural and cosmogenic sources, and optimizing the detector's energy resolution to enhance the spectral information available. Recent advances have provided new techniques in the form of pulse-shape analysis, detector segmentation and granularity (inter-detector coincidences), all of which rely on the differences between the spatial distribution of energy deposition between double-beta decay events and most background signals. Background signals arising from radioactive decay often include a beta and one or more γ-rays. In addition, in order to deposit 2 MeV in a detector, a γ-ray frequently requires multiple scatters. Since double-beta decay energy deposition occurs within a small volume ($\sim$1 mm^3) and is hence single site, it has an event topology distinct from most backgrounds. Fortunately, segmented, tightly packed Ge detectors allow for several cuts to be applied to take advantage of this distinction. Rejection of decay-product series using single-site, time-correlation analysis techniques are also possible in these ultra-low event rate experiments. These techniques are discussed below in terms of their relevance and implementation within the framework of Majorana. A quantitative estimate of their effciencies at reducing background is given in section 4.2.

4.1.1 Ultra-Pure Materials

Low-background experiments must be constructed out of ultra-pure materials. The production process for germanium detectors (zone refining and crystal growth) assures that natural radioactive impurities are excluded for the bulk of the germanium. But, cosmogenically produced ^{60}Co and ^{68}Ge are potentially serious sources of background created by high energy cosmic-secondary neutrons while the germanium is above ground. Ideally one would pull germanium crystals and fabricate the detectors underground to minimize cosmogenic isotope production. Such manufacturing is expected to significantly reduce ^{68}Ge and ^{60}Co backgrounds and the cost/benefit of underground manufacturing is being studied. As an alternative, the cosmogenic exposure can be inexpensively reduced by use of passive shielding during many stages of transport and manufacture, and by storing bulk materials in shielded bunkers when not in use during the manufacturing process. Controlling the cosmic ray exposure is particularly important after crystal growing which reduces all isotopes except those of germanium.

[6]Note that throughout this chapter we are assuming that the region-of-interest centered around the 2039 keV $0\nu\beta\beta$ decay peak is 4 keV wide. The actual analysis will likely employ a more sophisticated method of optimizing the analysis region.

Copper is one of the very few elements having no relatively long-lived radioisotopes. It also has excellent physical, chemical, and electronic properties that make it particularly useful in the fabrication of low-background radiation detectors. Nevertheless, one must take care to ensure that it is not contaminated with radioactive impurities, and that it does not have significant quantities of cosmic ray generated radioisotopes. The most serious of these latter impurities is ^{60}Co, which is generated by (n,α) reactions on ^{63}Cu. Ultra-pure copper for use in Majorana will be produced by an electroforming process deep underground.

The electroforming process uses an acidic $CuSO_4$ solution through which positive copper ions are induced from a copper anode to a stainless steel mandrel which initially serves as the cathode. The sacrificial copper anode material is consumed and replaced as necessary as the electroformed part is formed at the cathode. Highest purity copper is obtained by carefully limiting the electroforming potential. This selectively eliminates a wide variety of contaminants which reside in the bath as the less pure anode copper source material is consumed. The slow electroforming process tends to form large, high purity copper crystals at the cathode. However, mechanically sound copper is obtained by forming crystals of smaller size. Management of these two diverging requirements is one of the chief difficulties. This is achieved by controlling the rate of plating (i.e. current density at the Cu surface), manipulation of electrode surface boundary layers (via agitation, reverse pulse plating, etc.) and the use of crystal growth inhibiting chemicals. The optimization of electroforming copper with adequate structural integrity and high purity is underway.

Analysis of the materials used in the production of the bath solution has shown that satisfactory initial quality can be obtained by successive recrystallizations of the $CuSO_4$ used in the bath. In addition, because imperfect copper anode material is continually dissolved into the bath, it is necessary to constantly purify the bath. By pumping the bath solution through a high efficiency filter prepared with a $BaSO_4$ treatment, radium exchange reactions occur and particulate is removed. Additionally, the electroforming bath itself is kept under a cover gas and in a secondary containment. These precautions prevent ingress of Rn and aerosols as well as protect the valuable resource of the ultra-pure materials used in the bath. Predictive thermodynamic calculations based on assays of the anode material help to determine how long a bath can remain in production.

Most plastic materials have been empirically found to be radiologically pure. In particular, those produced from natural gas are likely to be sufficiently clean [Heu95]. Nevertheless, a sensitive screening program will be employed to verify that any proposed plastic material is adequately clean. Because of its use in germanium γ-ray spectrometers, the use of Teflon® and certain other plastics, which have proven to be sufficiently pure, is especially important. These have been screened using special mass spectrometry methods [Arp02].

With Majorana's low-mass modular design, much of the inactive mass close to the crystals is in the cabling and small parts. Reasonable purity for these components has been achieved in, for example, the custom-built SNO NCD cables [Ams06]. Majorana proposes a moderate R&D effort to improve cable purity further, by at least an order of magnitude. The cable purity goals may be lessened if lower-mass cabling technology can be shown to fulfill the mechanical and electrical specifications for Majorana. For example, Kapton® flex circuits may buy an order-of-magnitude reduction in cable mass over the traditional coax cabling used in IGEX. Such circuits with clean plastics and pure Cu used as base materials may be sufficiently pure for use in Majorana.

4.1.2 Shielding

Care must be taken to shield the detector from external radiation, whether it is generated naturally in the surrounding environment or cosmogenic in origin. To accomplish this task a graded bulk shield is required. An inner shield of at least 10 cm of Cu should suffice to screen out contributions from the bulk Pb itself. Cosmogenic radiation is not so easily attenuated and requires careful attention.

Cosmic rays are composed of muons (μ) and neutrinos at the depths at which the Majorana experiment will be conducted. Neutrinos have a very small probability of interaction in the detector

and are a negligible contribution to the Majorana background. Muons, on the other hand, produce copious ionization in the materials they penetrate and will register as pulses in the Ge detectors whenever they traverse a crystal. Additionally, muons are capable of direct interactions with nuclei, resulting in remnant spallation and fragmentation products as well as hadronic showers. While secondary protons are no more debilitating than the primary μ itself, high-energy secondary neutrons can travel through significant quantities of material before being thermalized and absorbed. These secondary neutrons undergo further nuclear interactions resulting in new isotope production. These resulting nuclei can have half-lives and decay energies sufficient to generate background events, if produced in the detector materials. Several techniques are described below to mitigate these cosmic ray muons and induced neutrons backgrounds. Details on the shield dimensions can be found in Section 3.8.

An outer-most, electronic anti-cosmic shield can effectively tag muons that pass through the primary shield and thus eliminate the primary energy deposition events in the Ge detectors and much of the secondary γ-rays, bremsstrahlung radiation, and neutron-induced backgrounds generated in the vicinity of the detectors via interactions in the lead or other materials. Given that the area of the μ veto system is a few m^2, the μ rates expected in any of the available underground labs can be efficiently tagged.

Muons that traverse near the detector but miss the active veto shield may undergo interactions in the surrounding rock that generate high-energy neutrons, which can penetrate the sensitive region of the detector and produce untagged backgrounds. We plan to mitigate the fast-neutron background by using large amounts of passive shielding within the active veto system, and by going to large depth, as discussed in the following section. Ambient, low-energy (thermal to $\approx$10 MeV) neutrons released by fission or (α, n) reactions from natural radioactivity in the experimental hall also pose a problem. The latter may be efficiently shielded with an intermediate layer of neutron absorber such as Cd or borated polyethylene.

The collaboration has identified about 4.5 tons of ancient Pb, which can be smelted into inner shielding. However, electroformed shielding may be a safer choice, as our electroforming process allows great control over purity. Thus, the provision for a replaceable inner shield allows a flexible approach. An optimum design will be selected based on detailed simulations.

4.1.3 Depth Underground

The most effective way to reduce cosmogenic backgrounds is to choose a deep underground site. The depth requirement for Majorana has been studied by Mei and Hime [Mei05] with an extensive FLUKA-based Monte Carlo calculation of estimated background contributions from untagged fast neutron elastic and inelastic scattering, cosmogenic radioactive isotope production, muon capture, and direct contributions from untagged muons. The results of the calculation using the proposed Majorana shielding configuration are plotted versus depth in Figure 4.1. The dominant contribution is from fast neutron elastic and inelastic scattering, with subdominant contributions primarily from neutron capture on the Cu cryostat structures. Although a variety of cosmogenic isotopes are produced, the dominant background contributions come from ^{77}Ge, ^{76}Ga, ^{75}Ga, and ^{60}Co. A site such as SNOLAB or DUSEL would minimize these backgrounds. Ref. [Mei05] indicates that if an experiment such as Majorana is not sited at a depth greater than $\sim$4500 m.w.e., then a sophisticated shield will be required.

4.1.4 Energy Resolution

A key advantage of intrinsic solid-state Ge detectors is their inherent excellent energy resolution, associated with the low threshold for electron-hole pair production. $0\nu\beta\beta$ produces a monoenergetic peak in the measured spectrum at 2039 keV. Improving the resolution by some factor decreases the continuum backgrounds in the ROI by the same factor. It may additionally improve identification and rejection of peaks in the spectrum. Good resolution also improves the calibration of the detector.

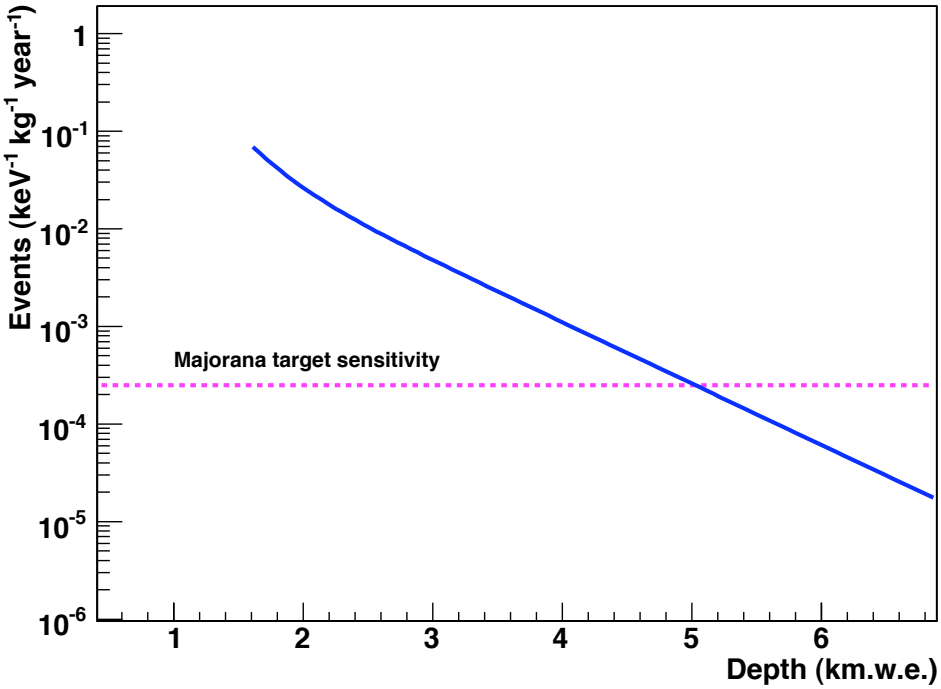

Figure 4.1: Sensitivity to muon induced backgrounds in a Majorana-like geometry as a function of depth. Details of the Monte Carlo simulation can be found in [Mei05]. Reduction factors due to analysis cuts have been applied. Reducing these backgrounds further would require more advanced shielding.

Better identification of peaks from background radioactivity in regions away from the ROI can lead to an improved background model and smaller uncertainties for estimates of backgrounds within the ROI. Perhaps most importantly, a good energy resolution is the *only* line of defense against the irreducible background from the $2\nu\beta\beta$ mode. It is not unusual to expect an energy resolution at 2 MeV of approximately 3 keV in germanium detectors, or about 0.2%. At this resolution, contamination in the ROI from ^{76}Ge $2\nu\beta\beta$ will be completely negligible[7].

The selectivity in identifying contaminant radionuclides with high resolution is an important feature. Spectra from complex environmental sources can be used to identify perhaps as many as 200 individual isotopes and quantify their activity. For example, the activity level of ^{214}Bi can be determined from the most intense peaks in the spectra and the expected intensities of the lines in the vicinity of 2039 keV can be predicted and their influence on the ROI determined with Monte Carlo simulation.

4.1.5 Detector Granularity

In a closely packed array of detectors, there is a large probability for hits in multiple detectors from internally generated γ-rays that escape a crystal, Compton scatter γ-rays from external sources, and traversing muons. The appearance of hits in several nearby detectors within a short (few

[7]See equation (36) in Elliott and Vogel [Ell02].

microsecond) coincidence window provides a large-scale multiplicity cut. Our terminology for such detector-to-detector coincidence background rejection is *granularity*.

Granularity rejection complements the pulse-shape analysis and segmentation rejection of internal radiation. In particular, external ^{208}Tl, ^{214}Bi, and ^{60}Co (i.e. in the shield/cryostat structures) have decay schemes well suited to granularity rejection and possibly general localization of hot spots. For example, external ^{208}Tl 2615 keV γ-rays can impinge on an outer crystal in the 57-detector array. Assuming that only 2039 keV is deposited in the crystal, there is a reasonable chance that the remaining 576 keV will be deposited in an adjacent crystal. Because the integrated count rate of the system is expected to be quite low, any two-detectors hit within 1 μs can be discarded with negligble loss of live time.

4.1.6 Pulse-Shape Analysis

Modern signal digitization techniques allow for the discrimination between $0\nu\beta\beta$ and a large fraction of γ-ray backgrounds. $0\nu\beta\beta$ ejects two electrons with a net energy of $\sim$2039 keV. The energy deposited by the two beta particles frees a cloud of holes and electrons, which move toward their respective electrodes. Depending on the radial location inside the detector, one or the other of the species arrives first, resulting in a double-humped pulse structure, as shown in the upper panel of Figure 4.2. Backgrounds from external and internal γ-rays, on the other hand, may deposit their energy in multiple-sites through Compton scattering. The resulting pulse shape is a superposition of double-humped pulses, an example of a multi-site event is given in the lower panel of Figure 4.2.

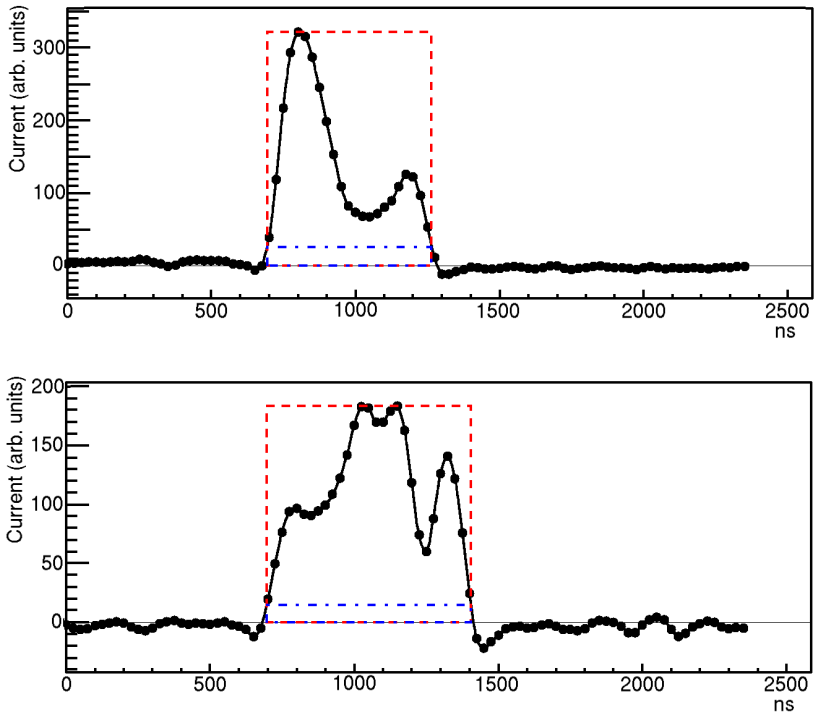

Figure 4.2: Waveforms from single-site (top) and multi-site events (bottom). Shown is the derivative of a raw preamplifier charge pulse [Aal00].

Modern front-end analog and digitization electronics are capable of collecting preamplifier pulse

shapes with sufficient bandwidth to extract key pulse parameters, including the width, asymmetry, kurtosis, and higher moments. In addition to indicating whether an event is single- or multi-site, these parameters also give the radial position of events within the crystal. A map of the pulses built from a training set of double escape events from ^{208}Tl or ^{56}Co can be formed such that any desired percentage of the single-site pulses can be kept. Using such training pulses we have been able to discard large fractions of events from complex decay schemes such as ^{68}Ge and ^{60}Co. When these isotopes are internal to the detector, the interaction site multiplicity is much larger than for neutrinoless double-beta decay and this method is very effective. Pulse-shape analysis is less effective at rejecting a single γ that impinges on the detector from outside. These must be mitigated via other means.

4.1.7 Detector Design and Segmentation

Electrically subdividing the detector into smaller elements gives additional discrimination between single site events like $0\nu\beta\beta$ and internal or external γ-ray backgrounds. The virtual segmentation of a germanium crystal into electronically distinct pieces is done for example by simple masking of electrode deposition on the surface of the crystal. In this way, a $\sim$1 kg crystal can effectively be a collection of many smaller detectors that are in very close proximity. If the segment dimensions are chosen carefully, it is possible to enhance the probability that multi-site interactions distribute their energy depositions among different detector segments. Typical segmentation schemes are shown in Figure 3.11. In its simplest form, segmentation provides an effective method of achieving higher granularity without introducing dead layers that would be present in separate detectors of similar size. Segmentation enhances rejection of multi-site events distributed in the azimuthal (φ) and axial (z) directions respectively. Hence segmentation rejection is largely orthogonal to PSA, which is most efficient at removing radially distributed multi-site events.

The efforts of the GRETINA collaboration to develop a Ge detector array capable of γ-ray tracking within segmented detectors has produced methods to reconstruct energy depositions within a segmented crystal with a spatial resolution of $\sim$2 mm. Event reconstruction involves advanced pulse-shape digitization and processing for the segments, and analyzes real and image charges to deduce position, energy, and time of the events. GRETINA-style event reconstruction enables analysis of backgrounds and possible $0\nu\beta\beta$ signals in a multi-dimensional parameter space, effectively serving as a time-projection-chamber.

Segmentation requires more contacts, cables, and preamp front ends, but the payoff in rejection is large. Internal isotope (^{68}Ge and ^{60}Co) rejection factors are particularly large due to the fact that both of these decays can only produce an energy deposit at 2 MeV via multiple particle interactions naturally leading to multiple-site events. For example, a detector with 2 ϕ and 3 z segments has a rejection factor of 55 for internal ^{6}0Co. This can counter cosmogenic radioactivity formed from the exposure of the detector during manufacture. More modest rejection is found for external ^{208}Tl.

Segmentation is a proven method. Efforts at several universities and national laboratories have validated the tracking concept and demonstrated reliable event reconstruction in Ge. We have leveraged this work and have begun to adapt it for double-beta decay studies. The collaboration has carried out experiments with modest segmentation (2 azimuthal segments) to heavy segmentation (32 segments in a mixed pattern), as well as many simulations. The simulations show substantial suppression levels, and the experiments have verified that these are obtainable. Optimization is needed to find a segmentation pattern with a high rejection efficiency, one that is easily and reliably manufactured, assembled, and maintained underground, and which minimizes the introduction of additional backgrounds with the addition of small parts in proximity to the crystals. For the purpose of this proposal we invoke a simplified event reconstruction and not the full event reconstruction power demonstrated by GRETINA. Although we feel no sense of urgency to select a specific segmentation scheme at this time, for definiteness we have chosen a modest segmentation scheme (2×3) that is manufacturable and provides good background rejection.

4.1.8 Modified Electrode Ge Detector (Unsegmented)

The collaboration is exploring a recently developed Ge-drift-like detector. Typical closed-end coaxial HPGe detectors have bore holes that reach through about 80% of the detector crystal. The modified electrode geometry reduces the depth of this hole to only a few millimeters. This design was recently demonstrated to provide low noise resulting in a low energy trigger threshold and excellent energy resolution as well as excellent pulse-shape capabilities to distinguish multiple interactions. The latter is due to the low electrical fields in the crystal and the increased range of drift distances as well as the small electrode configuration enabling the so-called small pixel effect reflecting the fact that the signal at the small central readout electrode is only measured just before the charge is actually collected. Though this detector is intrinsically slow, the low-background environment of Majorana will not result in any significant dead time. This detector type offers a potential alternative to segmented detectors and its feasibility is currently being explored by the collaboration.

4.1.9 Time Correlations

Single-site, time-correlated (SSTC) cuts are a decay-chain-specific cut. This method looks forward or backwards in time from an event in the ROI to find signatures of parent or daughter isotopes [Eji04, Eji05]. Given a raw event rate of roughly 1 event per crystal per day, this method will work exceptionally well for internal, short-lived parent-daughter pairs like ^{68}Ge-^{68}Ga and for decays of internal contaminants, with somewhat lower rejection efficiency. It will also play an important role in diagnosing and eliminating surface contamination of U and Th chain isotopes.

The decay of ^{68}Ge via capture of an inner electron releases 10.367 keV of energy in a series of soft x-rays, which are observable >95% of the time. Within a few half-lives of ^{68}Ga ($T_{1/2} = 67.6$ min), we expect to observe a positron emission with maximum energy 1.9 MeV plus two 511 keV annihilation gammas, for a total energy deposit of 2.9 MeV. We should be able to look within 5-6 half-lives backward in time from any positron event near 2039 keV and see the x-ray from the parent ^{68}Ge decay to veto those that have not already been removed by the PSA, segmentation, or granularity cuts, with 90% efficiency. In addition, we should be able to make a spectrum of such coincidences to isolate and quantify the ^{68}Ge contribution. Excellent energy resolution and low thresholds are essential for this type of contamination isolation. Because this effect is limited to a single segment, the segment's count rate in the x-ray window determines how far back in time we can look for the precursor signal. Looking back several half lives gives high efficiency to identify ^{68}Ge decay, while reducing the live time of the experiment negligibly (by <1%). Simulations of SSTC yield reduction factors larger than 10, depending on the time window, see Figure 4.3. This method can also be used to reject backgrounds due to ^{208}Tl ($T_{1/2} = 3.05$ min) and ^{214}Bi ($T_{1/2} = 19.9$ min) in the Ge crystals and the inner mount, albeit with lower efficiency. SSTC can also be used to study backgrounds outside the region-of-interest and improve detector understanding.

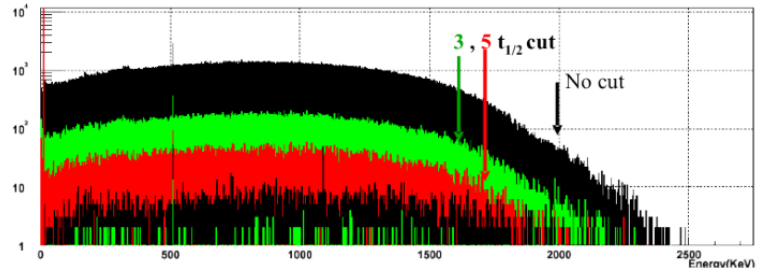

Figure 4.3: The rejection of ^{68}Ge via the single site time correlation is shown with look-back of 3 half lives and 5 half lives, yielding rejection factors of 8 and 32, respectively.

4.2 The Majorana Background Budget

The backgrounds in the Majorana experiment and most other double-beta decay experiments that use internal source techniques can be divided into nine categories. These categories facilitate identification of problematic components and in some cases may allow comparison with other experiments. By applying estimates of the background rejection capabilities of granularity (crystal-to-crystal) cuts, pulse-shape analysis, simplified event reconstruction in segmented detectors, and single-site-time-correlation (SSTC), we can estimate the maximum tolerable concentrations of specific radioactive isotopes in different detector components required to reach a proposed $0\nu\beta\beta$ decay half-life sensitivity.

The radioactive contamination in a detector component is most often specified in μBq/kg or sometimes, when measured via mass spectrometry, in picograms/gram. Using Monte Carlo calculations of detector response, these impurities can be linked to background counts in the 4 keV region of interest per detector operating time, expressed in this work as cnts/ROI/t-y. For instance, a 0.3 μBq/kg ^{232}Th activity (0.08 pg/g Th) in Cu would translate into a background rate (after all cuts) of 0.09 cnts/ROI/t-y from γ rays originating from the cryostat, assuming equilibrium in the decay chain. For the purposes of estimating the achievable background levels of the Majorana components, we have in some cases made assumptions about the achievable levels of purity in key materials. Attaining these levels requires that we assay construction materials and eventually assay each component that goes into the apparatus. Table 4.1 summarizes the target purity levels we wish to achieve and current progress against that goal. The most important element is the electroformed copper. We anticipate meeting these purity goals, but also are continuing to investigate alternative strategies. Based on the contaminant goals in Table 4.1 that we have obtained or expect to obtain, our current background estimation is summarized in Table 4.2. We are certain that these numbers will evolve, in particular as we continue to refine and develop our more realistic and detailed Monte Carlo simulation.

The final net number of background counts expected in the region-of-interest depends on a number of factors, including the purity of the materials used, the exact configuration of the expected sources, the analysis cuts used to distinguish signals from backgrounds, and the build-up and decay profiles of the given sources. These factors stemming from purity have been directly related to final background counts using our current Monte Carlo simulations. A summary of the expected background, before and after analysis cuts is given in Table 4.2. The acceptance efficiencies on a component-by-component basis for the analysis cuts as estimated from our Monte Carlo simulations are presented in Table 4.3. The total estimated background for the current Majorana reference design is 1.6 cnts/ROI/t-y. Based on our simulation estimates and assay capabilities, we believe that we are close to achieving our target background of 1 count/ROI/t-y.

Details on the background categories, the expected initial contamination levels for the given components, and our plans for addressing them are as follows.

1. **Radioactive decays inside the germanium:** It is estimated that the activation rate of ^{68}Ge and ^{60}Co are 1 atom/kg/day on the earth's surface and that the detector production process is 100 days. Similar activation rates were observed by collaboration members [Avi92] when ultra-low background detectors were moved from long operation underground to the surface for repairs and then again operated underground. Achieving the integrated 100-day surface exposure includes estimates of 45-90 days for detector manufacture and 35 days of shipping from the enrichment plant to the detector manufacturer, plus several trips within the US to account for the processing from GeO_2 to finished detector crystals. Minimizing surface exposure by the use of shielded transportation (2 meter water equivalent (mwe)) and modest surface shielding (4 mwe) should reduce the transportation and idle periods by at least a factor of 10 in effective exposure for ^{68}Ge production. As shown in Table 4.2, event reconstruction, pulse-shape analysis, and time correlation cuts can greatly reduce the cosmogenic background from the highest gross expected background count rate to an subdominant expected post-cut

Table 4.1: Component material radioactivity goals for the major contributors to backgrounds in the $0\nu\beta\beta$ - decay region of interest. The column titled Equivalent Achieved Assay specifies the existing best limit on the component's ^{208}Tl activity deduced from a measured quantity of ^{232}Th. An activity of ^{208}Tl of 0.1 μBq/kg would correspond to an activity of ^{232}Th of 0.3 μBq/kg. We have focused on the Th contamination levels, since it has the more complex chemistry and hence is more difficult to remove. It is also more efficient at producing background in the ROI than is the U chain.

Material	**Uses**	**Contaminant Goals**	**Equivalent Achieved Assay**	**Reference**
Germanium	Detectors	1 atom/kg/day ^{68}Ge 3.5 atom/kg/day ^{60}Co		[Avi92]
E-formed Cu	Support Rods, Cryostat, Inner Cu Shield	0.1 μBq/kg ^{208}Tl 0.4 μBq/kg^{214}Bi	0.7-1.3 μBq/kg	Current work also [Arp02]
NOSV Cu	Outer Cu Shield	0.26 μBq/kg ^{208}Tl 0.3 μBq/kg ^{214}Bi	<6 μBq/kg	[Heu04]
Pb	Lead Shield	1 μBq/kg ^{208}Tl 5 μBq/kg ^{214}Bi	<7 μBq/kg	[Heu04]
Plastic	Trays, Rings	10 μBq/kg ^{208}Tl 10 μBq/kg ^{214}Bi	1000 μBq/kg	Current work also [Arp02]
Front End Electronics	LFEPS, Contacts, Capacitors	30 μBq/kg ^{208}Tl 200 μBq/kg ^{214}Bi	1000 μBq/kg	Current work also [Arp02]
Cable	Cable	3 μBq/kg ^{208}Tl 10 μBq/kg ^{214}Bi	400 μBq/kg	[Ams06]

Table 4.2: Summary of background sources for the Majorana experiment. "Gross" indicates the ROI count rate with only a granularity cut before any other analysis cuts are applied. "Net" indicates level of activity after all cuts have been applied. The total estimated background for the current Majorana reference design is 1.6 cnts/ROI/t-y. Based on our simulation estimates and assay capabilities, we believe that we are close to achieving our target background of 1 count/ROI/t-y.

Background Source		**Rates for Important Isotopes** cnts/ROI/t-y				**Total Est. Background** cnts/ROI/t-y
		^{68}Ge	**^{60}Co**			
Germanium	Gross:	15.76	1.65			
	Net:	0.10	0.05			0.15
		^{208}Tl	**^{214}Bi**	**^{60}Co**		
Support Rod, Tray, Ring	Gross:	0.22	0.09	0.00		
	Net:	0.10	0.03	0.00		0.13
Cryostat	Gross:	0.16	0.07	0.15		
	Net:	0.09	0.02	0.00		0.11
Inner Copper Shield	Gross:	0.21	0.26	0.03		
	Net:	0.10	0.08	0.00		0.18
Outer Copper Shield	Gross:	0.15	0.06	0.00		
	Net:	0.05	0.02	0.00		0.07
Lead Shield	Gross:	0.14	0.16	0.00		
	Net:	0.04	0.05	0.00		0.09
Front-End Electronics, Contacts	Gross:	0.20	0.16	0.00		
	Net:	0.10	0.06	0.00		0.16
Cables	Gross:	0.18	0.14	6.15		
	Net:	0.08	0.04	0.13		0.25
Surface Alphas	Alphas originating from all surfaces					0.09
		μ	**cosmic activity**	**γ**	**(α, n)**	
External Sources	Gross:	0.03	1.50	0.05	0.06	
	Net:	0.003	0.21	0.05	0.06	0.32
$2\nu\beta\beta$						<0.01
Solar ν						0.01
Atm. ν						0.02
			TOTAL SUM			1.59

net rate of 0.15 cnts/ROI/t-y. A factor of a few increase in the activation rate would not have a serious impact on the sensitivity of the experiment. For the estimate in Table 4.2, we assume a 100-day (30-day) activation for ^{68}Ge (^{60}Co)and a 90-day cool-down period underground before data taking begins. The zone refinement process and crystal growth of the Ge ensures that the U and Th levels produce a negligible background.

2. **Radioactive decays in the inner crystal support structures:** We are developing and testing a very low mass support system composed of Cu, plastic, and possibly Si or Ge. For each module the total mass of the 57 support rods is 300 g, the total mass of the 57 Ge trays is 200 g and the total mass of the 171 contact rings is 340 g. Monte Carlo calculations indicate that radioactive backgrounds in this system will contribute about 8% of the total background budget.

3. **Radioactive decays in the copper cryostat**: The cryostat provides vacuum and thermal conductivity to the liquid nitrogen reservoir and is discussed in Section 3.7.1). At this time, it appears that the cryostat background contribution will be about 0.11 cnts/ROI/t-y or about 7% of the total background. Note we need for the Cu to have impurities of 0.3 μBq/kg ^{232}Th

Table 4.3: Acceptance Efficiency for $0\nu\beta\beta$ decay and various background sources using granularity, segmentation, pulse-shape analysis (PSA) and single-site time correlation (SSTC) cuts. For the $0\nu\beta\beta$ entry the Total column entry includes an 84% cut for an energy acceptance cut and a ∼5% loss due to edge effects and lost bremsstrahlung. For the cables, LFEPs, capacitors and contacts, the acceptance efficiencies are taken to be similar to those for other nearby parts and were not simulated separately. The PSA efficiency was estimated from simulation by assuming events could be identified as multi-site if there were energy deposits >50 keV with a radial separation of 4 mm or more. To estimate the background level from the presently incomplete Bi simulations, we scaled the acceptance efficiencies from the Tl values.

Process	Granularity	Segmentation	PSA	SSTC	Total
$0\nu\beta\beta$	96%	95%	98%	89%	71%
^{68}Ge in Ge	22%	24%	25%	11%	<1%
^{60}Co in Ge	13%	18%	18%	100%	<1%
^{208}Ti in support rods	19%	58%	81%	65%	6%
^{214}Bi in support rods	22%	48%	63%	50%	3%
^{60}Co in support rods	4%	12%	18%	100%	< 1%
^{208}Ti in cryostat	43%	68%	80%	100%	24%
^{214}Bi in cryostat	35%	54%	62%	100%	12%
^{60}Co in cryostat	5%	13%	24%	100%	< 1%
^{208}Ti in inner Cu shield	47%	62%	76%	100%	22%
^{214}Bi in inner Cu shield	41%	52%	60%	100%	13%
^{60}Co in inner Cu shield	3%	8%	18%	100%	< 1%
^{208}Ti in outer Cu shield	47%	55%	67%	100%	17%
^{214}Bi in outer Cu shield		Simulation in Progress			
^{60}Co in outer Cu shield	3%	Low sim. stat.		100%	<1%
^{208}Ti in Pb shield	48%	46%	56%	100%	12%
^{214}Bi in Pb shield		Simulation in Progress			
^{208}Ti in Ge tray	20%	59%	74%	100%	9%
^{214}Bi in Ge tray	21%	49%	61%	100%	6%
^{208}Ti in ring	17%	53%	80%	100%	7%
^{214}Bi in ring	20%	45%	63%	100%	6%
Muons	10%	100%	100%	100%	10%
Neutron capture on Cu	7%	40%	25%	100%	1%
Cosmogenic activity	15%	98%	100%	100%	14%
(α,n) neutrons	100%	100%	100%	100%	100%

in order to meet our background goals. (This translates into 0.1 μBq/kg of ^{208}Tl, the source of a problematic 2615 keV γ-ray.) We expect to achieve these values via the Cu electroforming techniques discussed earlier. Because the cleanliness of the Cu is a critical feature of the experiment, it is an important part of our R&D program.

4. **Radioactive decays in the shielding materials:** The total expected background rate is very sensitive to the radiopurity of the shield. The reason for this dependence is because of the large mass of the shield itself. Assuming an inner shield of electroformed copper, we anticipate that the count rate from the shielding would be 0.34 cnts/ROI/t-y, or about 1/5 of the total count rate. The shield is currently the largest source of background. It has similar Cu purity requirements to the cryostat and reinforces the need to produce extremely pure electroformed copper.

5. **Radioactive decays in front-end electrical components and cables:** The front-end

electronics, contacts and cables are estimated to contribute ≈25% to the total expected background count rate, or 0.41 cnts/ROI/t-y. To achieve this level requires cable material that is extremely clean (3 μBq/kg ^{208}Tl). This specification however is coupled to the cable mass. Although our reference design employs low-mass flex circuitry, this estimate conservatively assumes a cable design comparable to that used in IGEX. Our estimates of the total cable mass in the immediate vicinity of the detectors is ≈1.3 kg. Since the cables run from the detectors through the shield, we calculated the background rejection efficiencies for different spans of the cable run. As expected it is the cable nearest the detectors that dominates this background contribution.

This cable design can be greatly improved upon with respect to mass. Because of the importance of this background contribution and its large uncertainty due to the conceptual nature of the cable design, the cable design is a critical component of our R&D plan. The LFEP and capacitor are better defined in terms of mass. Hence the specification for these parts (30 μBq/kg ^{208}Tl) is less flexible. We will assay these parts in bulk to study their cleanliness. Note that the ^{60}Co contribution from the cables is appreciable because the Cu in the cable was assumed to have Co activity at equilibrium with the cosmogenic production (180 atoms/kg d) and because the cables are so close to the detectors.

6. **Depth-dependent or site-specific activity:** In addition to material contamination and activation, one must also consider backgrounds from radioactivity from the surrounding rock and from cosmic and cosmogenic activity present at the given depth. Direct muon contributions at 6000 mwe would be more than adequately addressed by a modest muon veto system. Assuming a poor 90% efficiency, the contribution from direct muons would be about 0.003 cnts/ROI/t-y, or 0.1% of the total. More of a concern are backgrounds coming from muon-induced activity. This includes fast neutron elastic and inelastic scattering, cosmogenic radioactive isotope production, and muon capture. Using a FLUKA-based Monte Carlo, we have made a preliminary estimate of the contribution from these sources at ∼1.50 cnts/ROI/t-y. Applying cuts based on segmentation, pulse-shape analysis, and granularity reduces this background by a factor of 7.4, or 0.21 cnts/ROI/t-y. This is the dominant activity expected from this source of background. Finally, one must also consider activity due to gammas and from (α,n) coming from the surrounding rock activity. Neutrons from (α,n) reactions are strongly suppressed by moderate amounts of borated polyethylene. A polyethylene shield 35 cm-thick, with the inner 5 cm composed of borated polyethylene, would reduce the ambient neutrons by a factor of 3×10^{-4}. Given that the Heidelberg-Moscow experiment observed a 20% decrease in background signal at 2 MeV with the addition of 10 cm of borated poly, and assuming all else to be the same, the Majorana experiment might expect to see a raw (α,n) signal as large as 50 counts in the 516 kg-year exposure. With the 40 cm poly shield, however, this rate reduces to 0.06 cnts/ROI/t-y, and we have for the moment conservatively assumed no differences between the net and gross counts. The net effect of these backgrounds is about 20% of the total expected background rate.

7. **Surface Alphas:** The depth of the outer dead layer of n-type detectors is smaller than the range in Ge for alphas emitted by some nuclides. Hence these alphas, when emitted on the surface of a detector, can pass through the dead layer and deposit energy in the sensitive region of the detector. Similarly alphas penetrating the passivated detector face will also contribute to backgrounds. Our simulations indicate that approximately 6×10^{-6} of such decays populate the ROI, and so a surface contamination of 5×10^{-10} Bq/cm^2 would produce a background level of ∼0.09 cnts/ROI/t-y. For alphas at the passivated surface, potential incomplete charge collection due to trapping and surface field effects may increase these levels.

   There are a number of surfaces from which alpha particles could strike a detector. However, the Monte Carlo shows the dominant contribution (90%) comes from alpha emitters on the

detector surface. For other surfaces, either the surface area is smaller or the efficiency for producing counts in the ROI is less.

8. **Rn gas within the shield volume:** The inner volume of the shield is ∼230 L. If the air in this volume is displaced by LN_2 boil off gas that contains Rn (assumed to be entirely ^{222}Rn) at the level of 1x10^{-9} Bq/l (Borexino result), the total activity will be approximately 0.5 μBq. To estimate the acceptance for these decays to produce an event within the ROI, we use the calculations for ^{214}Bi activity in the cryostat. This results in an approximate contribution from radon that is 0.0001 cnts/ROI/t-y.

9. **Two-neutrino double-beta decay:** This background is completely mitigated by the intrinsically good energy resolution of germanium detectors, as was discussed in more detail in Section 4.1.4. The overall contribution of the $2\nu\beta\beta$ is expected to be negligible for the proposed running time of the experiment.

Majorana will be one of the most sensitive low background systems in the world and may be subject to currently unknown sources of background. It is crucial to add contingencies designed to mitigate these backgrounds. We are designing our shielding to have an inner layer to allow replacement in case the shielding contributes an unacceptable background. Alternatively, we are also currently investigating alternative active shielding methods based on liquid argon, while also communicating with the GERDA collaboration which plans to use a liquid nitrogen based shield. Such methods, whose technical feasibility have yet to be demonstrated, should be able to reduce the shielding background contributions significantly, and in the case of liquid argon also offer the advantage of active shielding of the outer array surface.

The collaboration will continue to pursue R&D investigations to understand, control, and mitigate the impact of irreducible backgrounds. Obviously, a balanced approach requires minimizing the cost and effort involved, but this is not possible without a detailed understanding of the leading backgrounds.

4.3 Demonstration of Backgrounds

The background goal for the 120 kg Majorana Ge $0\nu\beta\beta$ decay measurement requires pushing down backgrounds a factor of 400 lower than demonstrated in previous Ge experiments. Many of the reduction factors are obtained from analysis cuts, but we must also reduce the impurities in our construction materials. Demonstrating that the ultra-pure materials can achieve these levels requires the development of more sensitive assay capabilities. It also requires implementing an accurate model of the backgrounds in our simulation code. In brief Majorana relies on the fact that Ge crystals have been found to be intrinsically very clean (Primordial activity in Ge crystals should be less than 1x10^{-3} cnts/ROI/t-y.) and on our plan to utilize pure electroformed copper for the internal parts, cryostats and shielding.

For the bulk of materials we plan to use in Majorana our stated goal is that we need to achieve background levels in our structural materials of 0.3 μBq/kg ^{232}Th. To date, we estimate that we have demonstrated a background value of <2-4 μBq/kg. As discussed in the subsequent sections, based on our successes with electroforming copper and recent improvements in assay sensitivity we should be able to build a detector with materials that meet our desired goal of 0.3 μBq/kg ^{232}Th.

We will use direct radiometric counting, mass spectrometry, and neutron activation analysis to verify the target radiopurity levels for the components of the Majorana experiment that are summarized in Table 4.1. We will then use simulation to estimate how these levels of activity translate into background in the ROI. The basic verification plan is to first test all components with direct radiometric counting where achieved sensitivities of one mBq/kg for ^{232}Th and ^{238}U are routine. All components that have target radiopurity levels lower than 1 mBq/kg will then be tested by either mass spectrometry or neutron activation analysis, which ever is more appropriate. The individual radiopurity verification methods are described in detail below.

4.3.1 Monte Carlo Modeling

Confidence in the results from the simulation package used for Majorana (MaGe) is important. The MaGe framework is used to generate background estimates and other results used in developing the Majorana plan. As part of this Monte Carlo effort, described in Section 3.11, the following validation efforts for the MaGe simulation package are underway:

- Simulations were performed to reproduce existing experimental data sets for detectors such as a Canberra Clover detector and a highly-segmented MSU detector. Initial results show that these simulations reproduce the detector data very well.
- Multiple-Element Gamma Assay (MEGA), the Segmented Enriched Germanium Array (SEGA), LArGe, the LLNL Compton telescope, PNNL low-background detectors, The WIPP-n low background n-type detector operating underground at WIPP, the SOLO low-background detectors, and the Oroville Low Background Counting Facility, will also be simulated and will provide additional validation data.
- The cooperative simulation effort with the GERDA collaboration provides independent confirmation of the simulated physics processes, as well as additional comparisons between simulated and real data from their prototypes. It also provides a valuable exchange of information on bugs and limitations in the code, as they are uncovered.

Finally, the core of the simulation package, GEANT4, is a common tool with a large, active international user community, ensuring constant testing and improvements.

4.3.2 Radiometric Measurements

Table 4.4: Radiometric screening sensitivities at the Lawrence Berkeley National Laboratory surface low background counting facility (LBCF) and at the underground LBCF at Oroville (180 mwe).

Contaminant	Surface Facility	Oroville Facility
^{238}U and daughters	0.5 ppb (6 mBq/kg)	50 ppt (0.6 mBq/kg)
^{232}Th and daughters	2 ppb (8 mBq/kg)	200 ppt (0.8 mBq/kg)
^{40}K	1 ppm	100 ppb
^{60}Co	0.04 pCi/kg	0.004 pCi/kg

Table 4.5: A summary of low background counting facilities that are available to Majorana.

Counting Facility	Depth	Detectors
Berkeley Laboratory (LBNL)	surface	HPGe
Oroville (LBNL)	180 mwe	HPGe
Waste Isolation Pilot Plant (WIPP)	1585 mwe	HPGe
Soudan Underground Mine	2090 mwe	HPGe and α/β
Sudbury Neutrino Observatory Laboratory (SNOLAB)	6010 mwe	HPGE

Radiometric screening methods, where minute amounts of contaminants can be identified through the detection of characteristic γ-rays, is an established form of material verification. The sensitivity

of this method is dependent on the total mass of the sample, the counting time, signal to background ratio, and detector efficiency. High-resolution, high-purity germanium (HPGe) detectors with low-activity components in special shielded low-background facilities are typically used to optimize the signal to background ratio. Although a large sample mass would be ideal, the effectiveness of the sample mass is limited by self shielding effects. The optimal counting time is typically determined by the background level.

The Lawrence Berkeley National Laboratory (LBNL) maintains a shielded surface low background counting facility (LBCF) in Berkeley and an underground facility beneath the Oroville dam (180 mwe) in northern California [Smi03, Smi04]. The surface facility, which was established in 1963, currently has two 80% p-type HPGe detectors and the Oroville facility has one 80% p-type HPGe detector. The Oroville facility has a long history of certifying materials for many low background experiments including SNO, KamLAND, CDMS, and CUORE. Routine sensitivities for various contaminants at the surface and Oroville facilities are shown in Table 4.4. The counting time required to achieve these sensitivities are about one day at the surface facility and about one week at the Oroville facility. Both LBNL facilities are designed to count samples with a maximum volume of two liters. This relatively large volume will allow greater sensitivity to the counting of small parts where kilograms of material are to be counted when only milligrams of material are actually needed for the Majorana experiment. All measurements at the LBNL facilities are made relative to reference samples with calibrated activity and with similar specific gravities and geometries as the material being certified making the screening results independent of any calculated efficiency, geometry, and self-shielding effects. Additional low background counting facilities that are available for use by Majorana are listed in Table 4.5.

As shown in Table 4.4, the routine sensitivity of the Oroville facility is about 1 mBq/kg for ^{232}Th and ^{238}U. The primary limitation to the sensitivity is due to the activity in the detector components. Higher sensitivities have been achieved with HPGe detectors with lower activity components, with a more heavily shielded facility, and with longer counting times. For example, reference [Bro95] obtained a sensitivity of 9 μBq/kg in the ^{232}Th chain for 8 kg of copper with a decommissioned double-beta decay detector over a ninety day counting period. Reference [Heu95] has estimated that the best sensitivity level for this class of radiometric count about 4-5 μBq/kg.

The decommissioned double-beta decay detector mentioned is currently located at the Soudan Low Background Counting Facility[8] (2000 mwe) and it has recently been commissioned as the SOudan LOw Background Gamma Counting Facility (SOLO)[9]. The SOLO facility will be used by Majorana to verify some critical items that require less than one mBq/kg sensitivities. Due to the long counting times (about 90 days) required to achieve the 10 μBq/kg sensitivity, the number of these critical samples will be limited to about ten.

In summary, the sensitivity of direct radiometric measurements is limited to about 1 mBq/kg for routine counting times and to about 10 μBq/kg for very long (90 day) counting periods. As seen in Table 4.1, this level of sensitivity is not sufficient by an order of magnitude for many of the Majorana components, and higher sensitivity assay techniques such as Inductively-Coupled Plasma Mass Spectrometry (ICPMS) and Neutron Activation Analysis (NAA) are needed. However, for these components, the radiometric measurements will play an important role for initial certification before an investment in ICMPS or NAA counting is made.

4.3.3 Mass Spectrometry

The purity levels required for Majorana have rendered direct radiometric counting impractical. As a result, a number of analytical approaches have been evaluated for assay of copper with Inductively-Coupled Plasma Mass Spectrometry (ICPMS) being the most promising. ICPMS is a variant of mass spectrometry that has been successfully used for ultra-trace measurements. For radioisotopes

[8] `http://www.hep.umn.edu/lbcf/index.html`
[9] `http://particleastro.brown.edu/SOLO/`

with half lives over a few hundred years ($T_{1/2}$ for ^{232}Th = 1.4×10^{10} y), ICPMS is expected to be better than direct radiometric counting. A significant advantage is the speed of the analysis, returning results in days rather than months at the highest level of sensitivity. The performance of ICPMS can depend sensitively on the chemical processing of the sample. For the Majorana project, R&D has been pursued to greatly improve ICPMS sensitivity for ^{232}Th in copper. A new chemical separation process, combined with ICPMS, has been developed.

Although assay by ICPMS has demonstrated adequate sensitivity, it has been hindered by high thorium and uranium backgrounds. With lead samples, these backgrounds have been shown to result from the sample preparation processes where attempts to isolate the analytes from the high concentration of lead using ion exchange were performed [Gri05]. Preliminary results with Cu samples indicate that the same is true for copper [Aal05a]. Other preparation methods employing electrodeposition have resulted in too much copper remaining in the sample solution and this in turn has limited the dynamic range of the instrument and obscured the analytes of interest.

A key point of this process is that a ^{229}Th tracer is added at the pg/g level. This tracer follows the sample throughout the subsequent steps and provides an absolute reference as to the chemical yield of the assay and thus the ultimate sensitivity should no signal above background be seen. The ratio of ^{229}Th to ^{232}Th is measured as the ratio of mass 229 and 232 signals in the instrument. Combining this ratio with the ^{229}Th tracer concentration gives the measured ^{232}Th value. If the mass 229 to mass 232 ratio is unperturbed from that seen in process blanks, an upper limit for ^{232}Th is obtained.

Current instrumental studies give a measurement background of about 10 μBq/kg for ^{232}Th, with a variance over several samples of about 1.2 μBq/kg [Hop05, Hop06a]. So a copper sample containing ^{232}Th at the 2-4 μBq/kg level can be measured as a change in the observed mass ratio. This research hopes to improve this sensitivity down to the 0.1-1 μBq/kg level.

Measurements with ICPMS can be complementary to assay via direct radiometric counting for other materials. For example, small chip resistors, FET silicon dies, and other small parts may be able to be assayed faster with ICPMS than with direct radiometric measurements. A small amount of chemistry and process development is typically needed to validate an ICPMS procedure for a new sample type.

4.3.4 Neutron Activation Analysis

The ^{238}U and ^{232}Th decay chains have half-lives on the order of a billion years, which limits measurements of these activities through direct radiometric counting techniques to sensitivities not much better than 1 mBq/kg due to limitations in sample size and self-shielding effects. With Neutron Activation Analysis (NAA), which is described in detail elsewhere [Soe72], the sample is activated through an exposure to neutrons from a research reactor. The short-lived ^{238}U and ^{232}Th activation products (^{239}Np and ^{233}Pa) are then counted with the radiometric techniques described above. Neutron Activation Analysis has achieved sensitivity levels of better than 10^{-15} g/g sensitivity levels in measuring trace amounts of ^{40}K, U, and Th in organic scintillators [Ang98, Hen99, Dju03]. This is three orders of magnitude more sensitive than the ICPMS measurements described above. Unfortunately, NAA will only work on samples with no long-lived activation products and NAA is essentially limited to testing teflon, plastics, and other hydrocarbons. Neutron Activation Analysis will not work with germanium or copper.

Due to the short half-lives of the activation products (12 hours if ^{40}K is being counted), transportation between the research reactor and the counting facility should be reasonably short. Since 2004, the LBNL low background counting group have been irradiating samples at the research reactor at the University of California, Davis (UCD) McClellan Nuclear Radiation Center (MNRC)[10], including teflon being used for the CUORE experiment [Smi04]. Samples irradiated at the MNRC

[10] `http://mnrc.ucdavis.edu/about.html`

could be transported by a licensed technician by government vehicle in about two hours or in less than twelve hours by next morning commercial delivery.

4.3.5 Surface Screening

Daughters from radon decay can accumulate on the surfaces of the sensitive items such as the copper cryostat and germanium detector itself. This can be reduced by storing these sensitive items in a low radon environment. However, ^{210}Pb, which is a daughter of ^{222}Rn, has a very long half-life (22.3 years) and can contaminate the surfaces prior to storage in a low radon environment. As described in Section 4.2, the goal for ^{210}Pb surface contamination gives an upper limit of 5×10^{-10} Bq/cm^2 for the copper cryostat and the germanium detectors.

The radiometric screening methods described above are insensitive to ^{210}Pb and its progeny ^{210}Bi and ^{210}Po, since these isotopes do not have any intense characteristic γ-ray lines. The primary method for screening for ^{210}Pb surface contamination is through the detection for the ^{210}Po 5.3 MeV alpha with either a gas proportional counter or liquid scintillator detector. The screening of surfaces for alpha contamination has been of interest to the integrated circuit (IC) industry, especially in regards to soft error upsets, and commercial gas proportional counters for surface counting are available. These commercial devices have typical sensitivities to the level of 5×10^{-7} Bq/cm^2 [Cla05] for a seven day counting time. Unfortunately, this sensitivity is insufficient for Majorana by three orders of magnitude.

The primary limitation of the commercial screening devices are the backgrounds that are intrinsic to the proportional counters and limited surface area of the sample ($< 10^3$ cm^2). As part of the R&D plan, the Majorana experiment is considering developing, in collaboration with a possible SBIR, large area (a few $\times 10^4$ cm^2) proportional counters made from ultra-pure electroformed copper. This detector should, in principle, achieve the required sensitivity of 5×10^{-10} Bq/cm^2 with a counting time the order of several weeks.

4.4 Demonstrating Cu Purity

The effort to produce ultra-high purity copper has been characterized by a two-pronged approach: the development of adequately sensitive assay methods and predictive modeling of the electrochemical system.

One of the greatest challenges for Majorana is demonstrating the necessary assay sensitivity level for the electroformed copper. There has been significant recent progress, our assay capability for ^{232}Th has recently improved from a sensitivity of a few hundred μBq/kg to 2-4 μBq/kg. But to meet our background goal, we need to achieve 0.3 μBq/kg in our materials. At the this level, we expect to become limited by Th in the ultra-pure reagents used to prepare the copper for analysis. However, these reagents can also be enhanced by repeated sub-boiling distillation. Indeed, use of high resolution ICPMS with specialized source nebulizers and very special sample preparation has yielded sensitivity to ^{232}Th an order of magnitude greater than we need [Arp02]. Some highlights of our program to demonstrate pure Cu are:

- In 1995, a limit of <9 μBq/kg for ^{232}Th was measured in IGEX electroformed copper. This was a 90 day radiometric measurement of ~10 kg Cu at 4000 mwe [Bro95].
- In November 2004, it was shown that the $CuSO_4$ bath used in electroforming could be purified extensively through recrystallization of the $CuSO_4$ starting material [Ree04].
- In April 2005, a limit of <8 μBq/kg for ^{232}Th was measured on MEGA copper. This was a 1 minute measurement of <1 g Cu with ICPMS [Aal05].
- Electroforming was shown in April 2005 to suppress ^{229}Th by a factor of >8000 [Aal05a].

- In May 2005, improved methods yielded assay sensitivities of 2-4 μBq/kg ^{232}Th. This was performed on reagents handled precisely as Cu eluent would be [Aal05].
- New sources of purer materials have been found for starting stock. Notably, a source of commercially electroformed copper tested to <12 μBq/kg for ^{232}Th has been located [Heu04b].
- In April 2006, samples prepared using electrochemical methods show levels of ^{232}Th that were essentially at background, indicating <2 μBq/Kg in Cu is likely attainable. Additional rejection rate information for Th and U was obtained [Hop06a].

In the absence of a current assay which is capable of the desired limits of detection, predictive modeling is playing an ever more important role. The predictive modeling has consisted of the empirical delineation of rejection rates for thorium and uranium in an electrochemical bath, as well as the application of thermodynamic equilibrium models, such as the Pitzer equations, to our electrochemical system.

Although there are a great number of variables in our electrochemical system (copper concentration, pH, potential, current, temperature, cathode/anode distance and surface area to name just a few), an effort has been made to create a model to describe the chemistry of the plating bath and thereby predict the amount of Th, U, or other contaminants in the final electrodeposited copper. Fluid dynamics, as well as kinetics and thermodynamics, must be considered to produce an accurate model.

Developing such a predictive model has proven to be difficult. The Nernst equation describes the tendency of an electrochemical reaction to go toward completion, and can be used to model the behavior of ions in an electrochemical cell when that cell is in equilibrium. As an approximation of the cell behavior, substitution of concentrations into the Nernst equation instead of activities is often done for convenience. This can lead to significant error in the calculated value of E_{cell}, especially in solutions of high ionic strength such as in our copper electroforming baths. The Debye-Hückel (DH) equation can be used to calculate the activity coefficient of an ion based on its charge (z), hydrated radius (α), and the ionic strength of the solution (μ). However, as ionic strength increases, activity is no longer a universal function of ionic strength, but is influenced by specific interactions between ions, leading to the necessity for more complex models. Activities calculated from the DH equation are only accurate for $\mu < 0.1$ M. The Davies equation, derived from the DH equation, is accurate to $\mu < 0.5$ M. However, as in our case many electroplating systems require solutions of ionic strength much greater than $\mu = 0.5$ M. Guggenheim further expanded the DH equation by adding a second virial coefficient (β_{MX}) to account for short-range forces between cation-anion pairs. The short-range forces between ions of like charge and three-ion interactions were assumed to be negligible. The set of equations that Pitzer developed includes the short range elements and has been widely used to model complex electrolyte solutions [Har80, Fel99].

The Pitzer model is often difficult to use because of the wide number of parameters needed even for a two-component system. However, as it is the preferred model for solutions of moderate to high ionic strength, calculated parameters and data fits are available in the published literature for a number of systems, including the $CuSO_4$-H_2SO_4-H_2O system [Bae93]. The Pitzer model has been applied to the aqueous thermodynamics of actinides in complex electrolytes, as well [Fel99].

The activity coefficient calculated from the Pitzer model for Th^{4+} in our system ultimately indicates that even less Th^{4+} should plate out than calculated using the concentration. Thus, it is evident that the deposition of Th at the half-cell potential of copper is not predominantly controlled by thermodynamics. The presence of thorium in electroplated copper seems to be primarily a result of high mass transport: thorium, unable to resist the flow of the copper ions toward the cathode, becomes encapsulated on its surface.

While developing predictive models, we have empirically determined the amount of Th in the bulk bath that deposits in copper for a set of conditions. We have defined the rejection rate as the number of impurity ions reduced at the cathode per total number of impurity ions in solution at

a given concentration. The Th/U rejection rates at a bath concentration of 1000 ng/ml have been demonstrated to be roughly 1 in 1000 [Hop06a]. Thermodynamics is playing a reduced role in the deposition of thorium at these concentrations since the existing models predict it to be many orders of magnitude greater. Minimizing the mass action effect by plating copper under current-limited conditions may bring the behavior of our system back under thermodynamic control, allowing for the simulation of contaminant behavior via application of the Pitzer equations.

To extend our understanding of electrochemical behavior to provide data so that we may modify existing models, we intend to determine the rejection rates at lower concentrations of Th. Experiments using ^{228}Th as a tracer have been developed. These investigations are underway to add known quantities of ^{228}Th to the bulk electroplating solution and the resulting electrodeposited copper will undergo radioassay to determine the amount of ^{228}Th co-deposited with the copper. This work will be performed at pg to ng concentration levels in the electrochemical bath, resulting in measurable quantities of <0.01 pg Th/g of electrodeposited copper. This is roughly two orders of magnitude lower than the Majorana target. We intend to eventually extend this work to other species which exhibit significantly different E_{cell} values such as ^{60}Co in order to develop a model which will comprehensively allow us to determine what concentrations of electrochemical bath contaminant species should be of concern.

Calculation of the rejection rates for thorium and uranium and other predictive efforts will not only afford insight into the behavior of these target contaminants during electrodeposition, but will also provide guidelines for plating parameters and bath composition at the production level. The concentration of impurities in the plating bath increases as more and more copper is plated, and our rejection rates will allow us to determine the point at which contamination is too great to plate copper of the desired purity during Majorana copper production activities.

4.5 Demonstrating Cable Purity

The mass of cable required to instrument our detector is highly dependent upon the cable design. Previous experiments have used specially fabricated or selected shielded coaxial cables to readout the signals from the crystals and from the front-end FETs. The measured activities of these cables when coupled with the total mass of material will likely not be of sufficient cleanliness to meet Majorana's needs. Although the cable has to meet certain mechanical and electrical specifications, it seems likely that different acceptable designs can be reduced in mass by a factor of 10 or more. Since the acceptable level of activity scales with the cable mass, it is the total activity that is the critical parameter.

The collaboration is examining several alternative flex cable based designs. We are considering several different plastic backing materials. Although Kapton (polyimide) is the typical backing of choice, commercial venders also offer other plastics such as Polyethylenenapthalate (PEN) and Polyethylene Terphtalate (PET). The GERDA collaboration has recently studied the activities of these materials and has found that the PEN material is significantly cleaner (by several orders of magnitude) than the PET or Kapton material.

We intend to build on these studies and through direct counting techniques we will identify candidate material for cable fabrication. We will test various cable designs that can incorporate the cleanest materials. We recognize that the cable design requires significant study and it is a high priority R&D item.

4.6 Sensitivity of the Majorana Experiment

In the presence of a positive signal, the half-life of $0\nu\beta\beta$ decay of ^{76}Ge atoms can be derived from the following formula:

$$T_{1/2} = \frac{\ln(2) \times atoms \times time}{decays}$$

However, in the limiting case where no decays can be identified, the quantity *decays* is replaced by a statistical estimation of variance in the background signals, B.

$$T_{1/2} > \frac{\ln(2) \times atoms \times time}{\sqrt{\int B_i(t) \cdot dt}}$$

Here, the various background rates, B_i in the region of interest (ROI) are summed.

For the limits quoted here, there are two modifications to the above equations. One is that we include the efficiency for detection of the signal. The other is that the equation is modified by replacing the square root with the 90% Feldman-Cousins upper limit [Fel98]. While this formula is more complicated than those frequently shown to describe the relationship of background to half-life, it is still a simplification, as the background rate in Ge may arise from several sources, and has significant uncertainty. In addition, some of the backgrounds we expect, particularly ^{68}Ge, have fairly modest half-lives and will contribute in a complex way (buildup and decay) as new crystals are added.

To calculate the sensitivity of the 120-kg Majorana experiment, we used the background model and reference detector design presented above, with the exception that we based our calculations on our goal background of 1 count/ROI/t-y.[11] We assumed 5 years of live-time running with the full 120-kg detector[12] and that we will use granularity, pulse-shape analysis, segmentation, event reconstruction and time correlation analyses to reduce backgrounds. The anticipated energy resolution is 0.16% FWHM at 2039 keV (the endpoint energy). The analysis that is done compares the measured number of counts in a region-of-interest of width 2.8σ (2037-41 keV). The efficiency for observing neutrinoless double-beta decay includes acceptance factors for the energy region-of-interest (83.8%), analysis cuts (pulse shape discrimination + segmentation, 84%) and time correlations ($\sim$100%).

Under these assumptions, the Majorana 120 kg experiment expects to set a limit on the half-life for neutrinoless double-beta decay of $\sim 7 \times 10^{26}$ years at the 90% confidence level. This corresponds to an exposure of 516 kg-years of ^{76}Ge. Using the Rodin RQRPA calculation this translates into an effective neutrino mass upper limit of 90 meV. Figure 4.4 shows a calculation of the sensitivity of Majorana as a function of exposure under the assumption of different backgrounds in the ROI.

For the best fit Klapdor-Kleingrothaus result ($T_{1/2} = 1.19 \times 10^{25}$ y), after 5.0 years of live-time we would expect to observe a mean of 140 neutrinoless double-beta decay events, with less than half a background event expected for our assumed background model. This would give a measurement with statistical precision better than 10%. The estimated contributions to the $\sim$5% systematic error are listed in Table 3.6. In the event of no observed signal events and less than one expected background event, the Klapdor-Kleingrothaus result would be ruled out at the 4.2 sigma level, which is the level of significance above zero that Klapdor-Kleingrothaus states for the signal.

4.7 Current Majorana Simulation Efforts

The Majorana collaboration is actively performing more detailed simulation studies of the Majorana Reference Design, using the Majorana-Gerda simulation package, MaGe, described in Section 3.11. These simulations are using more detailed geometry and component information than were available in our early simulations, used to estimate the backgrounds presented in Section 4.2.

The main task of the simulation during the proposal phase of Majorana is to estimate the contamination in the ROI from all the potential background sources. It also has to estimate the efficiency of reducing these background using the different analysis cuts described in Section 4.1.

[11] As we have refined our reference design and updated our background model the total estimated background has fluctuated. We believe that we are close to achieving our target background of 1 count/ROI/t-y and hence use this background level in our sensitivity calculations.

[12] An enrichment of 86% implies a total mass of 103 kg of ^{76}Ge

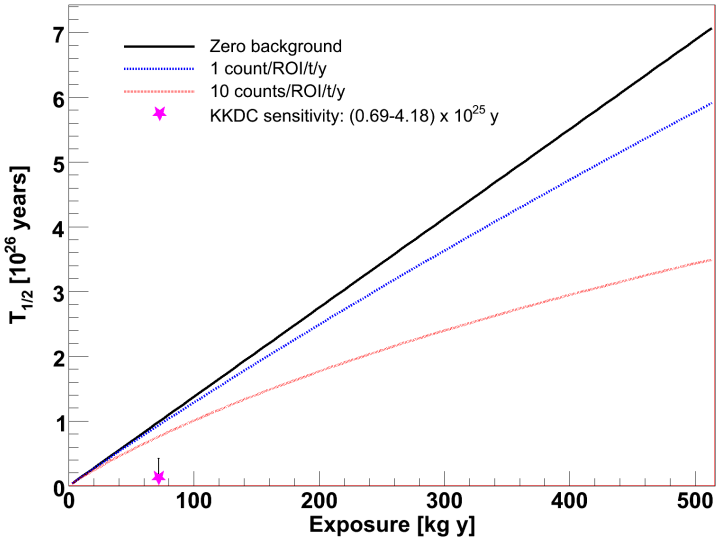

Figure 4.4: Majorana sensitivity at 90% C.L. for the half-life of ^{76}Ge $0\nu\beta\beta$ as a function of exposure. Three different background models are shown, zero background, our goal of 1 count/ROI/t-y, and 10 cnts/ROI/t-y.

This information will be used to determine acceptable levels of contamination in various detector components. The simulation activities can be grouped as follows:

4.7.1 Radioactive Backgrounds in the Bulk of Detector Parts and Shields

Radioactive contamination in the bulk of detector components contribute primarily to the background in the ROI by the gamma-rays these decays produce. Majorana has undertaken an extensive simulation effort to systematically simulate and categorize the detector response to many different radioactive isotopes in all detector parts. This simulated dataset will serve other functions as well. For example, it would provide a background estimate required to extract the $2\nu\beta\beta$ spectra. The list of simulated backgrounds is extensive and includes isotopes such as ^{214}Bi, ^{208}Tl, ^{68}Ge, ^{60}Co, and ^{56}Co in the crystals, support structures, cryostat and shield. The efficiency of segmentation and PSD for rejecting background are also estimated. Figure 4.5 shows a typical simulated spectra. Figure 4.6 shows a comparison of the different crystal segmentation schemes considered for Majorana. This systematic study is completed, although it will be continuously modified and updated as the Majorana design grows in detail and when a full-pulse-shape simulation package becomes available.

4.7.2 Alpha Sources on Surfaces

Alpha emitters on detector surfaces near crystals and on the crystal surfaces themselves are a potential source of backgrounds. The MaGe collaboration has developed a surface-sampler that samples points uniformly on an arbitrarily shaped surface; a crucial tool for performing surface alpha contamination simulations. Shown in Figure 4.7 is a spectrum from an n-type detector with an α peak at 5.3 MeV from ^{210}Po compared with a simulation from MaGe.

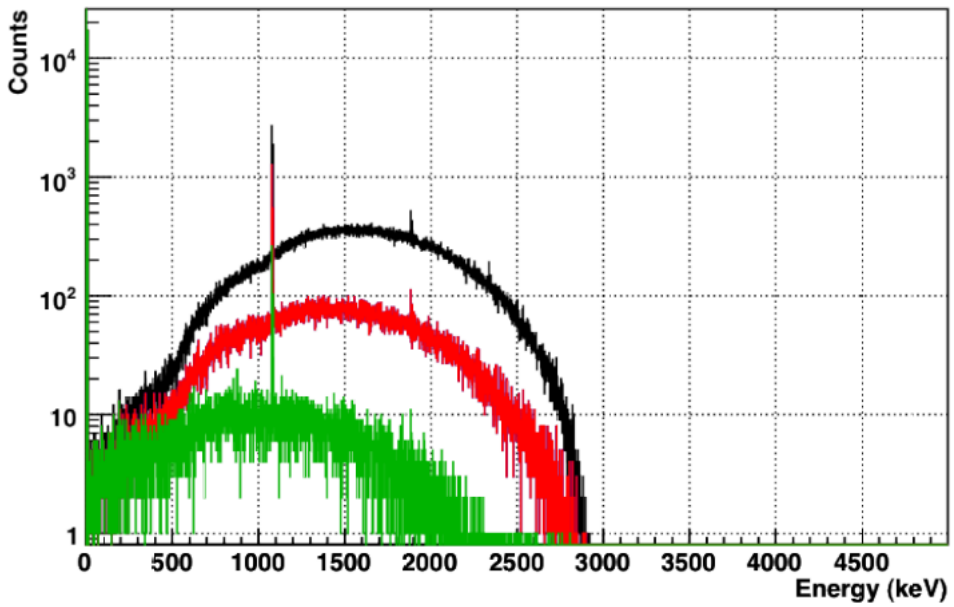

Figure 4.5: Example spectra of simulated ^{68}Ge decays in one of the outer crystals. The black spectra is a histogram of the sum of energy deposits in each crystal for each event, the red are events that have only one crystal hits and the green are one crystal hits with an radial PSD cut of 4 mm.

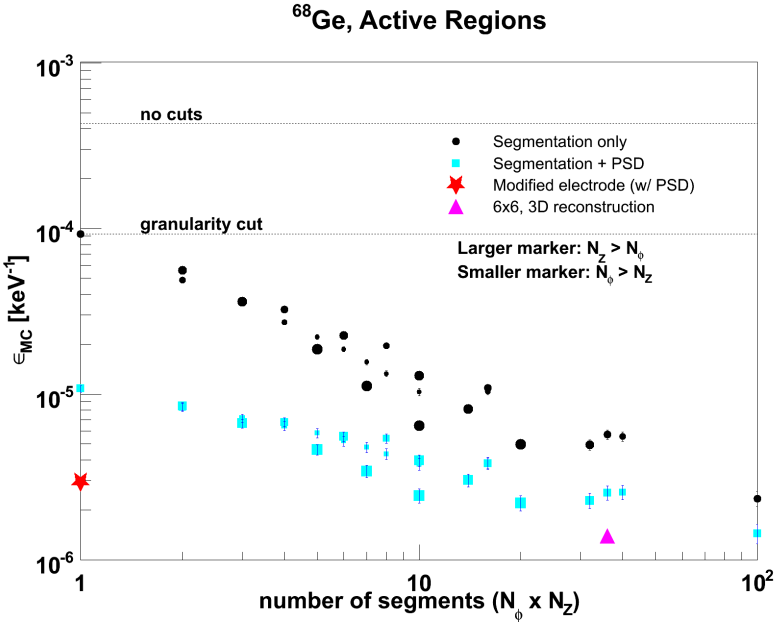

Figure 4.6: Comparison of Monte Carlo efficiencies (ϵ_{MC}) for decays of ^{68}Ge inside the crystals to give a hit in the ROI, in units keV^{-1}, for different detector designs and segmentation schemes, with and without radial PSD. Vertical error bars are statistical uncertainties in the simulations. The marker size signifies for a given number of segments whether there are more z-segments (larger markers) or ϕ-segments (smaller markers).

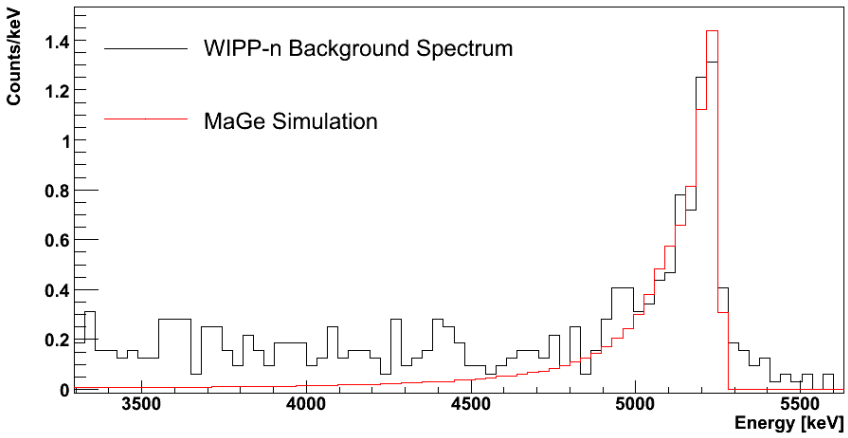

Figure 4.7: Comparison of a surface α peak from an n-type detector with simulation.

4.7.3 Muon-Induced Neutrons

Recent work [Mei05] has shown that hard neutrons from cosmic-ray muons at depth could be a significant source of background. This is a complex simulation task, and the detector response to these neutrons is sensitive to the geometry and materials used in the detector. The Majorana collaboration has a undertaken an systematic study of these backgrounds in the Reference Design using the MaGe-Geant4 package. Initial work has been focused on verifying that MaGe can accurately reproduce the neutron spectra from muon and electron beam experiments, as well as simulate the response of known detectors to neutrons. These projects are nearing completion and indicate that Geant4 would work, but may require modification.

4.7.4 Pulse-Shape Analysis

To date we have simulated pulse shape discrimination capabilities of different detector designs using a somewhat heuristic approach in which cuts are made on the spatial distribution of simulated energy depositions among crystal segments. We are in the process of implementing the generation of pulse shapes within MaGe itself by calculating the electric field and weighting potentials within the crystals, and simulating charge collection and the electronics chain, including noise sources. The simulated pulses will then be analyzed using the same signal processing techniques that will be employed on data to obtain more robust predictions of the rejection factors achievable with PSA. This effort draws from experience in performing such simulations by the GRETINA collaboration, although a second, independent code base is also under development.

4.8 Summary

The 120-kg Majorana detector will allow us to answer several outstanding issues in double-beta decay. In five years of running it will either establish the Klapdor-Kleingrothaus claim of double-beta decay conclusively, or will allow us to improve lifetime limits significantly, from the current level of about 2×10^{25} years to about 7×10^{26} years. Technical risks in double-beta decay experiments are primarily due to backgrounds, and our pursuit of multiple techniques- materials processing, shielding, a deep underground location, excellent energy resolution, pulse-shape analysis, segmentation, granularity, and time correlations - allow us to set a better limit and to limit risks in the proposed experiment. In addition, if neutrinoless double-beta decay is not observed, it will have provided us with experience

and data with which to validate these techniques and to optimize them so that the background can be decreased even more for future, larger experiments. The phased approach we are following is very similar to that proposed in the APS neutrino study [Fre04].

References

[Aal96] C. E. Aalseth et al., Nucl. Phys. B (Proc. Suppl.) **48**, 223 (1996).

[Aal00] C. E. Aalseth, Ph.D. thesis, University of South Carolina (2000).

[Aal02a] C. E. Aalseth, F. T. Avignone, R. L. Brodzinski, S. Cebrian, E. Garcia, D. Gonzalez, W. K. Hensley, I. G. Irastorza, I. V. Kirpichnikov, A. A. Klimenko, et al., Physical Review D **65**, 092007 (2002).

[Aal05] C. E. Aalseth, *Material purity: Ultra low-background, icpms assay, and lead surface preparation for the majorana project* (2005), US - Japan Seminar on Double Beta Decay and Neutrino Mass Meeting, Maui, HI.

[Aal05a] C. E. Aalseth and E. W. Hoppe (2005), unpublished.

[Abt04] I. Abt et al. (2004), `hep-ex/0404039`.

[Abu00] R. Abusaidi et al. (CDMS), Physical Review Letters **84**, 5699 (2000), `astro-ph/0002471`.

[Ago03] S. Agostinelli et al. (GEANT4), Nuclear Instruments and Methods in Physics Research A **506**, 250 (2003).

[Aha05] B. Aharmim et al. (SNO), Phys. Rev. **C72**, 055502 (2005), `nucl-ex/0502021`.

[Ahm01] Q. R. Ahmad et al. (SNO), Physical Review Letters **87**, 071301 (2001), `nucl-ex/0106015`.

[Ahm04] S. N. Ahmed et al. (SNO), Phys. Rev. Lett. **92**, 181301 (2004), `nucl-ex/0309004`.

[AID06] Abstract Interfaces for Data Analysis, http://aida.freehep.org/, last accessed Nov 15 2006.

[AKA06] The KamLAND Collaboration, private communication (2006).

[Aki05] D. Akimov et al., Nucl. Phys. Proc. Suppl. **138**, 224 (2005).

[Ale00] A. Alessandrello et al., Physics Letters B **486**, 13 (2000).

[All06] J. Allison et al., IEEE Transactions on Nuclear Science **53** (2006).

[Ams06] J. F. Amsbaugh et al., in preparation for submission to NIM-A (2006).

[Ang98] G. Angloher et al., Journal of Radioanalytical and Nuclear Chemistry **234**, 37 (1998).

[Apo99] M. Apollonio et al. (CHOOZ), Physics Letters B **466**, 415 (1999), `hep-ex/9907037`.

[Ara04] T. Araki et al. (KamLAND), Phys. Rev. Lett. **94**, 081801 (2005), `hep-ex/0406035`.

[Arn98] R. Arnold, C. Augier, J. Baker, A. Barabash, D. Blum, V. Brudanin, A. J. Caffrey, J. Campagne, E. Caurier, and D. Dassi, Nuclear Physics A **636**, 209 (1998).

[Arn04] C. Arnaboldi et al. (CUORE), Nucl. Instrum. Meth. **A518**, 775 (2004), `hep-ex/0212053`.

[Arp02] C. Arpesella, H. O. Back, M. Balata, T. Beau, G. Bellini, J. Benziger, S. Bonetti, A. Brigatti, C. Buck, B. Caccianiga, et al. (BOREXINO), Astroparticle Physics **18**, 1 (2002).

[Art93] V. A. Artemev et al., Journal of Experimental and Theoretical Physics Letters **58**, 262 (1993).

[Ash04] Y. Ashie et al. (Super-Kamiokande), Phys. Rev. **D71**, 112005 (2005), `hep-ex/0501064`.

[Aun96] M. Aunola and J. Suhonen, Nuclear Physics A **602**, 133 (1996).

[Aun98] M. Aunola and J. Suhonen, Nuclear Physics A **643**, 207 (1998).

[Avi88] F. T. Avignone and R. L. Brodzinski, Progress in Particle and Nuclear Physics **21**, 99 (1988).

[Avi91] F. T. Avignone et al., Physics Letters B **256**, 559 (1991).

[Avi92] F. T. Avignone et al., Nuclear Physics B Proceedings Supplements **28**, 280 (1992).

[Avi94] F. T. Avignone, Progress in Particle and Nuclear Physics **32**, 223 (1994).

[Avi98] F. T. Avignone et al. (SOLAX), Physical Review Letters **81**, 5068 (1998), astro-ph/9708008.

[Avi99] F. T. Avignone et al. (SOLAX), Nuclear Physics B Proceedings Supplements **72**, 176 (1999).

[Avi02] F. T. Avignone and G. S. King (2002), Prepared for 4th International Workshop on the Identification of Dark Matter (IDM 2002), York, England, 2-6 Sep.

[Avi05] F. T. Avignone, G. S. King, and Y. Zdesenko, New Journal of Physics **7**, 6 (2005).

[Bac02] H. O. Back et al., Physics Letters B **525**, 29 (2002).

[Bae93] C. F. Baes, E. J. Reardon, and B. A. Moyer, J. Phys. Chem. **97**, 12343 (1993).

[Bah03] J. N. Bahcall and C. Pena-Garay, Journal of High Energy Physics **11**, 004 (2003), hep-ph/0305159.

[Bal01] E. A. Baltz and P. Gondolo, Physical Review Letters **86**, 5004 (2001), hep-ph/0102147.

[Bar90] A. S. Barabash, Journal of Experimental and Theoretical Physics Letters **51**, 207 (1990).

[Bar94] A. S. Barabash, Journal of Experimental and Theoretical Physics Letters **59**, 677 (1994).

[Bar95] A. S. Barabash et al., Physics Letters B **345**, 408 (1995).

[Bar99] A. S. Barabash, V. I. Umatov, R. Gurriaran, F. Hubert, and P. Hubert, Physics of Atomic Nuclei **62**, 2039 (1999).

[Bar00] A. S. Barabash, Czechoslovak Journal of Physics **50**, 447 (2000).

[Bar01] A. S. Barabash (2001), Prepared for International Workshop on Technique and Application of Xenon Detectors, Kashiwa, Japan, 3-4 Dec 2001.

[Bar02] V. Barger, S. L. Glashow, D. Marfatia, and K. Whisnant, Physics Letters B **532**, 15 (2002), hep-ph/0201262.

[Bar04] A. S. Barabash, Physics of Atomic Nuclei **67**, 438 (2004).

[Bar05] A. S. Barabash, Physics of Atomic Nuclei **68**, 414 (2005).

[Barb99] C. Barbero, F. Krmpotic, A. Mariano, and D. Tadic, Physics Letters B **445**, 249 (1999), nucl-th/9810072.

[Bat01] M. Battaglia et al., European Physical Journal C **22**, 535 (2001), hep-ph/0106204.

[Bau01] L. Baudis et al., Physical Review D **63**, 022001 (2001), astro-ph/0008339.

[Bed97] V. A. Bednyakov, S. G. Kovalenko, H. V. Klapdor-Kleingrothaus, and Y. Ramachers, Zeitschrift für Physik A **357**, 339 (1997), hep-ph/9606261.

[Bed99] P. F. Bedaque, M. J. Savage, R. Seki, and U. van Kolck (1999).

[Bel99] P. Belli et al., Physics Letters B **465**, 315 (1999).

[Bel02] P. Belli, R. Cerulli, N. Fornengo, and S. Scopel, Physical Review D **66**, 043503 (2002), hep-ph/0203242.

[Ben03] C. L. Bennett et al., The Astrophysical Journal Supplement Series **148**, 1 (2003), astro-ph/0302207.

[Ber93] T. Bernatowicz, J. Brannon, R. Brazzle, R. Cowsik, C. Hohenberg, and F. Podosek, Physical Review C **47**, 806 (1993).

[Ber01] L. Bergstrom, Reports on Progress in Physics **63**, 793 (2000), hep-ph/0002126.

[Bob01] A. Bobyk, W. A. Kaminski, and F. Simkovic, Physical Review C **63**, 051301 (2001), nucl-th/0012010.

[Boe01] F. Boehm et al., Physical Review D **64**, 112001 (2001), hep-ex/0107009.

[Bos06] A. Boston, Private Communication (2006).

[Bot00] A. Bottino, F. Donato, N. Fornengo, and S. Scopel, Physical Review D **62**, 056006 (2000), hep-ph/0001309.

[Bot01] A. Bottino, F. Donato, N. Fornengo, and S. Scopel, Physical Review D **63**, 125003 (2001), hep-ph/0010203.

[Bot03] A. Bottino, N. Fornengo, and S. Scopel, Physical Review D **67**, 063519 (2003), hep-ph/0212379.

[Bro84] R. Brodzinski, D. Brown, J. Evans, W. Hensley, J. Reeves, N. Wogman, F. Avignone, H. Miley, and R. Moore, Fifth International Conference on Nuclear Methods in Environmental and Energy Research p. 118 (1984).

[Bro85a] R. Brodzinski, D. Brown, J. Evans, W. Hensley, J. Reeves, N. Wogman, F. Avignone, and H. Miley, AIP Conference Proceedings **126**, 50 (1985a).

[Bro85b] R. Brodzinski, D. Brown, J. Evans, W. Hensley, J. Reeves, N. Wogman, F. Avignone, and H. Miley, Nuclear Instruments and Methods in Physics Research A **239**, 207 (1985b).

[Bro95] R. Brodzinski, H. Miley, J. Reeves, and F. Avignone, Journal of Radioanalytical and Nuclear Chemistry **193**, 61 (1995).

[Bru97] R. Brun and F. Rademakers, Nuclear Instruments and Methods in Physics Research A **389**, 81 (1997).

[Buc00] W. Buchmuller and M. Plumacher, International Journal of Modern Physics A **15**, 5047 (2000), hep-ph/0007176.

[Cap05] S. Capelli (CUORICINO) (2005), hep-ex/0505045.

[Cau96] E. Caurier, F. Nowacki, A. Poves, and J. Retamosa, Physical Review Letters **77**, 1954 (1996).

[Cau99] E. Caurier, F. Nowacki, A. Poves, and J. Retamosa, Nuclear Physics A **654**, 973c (1999).

[Ceb01] S. Cebrian et al., Astroparticle Physics **14**, 339 (2001), `hep-ph/9912394`.

[Civ03] O. Civitarese and J. Suhonen, Nuclear Physics A **729**, 867 (2003), `nucl-th/0208005`.

[Cla05] B. Clark, *Low alpha materials and metrology in the ic industry: Current status and future requirements* (2005), presented at the Synergies in Low-Background, Ultra-Sensitive Radiation Techniques Workshop, University of Minnesota, July 25-26, 2005, http://www.hep.umn.edu/lbcf/workshop/.

[Col92] J. I. Collar, Ph.D. thesis, University of South Carolina (1992).

[Col99] J. I. Collar, Physical Review D **59**, 063514 (1999), `astro-ph/9808058`.

[Col00] J. I. Collar et al., New Journal of Physics **2**, 14 (2000), `astro-ph/0005059`.

[Cor00] A. Corsetti and P. Nath, Physical Review D **64**, 125010 (2001), `hep-ph/0003186`.

[Cre98] R. J. Creswick et al., Physics Letters B **427**, 235 (1998), `hep-ph/9708210`.

[Dan00] F. A. Danevich, A. S. Georgadze, V. V. Kobychev, B. N. Kropivyansky, A. S. Nikolaiko, O. A. Ponkratenko, V. I. Tretyak, S. Y. Zdesenko, Y. G. Zdesenko, P. G. Bizzeti, et al., Physical Review C **62**, 045501 (2000).

[Deb01] L. De Braeckeleer, M. Hornish, A. S. Barabash, and V. I. Umatov, Physics of Atomic Nuclei **63**, 1214 (2000).

[Des97] A. De Silva, M. K. Moe, M. A. Nelson, and M. A. Vient, Physical Review C **56**, 2451 (1997), `nucl-ex/9706005`.

[Des05] M. Descovich, I. Y. Lee, P. Fallon, M. Cromaz, A. O. Macchiavelli, D. C. Radford, K. Vetter, R. M. Clark, M. A. Deleplanque, F. S. Stephens, et al., Nuclear Instruments and Methods in Physics Research A **553**, 535 (2005).

[Dju03] D. Djurcic, D. Glasgow, L.-W. Hu, R. D. McKeown, A. Piepke, R. Swinney, and B. Tipton, Nuclear Instruments and Methods in Physics Research A **507**, 680 (2003).

[Doc06] http://l10n.kde.org/docs/markup, last accessed Nov 15 2006.

[Dou01] G. Douysset, T. Fritioff, C. Carlberg, I. Bergstrom, and M. Bjorkhage, Physical Review Letters **86**, 4259 (2001).

[Dox06] Doxygen documentation system, http://www.doxygen.org, last accessed Nov 15 2006.

[Dru86] A. K. Drukier, K. Freese, and D. N. Spergel, Physical Review D **33**, 3495 (1986).

[Dru92] A. K. Drukier et al., Nuclear Physics B Proceedings Supplements **28A**, 293 (1992).

[Ebe01] J. Eberth et al., Progress in Particle and Nuclear Physics **46**, 389 (2001).

[Eds97] J. Edsjo and P. Gondolo, Physical Review D **56**, 1879 (1997), `hep-ph/9704361`.

[Egu03] K. Eguchi et al. (KamLAND), Physical Review Letters **90**, 021802 (2003), `hep-ex/0212021`.

[Eji91] H. Ejiri et al., Journal of Physics G **17**, S155 (1991).

[Eji96] H. Ejiri et al., Physical Review C **63**, 065501 (2001).

[Eji04] H. Ejiri, Czechoslovak Journal of Physics **54**, B299 (2004).

[Eji05] H. Ejiri, Journal of the Physical Society of Japan **74**, 2101 (2005).

[Ell87] S. R. Elliott, A. A. Hahn, and M. K. Moe, Physical Review Letters **59**, 2020 (1987).

[Ell91] S. R. Elliott, M. K. Moe, M. A. Nelson, and M. A. Vient, Journal of Physics G **17**, S145 (1991).

[Ell92] S. R. Elliott, A. A. Hahn, M. K. Moe, M. A. Nelson, and M. A. Vient, Physical Review C **46**, 1535 (1992).

[Ell93] S. R. Elliott, M. K. Moe, M. A. Nelson, and M. A. Vient, Nuclear Physics B Proceedings Supplements **31**, 68 (1993).

[Ell97] J. R. Ellis, T. Falk, K. A. Olive, and M. Schmitt, Physics Letters B **413**, 355 (1997), `hep-ph/9705444`.

[Ell00] J. R. Ellis, T. Falk, G. Ganis, and K. A. Olive, Physical Review D **62**, 075010 (2000), `hep-ph/0004169`.

[Ell01a] J. R. Ellis, A. Ferstl, and K. A. Olive, Space Science Reviews **100**, 235 (2002), `hep-ph/0106148`.

[Ell01b] J. R. Ellis, A. Ferstl, and K. A. Olive, Physical Review D **63**, 065016 (2001), `hep-ph/0007113`.

[Ell02] S. R. Elliott and P. Vogel, Annual Review of Nuclear and Particle Science **52**, 115 (2002).

[Ell02a] J. R. Ellis, J. L. Feng, A. Ferstl, K. T. Matchev, and K. A. Olive, European Physical Journal C **24**, 311 (2002a), `astro-ph/0110225`.

[Ell02b] J. R. Ellis, A. Ferstl, and K. A. Olive, Physics Letters B **532**, 318 (2002b), `hep-ph/0111064`.

[Ell04] S. R. Elliott and J. Engel, Journal of Physics G **30**, 183 (2004).

[Eug03] K. Eguchi et al. (KamLAND), Physical Review Letters **90**, 021802 (2003), `hep-ex/0212021`.

[Far96] J. Farine, Ph.D. thesis, Neuchatel University (1996).

[Fel98] G. J. Feldman and R. D. Cousins, Phys. Rev. D **57**, 3873 (1998).

[Fel99] A. R. Felmy and D. Rai, J. Solution Chem. **28**, 533 (1999).

[Fer02] F. Feruglio, A. Strumia, and F. Vissani, Nuclear Physics B **637**, 345 (2002).

[Fio67] E. Fiorini, A. Pullia, G. Bertolini, F. Cappellani, and G. Restelli, Physics Letters B **25**, 602 (1967).

[Fir48] E. L. Fireman, in *Proceedings of the American Physical Society* (1948), vol. 74, p. 1238.

[Fir52] E. L. Fireman and D. Schwarzer, Physical Review **86**, 451 (1952).

[Fra04] G. de France, European Physical Journal A **20**, 59 (2004).

[Fre92] K. Freese, J. A. Frieman, and A. Gould, Physical Review D **37**, 3388 (1988).

[Fre04] S. J. Freedman and B. Kayser (APS Multidivisional Neutrino Study) (2004), `physics/0411216`.

[Fuk86] M. Fukugita and T. Yanagida, Physics Letters B **174**, 45 (1986).

[Fuk02] S. Fukuda et al. (Super-Kamiokande), Physics Letters B **539**, 179 (2002), hep-ex/0205075.

[Gai01] R. J. Gaitskell (2001), astro-ph/0106200.

[Gai03] R. Gaitskell and V. Mandic, http://dmtools.brown.edu (2005).

[Goo85] M. W. Goodman and E. Witten, Physical Review D **31**, 3059 (1985).

[Gra05] G. Gratta, EXO Presentation to NuSAG (2005).

[Gri92] A. Griffiths and P. Vogel, Physical Review C **46**, 181 (1992).

[Gri05] P. Grinberg, S. Willie, and S. R. E., Anal. Chem. **77**, 2432 (2005).

[Gun97] M. Gunther et al., Physical Review D **55**, 54 (1997).

[Hag02] K. Hagiwara et al. (Particle Data Group), Physical Review D **66**, 010001 (2002).

[Hai03] T. Haines, Private Communication (2005).

[Har80] C. E. Harvie and J. H. Weare, Geochim. Cosmochim. Acta. **44**, 981 (1980).

[Har02] H. L. Harney (2001), hep-ph/0205293.

[Hax84] W. C. Haxton and G. J. Stephenson, Progress in Particle and Nuclear Physics **12**, 409 (1984).

[Hax06] W. Haxton, Private Communication (2006).

[Hen99] R. Hentig et al., Nuclear Physics B Proceedings Supplements **78**, 115 (1999).

[Heu95] G. Heusser, Annual Review of Nuclear and Particle Science **45**, 543 (1995).

[Heu04] G. Heusser, presentation at LRT 2004 at SNO (2004).

[Heu04b] G. Heusser et al., Proc. of Intern. Conf. Isotop. Environm. Studies Aquatic Forum 2004, Monte-Carlo, Monaco (2004).

[Hir94] M. Hirsch, K. Muto, T. Oda, and H. V. Klapdor-Kleingrothaus, Zeitschrift für Physik A **347**, 151 (1994).

[Hir96a] M. Hirsch, H. V. Klapdor-Kleingrothaus, and S. G. Kovalenko, Physical Review D **54**, 4207 (1996a), hep-ph/9603213.

[Hir96b] M. Hirsch, H. V. Klapdor-Kleingrothaus, and S. G. Kovalenko, Physical Review D **53**, 1329 (1996b), hep-ph/9502385.

[Hir00] M. Hirsch, J. C. Romao, and J. W. F. Valle, Physics Letters B **486**, 255 (2000), hep-ph/0002264.

[Hon02] M. Honma, T. Otsuka, B. A. Brown, and T. Mizusaki, Nuclear Physics A **704**, 134 (2002).

[Hop05] E. W. Hoppe, O. T. F. III, and J. H. Reeves, *Electroformation of ultra high purity copper and material assay using isotopic dilution icp/ms* (2005), presented at the Northwest Regional American Chemical Society Conference, Fairbanks, Alaska, June, 2005.

[Hop06a] E. W. Hoppe, C. E. Aalseth, R. Brodzinski, A. R. Day, O. T. Farmer, T. W. Hossbach, J. I. McIntyre, H. S. Miley, E. E. Mintzer, A. Seifert, et al. (2006), Accepted for publication in J. Nuc. Anal. Chem.

[How04] M. Howe, G. Cox, P. Harvey, F. McGirt, K. Rielage, J. Wilkerson, and J. Wouters, IEEE Transactions on Nuclear Science **51**, 878 (2004).

[Ing50] M. G. Inghram and J. H. Reynolds, Physical Review **78**, 822 (1950).

[Ira00] I. G. Irastorza et al., Nuclear Physics B Proceedings Supplements **87**, 102 (2000), `astro-ph/9912491`.

[Jam75] F. James and M. Roos, Computer Physics Communications **10**, 343 (1975).

[Jun96] G. Jungman, M. Kamionkowski, and K. Griest, Physics Reports **267**, 195 (1996), `hep-ph/9506380`.

[Kal52] M. I. Kalkstein and W. F. Libby, Physical Review **85**, 368 (1952).

[Kay82a] B. Kayser, Physical Review D **26**, 1662 (1982).

[Kay82b] B. Kayser and R. E. Shrock, Physics Letters B **112**, 137 (1982).

[Kaz04] K. Kazkaz, C. E. Aalseth, T. W. Hossbach, V. M. Gehman, J. D. Kephart, and H. S. Miley, IEEE Transactions on Nuclear Science **51**, 1029 (2004).

[Kir67a] T. Kirsten et al., Verlag der Zeitschrift für Naturforschung A **22**, 1783 (1967a).

[Kir67b] T. Kirsten, W. Gentner, and O. Schaeffer, Zeitschrift für Physik p. 202 (1967b).

[Kla01a] H. V. Klapdor-Kleingrothaus, H. Pas, and A. Y. Smirnov, Physical Review D **63**, 073005 (2001), `hep-ph/0003219`.

[Kla01b] H. V. Klapdor-Kleingrothaus, A. Dietz, L. Baudis, G. Heusser, I. V. Krivosheina, B. Majorovits, H. Paes, H. Strecker, V. Alexeev, A. Balysh, et al., European Physical Journal A **12**, 147 (2001a).

[Kla01c] H. V. Klapdor-Kleingrothaus, A. Dietz, H. L. Harney, and I. V. Krivosheina, Modern Physics Letters A **16**, 2409 (2001b).

[Kla01d] H. V. Klapdor-Kleingrothaus, Nuclear Physics B Proceedings Supplements **100**, 309 (2001), `hep-ph/0102276`.

[Kla02a] H. V. Klapdor-Kleingrothaus (2002), `hep-ph/0205228`.

[Kla02b] H. V. Klapdor-Kleingrothaus, A. Dietz, and I. Krivosheina, Foundations of Physics **32**, 1181 (2002).

[Kla04] H. V. Klapdor-Kleingrothaus, I. V. Krivosheina, A. Dietz, and O. Chkvorets, Physics Letters B **586**, 198 (2004).

[Kol90] E. W. Kolb and M. S. Turner (1990), Redwood City, USA: Addison-Wesley (1990) 547 p. (Frontiers in physics, 69).

[Kud01] V. A. Kudryavtsev et al., Astroparticle Physics **17**, 401 (2002), `hep-ex/0109013`.

[Law51] J. J. Lawson, in *Proceedings of the American Physical Society* (1951), vol. 81, p. 299.

[Lee77] B. W. Lee and S. Weinberg, Physical Review Letters **39**, 165 (1977).

[Lee03] I. Lee, M. Deleplanque, and K. Vetter, Reports on Progress in Physics **66**, 1095 (2003).

[Lew96] J. D. Lewin and P. F. Smith, Astroparticle Physics **6**, 87 (1996).

[Li82] L. F. Li and F. Wilczek, Physical Review D **25**, 143 (1982).

[Lue98] R. Luescher, J. Farine, F. Boehm, J. Busto, K. Gabathuler, G. Gervasio, H. E. Henrikson, V. Jörgens, K. Lou, A. Paić , et al., Physics Letters B **434**, 407 (1998).

[Mac89] R. Machleidt, Advances in Nuclear Physics **19**, 189 (1989).

[Mei05] D.-M. Mei and A. Hime, Physical Review D **73**, 053004 (2005), `astro-ph/0512125`.

[Mil90] H. S. Miley, R. L. Brodzinski, J. H. Reeves, F. T. Avignone, and J. I. Collar, Physical Review Letters **65**, 3092 (1990).

[Moh75] R. N. Mohapatra and J. C. Pati, Physical Review D **11**, 2558 (1975).

[Moh86] R. N. Mohapatra, Physical Review D **34**, 3457 (1986).

[Mue01] W. Mueller, J. Church, T. Glasmacher, D. Gutknecht, G. Hackman, P. Hansen, Z. Hu, K. Miller, and P. Quirin, Nuclear Instruments and Methods in Physics Research A **466**, 492 (2001).

[Mut89] K. Muto, E. Bender, and H. V. Klapdor, Zeitschrift für Physik A **334**, 177 (1989).

[Net02] C. B. Netterfield et al. (Boomerang), The Astrophysical Journal **571**, 604 (2002), `astro-ph/0104460`.

[NUSAG05] Neutrino Scientific Assessment Group (2005).

[Oga04] I. Ogawa et al., Nucl. Phys. **A730**, 215 (2004).

[Ohs02] T. Otsuka, Y. Utsuno, R. Fujimoto, B. Brown, M. Honma, and T. Mizusaki, European Physical Journal A **15**, 151 (2002).

[Osi01] A. Osipowicz et al. (KATRIN) (2001), `hep-ex/0109033`.

[P5RM06] The Particle Physics Project Prioritization Panel (P5) High Energy Physics Advisory Subpanel, *Particle physics roadmap*, available at http://www.science.doe.gov/hep/P5RoadmapfinalOctober2006.pdf, last accessed Nov 15, 2006 (2006).

[Pan96] G. Pantis, F. Simkovic, J. D. Vergados, and A. Faessler, Physical Review C **53**, 695 (1996), `nucl-th/9612036`.

[Pas02] S. Pascoli and S. T. Petcov, Physics Letters B **544**, 239 (2002), `hep-ph/0205022`.

[Pec77] R. D. Peccei and H. R. Quinn, Physical Review Letters **38**, 1440 (1977).

[Pec89] R. Peccei and E. . Jarlskog, C., p. 723 (1989), Advanced Series On Directions In High Energy Physics, 3.

[Pee93] P. J. E. Peebles (1993), Princeton, USA: Univ. Pr. (1993) 718 p.

[Pil99] A. Pilaftsis, International Journal of Modern Physics A **14**, 1811 (1999), `hep-ph/9812256`.

[Pos06] Object relational database management system, http://www.postgresql.org/, last accessed Nov 15 2006.

[Pov06] A. Poves, *Shell model calculations of the $0\nu\beta\beta$ decay* (2006), presented at the 2nd Symposium On Neutrinos and Dark Matter in Nuclear Physics (NDM06), Paris (http://events.lal.in2p3.fr/conferences/NDM06/).

[Pre03] G. Prezeau, M. Ramsey-Musolf, and P. Vogel, Physical Review D **68**, 034016 (2003), hep-ph/0303205.

[Pri88] J. R. Primack, D. Seckel, and B. Sadoulet, Annual Review of Nuclear and Particle Science **38**, 751 (1988).

[Pry02] C. Pryke et al., The Astrophysical Journal **568**, 46 (2002), astro-ph/0104490.

[QSN06] Sudbury Neutrino Observatory Collaboration, private communication (2006).

[Raf96] G. G. Raffelt (1996), Chicago, USA: Univ. Pr. (1996) 664 p.

[Ree04] J. Reeves (2004), unpublished.

[Rod03] V. A. Rodin, A. Faessler, F. Simkovic, and P. Vogel, Physical Review C **68**, 044302 (2003), nucl-th/0305005.

[Rod06] V. A. Rodin, A. Faessler, F. Simkovic, and P. Vogel, Nucl. Phys. **A766**, 107 (2006), nucl-th/0503063.

[Ros01] L. J. Rosenberg and K. A. van Bibber, Physics Reports **325**, 1 (2000).

[Sar05] X. Sarazin, Nuclear Physics B Proceedings Supplements **143**, 221 (2005), hep-ex/0412012.

[Sch82] J. Schechter and J. W. F. Valle, Physical Review D **25**, 2951 (1982).

[Scr05] H. C. Scraggs, C. J. Pearson, G. Hackman, M. B. Smith, R. A. E. Austin, G. C. Ball, A. J. Boston, P. Bricault, R. S. Chakrawarthy, R. Churchman, et al., Nuclear Instruments and Methods in Physics Research A **543**, 431 (2005).

[Sen75] G. Senjanovic and R. N. Mohapatra, Physical Review D **12**, 1502 (1975).

[Sik83] P. Sikivie, Physical Review Letters **51**, 1415 (1983).

[Sim97] F. Simkovic, J. Schwieger, M. Veselsky, G. Pantis, and A. Faessler, Physics Letters B **393**, 267 (1997), nucl-th/9612037.

[Sim99] F. Simkovic, G. Pantis, J. D. Vergados, and A. Faessler, Physical Review C **60**, 055502 (1999), hep-ph/9905509.

[Sim00] J. Simpson, F. Azaiez, G. deFrance, J. Fouan, J. Gerl, R. Julin, W. Korten, P. Nolan, B. Nyako, G. Sletten, et al., Acta Physica Hungarica New Series: Heavy Ion Physics **11**, 159 (2000).

[Sim01] F. Simkovic, M. Nowak, W. A. Kaminski, A. A. Raduta, and A. Faessler, Physical Review C **64**, 035501 (2001), nucl-th/0107016.

[Sim02] F. Simkovic and A. Faessler, Progress in Particle and Nuclear Physics **48**, 201 (2002), hep-ph/0112272.

[Sim05] J. Simpson, Journal of Physics G **31**, S1801 (2005).

[Smi03] A. R. Smith, D. L. Hurley, R. J. McDonald, and E. B. Norman, *Low background counting facilities* (2003), 2003 Annual Report of the Nuclear Science Division, Lawrence Berkeley National Laboratory.

[Smi04] A. R. Smith, R. J. McDonald, D. L. Hurley, and K. T. Lesko, *Low background facilities* (2004), 2004 Annual Report of the Nuclear Science Division, Lawrence Berkeley National Laboratory.

[Soe72] D. D. Soete, R. Gijbels, and J. Hoste, *Neutron Activation Analysis* (Wiley Interscience, London, New York, Sydney, Toronto, 1972).

[Spe03] D. N. Spergel et al. (WMAP), The Astrophysical Journal Supplement Series **148**, 175 (2003), `astro-ph/0302209`.

[Sre00] M. Srednicki, European Physical Journal C **15**, 143 (2000).

[Sta90] A. Staudt, K. Muto, and H. V. Klapdor-Kleingrothaus, Europhysics Letters **13**, 31 (1990).

[Ste01] P. Di Stefano (EDELWEISS), Astroparticle Physics **14**, 329 (2001).

[Sto94] S. Stoica, Physical Review C **49**, 2240 (1994).

[Sto00] S. Stoica and H. V. Klapdor-Kleingrothaus, European Physical Journal A **9**, 345 (2000), `nucl-th/0010106`.

[Sto01] S. Stoica and H. V. Klapdor-Kleingrothaus, Nuclear Physics A **694**, 269 (2001).

[Suh92] J. Suhonen, O. Civitarese, and A. Faessler, Nuclear Physics A **543**, 645 (1992).

[Suh98] J. Suhonen, Physics of Atomic Nuclei **61**, 1186 (1998).

[Suh00a] J. Suhonen, Physics Letters B **477**, 99 (2000a).

[Suh00b] J. Suhonen, Physical Review C **62**, 042501 (2000b).

[Suh05] J. Suhonen, Physics Letters B **607**, 87 (2005).

[Sve05a] C. E. Svensson et al., Journal of Physics G **31**, S1663 (2005).

[Sve05b] C. E. Svensson, G. Hackman, C. J. Pearson, M. A. Schumaker, H. C. Scraggs, M. B. Smith, C. Andreoiu, A. Andreyev, R. A. E. Austin, G. C. Ball, et al., Nuclear Instruments and Methods in Physics Research A **540**, 348 (2005).

[Tak66] N. Takaoka and K. Ogata, Verlag der Zeitschrift für Naturforschung A **21**, 84 (1966).

[Tal06] http://www.cubik.org/mirrors/taligent/Docs, last accessed Nov 15 2006.

[Tan03] S. Taniguchi, T. Nakamura, T. Nunomiya, H. Iwase, S. Yonai, M. Sasaki, S. H. Rokni, J. C. Liu, K. R. Kase, and S. Roesler, Nuclear Instruments and Methods in Physics Research A **503**, 595 (2003).

[Tom86] T. Tomoda, A. Faessler, K. W. Schmid, and F. Grummer, Nuclear Physics A **452**, 591 (1986).

[Tom91] T. Tomoda, Reports on Progress in Physics **54**, 53 (1991).

[Tos01] T. Toshito (Super-Kamiokande) (2001), `hep-ex/0105023`.

[Vas90] A. A. Vasenko et al., Modern Physics Letters A **5**, 1299 (1990).

[Ver87] J. D. Vergados, Physics Letters B **184**, 55 (1987).

[Ver02] J. D. Vergados, Physics Reports **361**, 1 (2002), `hep-ph/0209347`.

[Ver05] J. D. Vergados, in *Proceedings of Neutrino Nuclear Responses, Osaka, Japan* (2005), see http://www.spring8.or.jp/ext/en/appeal/nnr05/, last accessed Nov 15 2006.

[Vog86] P. Vogel and M. R. Zirnbauer, Physical Review Letters **57**, 3148 (1986).

[Wei78] S. Weinberg, Physical Review Letters **40**, 223 (1978).

[Wil78] F. Wilczek, Physical Review Letters **40**, 279 (1978).

[Wir95] R. B. Wiringa, V. G. J. Stoks, and R. Schiavilla, Physical Review C **51**, 38 (1995), `nucl-th/9408016`.

[You91] K. You, Y. Zhu, J. Lu, H. Sun, W. Tian, W. Zhao, Z. Zheng, M. Ye, C. Ching, T. Ho, et al., Physics Letters B **265**, 53 (1991).

[Zde02] Y. G. Zdesenko, F. A. Danevich, and V. I. Tretyak, Physics Letters B **546**, 206 (2002).

[Zim03] S. Zimmermann, *Front end digital signal processing for majorana* (2003), presented at the Majorana Collaboration Meeting, Seattle, WA.

[Zio99] K. Zioutas et al., Nuclear Instruments and Methods in Physics Research A **425**, 482 (1999), `astro-ph/9801176`.

Appendices

A Other Science Applications of the Majorana Experiment

The Majorana experiment is foremost a neutrino mass experiment. However, we will capitalize on its unique capabilities to realize other interesting physics at little added cost. Several examples are discussed here. Care in the construction of the Majorana apparatus should yield significant sensitivity for both of these purposes.

A.1 Search for Double-Beta Decay Transitions to Excited States

Although the matrix element calculations for $0\nu\beta\beta$ and $2\nu\beta\beta$ are different, they have many commonalities. These commonalities permit studies of the $2\nu\beta\beta$ matrix elements, which can be compared to experiment to constrain the calculation techniques of the $0\nu\beta\beta$ matrix elements that have no direct experimental test. In a similar way, studies of $\beta\beta$ transitions to excited-states in the daughter nuclide allow one to obtain supplementary information about $\beta\beta$. It is very important to note that in the framework of QRPA models, the behavior of nuclear matrix elements with respect to the so-called g_{pp} parameter is completely different for transitions to the ground state (a 0^+ - 0^+ transition) and those to excited states (0^+ - 0^+ or 0^+ - 2^+ transitions) [Gri92, Suh98, Aun96]. As a result, the decay to excited states may probe different aspects of this calculation method than the decay to the ground states. This additional opportunity for insight into the nature of the matrix elements drives the interest in these decay modes.

Because of smaller transition energies, the probabilities for $\beta\beta$ transitions to excited states are substantially suppressed compared to ground-state transitions due to the reduced phase space. However, the decay of the excited state emits mono-energetic γ-rays that can be detected in coincidence with the $\beta\beta$ electrons. These γ-rays provide a very clear signature of the decay and can greatly increase the sensitivity of the measurement [Bar90]. In effect, these γ-rays permit the identification of the daughter in real-time coincidence. In the nuclei ^{100}Mo, ^{96}Zr, and ^{150}Nd for example, the excited-state $\beta\beta$ transition energies are large enough (1903, 2202 and 2627 keV, respectively) that the expected half-lives (10^{20}-10^{21} y) are potentially detectable. Currently only ^{100}Mo has had this transition measured [Bar95, Bar99, Deb01] with half-life of (6-9) $\times 10^{20}$ y. Recently, several isotopes, ^{82}Se, ^{130}Te, ^{116}Cd and ^{76}Ge, have also become of interest to studies of the $2\nu\beta\beta$ decay to the 0^+ level. (See the recent review by Barabash [Bar00].)

Theoretical estimates of the $2\nu\beta\beta$ to a 2^+ state have shown that for a few nuclei (^{82}Se, ^{96}Zr, ^{100}Mo, and ^{130}Te) the half-lives can be as short as 10^{22}-10^{23} y [Suh98]. Many of the present experimental limits are approaching these theoretically predicted values. This would mean that the detection of such decays becomes possible using the present and new installations in the near future. Table A.1 summarizes the theoretical calculations.

Until now, attention was concentrated mostly on the $0\nu\beta\beta$ transition to the ground state of the final nucleus. However, there might be a chance that the transitions to the excited 0^+ and/or 2^+ final states are favored experimentally, at least for a particular mechanism for $0\nu\beta\beta$ [Bar00]. This potential advantage depends on the ratio of the corresponding nuclear matrix elements to the excited and ground states and the multi-hit background. If the matrix element values are comparable, the $0\nu\beta\beta$ decay experiment measuring transitions to ground and excited final states could have a similar sensitivity to the neutrino mass. A further motivation for the interest in these excited state transitions was described in [Sim02] where it was shown that it is possible to distinguish among the light and heavy Majorana neutrino mass and R-parity breaking SUSY mechanisms of the $0\nu\beta\beta$ decay by studying the transitions to the first excited 0^+ states.

Using the Majorana detector the $0\nu\beta\beta$ of ^{76}Ge to the 0^+ excited state of ^{76}Se will be investigated with a half-life sensitivity $\sim 10^{28}$ y, which corresponds to a sensitivity to neutrino mass $|\langle m_\nu \rangle| \sim$

Table A.1: Theoretical estimates of half-lives for $2\nu\beta\beta$ and $0\nu\beta\beta$ to the 2^+ and 0^+ excited states of a daughter nuclei in years. Values without references are taken from [Suh98]. For the $0\nu\beta\beta$, the half-lives are calculated for $|\langle m_\nu \rangle| = 1$eV.

Isotope	$2\nu\beta\beta$ 0^+ - 2^+	$2\nu\beta\beta$ 0^+ - 0^+	$0\nu\beta\beta$ 0^+ - 0^+
^{48}Ca	5×10^{26} [Hax84]		
^{76}Ge	5.8×10^{25} – 5×10^{26}	1.7×10^{21} – 1.7×10^{24}	4.9×10^{26} [Suh00a] $(2.4 - 4) \times 10^{26}$ [Sim01]
^{82}Se	1.4×10^{21} – 3.3×10^{26}	1.4×10^{21} – 3.3×10^{21}	9.4×10^{26} [Suh00a] $(4.5 - 9) \times 10^{25}$ [Sim01]
^{96}Zr	3.3×10^{20} – 7.2×10^{26}	2.1×10^{20} – 1.5×10^{22}	2.3×10^{24} [Suh00b]
^{100}Mo	5.3×10^{20} – 1.1×10^{26}	5.4×10^{19} – 5.5×10^{21}	7.6×10^{24} – 1.5×10^{26}[Sim01]
^{116}Cd	1.1×10^{24} – 7.8×10^{25}	1.1×10^{22} – 9.5×10^{25}	1.3×10^{27}
^{124}Sn	6.5×10^{26}	2.7×10^{21}	
^{130}Te	3.2×10^{22} – 2.8×10^{24}	5.1×10^{22} – 1.4×10^{25} [Bar01]	
^{136}Xe	4×10^{23} – 5.4×10^{24}	2.5×10^{21} – 3×10^{21}	4.8×10^{24} – 4.8×10^{26}[Sim01]
^{150}Nd	7.2×10^{24} – 1.2×10^{25}	8.6×10^{21}	

50-160 meV (depending on the nuclear matrix element used). In this case it is really possible to have a "zero"-background experiment because of the clear signature of the events. Sensitivity with passive samples (up to 10-20 kg) can reach $T_{1/2} \sim 10^{24}$-10^{25} y.

A.2 $\beta^+\beta^+$, β^+EC, and EC-EC Processes

Contrary to the intensive interest in $2\nu\beta\beta$, the $\beta^+\beta^+$, β^+EC (electron capture), and EC-EC modes have attracted almost no attention. The $2\nu\beta^+\beta^+$ processes are much slower than $2\nu\beta\beta$ due to the small phase space, and the Coulomb barrier for positrons. However they are attractive from the experimental point of view due to the possibility of detecting the coincidence signal from four (two) annihilation γ-rays and two (one) positrons, or the annihilation γ-rays only. The 2νECEC-process can have a large decay energy (up to ∼2.8 MeV) but the experimental detection for the transition to the ground state is made difficult by the fact that only x-rays are emitted.

Detection of the two-neutrino mode of these processes would provide additional nuclear matrix element information. Such data are very important in view of the need for cross checks of the theoretical calculations for $0\nu\beta\beta$. If $0\nu\beta\beta$ is ever detected, the experimental results (or even limits) on $0\nu\beta^+$EC half-lives offer a possibility to determine whether the observed decay is dominated by the neutrino mass mechanism or by right-handed weak currents [Hir94]. The next generation of low-background experiments can potentially increase the half-life sensitivity for these decays to $\sim 10^{22}$-10^{23} y. This should be sufficient to detect the 2νECEC (0^+ - 0^+) process in ^{96}Ru, ^{106}Cd, ^{124}Xe, ^{136}Ce, and ^{156}Dy [Bar94]. With Majorana, a half-life sensitivity of 10^{24}-10^{25} y can be reached for the double-beta decay for $\beta^+\beta^+$, β^+EC, and EC-EC -processes. Finally, the very rare single beta decays in ^{96}Zr and ^{48}Ca might be measured for the first time with such a detector.

A.3 ^{76}Ge $2\nu\beta\beta$ Spectrum Shape

The energy carried away by the two electrons $2\nu\beta\beta$ is characterized by a continuous energy spectrum out to the endpoint energy of 2039 keV. The spectral shape is determined, to a first approximation,

simply by the phase space available in the decay. Recoil order corrections to the charged nucleon current correct this spectrum by roughly 10%, and have been calculated recently [Barb99]. Decay modes in which majorons are emitted also distort the spectrum, and a search for this mode can be obtained from a simultaneous fit of the residual spectrum to a combination of conventional $2\nu\beta\beta$ and a possible majoron-emitting mode.

The half-life for ^{76}Ge has been measured with systematic-dominated uncertainties on the order of 10-20% in previous-generation experiments [Aal96, Kla01b]. These measurements are extremely challenging, in that they require a detailed model of the background to accurately extract the spectrum and the half-life. They also represent our most stringent test of the physics models used to calculate double-beta decay.

The difficulty in measurements of $2\nu\beta\beta$ to the ground state is that the signal presents itself as a smooth continuum. The spectrum peaks at roughly 700 keV. From previous measurements, we expect the signal to be dominated by $2\nu\beta\beta$ decay above roughly 1 MeV, this may not be the case at lower energies. We also note that the dominant contributors to the backgrounds will probably be different than those relevant to the $0\nu\beta\beta$ mode. In particular, the external backgrounds from the copper cryostat components and lead shielding provide a significant source of potential backgrounds. Hence, in order to improve on the effectiveness of previous measurements, we must control and characterize these external sources of background.

Of primary concern for the $2\nu\beta\beta$ measurements are the external γ-ray backgrounds, particularly line radiation arising from the cryostat materials and ^{210}Bi bremsstrahlung from the lead shielding. We note that, although the efficiency of segmentation and PSA are reduced at lower γ energies, the self-shielding due to the outer portions of our detector array is increasingly effective at lower gamma energies. Two-neutrino double-beta decay in the dead layer will have degraded signals. Since the dead layer comprises about 2% of the volume, the study of spectral effects at the few percent level will need to consider the effect of the dead layer.

A.4 Majorana as a Weakly Interacting Massive Particle Detector(2003)

Majorana should be able to contribute significantly to dark matter searches. The Majorana sensitivity should be similar and complementary to that of CDMS-II.

Extensive gravitational evidence indicates that a large fraction of the matter in the universe is non-luminous, or "dark" [Ber01]. However, the nature and quantity of the dark matter remain unknown, providing a central problem for astronomy and cosmology [Kol90, Pee93]. Recent measurements of the cosmic microwave background radiation [Ben03, Pry02, Net02], as well as arguments based on big bang nucleosynthesis and the growth of structure in the universe [Sre00], suggest that dark matter is predominantly made up of non-baryonic particles outside the standard model of particle physics. Supersymmetric particle physics models provide a natural candidate for dark matter: the lightest superpartner (LSP), usually taken to be a neutralino with typical mass about 100 GeV/c^2 [Jun96, Ell97, Eds97, Bot00, Bot01, Ell02a, Ell02b]. Analysis of experimental bounds from LEP have been shown to give a lower limit of $\sim$50 GeV/c^2 for the LSP [Ell02a, Ell00], although treatment of special cases can be shown to permit a mass a factor 10 below this [Bot03].

More generically, one can consider a class of Weakly Interacting Massive Particles (WIMPs) [Lee77], which were once in thermal equilibrium with the early universe, but were "cold," i.e. moving non-relativistically at the time of structure formation. Their density today is then determined roughly by their annihilation rate, with weak-scale interactions if the dark matter is mainly composed of WIMPs. WIMPs are expected to have collapsed into a roughly isothermal, spherical halo within which the visible portion of our galaxy resides, consistent with measurements of spiral galaxy rotation curves [Kol90]. Direct detection of WIMPS is possible through their elastic scattering from nuclei [Goo85, Pri88]. Calculations of the fundamental WIMP-quark cross-sections require use of a model, usually the Minimal Supersymmetric Standard Model (MSSM) [Jun96]. This interaction, summed over the quarks present in a nucleon, gives an effective WIMP-nucleon cross

section. In the low-momentum-transfer limit, the contributions of individual nucleons are summed coherently to yield a WIMP-nucleus cross-section; these are typically smaller than 10^{-6} pb. (See for example [Ell01a, Ell01b, Bat01, Bed97, Bal01, Cor00].) The nuclear recoil energy is typically few keV (ionization energy) depending on the WIMP mass, up to tens of keV [Lew96] since WIMP velocities relative to the Earth should be typical of Galactic velocities.

An ultra-low-background segmented Ge detector array designed for double-beta decay has the potential to be used for a WIMP dark matter search. Several attractive features that the Majorana experiment displays as a WIMP detector are listed as follows:

1. *Close-packing (self-shielding) and segmentation of the crystals* will contribute to reducing the γ-ray background in the low-energy region where the WIMP signal is expected. Single isolated nuclear recoils are expected due to WIMP interactions, whereas γ-rays generally interact more than once in the detector ensemble, allowing them to be rejected in a large, spatially divided device like Majorana.

2. *Segmentation* also lowers detector capacitance, reducing the energy threshold and increasing the acceptance of the WIMP signal. Thresholds as low as 0.75 keV are achieved in segmented HPGe, a considerable reduction from a customary 5-10 keV in unsegmented large diodes.

3. *The spatial information revealed by pulse-shape analysis* (PSA) may help eliminate surface events such as low-to-medium energy betas or other surface contamination, already a limiting background in some WIMP detectors [Kud01].

4. *Majorana's ability to reject low-energy neutron events* is less evident but potentially important. In a typical deep underground location the dominant neutron flux arises from (α, n) and natural fission in rock, and to a lesser extent from hard neutrons originating in μ spallation in rock and shielding. The main concern here is from neutrons with energies above $\sim$200 keV and a typical flux $\sim 10^{-6}$ n/cm^2/s [Bel99, Ste01]. The referenced energy spectrum dies off rapidly above $\sim$5 MeV. The maximum recoil energy imparted by a neutron to a Ge nucleus is $\sim$1/18 of the incident energy, with only a few percent going into ionization, the rest being lost to phonons. This causes the neutron recoil signal to concentrate below $\sim$60 keV ionization energy. Neutron recoils are identical to those expected from WIMPs. They constitute the limiting background in any WIMP detector, unless a rejection method or substantial neutron shielding can be applied.

An estimate shows that the present low energy signal in IGEX detectors (0.05 counts/keV/kg/day) is indeed compatible with an origin in neutron-induced recoils. This same observation that neutron recoils may already be limiting WIMP searches has been emphasized by the EDELWEISS collaboration [Ste01]. The viability of using additional external shielding in Majorana (neutron moderator and active muon veto) without affecting $\beta\beta$ performance, or physical access to the detectors, will be studied with a full GEANT geometry that is under development.

Another worthy advantage of Majorana as a WIMP detector is the large exposure to be collected. The best WIMP sensitivity originates not from the standard signal-to-noise analysis method (i.e., comparing the expected WIMP signal in a spectral region with the background by means of a suitable statistical estimator), but from an absence of temporal modulations in the background that could otherwise be assigned to a time-dependent WIMP signal. A known example is the yearly modulation in scattering rate and deposited energy expected from the combined movement of Earth and Sun through an isotropic WIMP galactic halo [Dru86]. Germanium detectors have demonstrated long-term stability and are ideal for searching such temporal modulation.

For the time being, a first Monte Carlo calculation of the minimum detectable modulated background fraction after a 2500 kg-y exposure has been performed, using the statistical estimator proposed by Freese [Fre92]. In order to obtain sensitivity projections from this Monte Carlo it is necessary to make a working hypothesis about Majorana's achievable background in the energy

region between a few keV and a few tens of keV. A flat 0.005 counts/keV/kg/day from detector threshold (0.5 – 1 keV) to 20-keV ionization energy is assumed.

Some preliminary estimates have been made of the contributions from radioactive cosmogenic activation products to this energy region, based on the period of crystal exposure (∼60-90 days) at sea level shown in Table 3-3, leaving ample room for improvements [Bau01]. The cosmogenic background rates for natural Ge [Avi92, Col92] should be taken as a conservative upper limit for Majorana. Activation rates for ^{76}Ge are roughly one order of magnitude smaller due to the higher neutron spallation-reaction energy thresholds [Col00], with a possible exception for tritium production (see Table 3-2). This represents a clear advantage vis-à-vis other large-mass WIMP detectors planning to use natural Ge. The majority of the cosmogenics contribute activity well below 0.005 counts/keV/kg/day, however, we will summarize those that will need to be monitored.

Cosmogenic ^{68}Ge will be expected to accumulate at a rate of 0.5-1 atom/kg/day following its complete removal producing 86% ^{76}Ge enriched detectors. ^{68}Ge (270 day half-life) undergoes decay generating peaks at 10.4 (1.2) keV following the Ga K(L) shell electron capture with BR of 88%(10%) respectively (see Fig. 3-5). Taking the mid values for exposure, and production rate, 75 days of sea level exposure creates 51 atoms ^{68}Ge/kg. If these crystals are underground for 1 year, the ^{68}Ge will decay (60% reduction), resulting in a background contribution of 0.05(0.005) cts/kg/day at the K(L)-shell peak energies. The 1.2-keV peak region is near background projection, while the 10.4 keV peak will be a factor 10 above the projection. However, the K-peak region can be bracketed and rejected without significant effect on the dark matter sensitivity. Furthermore, preliminary investigations of vetoing ^{68}Ge decays by correlating them with the subsequent positron decay (89% BR) of ^{68}Ga (68 minute half-life) to ^{68}Zn from the same segment of the detector indicate that a significant further reduction (> 5) of the lines can be made. This will be studied further in the background Monte Carlos.

Tritium will also be cosmogenically regenerated in the detectors following its elimination at the time of crystal growth. There is some uncertainty in the sea level cosmogenic production rates with the values shown in Table 3-2 (∼110-140 atoms ^{3}H/kg/day) taken as conservative upper limits. The tritium beta end–point (12.3 year half-life) occurs at 18.6 keV with a peak in the differential spectrum at 3 keV of 0.005 cnts/keV/d/300 atoms ^{3}H. In order to achieve the target background this will require <2 days above ground exposure during/after crystal growth. It is clear that tritium creation in the detectors and possible contamination during production will have to be closely controlled. We will perform studies to obtain accurate ^{3}H cosmogenic production rates, methods for detector production underground, and final detector transportation under a few meters-water-equivalent (mwe) of shielding in order to minimize the direct limitation of the dark matter sensitivity due to this contaminant.

Although not a cosmogenic source, we also raise the issue of $2\nu\beta\beta$ background (∼10^{21} year half-life in ^{76}Ge) for dark matter. The differential spectrum (in enriched 86% ^{76}Ge) for the electron recoils falls below 10^{-4}events/keV/kg/day for energies <60 keV, and so it is not a concern at the projected dark matter sensitivity. However, in p-type Ge detectors it is estimated that less than ∼2% of the Ge will form a dead layer in proximity to the outer contact. The $2\nu\beta\beta$ background occurs in the enriched crystals at a rate of 10 decays/kg/day in the range 0-2 MeV. Preliminary studies of how higher energy events (<∼0.2 /kg/day) originating in the dead layer, but reaching the active volume, may produce partial energy signals that pile up at low energies indicate that this will be well below the target background 0-20 keV of 0.1 events/kg/day. In addition to this dead layer contribution, $2\nu\beta\beta$ events near the crystal edge may only deposit a few keV before exiting the detector. These effects will be simulated in further detail when the choice of detector and size of the dead layer are better known, however, they do not appear to be a limitation.

With this conservative approach, the expected sensitivity via annual modulation analysis approaches CDMS-II projections (Fig. A.1) after collection of the planned 2500 kg-y exposure, if a threshold ∼1 keV is achieved. In addition, if the neutralino scattering cross-section resides close to the limit of sensitivity for both experiments, ∼10^{-8} pb (Fig. A.1), Majorana may detect the annual

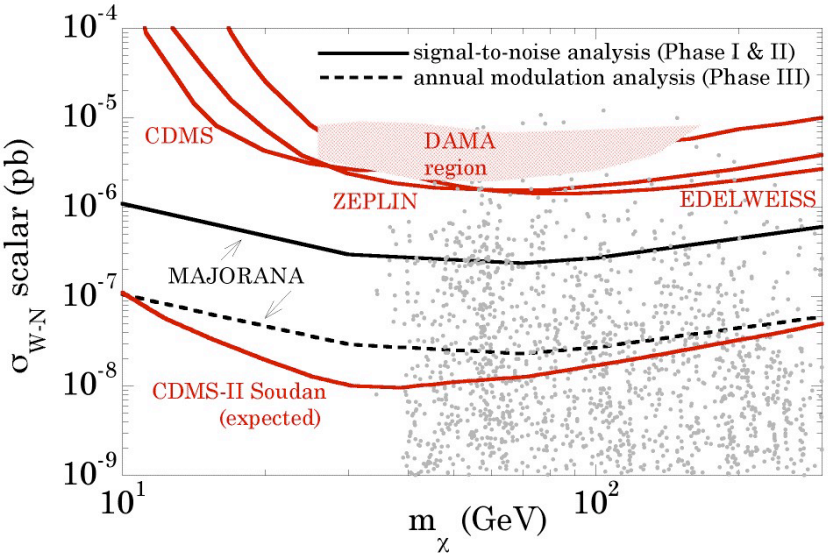

Figure A.1: Projected 95% C.L. Majorana WIMP limits for an assumed low-energy background of 0.005 counts/keV/kg/day, just one order of magnitude lower than in present unsegmented single HPGe detectors. Calculated for an ionization energy threshold of 1 keV, achievable via segmentation. "Signal-to-noise" limits are within reach after modest exposures < 1 kg-y. "Annual modulation" limits are calculated for the total exposure of 2500 kg-y. Present DAMA [Bel02], CDMS, EDELWEISS, and ZEPLIN limits (For references, and a complete list of Dark Matter search results see [Gai03]) and expected CDMS II limits are offered as a reference. The shaded region is presently favored by DAMA to explain an unconfirmed WIMP annual modulation in its signal. Dots represent the location in this phase space (spin-independent scattering cross section vs. WIMP mass) of plausible supersymmetric neutralino WIMP candidates, using the same parameters as in [Col00]. Even under these very conservative background assumptions, the expected WIMP Majorana sensitivity is comparable to the most promising cryogenic projects.

modulation signature, something that the much smaller CDMS-II future total exposure (∼10 kg-y) is unable to achieve. CDMS expects to disentangle a WIMP signal from neutron backgrounds using different targets (Si and Ge), for which WIMP and neutron responses differ. The observation of both responses would be highly complementary in making the argument for neutralino dark matter a convincing one.

Finally, if the present DAMA [Bel02] annual modulation claim were to survive the test of time, Majorana would not only confirm it as a >50-sigma effect, but also reveal a second WIMP signature: the tiny, ∼0.1% daily rate modulation arising from the coupling of the rotational speed of the Earth (∼0.45 km/s near the equator) to orbital and solar speeds through the halo [Col99]. Unfortunately, for cross sections any lower than in the DAMA favored region of Fig. A.1, an exposure even larger than 2500 kg-y would be required to detect this.

While its main goal is to measure the effective Majorana mass of the neutrino, the singular characteristics of the Majorana detector make it a promising tool in the quest for dark matter. The projected WIMP sensitivity is competitive even under the conservative background assumptions made. Thereafter, the new low-energy background information and associated Monte Carlo studies will be used to project (and then execute) further incremental improvements in the sensitivity of the experiment.

A.5 Exploitation of Majorana Data for Solar Axion Searches (2003)

The Majorana experiment will have 500 times the mass, twice the energy range, will run 10 times as long, and should be able to reduce the background over that of SOLAX, a previous germanium-based axion search, by at least a factor of 50. This should translate into a bound on the axion-to-two-photon coupling constant of $\sim 10^{-10}$/GeV [Ira00]. This would be about as sensitive as the bound set by Raffelt using the population distribution of red giant stars [Raf96] , and would represent the most sensitive laboratory search for axions of mass > 0.01 eV.

The theoretical motivation and history of experimental searches for axions has been recently reviewed by Rosenberg and van Bibber [Ros01]. Quantum chromodynamics (QCD) is very successful in describing many features of the strong interactions. However, the complete QCD Lagrangian contains some symmetries that do not survive quantum effects. Classically, complex terms that break these symmetries can be rotated away if the fermion fields have chiral invariant interactions. At the quantum level, however, such transformations involve a phase angle (θ) that is not arbitrary. Although it must be near zero so as not to introduce a T-violating term, the transformation that brings the quark-matrix to a real, diagonal chirally invariant form does not have a small phase angle (θ). Since QCD respects CPT symmetry, this phase leads to CP-violation, which predicts an electric dipole moment a factor of 10^{11} larger than the experimental upper bound [Pec89].

Peccei and Quinn solved this problem by recognizing that the quark mass-matrix is a function of vacuum expectation values (VEVs) of weakly coupled scalar fields (φ). The VEVs are determined by minimization of the associated potential V(φ). They assumed that the Lagrangian has a global U(1) chiral symmetry under which the determinant of the mass-matrix changes by a phase fixed only by instanton effects that spontaneously break the global U(1) symmetry. This results in an additional phase that cancels the offending one that leads to the large CP-violation [Pec77].

Spontaneous symmetry-breaking processes naturally produce Goldstone-bosons. The Goldstone-boson arising from the breaking of the Peccei-Quinn symmetry is called the axion. In two independent papers Weinberg [Wei78], and Wilczek [Wil78] pointed out that these axions could have physically observable and important properties.

The conventional wisdom says they could possibly couple to electrons, to photons, or directly to hadrons. Accordingly, they might have been produced in the Big Bang, and therefore are candidates for cold dark matter (CDM). They might also be produced in stellar burning and in stellar collapse, etc.

The Peccei-Quinn axion is the most plausible solution to the strong CP problem found to date.

This fact continues to motivate experimental searches. The technique presented below is one initiated by members of the Majorana collaboration and is an interesting side application of the Majorana array of detectors.

The first technique aiming at the detection of solar axions was suggested by Sikivie in 1983 [Sik83]. It involves Primakoff axion-to-photon conversion in an intense transverse magnetic field, in what is called a magnetic helioscope. This technique is highly efficient for very light mass axions and an experiment operating at CERN, CAST, uses a 10-m long magnet with a transverse magnetic field of 10 Tesla. This technique is nevertheless limited to axion masses up to about 0.1 eV. This limitation is due to the requirement that axion and photon wave functions stay in phase throughout the magnet (coherence loss) [Zio99]. In order to search for solar axions with masses ¿ 0.1 eV it is necessary to fill the magnet bores with a gas that will act like plasma, effectively slowing the speed of the photon, allowing it to remain coherent with the slower massive axion. However, this addition to the technique has its own limitations [Zio99]. For axion masses larger than 1 eV the needed gas density would require a pressure of 15 atmospheres and hence absorb the axion-induced photons (the signal) before they can reach the detectors. For masses beyond this range one needs a different experimental technique.

To address this problem, several members of the Ma jorana collaboration, at the time leading the SOLAX collaboration, designed a technique using an ultra-low background germanium detector to detect photons coherently converted by Primakoff scattering off the crystalline-Ge planes at times when the line of sight from the detector to the Sun makes an angle with one of the planes that fulfills a Bragg coherence condition. Creswick et al. [Cre98] developed the theory describing the expected conversion rate. A coAn experiment was performed in the Hiparsa iron mine in Sierra Grande, Argentina, during which 1.94 kg-years of data were collected. Each event in the energy region of interest was marked with the exact Julian time. For each day of every year, a pattern of the expected times for Bragg coherence was calculated for use in the analysis of the data. The resulting lower bound on the axion-to-two-photon coupling constant was 2.7×10^{-9}/GeV [Avi98].

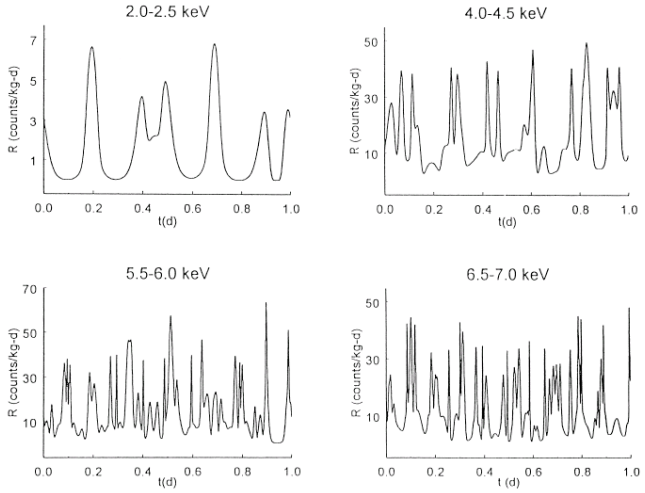

Figure A.2: Theoretical prediction [Avi99] of the count rate of photons converted ($g_{\alpha\gamma\gamma} = 10^{-8}$ GeV^{-1}) from axions incident at a Bragg angle, for a detector at Sierra Grande, Argentina.

The SOLAX experiment effectively served as a demonstration of the principle of detecting axions with single crystals. In SOLAX only the (100) crystal axis direction was known and the data had to be analyzed for every degree of rotation about this symmetry axis of the detector, which was along

the radius of the Earth. The Majorana experiment will have 500 times the mass of the SOLAX experiment, with crystal planes fixed as desired. In a granular experiment like Majorana, the axes can be oriented in a variety of ways so that background can be subtracted.

There are two significant improvements that can be made in the quality of the solar axion data obtained with the Majorana experiment, relative to that obtained by SOLAX. First, in SOLAX the low-energy background was high due to microphonic noise and cosmic-ray neutrons associated with an overburden of less than 1,000 mwe. Secondly, the pulse-shape analysis technique used in the SOLAX experiment was a crude, first generation technique. Recent developments have resulted in very sophisticated digital techniques for pulse-shape analysis. The digital electronics planned for the Majorana Experiment, described elsewhere in this proposal, should allow an energy threshold below 1 keV. Compared with the 4-keV threshold of the SOLAX experiment, this implies Majorana will be sensitive to significantly more of the critical low-energy fraction of the signal.

A.6 Supernova Neutrinos

Recently Horowitz has noted that the next-generation dark matter and double-beta decay experiments will have target masses large enough to observe neutral-current elastic scattering of the target nuclei by supernova neutrinos. The Majorana detector might expect to see a few tens of events.

A.7 Electron Lifetime

The Ge detectors in the Majorana experiment will contain approximately 5×10^{28} electrons of which about 3×10^{27} are in the k-shell. Furthermore there are a great number of electrons in the shield surrounding the Ge. This great number of electrons offers the opportunity to look for electron decay. Two signatures are possible: Observation of the Doppler-broadened, 255.5-keV γ-ray originating from the bound electron decay to ν plus γ-ray, and the search for the x-rays resulting from the relaxation of the atomic shell following a k-shell electron disappearance. Due to the excellent energy resolution of Ge detectors and the low levels of background expected for the detector array, Majorana should have good sensitivity to search for this process. Previous mean life limits on these two processes are t = 4.6×10^{26} y [Bac02] and 6.4×10^{24} y [Bel99].

The potential sensitivity of Majorana will depend on the efficiency of detecting the γ-rays and x-rays in the detector array and what levels of background are present at the two energy regions of interest. The efficiency will require a detailed simulation of the response of the array. We have not focused on what levels of background one might expect at these particular energies. However, one would expect to place significantly more sensitive limits on these processes.

A.8 Further Implications of $0\nu\beta\beta$

If $0\nu\beta\beta$ is observed it implies that neutrinos are massive Majorana particles [Sch82]. Even so, other mechanisms may mediate the process giving rise to a finite decay rate even in cases where the neutrino mass may be small. As a result, limits on the $0\nu\beta\beta$ decay rate provide stringent limits on many proposed extensions to the standard model of particle physics. The recent reference [Pre03] provides a nice overview of many of these non-standard model processes and their context with respect to $0\nu\beta\beta$ and is a useful guide to the literature. For example, a heavy right-handed neutrino arising in the left-right symmetric model might contribute to the process [Ver02, Moh75, Sen75]. Alternatively, lepton-number violating interactions arising in R-parity violating supersymmetric interactions involving the exchange of charged-lepton superpartners might mediate the decay instead of a neutrino [Moh86, Ver87, Hir96b, Hir00]. Furthermore, the process may also be mediated by an exchange of leptoquarks [Hir96a]. The indicated references describe the limits that can be placed on these and other extensions to the standard model from the experimental limits on $0\nu\beta\beta$.

The possibility that leptogenesis may provide an explanation for the baryon asymmetry of the Universe is very intriguing [Fuk86]. Neutrinos are massive particles and the seesaw mechanism [Li82, Kay82a, Kay82b] can motivate why neutrinos are so much lighter than their charged partners. This mechanism would also result in heavy right-handed Majorana neutrinos in addition to the light left-handed Majorana neutrinos one usually considers in the context of double-beta decay. These heavy neutrinos would be present in the early universe and, as it cools, they would decay into leptons and scalars via a Yukawa interaction coupling to the left-handed fermions and Higgs. The decay of these Majorana particles violate lepton number, so if they decay out of equilibrium, they can result in a net lepton number for the Universe so long as CP is also violated. Later on this net lepton number is converted to a net baryon number by non-perturbative sphaleron processes. (See Refs. [Pil99, Buc00] for a review of the topic.) Therefore the observation of $0\nu\beta\beta$ would indicate that neutrinos have many of the necessary characteristics for leptogenesis.

B Outreach Program

Aspects of the Majorana project can easily be presented to inspire the interest of the general population in science. However since the experiment will be sited deep underground, it is doubtful, although not infeasible, that tours of the laboratory itself will be available. Instead we envision kiosks or posters at visitor centers near the laboratory site that are mostly passive, but occasionally would be manned by members of the collaboration. The NUSEL proposal, for example, includes an extensive outreach program that includes a visitor center. The SNOLAB location is near the Science North educational facility that has included many presentations on the Sudbury Neutrino Observatory. (See Section 3.11 for a brief discussion of NUSEL and SNOLAB.) Some specific examples of educational topics for use in outreach include: Relative levels of radioactivity in various environments, half-lives, and applications of low-level background counting or products.

A discussion of the relative level of the activity in the human body ($\sim$12000 Bq ^{40}K) compared to the initial ^{68}Ge activity in the Ge crystals of our experiment ($\sim$500 decays/day for 500 kg) could form the cornerstone of a lesson on activity in the environment. This would make the point that radioactivity is everywhere and that the levels in our experiment are remarkably low. It could lead into the usual discussion of the typical exposures a person receives each year and how that compares to dangerous levels. This will contribute to the National discourse on the requirement for radiological remediation of DOE/NNSA legacy sites.

Two-neutrino double-beta decay remains the longest measured half-life of any process. Thus the science of the Majorana project naturally leads to a presentation on half-lives. The comparison of half-lives to the age of the universe (10^{10} y) for ^{76}Ge ($\sim 10^{21}$ y), ^{238}U ($\sim 10^{10}$ y) and shorter-lived activities such as our primary ^{60}Co background (278 d) can make the point succinctly.

Low level counting and low radioactivity products are becoming important in our society beyond just pure science. Low level counting has applications for national security and whole body counting, for example. The semi-conductor industry requires low-activity lead to make solder because α decays can cause single upset failures in sensitive electronic components. These topics will also elucidate the importance of this field of research to the public.

C Educational Outcomes

The Majorana project contains elements of several disciplines, and can be expected to produce advanced academic degrees on several fronts. The project opportunities for undergraduate and graduate students in physics, and mechanical, electrical, and computer engineering cover many diverse challenges. The Majorana collaboration institutions have produced many successful Ph.D. and Master's degree students in science and technology areas closely related to the Majorana project, and are cultivating graduate and undergraduate students now in anticipation of a number of exciting degrees.

We anticipate that students from our several organizations will work at some combination of their home institutions, the collaborating National Laboratories, and the experiment location during the course of their degree work. Several physics Ph.D. and/or Master's topics can be predicted with certainty:

Master's level topics

- Digital Filter Models for Optimal Low-Energy Threshold Operation of the Majorana experiment
- Optimization of HPGe Detector Segmentation for Background Rejection and Process Yield
- Monte-Carlo Analysis of Detector Segment Self-Shielding for the Majorana experiment
- Suppressing Cosmic Muon Induced Neutrons in an Underground Laboratory Scenario
- Identifying Low-Energy Backgrounds in an Ultra-Low Level Germanium Spectrometer

Doctoral level topics

- Annual Modulation Dark Matter Sensitivity of the Majorana experiment
- Precision Re-measurement of 2ν Double-Beta Decay of ^{76}Ge Using Multiplicity Cuts
- Measurement of the 2ν Double-Beta Decay to the Excited State of ^{82}Se, ^{96}Zr, ^{100}Mo, ^{130}Te, or ^{150}Nd
- Measurements or limits on the rates of 2νEC-EC, EC-β^+, or $\beta^+\beta^+$ in various isotopes
- New Bound on 0ν Double-Beta Decay with the Emission of a Majoron
- New Limits on Existence of Solar Axions from Majorana Data
- New Limits/Measurement on Majorana Mass of Electron Neutrino
- New limits on the lifetime of the electron
- New limits on the existence of the Goldstone boson, the Majoron

The Majorana experiment will also provide many opportunities for the educational development of students in a non-traditional or cross-disciplinary way. A significant number of Master's theses and Doctoral dissertations are expected to accompany the collaboration's progress toward and through its final stage. A brief list of some possible degree titles follows:

Master's level topics

- Mechanical and Thermal Design and Analysis of an Ultra-Low Background Cryostat for the Majorana experiment (mechanical engineering)
- Signal Routing for the Majorana Project: Ultra-Low Background Transmission Lines with Low Thermal Conductivity (electrical engineering, physics)

- Monte-Carlo simulation of the Majorana Integrated Active and Passive Shield (physics)
- A Control System and Data Server for the Majorana Installation (physics, computer science)
- Time-Correlation Analysis of Data from the Majorana Double-Beta Decay Experiment (physics, mathematics)
- Failure Prediction for the Majorana Apparatus (physics, mathematics)
- Optimizing Dark-Matter Sensitivity for the Majorana Experiment (physics)
- Shield Mechanical Design and Optimization for the Majorana Experiment (mechanical engineering)
- Failure Prediction of Solid State Systems Based on Regular Time Series Data (statistics)
- Alternate Cooling Methods for HPGe Detectors (physics, mechanical engineering)

Doctoral level topics

- Process Control and Material Quality Monitoring for the Electroforming of Ultra-Low Background Copper (chemistry, chemical engineering, physics)
- Pulse-Shape Analysis for Background Rejection in the Majorana Segmented Detector Array (physics, statistics)
- A High Bandwidth Charge-Integrating Preamplifier Suitable for Ultra-low-background, Cryogenic Sensor Signals (electrical engineering)
- Interaction Localization with HPGe Detector Segmentation and Pulse-Shape Analysis (physics, electrical engineering)
- Surface preparation methods for alternative detector segmentation

D Enrichment Documents

This appendix consist of two documents. The first is the text of a Memorandum of Understanding produced at a meeting hosted in 2001 by ITEP concerning the availability of enrichment services in Russia. The second describes recent experience in the procurement of enriched germanium by the GERDA collaboration.

D.1 ECP MOU

Memorandum of Agreement between ITEP, the ECP and the Majorana Collaboration: Enrichment Costs, Schedules, and Technical Issues

October 29, 2001

Introduction

The Majorana experiment requires 500 kg of germanium enriched to 85% in ^{76}Ge. This material is only available in this quantity from enrichment facilities such as the Electrochemical Plant of Zelenogorsk, formerly known as K-45. Only the ECP Department of Super Clean Materials has a track record in providing germanium which has been operated as ultra-low background detectors for approaching a decade. ITEP and ECP have a long term record of successful collaboration. The purpose of this document is to set out the main features of a discussion held on Oct 29, 2001 at ITEP, Moscow, Russia, on the subject of costs and technical features of a Majorana enrichment campaign. The Majorana collaboration charter identifying collaboration institutions and collaboration goals can be found at majorana.pnl.gov.

Common Specifications

It was agreed that the special standards used to produce the germanium used in previous germanium double-beta decay experiments were adequate. ECP agreed to guarantee this level of quality, which includes that the material will be at least 85% ^{76}Ge. ECP has agreed to store all enriched material while not in process in a location with a 20 meter water equivalent overburden to minimize the cosmogenic creation of ^{68}Ge. All local taxes and other costs are included in the quotes and estimates in this MOU. If transport by air is selected by the Majorana collaboration, quotes include shipment to a US port of entry from Zelenogorsk.

Costs and Schedules for Production in Fiscal Year 2002-2003

The ECP presented firm quotes of \$56k/kg for production of germanium in quantity up to 30 kg/year, and a firm quote for \$50k for the increase of the capacity from 30 kg/year to 50 kg/year. In all cases, the ECP requires 20% of the purchase cost of the material as a start up to procure raw materials. These quotes will be valid for proposals made by the Majorana collaboration between December 2001 and February 2002 for production up to September 2003. After capacity increase, the enriched material will cost \$56k/kg.It is the intent of the Majorana collaboration to produce a proposal for mid year funding which will be submitted in Dec 2001. If this is not funded, a regular schedule proposal will include costs for between 20 and 30 kg of enriched material and the cost of increasing capacity from 30 to 50 kg/year. This proposal will be submitted in February 2002 for fiscal year 2003 (October 2002-September 2003).

Future Production Costs and Schedules

The ECP has provided estimates of costs for increasing production substantially. The first possible increase, up to 100 kg/year, is estimated to cost \$3.5M. A second option would increase production

up to 200 kg/year at a cost of about $5M. Either option would require a year to effect after receipt of funding and would result in material costing about $45k/kg.

Unresolved Issues

- Mode of transportation: Since ^{68}Ge grows in at about 1 atom per kg per day at sea level and possibly 100 times that at airliner altitude, the Collaboration may opt to ship by ground/sea. In this case ECP agrees to ship to the Russian port of exit within the quotes given above.
- Contracting Mechanism: The Collaboration, ITEP, and ECP are considering the most efficient contracting mechanism and has no final solution at this time. Contracts with ITEP, ECP, the ISTC and other possible options will be compared in the near future.
- It is possible that the product of the ECP may be processed into zone refined metal by another institution within Russia. ITEP and ECP will explore this possibility.

Disposition

This document will be presented to members of the Collaboration for discussion as well as the US Department of Energy and the US National Science Foundation for fact-finding regarding enrichment for double-beta decay and other experiments, and to the Russian Ministry of Atomic Energy.

D.2 Recent Experience in the Procurement of Enriched Materials

In the 1980s the IGEX and Heidelberg-Moscow ^{76}Ge collaborations independently obtained enriched materials for detectors. This material had been previously enriched by the Svetlana plant in Zelenogorsk, Russia (Department of the Electrochemical Combine Plant, formerly K-45)[13]. This facility was created to exploit non-military applications of enrichment technology and has served many other types of customers. It also does not enrich uranium. Zelenogorsk is considered one of the best transitions of Russian closed cities from nuclear weapons production to commercial spin off activity.

The enriched oxide materials obtained by IGEX and HM were processed for chemical purity to the intrinsic level by the Eagle Pitcher company in Quapaw, OK (now UMICORE Quapaw), then manufactured into detectors in Oak Ridge TN by Tennelec and ORTEC, respectively. Other enrichment facilities exist in Russia and the US, but a preliminary market survey indicates that only a few have substantial production capacity.

The GERDA Collaboration has shared information related to their procurement of ∼44 kg of enriched Ge from the Svetlana plant in 2005. This material was ordered and obtained within one calendar year, ahead of schedule. The chemical purity of the material exceeded the purchase specification of 99.5%. A shallow underground storage area was arranged by the plant to store materials that were ready for shipment or in process[14].

The Svetlana Plants prices are negotiated in dollars. The cost of this GERDA material was within the cost estimates discussed with Majorana in 2001, despite national inflation of about 10% annually since then. The cost may be more related to the currency fluctuations between the dollar and the ruble which have been about 5% in the positive direction since that time, see Figure D.1. An analysis of currencies, Russian inflation and the potential impact on Majorana are being updated to help identify the level of contingency required for this important WBS element, as shown below in Figure D.2.

[13] http://www.ecp.ru/en/

[14] http://www.mpi-hd.mpg.de/ge76/tuebingen05/Talks_Nov09/13_AC_TG2Summary.ppt

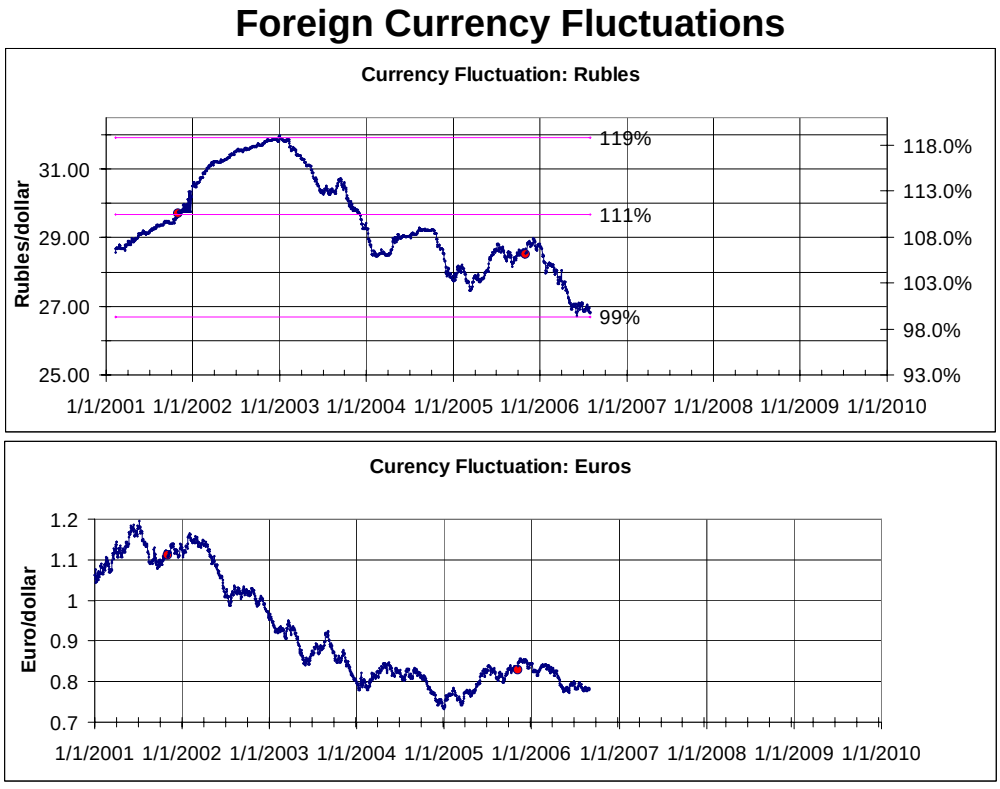

Figure D.1: Fluctuation of the ruble vs the dollar since 2001. The ruble has experienced a 20% variation since the first quotation, with about a 12% loss of dollar buying power since the quote.

Figure D.2: Russian inflation with worst case extrapolation to 2009. A quote in 2001 and an estimate in 2005 are shown against accumulated inflation. This indicates that Rusian inflation is not currently driving the price of enrichment.

E Underground Germanium Laboratory

6 May 2005

Paul Luke, Kevin Lesko, Yuen-Dat Chan, Reyco Henning
Lawrence Berkeley National Laboratory

E.1 Introduction

In neutrinoless double beta decay experiments, such as the proposed Majorana Experiment[15], the Majorana neutrino mass sensitivity is mainly determined by the total mass of the detectors, the counting time, and the background level. An important source of background comes from within the detectors themselves. For experiments using Ge detectors, cosmic rays and cosmic ray spallation neutrons present at the earth's surface interacting with Ge nuclei creates a number of long-lived radioisotopes that can produce significant background. These cosmogenic radioisotopes can be reduced or largely eliminated by performing the Ge crystal production in an underground facility that has sufficient overburden to effectively shield against cosmic rays. This would reduce the internal background of the Ge detectors and significantly increase the sensitivity of the experiment.

Some radioisotopes, such as Co-60 ($t_{1/2}$=5.27 years with $Q_\beta = 2.833$ MeV), can be significantly reduced by zone-refinement of the bulk Ge and by the process of creating Ge single crystals. However, Ge-68 ($t_{1/2}$=288 days followed by a Q_{EC}=2.921MeV) will be created and its concentration will continue to increase in the Ge, regardless of its form, at all stages of the material following isotopic enrichment. The scope of this report is to address factors that can reduce the cosmogenic radioisotopic backgrounds in the Ge, following the isotopic enrichment and transportation to the material purification or detector manufacturing facilities. We will examine the benefits, requirements and cost of building an underground Ge production laboratory. The Ge crystal production and Ge detector fabrication processes are discussed separately.

The information contained in this report is based in large measure on the inputs from a number of individuals including:

Larry Darken, Orren Tench (Canberra)
Pat Sangsingkeow, Tom Raudalph (Ortec/Ametek)
Frank Avignone (University of South Carolina)
William Hansen, Richard Pehl (Lawrence Berkeley National Laboratory)

Despite the many useful inputs from knowledgeable people in this area, the specific numbers given in this report, especially those related to cost, are just rough estimates. There are many factors that can affect these numbers greatly, depending on the details of the implementation that will ultimately be adopted. A reasonable expectation on the uncertainty in these numbers is about ±30%. In addition, the following assumptions were used in developing this report:

- A suitable space is available in an existing underground site to house the crystal growth and detector fabrication facilities. In this study, we do not include any cost or time that may be needed to locate and condition a site, to provide the basic infrastructure such as water, electricity and ventilation, or to use the space (rent). In other words, we assume there is no significant added cost or time incurred in building and operating a facility underground versus one that is above ground.

- The work to plan, design, equip, and operate the facilities will be carried out by established commercial supplier(s) of high-purity Ge crystals and detectors. This is considered to be the

[15]White Paper, "The Majorana zero-neutrino double-beta decay experiment", The Majorana Collaboration, Nov. 3, 2003.

most cost and time effective approach, given the extensive know-how and experience that are required for large scale crystal and detector production.

- The experiment will use n-type coaxial detectors.
- The facility and cost required to recover Ge from waste etchants is not included in this report, since the optimal process to perform this operation is still under study.

E.2 Cosmogenic Radioisotopes

Table E.1 shows the calculated and experimental production rates of radioisotopes in natural and enriched Ge. Of these, ^{68}Ge and ^{60}Co are the most important since they produce signals around the energy of the neutrinoless double beta decay.

Table E.1: Calculated and experimental production rates in natural Ge. Calculated rates in enriched Ge assuming 86% ^{76}Ge and 14% ^{74}Ge. Units are atoms per day per kilogram (see Majorana White Paper (previous footnote)).

	Natural Ge			Enriched Ge	
Isotope	Lal et al	Hess et al	Experiment	Lal et al	Hess et al
^{54}Mn	0.93	2.7	3.3 ± 0.8	0.37	1.4
^{57}Co	1.70	4.4	2.9 ± 0.4	0.28	1.0
^{58}Co	2.30	5.3	3.5 ± 0.9	0.59	1.8
^{65}Zn	24.6	34.4	38 ± 6	3.12	6.4
^{68}Ge	22.9	39.0	30 ± 7	0.54	0.94

E.3 Ge Crystal Production

E.3.1 Crystal Production Process

The starting material used in the Ge crystal production process is intrinsic Ge in the form of polycrystalline bars. For the Majorana Experiment, the starting Ge material is also isotopically enriched to ∼86% ^{76}Ge. The enrichment process and conversion of the enriched Ge to intrinsic grade material is not considered in this report. Intrinsic Ge refers to Ge crystals with electrical properties at room temperature dominated by the intrinsic properties of the Ge itself and not by the impurities. For this to be the case, the net electrically-active impurity concentration (i.e., the difference between the concentrations of acceptors and donors, $|N_A - N_D|$) has to be less than $\sim 10^{13}$ cm^{-3}. However, to produce large-volume γ-ray detectors, materials with$|N_A - N_D| \sim 1$ X 10^{10} cm^{-3} are needed. Therefore, the first step in the crystal production process is zone refining to purify the material to the level required.

In zone refining, the intrinsic Ge polycrystalline bar is put into a horizontal boat, usually made from silica with some form of carbon coating to prevent the freezing Ge from sticking to and breaking the boat. A narrow zone of the Ge bar is melted using an RF induction coil. The coil is then moved along the length of the bar, moving the melted zone along with it. Most impurities in Ge have a segregation coefficient of less than 1, meaning their concentrations are lower in the solid then in the melt at equilibrium. Therefore, as the melted zone travel along the Ge bar, the impurities are concentrated in the melt and swept along to the end of the bar. After multiple passes, the Ge bar is purified to the required impurity concentration. This process is carried out with the Ge in a flowing H atmosphere. Fig. E.1 shows a photograph of a zone refiner used at LBNL.

After zone refining, the Ge bar remains in polycrystalline form, whereas a single crystal is needed for detectors. This is achieved using the Czochralski crystal growth method. In this method, the zone-refined polycrystalline Ge is melted in a silica crucible. A single-crystal Ge seed is dipped into the melt and then withdrawn such that a Ge single crystal is grown onto the seed from the molten Ge. Typically the seed is rotated while the crystal is being formed. The seed and the resulting crystal is typically oriented with a (100) crystal axis parallel to the growth direction. The crystal growth process is conducted in a H atmosphere, with the H flowing inside a quartz envelope. Since Ge melt "wets" the silica crucible, it will crack the crucible if any Ge melt remains and allowed to freeze. Therefore, all the Ge in the crucible must be consumed during a crystal growth run. Some purification of the Ge also occurs during crystal growth due to impurity segregation, although it is not as effective as the multi-pass zone refining process. Fig. E.2 shows a Ge crystal being pulled in a Czochralski crystal grower at LBNL. The starting intrinsic polycrystalline bar, zone-refined bar, and the Czochralski grown single crystal is shown in Fig. E.3.

To be acceptable for large-volume coaxial Ge detector fabrication, the net impurity concentration of the Ge crystal needs to lie within a narrow range, typically $\sim 0.5 - 1.5\text{X}10^{10}$ cm^{-3} depending on the diameter of the detector. An impurity concentration that is too low will result in a highly non-uniform electric field, with high field concentrating at the center electrode. An impurity concentration that is too high will result in excessively high depletion voltage and risk of breakdown. In addition to impurity concentration requirement, the dislocation density of the crystal must also be controlled. Dislocation-free crystals do not yield good detectors due to the presence of defects which trap carriers. High dislocation density is also problematic, since the dislocations can trap carriers as well, and they can also lead to other problems such as high leakage current and noise.

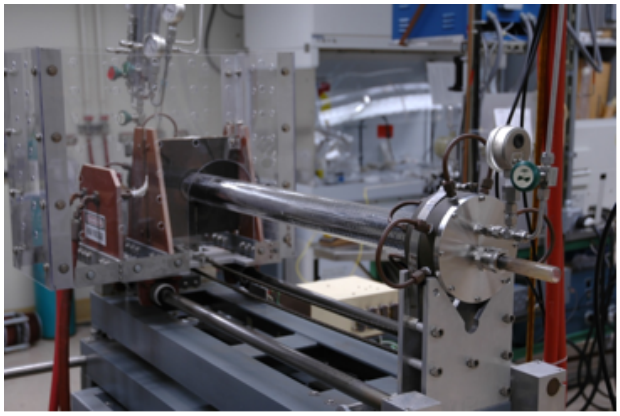

Figure E.1: A zone refiner used at LBNL.

E.3.2 Benefits of Underground Crystal Production

The main benefits of performing zone refining and crystal growth underground is to avoid the formation of cosmogenic radioisotopes in the Ge during the period of time it takes to perform these operations. The segregation coefficients of the most relevant elements are shown in Table E.2. Data on K, U and Th are not available, but they are likely to have small segregation coefficients as well.

With the exception of ^{68}Ge, all the radioisotopes of interest have, or are expected to have, very small segregation coefficients. Therefore, these radioisotopes will be effectively removed in the zone refining and crystal growth process. In fact, the segregation coefficients are so small that the Czochralski crystal growth process alone is quite effective in removing the radioisotopes. As the

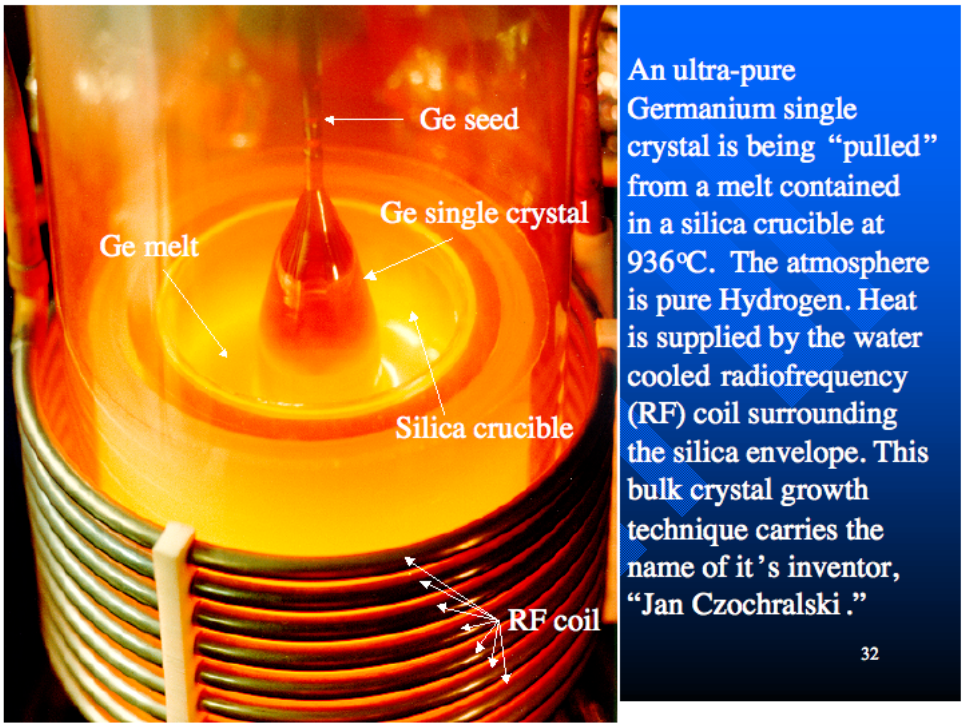

Figure E.2: A Ge crystal being grown in a Czochralski crystal grower (courtesy Eugene Haller).

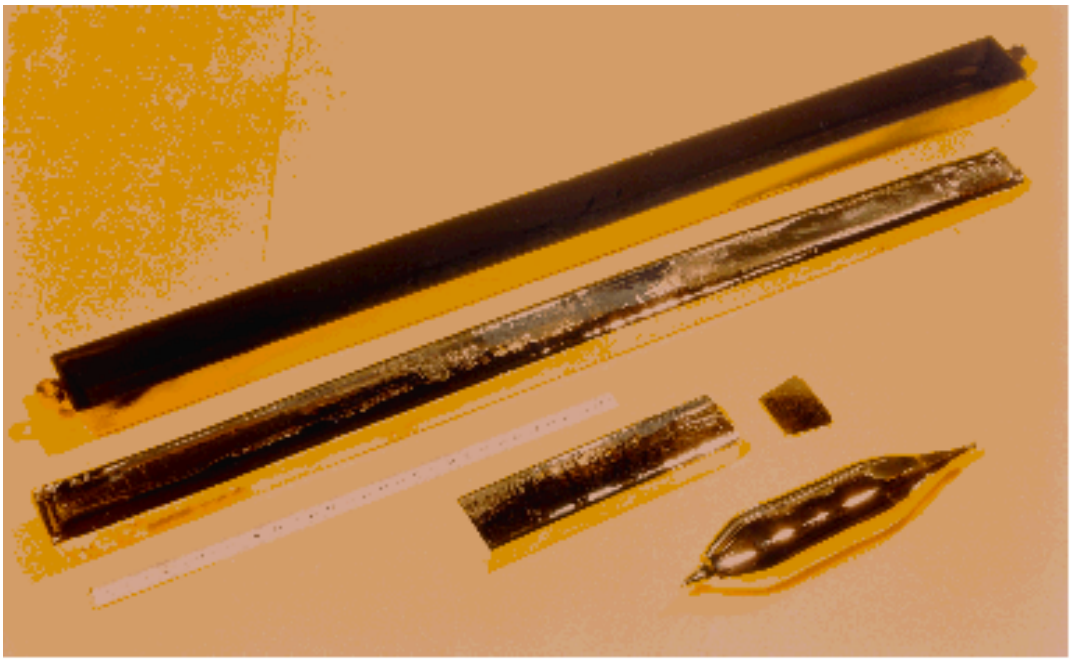

Figure E.3: Zone refined polycrystalline bar and Czochralski grown single crystal.

Element	Segregation coefficient
Co	1E-6
Zn	4E-4
Mn	1E-6
Fe	3E-5
Tl	4E-5
Bi	4.5E-5
K	?
U	?
Th	?

Table E.2: Segregation coefficients of relevant elements (see Landolt and Bornstein, new series, vol. 17, c, Technology of Si, Ge and SiC, 1984.).

crystal is grown, the radioisotopes will be concentrated towards the tail end of the crystal, which will be not be used in a detector (Fig. E.4).

The concentration of impurity along a grown crystal is given by:

$$N = N_o K(1-S)^{K-1}$$

where N_o is the concentration of the impurity in the starting Ge melt, K is the segregation coefficient of the impurity, S is the volume fraction along the crystal. For $K << 1$, and assuming that the last 10% of the crystal will not be used, the concentration of the impurity in a detector blank will be less than $10N_oK$.

For the radioisotopes in Table E.2, their concentrations will be reduced by a large factor just in the crystal growth process. Since the production rate of most of the cosmogenic radioisotopes in enriched Ge is estimated to be on the order of 1 per day per kilogram. The number of such nuclei will be less than 1000 per kilogram even if the Ge stays above ground for 1 year after enrichment. So, immediately after crystal growth, the major part of the crystal is essentially completely free of these radioisotopes even if zone refining and crystal growth were to be conducted above ground. The crystal can then be quickly transferred to an underground facility for storage or detector fabrication. Therefore, the only significant advantage of underground crystal production is the reduction in ^{68}Ge production, since the ^{68}Ge concentration is not reduced by the process. The zone refining process takes about 1 to 2 weeks, and the crystal growth takes 2 days. Since only a fraction of the Ge starting material ends up as detector blanks, the rest of the material will be recycled and brought back to the zone refining process (Fig. E.5). Therefore, the average time that the Ge material spent circulating in the crystal growth process is several times the time required for one cycle of zone refining and crystal growth. So, for above-ground crystal production, the effective exposure time for ^{68}Ge production calculation is estimated to be $\sim$8 weeks on average based on the anticipated crystal yield (see section E.3.3 (Throughput)).

E.3.3 Underground Crystal Growth Facility

Throughput The number of crystals that need to be grown per year depends on the required number of detector blanks per year and the crystal yield. The crystal yield (i.e., the number of useable detector blanks divided by the number of crystals grown) depends on the type and diameter of the detector blanks. The crystal yield for p-type detectors is significantly higher than that for n-type detectors. This is because the main p-type impurities in Ge tend to distribute evenly over a long section of the crystal, whereas n-type impurities tend to segregate towards the tail end of

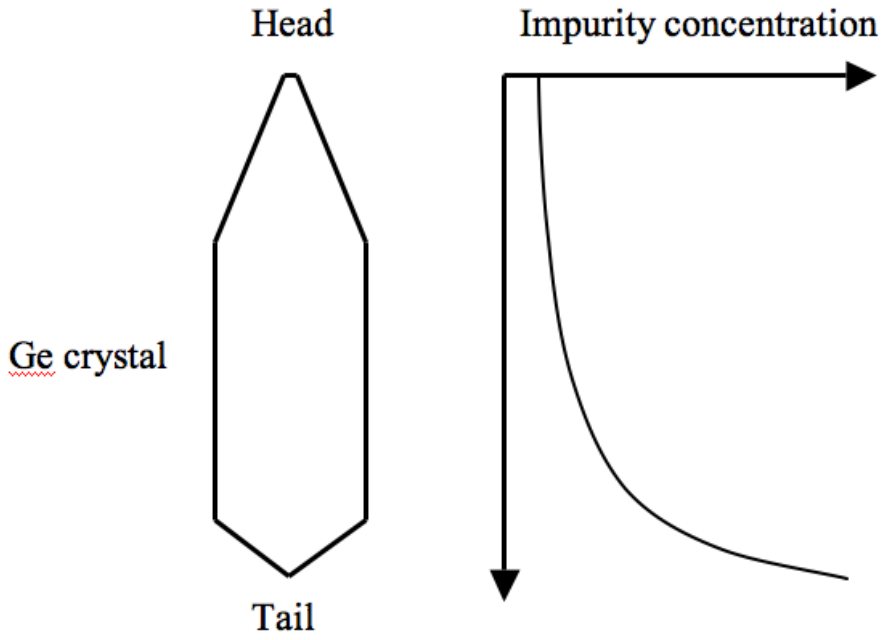

Figure E.4: Impurity concentration variation along a Ge crystal for segregation coefficient < 1.

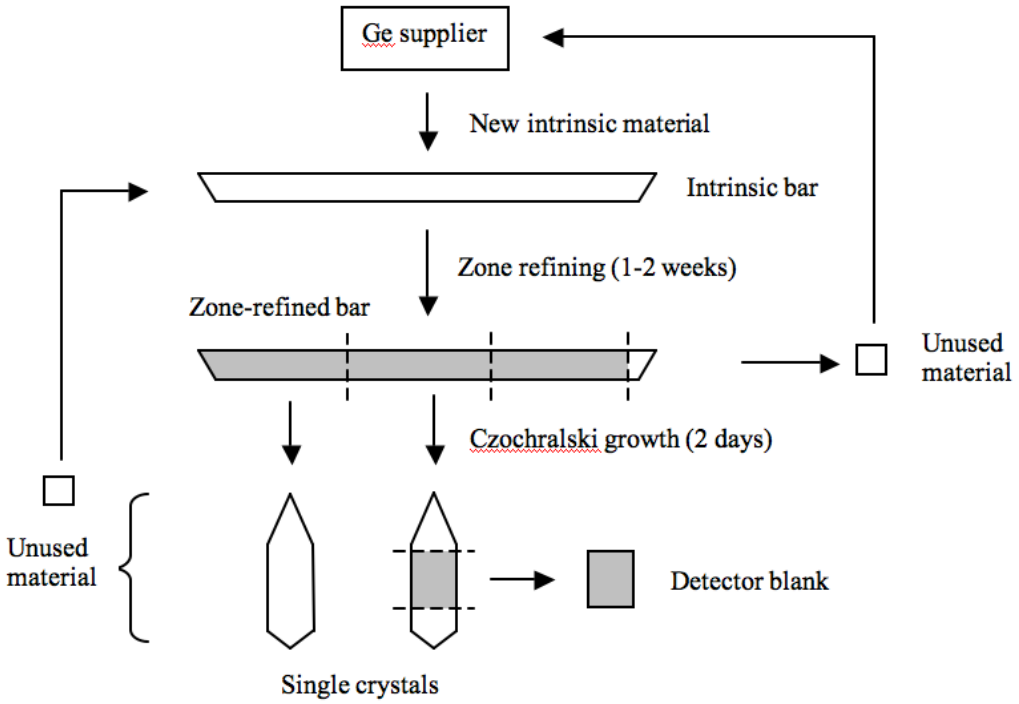

Figure E.5: The Ge crystal production process.

the crystal producing an increasing n-type impurity concentration profile. For p-type detectors, it is sometimes possible to obtain 2 useable coaxial detector blanks from one crystal, but for n-type, at most only one blank can be obtained. P-type coaxial detectors also have the advantage that they are much less sensitive to electron traps than n-type coaxial detectors. Low levels of electron traps commonly occur in Ge crystals and this is the reason n-type coaxial detectors typically have worse energy resolution than p-type coaxial detectors. However, this is not likely to be a significant issue affecting yield unless the absolutely best energy resolution is required. The crystal yield also depends strongly on the diameter of the detectors. Increasing the diameter just from 65 mm to 70 mm will decrease the yield substantially.

The requirements for an underground crystal production facility are broken down below in terms of equipment, facility and operation requirements. In this analysis, a production rate of 100 detector blanks per year is assumed. The detector is assumed to be n-type coax, 65 mm diameter and 65 mm long ($\sim$ 1.0 kg detector mass). Based on information gathered from commercial manufacturers of Ge crystals and detectors, we estimate that the crystal yield (number of detector blanks per crystal grown) will be roughly 50%. This means that 200 crystals need to be pulled per year to obtain 100 blanks for detector fabrication. We consider here detector blanks that meet the crystallography and impurity concentration requirements for detector fabrication. The number of working detectors that would result from 100 blanks will depend on the yield in detector fabrication, which is discussed later. The requirements listed below are only rough estimates based on inputs from various sources. The actual requirements may differ significantly depending on the process adopted.

Ge recovery A unique requirement of this project is the need to recover the enriched Ge that is normally lost during processing. Different forms of Ge "waste" are produced by various processes. It should be stressed that recycling of these components increases the mean time the bulk Ge is exposed to cosmic rays and consequently increases the ^{68}Ge concentration for entire stockpile, unless these steps are performed in a cosmic ray shielded environment. Simple arguments that detector manufacturing takes "x days" and consequently the levels of ^{68}Ge are fixed by this scale underestimate the true level of cosmogenic background concentrations – the mean age of the material will be affected by all material recycled, included the bulk and manufacturing waste streams as well as unsuccessful attempts in creating crystals. The normal recycled waste streams are listed below with an estimate on the amount of Ge waste generated for each detector blank produced:

- Bulk - unused sections of zone refined bars and grown crystals. 4 kg/blank.
- Sawing and grinding – Ge particles in cutting fluid. 0.5 kg/blank.
- Lapping – fine Ge particles mixed with lapping compound. 0.01 kg/blank.
- Etching – Ge in acid mixture (HNO3 + HF). 0.2 kg/blank.

The recovery of the bulk waste is simple because most of it can be put back directly into the zone refining process after surface cleaning. The tail ends of zone-refined bars, which have high impurity concentrations, will need to be returned to the Ge supplier for purification, but this is a small fraction ($\sim$10%) of the total bulk waste.

During sawing and grinding operations, the waste will need to be collected. The saws and grinding equipment will need to be modified such that the Ge waste can be efficiently captured. The Ge particles in the waste will need to be separated from the cutting fluid, cleaned, re-melted and refined back into intrinsic material.

The lapping waste contains fine Ge particles mixed with lapping compound such as SiC or Al_2O_3. To recover the Ge would likely require chemical separation. Since the amount of Ge in this waste is small, it may not be economical to perform the recovery.

For etching waste, the recovery of Ge involves chemical processing. One method is to evaporate off the etchant to leave behind Ge oxide (GeO_2). In the process, the etchant vapor can be condensed

and recovered. The GeO_2 can then be reduced in H at ∼650 °C (Ge sublimes at 710 °C) to obtain Ge. After that, the Ge will be refined into intrinsic material before returning to the zone refining process. This and other recovery methods, as well as the process requirements, are being studied by the Majorana Collaboration. It is logical to ultimately perform the recovery in the same underground facility to avoid ^{68}Ge production, and to reduce the complexity and cost involved in transporting large quantities of acid mixtures to a separate site. Since the Ge recovery process is still being investigated, the cost and facility requirements for Ge recovery are not included in this study.

Equipment requirements

- Zone refiners (2). Each zone refiner includes a RF generator, silica boat to contain the Ge, a silica envelope to contain a flowing H atmosphere, and a traveling RF heating coil. A supply of high purity H gas and cooling water (for the RF generators) are needed. The zone refining process takes 1-2 weeks to complete. Each zone-refined bar can supply several loads for the crystal pullers, the exact number of loads depends on the design of the refiners. While it may be possible to have only one zone refiner feeding the crystal pullers, a more conservative approach is to have 2 zone refiners.

- Crystal pullers (2). Each crystal puller includes a RF generator, crystal growth apparatus and associated control mechanism and electronics. A supply of high purity H gas and cooling water are needed. The crystal growth process takes 2 days to complete, with one day to clean and re-load the puller and 1 day to grow the crystal (and cool down). In principle, it is possible to have just one crystal puller to achieve the ∼200 crystal per year throughput. However, with likely down times due to maintenance and repairs, having 2 crystal pullers available is more viable. The crystal pullers should be installed in a clean room (class 100).

- Chemical hoods (3). The chemical hoods are needed for cleaning the Ge and parts for the crystal pullers and zone refiners, as well as for preparing samples for Hall measurements and evaluating dislocations. The hoods require DI water supply, industrial or tap water, dry nitrogen supply (nozzles) and drainage to collect waste acids for neutralization and disposal or recovery of Ge. A minimum of 3 hoods will be required, with at least one in the clean room to service the crystal pullers.

- Diamond saw (1 or 2). Diamond saws are needed to cut Ge crystals for processing. It is possible to use a diamond loaded wire saw or circular blade saw (OD or ID type).

- Grinding/lapping machines (2). These machines are used mainly to "machine" the crystals into the desired shape for detector fabrication.

- Hall and resistivity measurement station (1). This is used to measure the carrier (net impurity) concentration and mobility of the Ge crystals.

- Ge recovery equipment. This will include modifications to saws and grinding equipment to capture Ge waste, and process equipment to recover Ge from etchants.

Facility requirements

- Class 100 cleanroom: 300 sq. ft. The cleanroom will mainly house the crystal pullers and the associated equipment (hoods, etc.).

- General lab space (class 10,000 ?): 500 sq. ft.

- Ge machining lab: 500 sq. ft.

- Cooling water: 50 gal/min

- Acid neutralization system (acid recovery system?)
- DI water: 2 gal/min
- Electricity: 100 kW

Operation requirements

- Acid (HNO3 and HF mixture): 400 gal/yr
- Solvent (methanol): 100 gal/yr
- Water: 100,000 gal/yr.
- Hydrogen (high purity): 50,000 cu.ft./yr
- Staffing: 2-3 FTEs

E.3.4 Approach

The initial development of high-purity Ge crystal growth was carried out in the late 1960's and early 1970's primarily by two groups at General Electric and Lawrence Berkeley National Laboratory. Commercial involvement followed, which led to the successful commercialization of high-purity Ge detectors. While the crystals initially grown at LBNL have been limited to about 4 cm in diameter, the largest crystals successfully grown today at commercial facilities have diameters up to $\sim$10 cm.

The growth of Ge crystal for detectors requires substantial know-how and experience. The material requirements are very stringent. The required purity of the Ge crystals is at or below the parts-per-trillion level, and it has to be within a narrow range to be suitable for detector fabrication. In addition, the crystallography of the material needs to be well controlled to achieve a certain range of dislocation densities. Neither dislocation-free nor high-dislocation-density materials will result in acceptable detectors.

The two companies in the U.S. that currently have high-purity Ge crystal growth capability, Ortec (Ametek) and Canberra, have developed their crystal growth technology over many years. Because their crystal growth technology is now a fairly well established commercial process and largely proprietary, the most viable approach to building an underground crystal growth facility is to contract one of the commercial suppliers to carry out the project, operate the facility, and perform the crystal growth. Developing a crystal growth capability independent of the commercial suppliers, while not impossible, would be risky, time consuming, and likely not cost effective. If the facility is to be developed by a commercial supplier, it would obviously be advantageous logistically and economically to have the underground site located close to the supplier. Both U. S. suppliers have their crystal growth operations in Oak Ridge, TN.

E.3.5 Cost and Time

In this cost analysis, we assume that the establishment and operation of the underground Ge crystal growth facility will be carried out by one of the commercial suppliers. Since the construction and operation of such a facility is a significant undertaking and involves many technical as well as business considerations, an accurate estimate of the cost is not possible at this stage. However, based on information from the commercial suppliers and other sources, a rough estimate can be made that would at least serves as guidance in examining the cost-benefit tradeoff of such a facility.

The estimated cost for an underground crystal growth facility is broken down as shown below:

- Equipment - 2 crystal pullers, 2 zone refiners, diamond saws, chemical hoods, measurement systems, etc. $2 million.

- Facility - laboratory construction, clean rooms, utilities, and other supporting equipment. 1 year. $2 million.
- Effort - assembling and commissioning crystal growth equipment, ramp up crystal production. 3 staffs. 2 year. $2 million.
- Operation - crystal growth effort. 2 staffs, supplies, utilities. $1 million per year.

The estimated time from start of facility construction to beginning of crystal growth is 2 years. Additional time would be required to ramp up production to the rate of 100 blanks per year. The first 100 blanks would be obtained at the end of year 4 after construction start, at a total cost of $6 million. Thereafter, the production rate would be 100 blanks per year, at a cost of $1 million per year.

E.4 Ge Detector Fabrication

E.4.1 Fabrication Process

Detector fabrication typically involves the shaping of the Ge crystal to the desired geometry, removing mechanical damage by lapping and chemical etching, forming electrical contacts on the Ge crystal, and treating the intrinsic surfaces of the Ge to achieve low leakage current and low noise under the expected operating conditions.

Shaping of the Ge crystal is achieved by first cutting a section of the as grown crystal to the desired length and with the required range of impurity concentration. The outer part of the crystal is normally not perfectly cylindrical and it is ground down to obtain the desired diameter. For coaxial detectors, a center hole is produced by grinding, EDM, or other means. Typical coaxial detectors have a closed-end geometry, meaning the center hole does not go through the detector but stop at a distance ($\sim 1 - 2$ cm) from the closed end. Mechanical damage near the surface of the Ge from the shaping process is then removed by lapping and chemical etching. Etching is typically done using a HNO3 and HF acid mixture.

Typically for a Ge detector, an n+ (heavily-doped n-type) contact and a p+ (heavily-doped p-type) contact are needed to form a p-i-n diode structure. This allows the detector to operate under reverse bias to above full-depletion voltage with low leakage current. The n+ contact is usually produced by diffusing Li into the Ge at a temperature around 250 C, resulting in a doped layer around 1 mm thick. The p+ contact is typically formed using B ion implantation, which gives a contact around 1000 Angstrom thick. The contacts are then usually metalized to allow low-impedance electrical connections to be made and to reduce contact spreading resistance. For an n-type (p-type) coaxial detector, the n+ (p+) contact is formed on the inside surface of the hole, while the p+ (n+) contact is formed on the outer cylindrical and closed-end surface (Fig. E.6). This ensures that the detector depletes from the outer contact, which will result in a lower full-depletion voltage and a more uniform electric field distribution.

Following, or coincident with, the formation of the contacts, the intrinsic surface (i.e., the surface of the Ge detector not covered by contacts) is treated to achieve low leakage current, low noise and stable operation. This may involve different treatment methods such as chemical processing, coatings, etc.

After a detector is fabricated, it will be tested for depletion voltage, leakage current, noise, spectrometric performance, etc. If the detector does not meet requirements, it will be reprocessed. If the detector fails to meet requirements after a number of attempts, the detector will be recycled back to the zone refining process.

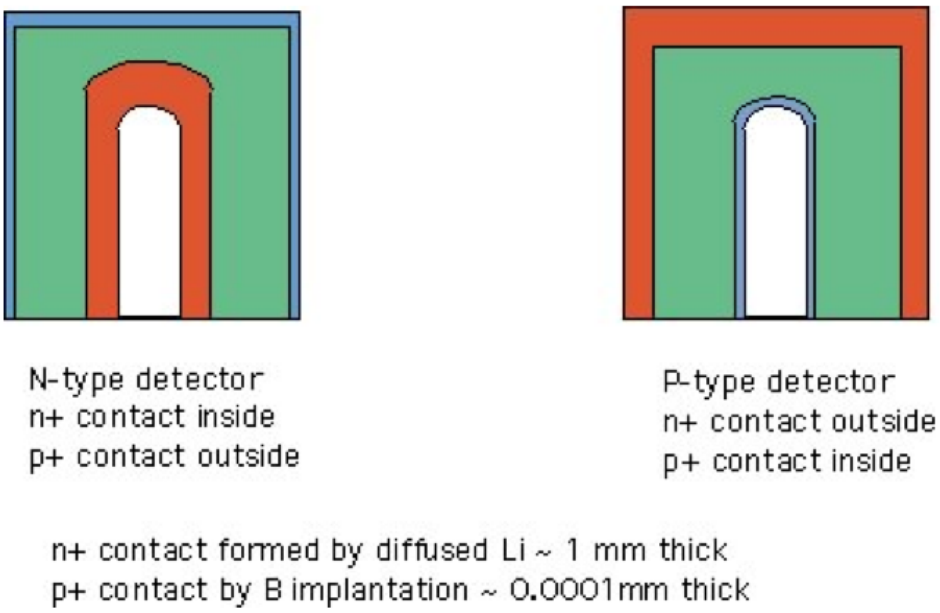

Figure E.6: Schematic of n- and p-type coaxial detectors.

E.4.2 Detector Fabrication Facility

Throughput Assuming the crystal growth process is well controlled, each detector blank, which has been selected base on impurity concentration and crystallography requirements, should yield a working detector. There will be occasional detectors that fail to work due to excessive trapping or damages during processing and testing, but for the present analysis, the detector yield can be assumed to be 100%. However, the time required to fabricate a detector can vary widely depending on how well the fabrication process is developed, the complexity of the detector, and the skill of the workers. Often time, repeated processing is required to produce a properly functioning detector. The fabrication and testing of a segmented coaxial detector is substantially more difficult than that of a single element coaxial detector, and it would require more time to produce.

A crucial issue that affect the detector throughput is which detector design will be adopted and how well developed is the fabrication process for that particular detector design. For segmented n-type coaxial detectors, the two commercial suppliers of Ge have the necessary technology to fabricate the detectors. However, it is not clear if the process is advanced enough to allow the fabrication of such detectors with the required throughput. Currently, on the order of 10-20 n-type segmented coaxial detectors are produced per year. To achieve throughput of ∼100 per year may required additional development to improve and streamline the process, and additional workers will need to be trained. Assuming that the detector design is not overly complex and that a relatively reliable fabrication process is established, the average time required to produce a working detector is estimated to be 4 weeks, including the time for testing and reprocessing. To produce 100 detectors per year would mean that on average 8 detectors will be worked on at any given time. This would require ∼4 skilled staffs to carry out the work.

Equipment The basic equipment needed for detector fabrication include:

- Evaporators (2). Typically 2 evaporators are needed. One for Li diffusion and one for metal-

lization of contacts.

- Sputter deposition system. This may be used for metallization or surface passivation coatings. It may or may not be required depending on the particular detector fabrication process.
- Ion implanter. This is used to perform ion (boron) implantation to produce contacts (p+).
- Chemical hoods (2). This is used for chemical etching and other chemical treatment processes.
- Test stations (4). Several test stations are needed to test fabricated detectors. Each station includes a test cryostat with appropriate front-end electronics, a vacuum pump, measurement electronics, and nuclear spectroscopy electronics. To expedite detector testing and reduce risks of detector failure, it is critical to have test cryostats designed for easy detector loading and short thermal cycling time.

Facility requirements

- Class 100 cleanroom: 200 sq. ft. A cleanroom may or may not be needed depending on the fabrication process requirements.
- General lab space (class 10,000 or better): 1000 sq. ft.
- Cooling water: 50 gal/min
- Acid neutralization system / acid recovery system (may be shared with crystal growth facility).
- DI water: 2 gal/min
- Electricity: 50 kW

Operation requirements

- Acid (HNO3 and HF mixture): 100 gal/yr
- Solvent (methanol): 50 gal/yr
- Water: 30,000 gal/yr.
- Staffing: 4 FTEs

Cost and time The cost of equipment for a detector fabrication facility is probably comparable to that for the crystal growth facility, while the cost to build the facility is likely less because of somewhat reduced demand on utilities, and, if this is built at the same location as the crystal growth facility, much of the supporting equipment can be shared. The cost to build and setup the detector fabrication facility is estimated to be $4 million, and it would take 1-2 years to complete. The operating cost is estimated to be $1.5 million per year for a throughput of 100 detectors per year, again assuming that a reliable process to fabricate the detectors is available.

E.5 Summary

The benefit of underground crystal growth and/or detector fabrication is reduced cosmogenic radioisotope production. The number of radioactive nuclei produced is determined by the time the Ge material spent above ground. Various combinations of underground and above ground operations for crystal growth and detector fabrication can be envisioned. Table E.3 presents a summary of the effective exposure time for different scenarios. Since the main radioisotopes of interest are effectively removed during crystal growth, the exposure time is considered to start right after crystal growth.

For ^{68}Ge, the exposure time starts right after the isotope enrichment process. The exposure times listed in the table only consider the crystal growth and detector fabrication process. The time that the Ge material spent between the Ge enrichment process and the beginning of the zone refining process will need to be added to get the total exposure time for ^{68}Ge production.

Table E.3: Estimated exposure times for the crystal growth and detector fabrication processes conducted above ground and underground.

Above ground	Growth+Fab	Growth	Fab	
Underground		Fab	Growth	Growth+Fab
Exposure time (days)				
^{68}Ge	90	60	30	0
Others	30	2	30	0

The estimated cost to construct the crystal growth facility and to produce the first 100 detector blanks is $6 million. This will take ∼4 years to complete. Thereafter, the production of 100 blanks per year will cost ∼$1 million per year. This assumes that the blanks are for 65 mm diameter n-type coaxial detectors.

The estimated cost to construct the detector fabrication facility is $4 million, and this will take ∼2 years to complete. Detector production at a rate of 100 per year will cost ∼$1.5 million per year. This assumes an established, reliable fabrication process is available. Additional process development may be required depending on the detector design, which would add cost and time.

F Reference Plan Summary

In this appendix we present a concise summary of the information and specifications for various components of the Majorana subsystems.

Reference Design Summary Table

Ge Production	
Enrichment	86% ^{76}Ge
Total Mass Production	160 kg of 86% ^{76}Ge
Technique	gaseous centrifuge
Chemical Form	GeO_2
Costed Rate of Production	75 kg/yr
Preferred Rate of Production	100 kg/yr
Transport Method	rail/ship/rail from Russia to U.S. with expedited service
Transport Time	∼30 days
Transport Shielding	1 m iron or 2 m concrete
Activation Reduction Factor	10-25
Ge Reduction and Refinement	
Form	Ge metal
Zone Refinement	7-8 passes
Impurities	$\sim 10^{10}$ cm^{-3}
Estimated Material Losses	20%
Crystals	
Configuration	closed-end coaxial cylinders
Size	62 mm diameter × 70 mm long (potential variable length, tolerances)
Required Production Rate	2 crystals/week
Mass	1.1 kg/crystal
Depletion	n-type
Axial Segments	3
Azimuthal Segments	2
Total Number	116 (57 crystals × 2 modules + 2 spares)
Estimated Material losses	5%
Fabrication Site	aboveground
Fabrication Location	Oak Ridge, TN
Assembly Location	various
Modular Detector Array	
Number of Modules	2
Array	
Geometry	3 crystals high in 19 closely packed stacks
Cryostat	
Type	vacuum
Material	electroformed Cu
Diameter	∼40 cm
Height	∼40 cm
Average Thickness	∼5 mm (conservative for implosion risk)
Access	fully removable top and bottom
Seal Technology	indium bead (CTFE possible)
Mass	∼40 kg (including coldplate, assuming 5 mm avg thickness of outer wall)
Cooling mechanism	IR cooling via thin Cu jacket on coldplate
Expected Cool Down Time	∼4 days
Crossarm Length	∼0.5 m
Crossarm Diameter	∼5 cm
Coldfinger Diameter	∼3 cm
Number of Crossarms	1-2

Hi-level Signal Conductor Length	∼1 m
String	
Number of Crystals	3
Support Mechanism	suspended from an aperture in the coldplate
Coldplate Mass	∼10 kg
Coldplate Thickness	∼1 cm
String Design	Cu tube and tray with thick cap in coldplate
Support Mass	∼800 g/module
Tubing Diameter (Thickness)	6 mm (0.2 mm)
Tubes Per String	3
Tray Design	circle with 3 radial spokes
Contacting Pressure	plastic loop, gravity in tray
Favored Materials	electroformed Cu, CTFE, Cu on Kapton®
LN_2 system	
Weekly LN_2 Consumption	∼500 L
Underground Storage	suggest 7 days
Dewar Hold Time	suggest 14 days
Radiopurity Requirements	Cooling: not much Cover gas: could be charcoal scrubbed
Shield	
Muon Veto Coverage	4π
Muon Veto Efficiency	>95%
Muon Veto Layers	1 (or possibly 2)
Muon Veto Thickness	10 cm
Veto Panel Dimensions	5 cm × 50 cm × 120 cm (check JINR)
Neutron Reduction (fission and α,n)	30 cm hydrogenous moderator
Outer Neutron Moderator	25 cm polyethylene
Inner Meutron Moderator	5 cm borated polyethylene
Outer Shield (bulk gamma absorber)	∼45 cm Pb
Inner Shield	10 cm Cu
Inner Shield Design	layered
Inner (replaceable) Layer	electroformed Cu
Outer Layer	electroformed or OHFC Cu
Inner Shield Mass	
Service Plan	removable sliding monoliths
Array readout	
Number of Channels per Crystal	6 + 1
Number of Conductors per Crystal	24 + 5
Conductor Design	ribbon
Ribbon Materials	Cu on Kapton®$or PEN$
Limiting Capacitance (high level)	<100 pf (assuming a 1 m cable)
Limiting Capacitance (low level)	
Capacitor	Cu on Kapton®$or PEN$
Capacitance	2 nf
Resistor, Feedback Technology	RuO
Resistor, Resistance	2 GΩ
High-speed Front-end Preamplifier	
Low-Energy Threshold	<5 keV desired
Electronic Noise	200 eV
Location	above cold plate
Crystal to Preamp Lead Length	30 cm max, 15 cm typical
Bandwidth	≥25 MHz
Heat Load	40 mW/channel
Mass	≤0.3 g/circuit/channel
Substrate Type	Teflon® or Kapton®
Type	hybrid bare dies
Bonding Method	TBD (wire bonding, eutectic Si/Au die bonding preferred)
Manufacturer	custom
Pulse Digitization Readout	

Number of Channels	57 × 7 per module
Manufacturer	commercial (others possible)
Digitization Speed	≥80 MHz (following manufacturers)
Digitization Record Length	1.2 μsec minimum (not counting energy: if you dont get it from the filter, you might need ∼8 μsec!)
Site	
Depth	>4500 mwe
Space	3500 ft^2
Basic Cleanliness	class 10000 clean room or better
Location	North America
Assembly Room	
Floor Space and Overhead	300 ft^2 × 12 ft
Cleanliness	class 100 clean room
Electrical Power	
Ventilation	
Allowed Radon Level	
Detector Room	
Floor Space and Overhead	600 ft^2 × 12 ft
Cleanliness	class 100 clean room
Electrical Power	
Ventilation	
Allowed Radon Level	
Vibration Isolation	
Facilities Needed	control room eforming shop machine shop storage assembly hall experiment hall air lock
Infrastructure Items	
	Rn scrubber particle filtration class 100 hoods

G Germanium Processing and Chemical Yield

Common commercial and enriched germanium detector production differ in one key respect: ordinary germanium is available in bulk for $0.70/g while enriched Ge for the Majorana experiment will cost in excess of $50/g. For this reason, the efficiency of processes in germanium detector production must be analyzed to maximize the return on investment in materials. To analyze this, a model has been constructed of the production process. While this is a simplified model, it serves to predict the initial mass needed, the rate of production possible as a function of capital equipment committed, and the integrated dose of the germanium to surface cosmic ray induced neutrons. A key feature of the model is the focus it provides on improvements needed in preventing material losses.

A schematic of the detailed Ge material flow path is shown in Figure G.1. Materials can be lost at several stages in the process. The design of the chemical purification apparatus is a key feature: systems designed for large batches leave very large absolute quantities behind as residue in the apparatus. These materials are not lost: most of the material is pushed out by the next batch. However, unless the purification occurs underground, this material will receive a large neutron dose, increasing Majorana backgrounds from ^{68}Ge. Several potential vendors for chemical purification have been investigated in the US, Europe, and Russia. Most have ∼70% efficiency in chemical yield.

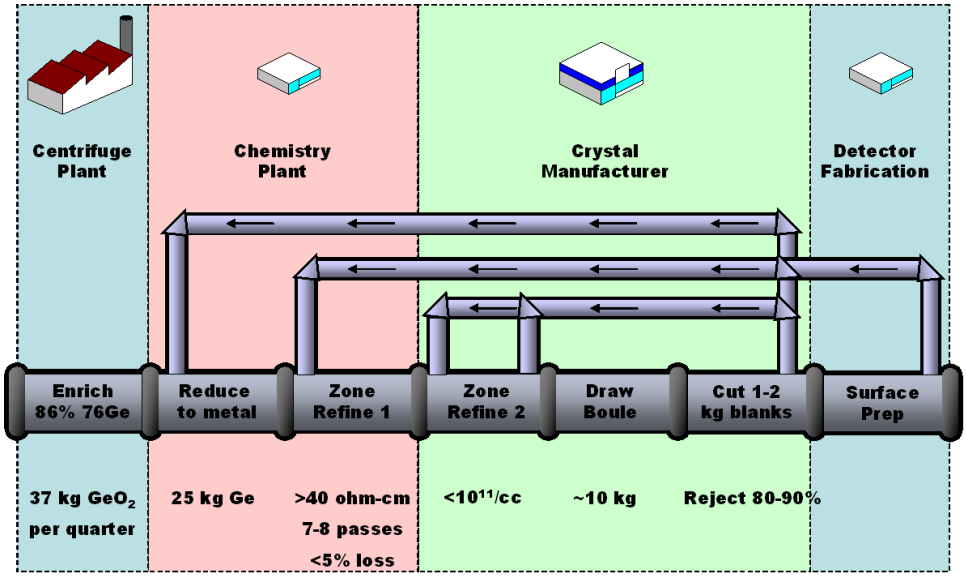

Figure G.1: Detailed Ge material flow path, from enrichment through surface preparations. Material losses at each stage will be recycled at earlier points in the path.

One facility has produced a small batch capability which can deliver 96% chemical yield in steady state, with a very minimal quantity left behind.

Detector manufacturing has two major steps: crystal pulling and detector fabrication from the crystal blanks. Preparation for crystal pulling includes zone refining steps that potentially generate waste when the ends of the zone-refined bars are trimmed to improve average purity. This material can be recycled readily after return to the chemical purification facility. The crystal pulling process rejects the majority of the remaining material. Only 1-2 kg of the boule go into crystal blanks. Most of the remainder can be recycled to the zone refinement within the manufacturer's facility. Cutting waste, (kerf) lapping, and etchants are also produced. Some of this material can be recovered readily; other parts are less easily cleaned and transformed into starting materials. Of particular concern are sludge: mixed etchants, Ge mixed with lapping compounds, and other similar wastes.

The IGEX experience was optimized for cost, not overall exposure, because the germanium obtained by IGEX was already at ^{68}Ge saturation. For this reason, procedures were developed to collect materials that would have ordinarily been wasted. IGEX achieved a ∼95% overall material efficiency. Majorana should attempt a similar efficiency.

G.0.1 Model Assumptions

Enrichment Assumptions:

- 160 kg input metal equivalent oxide mass in 3 shipments per year of ∼25 kg metal equivalent mass.

Purification Facility:

- First batch 80% chemical yield, all others 96% yield (assume no recovery).

Manufacturing Facility:

- Two crystal pullers in tandem available.

- One week to zone refine and pull crystal.
- Average 8 kg Ge per boule.
- 600 g loss in zone refiner per boule goes back to chemical purification.
- This material has same recovery percentage as input material.
- Average 1.5 finished crystals (1.1 kg each) per boule. Flat random distribution between 1 and 2 crystals per boule.
- Loss per boule of 200 g (assume unrecoverable).
- Remainder of boule (6-7 kg) recycles to zone refinement within manufacturer. Assume none of that goes back for chemical purification.

G.0.2 Model Results

Overall Efficiency:

- 160 kg in, 127.6 kg out (116 crystals produced, 114 needed, within random factors of the perfect amount)

Chemical purification:

- ∼150% of material is processed through chemical processing.
- ∼13.5 kg lost into undesirable chemical forms at chemical purification plant (with development, this amount could be reduced).

Detector Manufacturing:

- Pullers are not completely busy, could handle higher throughput. Assume detector fab is the hold up.
- ∼11.5 kg is lost into undesirable chemical/physical forms in the manufacturing process.
- About 7 kg of material will be rejected in the production of the last usable boule. This material would be a candidate for future experiments or for blending down to make lower enrichment crystals.
- Last detector is 9 months after last Ge delivery to chemical purification plant.

Table G.1: Summary of Ge material accounting

Loss at Chemical Purification:	13.5 kg
Loss at Manufacturer:	11.5 kg
Orphaned material at manufacturer:	7 kg
Detector mass:	127.6 kg (116 crystals)
Overall Efficiency:	80% (127.6/160)

H Development of the 57 Crystal Module Design

The development of the concept for a 57-crystal module arose from the original multi-crystal cryostat developed by the PNNL-USC double-beta decay collaboration, a search for double-beta decay, including excited states. The PNNL-USC concept employed two cryostats each with 7 crystals configured in a hexagonal close-pack arrangement [Bro84, Bro85a, Bro85b]. These 14 natural detectors in two cryostats were designed to maximize crystal-to-crystal background rejection and the probability of multi-crystal detection of excited state decay. Although the availability of enriched material changed collaboration plans and this design was never completely fielded, the cryostat was built and succeeded in cooling. Subsequent development of cryostat technology using only radiopure materials achieved improved thermal performance. Improved emissivity of Cu surfaces decreased the heat load from IR without requiring multi-layer insulation, a significant source of radioactivity. Improved mechanical supports decreased the heat load from direct conduction to negligible levels as compared to both IR and heat from front-end electronics. A recent large cryostat design (30 x 30 cm right circular cylinder) was designed to hold 16 crystals and had a heat budget of 3.5 W from IR, 3.5 W from front-end electronics, and only 150 mW from mechanical supports.

The idea that more than 7 crystals could be cooled simultaneously led to the first Majorana design including 21 crystals in three layers, each of 2.4 kg mass for a total of 50 kg. This array would have been housed in a ∼30 x 30 cm right circular cylinder of copper. To minimize the impact of radioactivity in the front end electronics, the electronics would be located on one end of the cylinder, behind a thick (∼1cm) copper shield. The capacitance and cross talk introduced by long, low-level cabling limited the number of layers and thus the length of the cylinder. Crystal-to-crystal suppression in such a 21-crystal array would have been powerful, and the use of detector segmentation would provide an additional single-site/multi-site background cut needed in early background calculations. A high degree of segmentation could make individual segments as small as 200 grams. In simulations it was noted that as the mass of the segments got smaller, the background rejection impact also shrank and it was thus noted that an optimization including cost, schedule, and performance was needed.

After construction of several segmented detectors by collaboration members, and after further discussions with manufacturers, it became clear that in order to manufacture large numbers of detectors, the yield of large (∼2kg) crystals was too low. A key parameter in ensuring adequate yield of detectors per month is the diameter and length of the finished crystal. Larger crystals are more sensitive to the homogeneity of the donor and acceptor dopants, and fewer large crystals with acceptable dopant profiles can be cut from each grown boule. Thus a smaller crystal diameter provides a greater yield of working detectors per kilogram of grown crystal stock and so is more likely to deliver low-cost, low-risk detectors. (Note: after a future merger with GERDA, it may be possible to house GERDA detectors in a cryostat of this design and performance.)

To keep the approximate mass of Ge per module the same, the next-larger hexagonal symmetry was chosen, again in a three-layer arrangement to limit the low-level signal path length. This close-pack array has 19 units per layer for a total of 57. If these units are 1.1 kg, the mass is 62.7 kg. The cryostat needed to house such an array would be ∼40 cm x 40 cm. There are several benefits to this conceptual design: higher detector yield, lower detector cost, and higher granularity. The resulting better crystal-to-crystal background rejection implies less need for segmentation. In fact, this design could support detectors of the same diameter in any length, opening the possibility of varied detector sizes to further maximize yield and so lower cost.

-

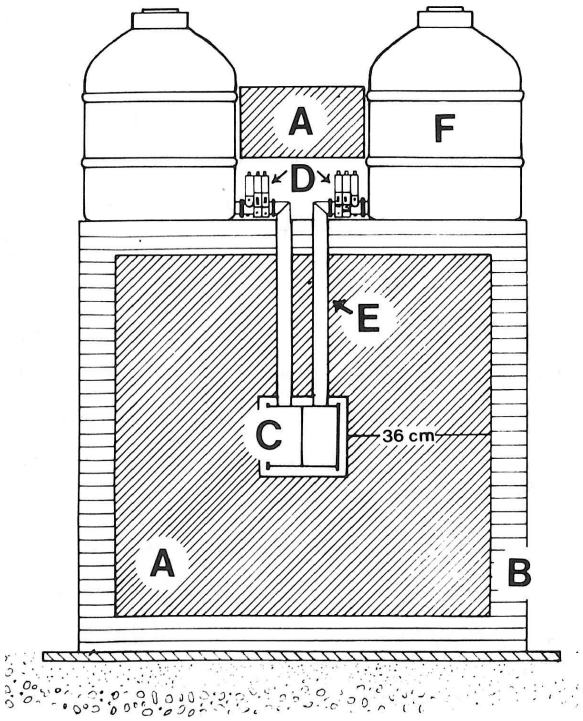

Figure H.1: A: Lead Shielding, B: Anti-cosmic scintillator, C: Cryostats with 7 each crystals, D: Preamplifiers, E: Coldfinger/vacuum cryostat, F: LN Dewar

Figure H.2:

I Radioactive Decay Chains

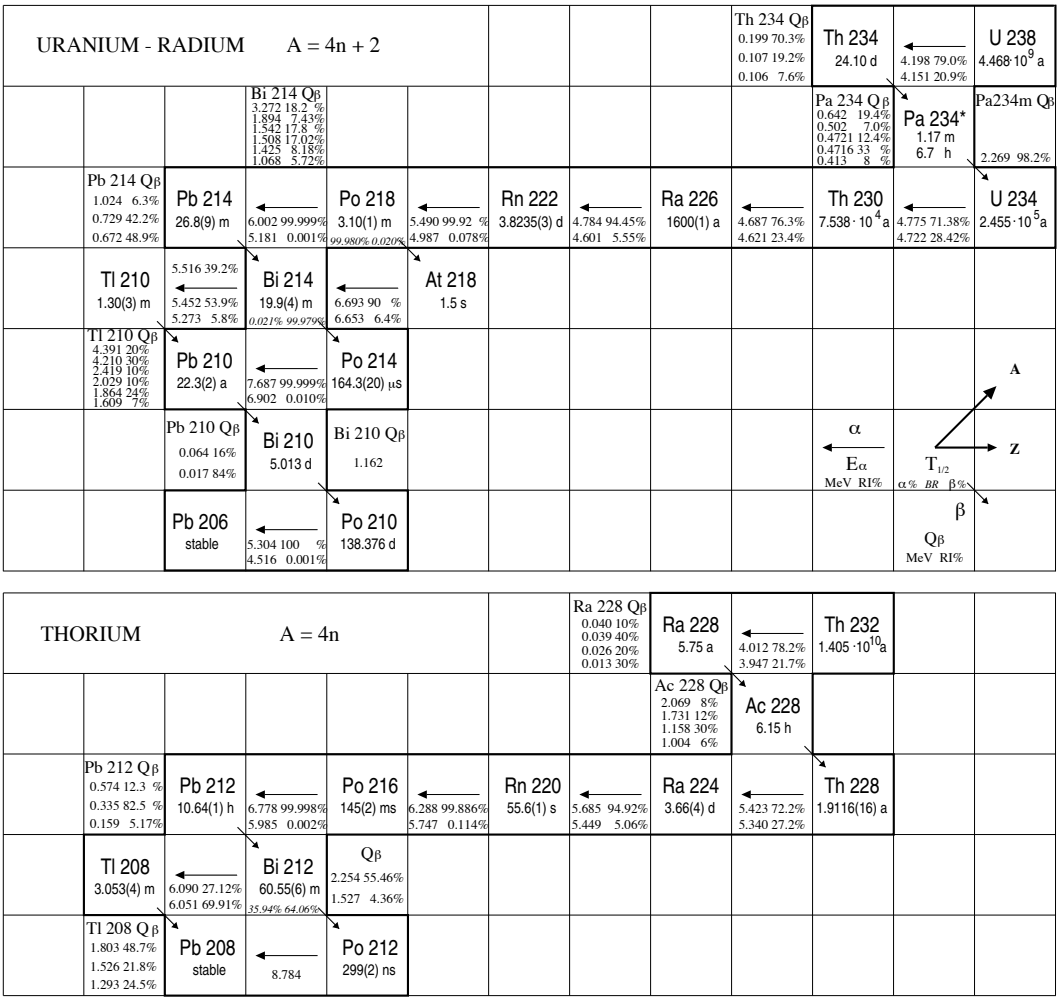

Figure I.1: The radioactive decay chains[Far96].